

## Wheel-Rail Interaction

### Enhanced explicit finite element modelling, verification and validation

Ma, Yuewei

**DOI**

[10.4233/uuid:22f68c51-9999-453c-a1f3-5a88bd2f8cd2](https://doi.org/10.4233/uuid:22f68c51-9999-453c-a1f3-5a88bd2f8cd2)

**Publication date**

2018

**Document Version**

Final published version

**Citation (APA)**

Ma, Y. (2018). *Wheel-Rail Interaction: Enhanced explicit finite element modelling, verification and validation*. [Dissertation (TU Delft), Delft University of Technology]. <https://doi.org/10.4233/uuid:22f68c51-9999-453c-a1f3-5a88bd2f8cd2>

**Important note**

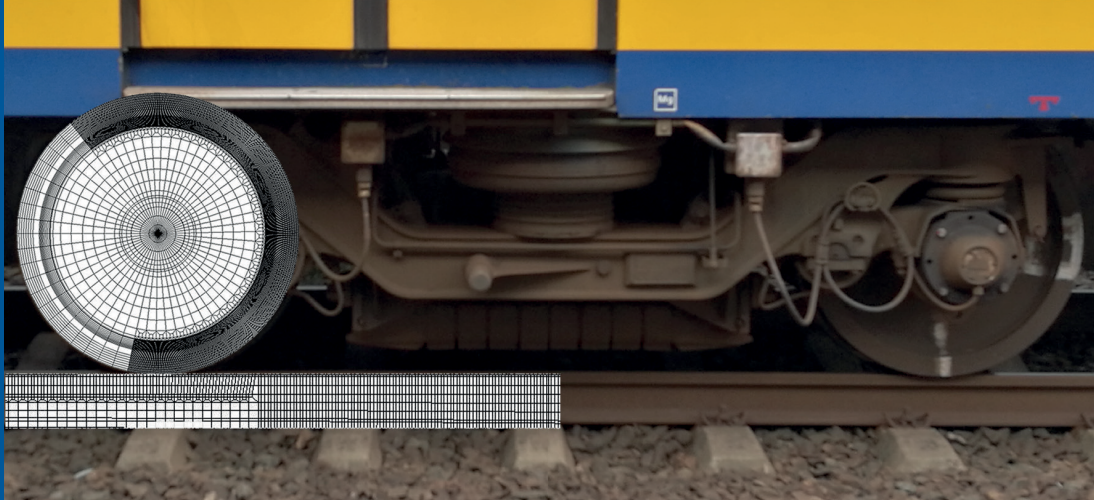
To cite this publication, please use the final published version (if applicable). Please check the document version above.

**Copyright**

Other than for strictly personal use, it is not permitted to download, forward or distribute the text or part of it, without the consent of the author(s) and/or copyright holder(s), unless the work is under an open content license such as Creative Commons.

**Takedown policy**

Please contact us and provide details if you believe this document breaches copyrights. We will remove access to the work immediately and investigate your claim.



# Wheel-Rail Interaction:

Enhanced explicit finite element modelling,  
verification and validation

Yuewei Ma

# **WHEEL-RAIL INTERACTION**

ENHANCED EXPLICIT FINITE ELEMENT MODELLING,  
VERIFICATION AND VALIDATION



# **WHEEL-RAIL INTERACTION**

ENHANCED EXPLICIT FINITE ELEMENT MODELLING,  
VERIFICATION AND VALIDATION

## **Proefschrift**

ter verkrijging van de graad van doctor  
aan de Technische Universiteit Delft,  
op gezag van de Rector Magnificus Prof. dr. ir. T.H.J.J. van der Hagen  
voorzitter van het College voor Promoties,  
in het openbaar te verdedigen op woensdag, 19 december, 2018 om 10:00 uur

door

**Yuewei MA**

Master of Engineering in Engineering Mechanics,  
Dalian University of Technology, China  
geboren te Ruzhou, China.

Dit proefschrift is goedgekeurd door de promotoren

Samenstelling promotiecommissie:

Rector Magnificus,	voorzitter
Prof. dr. ir. R.P.B.J. Dollevoet	Technische Universiteit Delft, promotor
Dr. ir. V.L. Markine	Technische Universiteit Delft, copromotor

*Onafhankelijke leden:*

Prof. dr. ir. J.G. Rots	Technische Universiteit Delft
Prof. dr. S. Bruni	Politecnico di Milano, Italy
Prof. dr. A. Ekberg	Chalmers University of Technology, Sweden
Prof. dr. ir. E. van der Heide	University of Twente
Dr. I.Y. Shevtsov	ProRail
Prof. dr. I.M. Richardson	Technische Universiteit Delft, reservelid

The author would like to thank China Scholarship Council of Chinese Government for their financial support.



*Keywords:* Wheel-rail interaction, Finite element modelling, Verification, Experimental validation

*Printed by:* Gildeprint - Enschede

Copyright © 2018 by Y. Ma (yueweima99@gmail.com)

ISBN 978-94-6323-453-5

An electronic version of this dissertation is available at  
<http://repository.tudelft.nl/>.

To my parents,  
my daughter & my wife

# Propositions

accompanying the dissertation

## **WHEEL-RAIL INTERACTION:**

ENHANCED EXPLICIT FINITE ELEMENT MODELLING, VERIFICATION AND VALIDATION

by

**Yuewei MA**

1. The best way to understand the wheel-rail (W/R) contact is to measure it.
2. The rapid development of numerical simulations of W/R interaction mirrors the increasing demand of well-established experimental techniques.
3. Using the finite element method, detailed modelling/analysis of the vehicle-track interaction can be performed, as long as the computing power is sufficiently high.
4. Verifications & validations ensure that the model has a sufficient accuracy, instead of being 100% accurate.
5. For newly-built cities the elevated monorail will be preferred over the subway.
6. The imperfections of other people help you to become better.
7. Passion for work is as air/water for human life.
8. For teenagers the earlier the social responsibility is taken, the better they are prepared for adult life.
9. Being critical on your past performance keeps you going upward.
10. Knowledge itself cannot create wealth, but making proper use of knowledge can.

These propositions are regarded as opposable and defensible, and have been approved as such by the (co)promoters Prof. dr. ir. R.P.B.J. Dollevoet and Dr. ir. V.L. Markine.





# SUMMARY

Nowadays, wheel-rail (W/R) interfaces are suffering from the practical problems (e.g. wear, rolling contact defects) with the increase of train speed and traffic density. For accurate prediction of wear and/or growth of rolling contact defects, rapid determination of detailed contact responses (i.e. contact stresses & strains) using numerical methods, is necessary.

As one of the numerical methods, the explicit finite element (FE) method has been increasingly used due to its striking versatility (i.e., the consideration of dynamic effects, material and geometrical non-linearities). But there are still several FE modelling challenges to be addressed. First, the calculation accuracy & efficiency of the FE method can not be automatically guaranteed. Second, the default values of the interface parameters provided in the commercial FE packages are not always suitable for the modelling of W/R rolling contact. Third, the detailed verification & validation methods/procedures for the FE model of W/R interaction are still in demand.

It is thus motivated to perform an in-depth study on the performance (i.e. accuracy and efficiency) of the explicit FE method applied to the analysis of the dynamic W/R frictional rolling contact behaviour. Through this study, it is aimed to enrich the detailed knowledge of W/R interaction, and help the researchers in the field of railway engineering to judge the benefits and drawbacks of explicit FE simulations. The dissertation is divided into four parts, in which four research problems are addressed.

The first part presents an explicit model of a wheel rolling over a rail developed in LS-DYNA and a study on how to improve the accuracy and efficiency of such a model. To begin with, a novel modelling strategy is devised. According to this strategy, a 2D geometrical W/R contact model is used for improving the performance of 3D FE W/R contact model by (1) adjusting the two contact bodies to the “just-in-contact” position, (2) detecting the potential contact areas wherein the FE mesh refinement to be applied, (3) determining the actual rolling radius of the wheel based on which the right amount of traction is calculated and applied to the wheel. The results of the 3D simulations performed showed that the use of such strategy can lead to: (1) almost 100% success rate of the FE simulations by decreasing the “gaps or penetrations” to the order of a micrometre or even less, (2) a significant reduction (2~3 times) of the calculation time as compared to the regular mesh by using the adaptive mesh refinement procedure, (3) efficient (within a short travelling distance of 50 mm) steady-state tangential solutions by applying the appropriate amount of traction.

The second part concentrates on how the choice of the four important interface parameters such as the penalty scale factor, mesh uniformity, mesh density and contact damping, affects the accuracy of the explicit FE-based contact solutions. The phenomenon of “contact instability”, which is associated with the unrealistic oscillated contact responses, can be observed, when the interface parameters are selected improperly:

(1) too small (e.g. 0.1 by default) or too large (e.g. 200) penalty scale factor, (2) non-uniform and coarse mesh (size of 2.0 mm or even larger), (3) over-critical contact damping (e.g. increased by a factor of 1.8). To maintain the contact stability, guidelines for selecting the proper interface parameters are formulated. Following these guidelines, a set of the interface parameters (i.e. penalty scale factor 12.8, mesh size 1.0 mm, default damping factor of 0.8), suitable for studied W/R contact problem has been determined and used in the simulations. The results of the numerical simulations have shown that the suggested interface parameters provide stable and accurate solution of the rolling contact problem, which indicates that the proposed guidelines may increase the use of explicit FE method for analysing the W/R contact problems.

The third part focuses on how to carry out the verification of a FE model of W/R interaction. Given the fact that the realistic W/R profiles are used in the FE model developed here, attention is focused specifically on the non-Hertzian and non-planar contact problems. For such problems, the verification of the FE models has not been performed adequately so far. A detailed procedure of the model verification via comparison of shear stresses, slip-adhesion areas, etc., with the results of CONTACT programme (based on Kalker's exact theory) has been developed. The good agreement of the FE results with those of CONTACT indicates that the FE-based contact solutions are accurate. Therefore, the model developed here can be used as a basis for prediction of wear and rolling contact fatigue life wherein the detailed contact responses are necessary. The effect of varying operational patterns such as friction, traction, lateral shift of wheelset, on the surface/subsurface material responses is also investigated using the developed model. The results have confirmed that stress concentrations in the rail move towards the rail-head surfaces with the increase of friction and/or traction, which can be helpful for devising proper lubrication strategies so as to mitigate the interface degradation (i.e., wear, rolling contact defects).

The fourth part demonstrates how to extend/upgrade the FE model of W/R interaction developed in this study to a new level for analysing the wheel-crossing (W/C) interaction, and how to validate this model experimentally. It was shown that using the novel modelling strategy developed here about 94% calculation time of explicit FE simulations of W/C impact can be saved. At the impact moment, the FE results show that the surface normal pressure can be 4 times higher than the material yield strength, and the subsurface stress is concentrated in a small volume of material. The results of this model give more insights on the causes of rapid degradation of railway crossings. The validity of the FE model is assessed by comparing the FE simulated results to the field observed running bands of W/C contact and to the measured acceleration of the crossing nose. The good agreement of the FE results with the field measurements confirms that the FE model enhanced by the proposed modelling strategy can represent the reality well and is an accurate tool to be used for further design or optimisation of railway crossings.

To summarise, the four research problems in the explicit FE modelling of the W/R interaction have been addressed here, and it was demonstrated that the novel modelling strategy proposed can strongly push forward the boundaries of what the explicit FE models can do. The acquired knowledge of W/R interaction will be useful for future scientific and industrial research activities.

# SAMENVATTING

Tegenwoordig, wiel-rail (W/R) interfaces lijden onder praktische problemen zoals slijtage en rollende contactdefecten, met de toenemende snelheden van de treinen en de toenemende verkeersintensiteit. Voor een nauwkeurige voorspelling van de slijtage en/of de groei van de rollende contactdefecten, is een snelle bepaling van de gedetailleerde contactreactie (d.w.z. spanningen & rekken) met gebruik van numerieke methoden noodzakelijk.

Als één van de numerieke methoden, de expliciete eindige elementen (EEM) methode wordt steeds frequenter gebruikt vanwege haar veelzijdigheid (d.w.z. de beschouwing van de dynamische effecten, materiaal en geometrische niet-lineariteiten). Ten eerste, de nauwkeurigheid van de berekening & efficiëntie van de EEM kan niet automatisch worden gegarandeerd. Ten tweede, de standaardwaarden van de interfaceparameters gegeven in de commerciële EEM pakketten zijn niet altijd geschikt voor het modelleren van W/R rollend contact. Ten derde, de gedetailleerde verificatie & validatie methoden/procedures voor de EEM model van W/R interactie zijn nog nodig.

Dit motiveert de uitvoering van een diepgaand onderzoek van de prestaties (dat wil zeggen de nauwkeurigheid en de efficiëntie) van deze expliciete methode toegepast op het rollend contactgedrag van wiel en rail. Dit onderzoek is erop gericht om gedetailleerde kennis van W/R interactie te verrijken, en om de onderzoekers in het vakgebied van railbouwkunde te helpen om voor- en nadelen van expliciete EEM simulaties af te wegen. Het proefschrift is verdeeld in vier delen, waarin vier onderzoeksproblemen worden aangepakt.

Het eerste deel presenteert een expliciet model van een wiel, ontwikkeld in LS-DYNA en een onderzoek naar de manier om de nauwkeurigheid te verbeteren. Om te beginnen, is een nieuwe modelleringsstrategie bedacht. Volgens deze strategie wordt een tweedimensionaal (2D) geometrisch wiel-rail contactmodel gebruikt om de prestaties van het driedimensionale (3D) eindige elementen wiel-rail contactmodel te verbeteren door middel van (1) het aanpassen van de twee contactlichamen aan de “just-in-contact” positie, (2) detectie van de potentiële contactgebieden waarin de EEM raster verfijning moet worden toegepast, (3) bepaling van de werkelijke rolradius van het wiel op basis waarvan de juiste hoeveelheid tractie wordt berekend en aangebracht op het wiel. De resultaten van de uitgevoerde 3D-simulaties laten zien dat het gebruik van een dergelijke strategie kan leiden tot: (1) bijna 100% slagingspercentage van de EEM simulaties door het terugbrengen van de “gaps of penetrations” tot de orde van een micrometer of zelfs minder, (2) een aanzienlijke verkorting van de rekentijd (2 tot 3 keer) in vergelijking met het gebruikelijke raster door gebruik te maken van de aangepaste rasterverfijningsprocedure, (3) efficiënte (binnen een ‘short travelling distance’ van 50 mm) steady-state tangentiële oplossingen door de juiste hoeveelheid tractie toe te passen.

Het tweede deel onderzoekt hoe de keuze van de vier belangrijke interfaceparame-

ters, zoals de schaalfactor, rasteruniformiteit, rasterdichtheid en contactdemping, van invloed is op de nauwkeurigheid van de op expliciete EEM gebaseerde contactoplossingen. Het fenomeen “contactinstabiliteit”, dat gerelateerd is aan onrealistisch oscillerende contactreacties, treedt op wanneer de interfaceparameters onjuist worden gekozen: (1) een te kleine (bijvoorbeeld standaard 0,1) of een te grote (bijvoorbeeld 200) penaltyschaalfactor, (2) een niet-gelijkmatig en te grof raster (2,0 mm of zelfs groter), (3) en over-kritische contactdemping (bijvoorbeeld verhoogd met een factor 1,8). Om de contactstabiliteit te behouden, zijn richtlijnen voor het selecteren van de juiste interfaceparameters geformuleerd. Op grond van deze richtlijnen is een set van interfaceparameters bepaald die geschikt is voor het hier bestudeerde wiel-rail contactprobleem EEM (een penaltyschaalfactor van 12,8; een maaswijdte van 1,0 mm en een standaard dempingsfactor van 0,8). Met deze set zijn de simulaties uitgevoerd. De resultaten van de numerieke simulaties hebben aangetoond dat de voorgestelde interfaceparameters een stabiele en nauwkeurige oplossing bieden voor het rolcontactprobleem EEM. Dit geeft aan dat de voorgestelde richtlijnen de toepassing van de expliciete EEM methode voor het analyseren van de wiel-rail contactproblemen kunnen bevorderen.

Het derde deel richt zich op de vraag hoe een verificatie van een EE -model m.b.t. W/R -interactie tot stand kan komen. Gezien het feit dat realistische W/R-profielen worden gebruikt in het ontwikkelde EE-model, is de aandacht specifiek gericht op de niet-Hertziaanse en niet-planaire contactproblemen. Voor dergelijke problemen is tot nu toe geen adequate verificatie van EE-modellen uitgevoerd. Een gedetailleerde procedure van de modelverificatie is ontwikkeld. Dit is bereikt door vergelijking van schuifspanningen, slip-adhesiegebieden, enz., met de resultaten afkomstig uit het CONTACT-programma (gebaseerd op de exacte theorie van Kalker). De goede overeenstemming van resultaten vanuit de EEM en die vanuit CONTACT indiceren dat de EE-gebaseerde contactoplossingen accuraat zijn. Vandaar kan het ontwikkelde model worden gebruikt als basis voor het voorspellen van slijtage en vermoeiing door een rollend contact, waarbij nauwkeurig de reacties in het contact bekend moeten zijn. Het effect van variërende operationele patronen, zoals wrijving, tractie, laterale verschuiving van wielstellen, op materiaalreacties aan het oppervlak en ondergrond wordt tevens onderzocht met behulp van het ontwikkelde model. De resultaten hebben bevestigd dat spanningsconcentraties in de rails naar de railkopoppervlakken toe bewegen wanneer wrijving en/of tractie toeneemt. Dit kan nuttig kan zijn bij het ontwikkelen van goede smeerstrategieën om de interfacedegradatie (dat wil zeggen slijtage, rollende contactgebreken) te verminderen.

Het vierde deel laat zien hoe het EE-model m.b.t. W/R-interactie, dat in deze studie is ontwikkeld, kan worden uitgebreid/verbeterd naar een niveau geschikt voor het analyseren van de wiel-wissel interactie (W/W) en hoe dit model experimenteel kan worden gevalideerd. Er is aangetoond dat met behulp van de nieuw ontwikkelde modelleringsstrategie ongeveer 94% van de rekentijd van expliciete EE-simulaties van W/W-impact bespaard kan worden. Op het moment van impact laten de resultaten vanuit EEM zien dat de oppervlaktespanning 4 keer hoger kan zijn dan de treksterkte van het materiaal en dat de ondergrondse spanning geconcentreerd is in een klein volume materiaal. De resultaten van dit model geven meer inzicht in de oorzaken van snelle degradatie van spoorwegovergangen. De validiteit van het EE-model wordt beoordeeld door de resulta-

ten vanuit de EE simulaties te vergelijken met de waargenomen veldmetingen van W/W-contact en de gemeten versnelling van het puntstuk. De goede overeenstemming tussen de EE-resultaten met de veldmetingen bevestigt dat het EE-model aangepast en verbeterd met de voorgestelde modelleringsstrategie de realiteit goed kan weergeven en een nauwkeurig hulpmiddel is om te worden gebruikt voor verdere ontwerpverbeteringen of optimalisatie van spoorwegovergangen.

Samenvattend, de vier onderzoeksproblemen in de expliciete EE-modellering van W/R-interactie zijn hier besproken en er is aangetoond dat de voorgestelde modelleringsstrategie de grenzen van wat expliciete EE-modellen kunnen sterk naar voren schuift. De opgedane kennis wat betreft W/R-interactie zal nuttig zijn voor toekomstige wetenschappelijke en industriële onderzoeksactiviteiten.



# CONTENTS

<b>Summary</b>	<b>vii</b>
<b>Samenvatting</b>	<b>ix</b>
<b>Thesis contents</b>	<b>xvii</b>
<b>1 Introduction</b>	<b>1</b>
1.1 Vehicle-track system . . . . .	2
1.2 Wheel-rail interface . . . . .	3
1.3 Solution of rolling contact problem . . . . .	4
1.4 Research problems . . . . .	6
1.5 Research approach . . . . .	8
1.6 Thesis outline . . . . .	9
References . . . . .	10
<b>2 Enhanced Explicit FE model of W/R Interaction</b>	<b>17</b>
2.1 Introduction . . . . .	18
2.2 W/R 3D-FE model. . . . .	19
2.2.1 Discretized FE model . . . . .	20
2.2.2 Challenges of FE analysis . . . . .	22
2.3 Coupling strategy . . . . .	24
2.3.1 2D-Geo analysis . . . . .	25
2.3.2 Coupled interface . . . . .	26
2.4 FE Results and discussions . . . . .	29
2.4.1 Contact clearance . . . . .	30
2.4.2 Travelling distance . . . . .	32
2.4.3 Initial slip . . . . .	36
2.4.4 Discussion: Pros of 'eFE-CS' model of W/R interaction . . . . .	38
2.5 Conclusions. . . . .	39
References . . . . .	39
<b>3 Effect of W/R Interface Parameters on Contact Stability</b>	<b>43</b>
3.1 Introduction . . . . .	44
3.2 Recap explicit FE theory . . . . .	46
3.2.1 Stability of central difference method . . . . .	46
3.2.2 Penalty method . . . . .	47
3.2.3 Contact stability . . . . .	48
3.3 Underlying challenges and possible solutions. . . . .	49
3.3.1 Interface parameters. . . . .	49
3.3.2 Approaches for addressing challenges . . . . .	49



3.4	Results and discussions . . . . .	50
3.4.1	Contact stiffness . . . . .	51
3.4.2	Mesh uniformity . . . . .	53
3.4.3	Mesh density. . . . .	56
3.4.4	Contact damping . . . . .	59
3.4.5	Discussion: Applicability of suggested guidelines & parameters . . . . .	61
3.5	Conclusions. . . . .	62
	References . . . . .	64
<b>4</b>	<b>Modelling verification and effect of operational patterns on contact responses</b>	<b>67</b>
4.1	Introduction . . . . .	68
4.2	Modelling verification. . . . .	69
4.2.1	CONTACT model. . . . .	69
4.2.2	Integration CONTACT with FE model . . . . .	70
4.2.3	Verification results . . . . .	73
4.3	Parametric study . . . . .	78
4.3.1	Friction coefficient. . . . .	79
4.3.2	Traction force . . . . .	82
4.3.3	Contact point . . . . .	85
4.3.4	Material property . . . . .	88
4.4	Discussions: experimental validations . . . . .	90
4.5	Conclusions. . . . .	92
	References . . . . .	93
<b>5</b>	<b>Modelling and experimental validation of wheel-crossing impact</b>	<b>97</b>
5.1	Introduction . . . . .	98
5.2	Modelling of W/C impact . . . . .	102
5.2.1	3D W/C FE model . . . . .	103
5.2.2	Coupling strategy . . . . .	106
5.2.3	Effectiveness of 'eFE-CS' model . . . . .	109
5.2.4	Discussion: Pros of 'eFE-CS' model of W/C impact. . . . .	114
5.3	Experimental validations . . . . .	116
5.3.1	Model validation via transition regions . . . . .	116
5.3.2	Model validation via crossing accelerations . . . . .	119
5.4	FE simulation results and discussions. . . . .	123
5.4.1	Surface stress response. . . . .	123
5.4.2	Subsurface stress response. . . . .	126
5.4.3	Discussions of results . . . . .	128
5.5	Conclusions. . . . .	128
	References . . . . .	129
<b>6</b>	<b>Conclusions and recommendations</b>	<b>133</b>
6.1	Conclusions. . . . .	134
6.2	Recommendations . . . . .	137

---

<b>Appendix A</b>	<b>139</b>
A.1 Experimental methods: recent advances . . . . .	139
References . . . . .	139
<b>Curriculum Vitae</b>	<b>143</b>
<b>List of Publications</b>	<b>145</b>
<b>Acknowledgements</b>	<b>147</b>



# THESIS CONTENTS

The material presented in this dissertation is based on the following papers:

## PAPER A

**Yuwei Ma**, Valeri Markine, Abdul Ahad Mashal, Mingfa Ren, *Improving the performance of finite element simulations on the wheel–rail interaction by using a coupling strategy*, Proceedings of the Institution of Mechanical Engineers, Part F: Journal of rail and rapid transit, **232**(6), 1741-1757 (2018).

## PAPER B

**Yuwei Ma**, Valeri Markine, Abdul Ahad Mashal, Mingfa Ren, *Effect of wheel-rail interface parameters on contact stability in explicit finite element analysis*, Proceedings of the Institution of Mechanical Engineers, Part F: Journal of rail and rapid transit, **232**(6), 1879-1894 (2018).

## PAPER C

**Yuwei Ma**, Valeri Markine, Abdul Ahad Mashal, Mingfa Ren, *Modelling verification and influence of operational patterns on wheel –rail tribological behaviour*, Tribology International, **114**, 264-281 (2017).

## PAPER D

**Yuwei Ma**, Abdul Ahad Mashal, Valeri Markine, *Modelling and experimental validation of dynamic impact in 1: 9 crossing panel*, Tribology International, **118**, 208-226 (2018).



# 1

## INTRODUCTION

*This chapter first introduces the background of this work, including the vehicle-track systems, the deterioration of wheel-rail interfaces, the solutions of rolling contact problems. Following that, the research problems, approaches as well as the outlines of this dissertation are presented.*

## 1.1 VEHICLE-TRACK SYSTEM

Railway provides one of the most important means of transferring passengers, raw materials, fuels, etc. Despite of certain limitations (e.g. huge capital investment for construction, reduced flexibility of time and routine, etc.), railway transport retains many distinct advantages, such as safe & dependable, energy-saving and large capacity, as compared to other modes of transport (e.g. road, air, waterway, etc.).

Figure 1.1a shows a typical example of railway passenger transportation, where the passing vehicle is supported and guided by the track fixed on the ground (also called vehicle-track system).

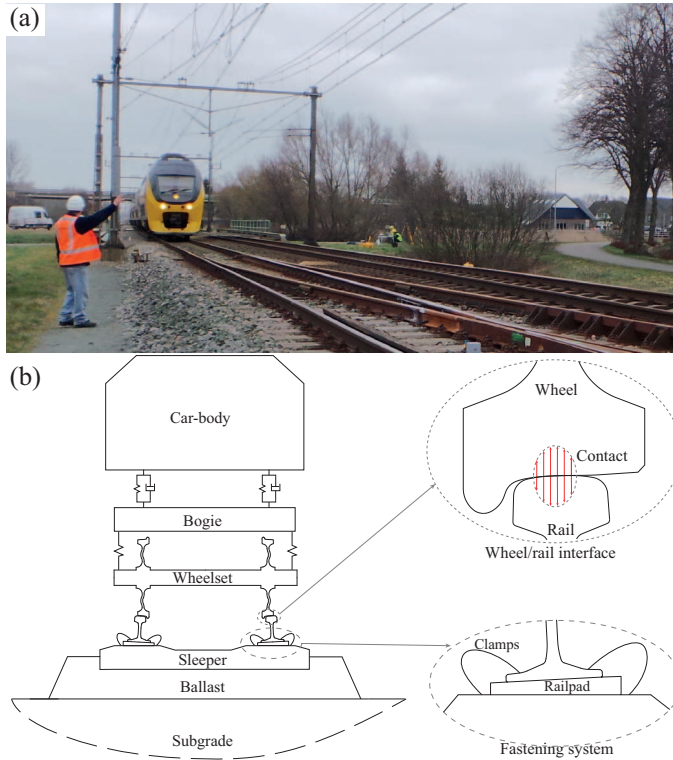


Figure 1.1: Railway transportation: (a) Vehicle and track (photo taken from the field); (b) Schematic graph of the components of vehicle-track interaction.

For the simplicity of notation, the vehicle-track system (See Figure 1.1b) is categorised as:

- The vehicle: including carbody, bogie and wheelset;
- Wheel/rail contact: referring to the interaction between W/R interfaces;
- The track: including the rail, the fastening system (i.e. the clamps and the rail pads), the sleeper and the sleeper support (i.e. ballast and subgrade).

This study focuses on the wheel-rail interface of the vehicle-track system.

## 1.2 WHEEL-RAIL INTERFACE

Nowadays, the ever-increasing train speed and axle loads lead to the excessive use and overloading of both the railway vehicles and the tracks. As a consequence, the rail damage problems, such as the wear, rolling contact defects (i.e. corrugation, head check, spalling, squats, etc.), are commonly seen on the wheel-rail (W/R) interfaces. Figure 1.2 shows the typical damage problems.

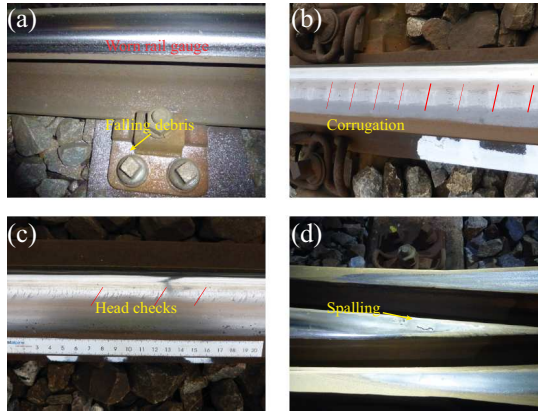


Figure 1.2: Damage of W/R interface: (a) Wear; (b) Corrugation; (c) Head checking; (d) Spalling at crossing rail.

W/R interface is thus widely recognised as one of the most sensitive elements of vehicle-track system. To gain deep insight into the mechanism of the damage phenomena, extensive studies have been carried out by a number of researchers and engineers during the last decades. Usually, three approaches, namely, experimental, numerical, or the combination of both, are used.

Detailed information about the recent advances of the experimental methods can be found in [Appendix A](#). Although the experimental studies are important, they share the same kind of disadvantages such as being time-consuming and expensive.

**Numerical methods: state-of-the-art** Alternatively, numerical methods are used to study the dynamic performance of the vehicle-track system and wheel-rail interaction.

For instance, using the multi-body system (MBS) dynamics method, the dynamic responses of the vehicle-track system such as displacements, accelerations and forces can be assessed and obtained [1, 2, 32, 75, 78]. Yet, in the MBS simulations, all the components of the vehicle-track system are usually assumed to be rigid. The contact models used therein are often based on the assumptions of elastic (no material plasticity considered) half-space [40]. Thus, the detailed contact solutions (i.e. stress/strain results in the W/R interfaces) are not available.

The (explicit) FE method [100, 101, 107], as opposed to the MBS method, is more frequently used due to its striking versatility (i.e., the consideration of dynamic effects, material and geometrical non-linearities) [60, 61, 95, 98, 99, 104]. However, such FEM simulations usually demand more computational expense/power than that of MBS because of the large number of elements discretised. Also, it is difficult to be used in the



analyses, where the multiple simulations are necessary e.g. in the design improvement and optimisation [51]. It should be noted that for a fast analysis of W/R interaction, a 2-D FE model can be used as well [59].

The aforementioned numerical methods provide the great flexibility to analyse the effect of varying material properties [48, 66, 97], local contact geometries [19, 33, 34, 55] and W/R kinematics [9, 21–23, 31], on the performance of vehicle-track system at lower computational and financial costs as compared to the experimental methods. Also, the contact responses such as the size and shape of contact areas, the normal & shear contact stresses [40, 104], which are still difficult to measure directly with the current available experimental techniques [50], can be determined.

Moreover, using the engineering models such as Archard's law [5], Whole life rail model [11, 13], Dang van criterion [84], Ekberg's model [20], Paris' law [65], etc., the evolution of W/R profiles through wear [4, 7, 12, 49, 82], and/or the growth of RCF defects [8, 17, 18, 24, 35, 52, 72] can be predicted.

Aiming to the compromise between wear and RCF, the optimal design of contact profiles [42, 44, 58, 63, 64, 77, 80, 94, 96], material microstructures [14, 41, 57, 70], as well as maintenance procedures [25, 54, 73] could be found.

From the literature review presented above, it can be learned that numerical methods have been increasingly used to deal with the practical problems (e.g. wear, RCF damage) of vehicle-track interaction. The results of numerical simulations tend to enrich the knowledge of the formation & evolution mechanisms of wear and RCF damage. Also, using the knowledge acquired, appropriate strategies of maintenance such as grinding, welding, lubrication, etc., can be made and implemented. This will ultimately contribute to a long service life of both the wheels and the rails.

However, regarding the validity of these simulation results, the solution of rolling contact problem always plays an important role, since the resulting contact responses are used as inputs for the numerical simulations [88]. Thus, a detailed literature study on the solution of rolling contact problems is presented in the next section.

### 1.3 SOLUTION OF ROLLING CONTACT PROBLEM

Usually, the rolling contact problem is divided into two subproblems [40], namely:

- Normal contact: to determine the area of contact patches and to predict the distribution of normal pressure.
- Tangential contact: to explore the relationship between creepage and creep force, and to estimate the distribution of tangential shear stress.

To tackle the problem of normal contact, the classical Hertz theory, in which the contact patch is considered to be elliptical and the normal surface pressure is assumed to be semi-ellipsoidal, was developed [27]. But this theory is limited to the study on the straight track [75], in which the Hertzian assumptions are applicable. For the study on the curved track or turnouts, non-Hertzian theories (i.e. multi-Hertzian [67, 68], semi-Hertzian [6]) can be used alternatively. These normal contact theories have been incorporated with the commercial MBS computer codes (e.g. CONPOL, DYNARIL, VAMPIRE, etc. [75]).

Regarding the problem of tangential contact, significant contributions were made by Prof. J.J. Kalker, as one of the key contributors [45], to describe the relationship between creepages and creep forces [74, 103]. A series of representative theories (See Ref.[103]) such as linear theory [36], simplified theory [37], etc., were developed. For instance, linear theory [36], which uses the well known “Kalker coefficients”, is shown to be quite effective in the cases of small creepages and spin [93]. For large creepages, the non-linear creepage-force relations of Vermeulen-Johnson [86] and Shen-Hedrick-Elkins [76] are suggested according to [93].

In general, those contact methods can be divided into three categories [88]: (1) Simplified/approximate methods, (2) boundary element method, and (3) finite element method. The latter two are the advanced numerical methods [79]. A general overview on the three classes of contact methods is given next.

**Simplified/approximate methods** The simplified theory [37] is based on approximating the relation between the surface traction and the surface displacement by using compliance (flexibility) parameters [103]. Nowadays, the simplified theory is still commonly used for predicting the creep forces [103].

Based on the simplified theory, the computational programme of FASTSIM was developed [92]. This programme has been further incorporated with the commercial MBS computer packages [75].

However, the simplified theory introduce errors in the tangential forces in the range of 5–10% as compared to that of CONTACT (based on Kalker’s exact theory) [93] described below.

**Boundary element method** As opposed to the simplified theory, the complete/exact three-dimensional rolling contact theory [38] is derived from the principle of complementary virtual work. Using this principle, the solution of the rolling contact problem, which is a strictly convex minimisation problem with linear equality and inequality constraints [39], is determined by maximising the complementary energy over all admissible functions that satisfy those constraints [40, 89].

This theory is implemented in the well-known program CONTACT [40, 90] using the boundary element (BE) method. The exact theory is also called BEM(boundary element method)-based theory/method [79].

As one distinct feature of the BEM-based method ([40, 90]), only the surfaces of two contact bodies need to be discretised. Thus, a much smaller amount of elements would be generated than that of finite element (FE) method, where both the surfaces and the interior of contact bodies are divided into a finite number of non-overlapping regions [40]. On the other hand, the use of half-space assumptions [103] in this theory allows for the prompt determination of influence functions, through which the deformations of the surface in contact are related to the tractions [89]. All of these prominent features contribute to a much better calculation efficiency than FE method.

Moreover, CONTACT [90] is able to deal with arbitrary surfaces of the two contacting bodies, which result in the non-elliptic contact patches. It is widely used for detailed investigating the effect of rail irregularities and noise [89] and for the modelling of the relation between creep and creep forces [91].

However, due to the assumption of elastic half-space, CONTACT used to be not capable of taking the plastic deformation into account [46]. More recently, preliminary attempts [85] have been made to model the local plasticity and study the effect of material plasticity on the wheel-rail friction.

**Finite element method** As another advanced numerical method, FE method is generic, flexible [79, 88] for addressing the contact problems [106]. This is because it accounts for the material and geometrical non-linearities [107].

Nowadays, it becomes a popular tool used in the field of railway engineering. A variety of models have been created for different engineering purposes [10, 16, 56, 71, 72, 83, 87, 99, 99, 104].

Generally, based on the different solving procedures, the FE methods are classified into two main categories: namely [26, 81], implicit and explicit.

In implicit FE method, the dynamic equilibrium equation is solved iteratively (e.g. Newton-Raphson iterations), until the convergence criteria are satisfied. As one drawback of this method, the calculation of the inverse stiffness matrix, which is computationally expensive [81], is needed. Moreover, due to the inaccurate modelling of the dynamic effects [26, 81], the implicit FE method [10, 56, 71, 72, 83, 99] is no longer able to meet the increasing expectations of higher degree of realism.

As opposed to the implicit method, the explicit method finds the new state directly based on information of previous states [15, 26, 100, 101]. The equation of motion for the body is solved using the central difference method [81]. Using this method, there is no need to invert the stiffness matrix [3, 26, 29, 81]. This enables the explicit FE method to avoid certain difficulties of non-linear programming that the implicit method usually has [102]. Moreover, the contact constraints are relatively easy to implement by using the penalty method [106], and the dynamic effects are fully considered. However, as one of the disadvantages, the explicit FE method is computationally expensive due to the small time integration steps.

From the overview of the solutions of rolling contact problems, it can be learned that all the three kind of methods have their own strengths and weaknesses. Thus, every model should be made useful based on its advantages. For instance, simplified/approximate methods can be used, if a quick calculation of forces is needed. BE method (CONTACT) should be used, when the contact stresses are needed for multiple loading scenarios. FE method can be used, if it is necessary to study the single cases in full detail.

In the present work, only the latter two, namely BE and FE methods, are used. Among them, BEM (i.e. CONTACT See Chapter 4) is used as a reference for the purpose of FE model verification, while the explicit FE method is adopted to model the W/R interaction and is discussed all throughout this dissertation.

## 1.4 RESEARCH PROBLEMS

Although the explicit FE method, nowadays, is a preferable choice due to its striking versatility (i.e. the consideration of dynamic effects, material and geometrical non-linearities) for the analysis of rolling contact problems, there are still several challenges of FE-based contact modelling to be addressed. These challenges involve:

- Accuracy & efficiency of FE models: The calculation accuracy & efficiency of the FE method applied for determining the detailed contact responses of W/R interaction, can not be automatically guaranteed [102]. For instance, the initial “gap or penetration” between contact bodies would trigger the problems of divergence in the implicit FE analyses [3] or the failure of the explicit FE analyses [102]. Here, the “gap or penetration” are induced by a-priori unknown contact area. Also, redundant, insufficient or mismatched mesh refinements in that area can lead to either prohibitive calculation expenses or inaccurate implicit/explicit FE solutions [3].
- Rules/guidelines for the choice of interface parameters: Program-default values of interface parameters (i.e. contact stiffness/damping) are not always suitable for the analysis of W/R interaction. The improper choice of interface parameters will lead to the unrealistic contact responses [102]. Also, there are no rules/guidelines for making the choice of interface parameters that are universally applicable [28, 30, 47, 105, 106]. Regarding the specific problem of W/R frictional rolling contact, more research attention on the effect and the selection of interface parameters should be drawn.
- Procedures of FE model verification: The detailed methods/procedures of FE model verification are still in demand. The verification of FE models, which focus on the Hertzian contact problems [16, 104], has been performed successfully through the comparison of FE results of normal pressure, shear stress and slip-adhesion areas with that of CONTACT. In contrast to the Hertzian contact problems, the accuracy of the FE models, which are developed to analyse the non-Hertzian contact problems (the realistic W/R profiles are used [87, 99]), has been assessed mainly through the comparison of contact forces and/or normal pressure. The other responses of shear stress, slip-adhesion area, are excluded. Thus, for the problems of non-Hertzian contact, the verification of FE models has not been performed adequately. Consequently, the model without being verified may generate subtle inaccuracy in the simulation results that being unnoticed can lead to wrong decisions [102].
- Flexibility of FE model & Procedures of experimental validation: The lack of model flexibility often costs much time/efforts to analyse different scenarios. Here, the flexibility refers to whether the FE model is capable of easily adjusting from one scenario to another. To examine the flexibility of the developed FE model of W/R interaction, it should be extended/upgraded first and further applied for analysing the dynamic behaviour of wheel-crossing (W/C) interaction.

Also, to assess the validity of the FE model of W/C interaction, well-demonstrated experimental validations are necessary. Here, the validation is defined as the assessment of the computational accuracy of the numerical simulations by comparing it with the experimental data [62]. The major difference between validation and verification lies in whether the real world results (experimental data) are used. Nowadays, there are no well-accepted experimental methods available that can directly measure the intangible local stresses within the contact patches [104]. For this reason, the accuracy of the FE models has to be assessed indirectly [53]

through the comparison of the acquired real-time strains and/or accelerations with that of FE results. However, these experimental validations are mostly focused on the single selected measurement instead of validating from the statistical/stochastic perspectives [43, 69]. In short, the problem of the experimental validations in terms of the FE-based contact models is still open to be addressed.

Learning from the modelling challenges listed above, four research questions are formulated as follows.

- Q1:** *What kind of measures should be taken to guarantee and to improve the calculation accuracy and efficiency of the FE model for the analysis of W/R interaction?*
- Q2:** *What is the effect of the interface parameters (penalty scale factor, mesh density, mesh uniformity, contact damping) on the performance of the explicit FE model of W/R interaction? How to make the choice of interface parameters, that are suitable for the analysis of W/R interaction?*
- Q3:** *How to carry out the verification of the FE models that use realistic W/R profiles?*
- Q4:** *Is it possible to extend/upgrade the FE model of W/R interaction to a new level for analysing the W/C impact behaviour? How to validate the accuracy of this model experimentally?*

In this dissertation, all these four research questions, which are novel and have not been resolved before, are to be dealt with.

## 1.5 RESEARCH APPROACH

To address the research problems listed above, both numerical and experimental studies are carried out. The research approach, which is based on the following numerical models and field measurements, is briefly described here.

**3D finite element model** The 3D FE models of wheel and rail is developed in ANSYS LS-DYNA. By using the FE model, among others the following contact properties can be obtained:

- Surface responses: including the contact pressure, shear stress, stick-slip areas, etc.
- Subsurface responses: including the Von-Mises stresses, plastic deformations, etc.

**2D geometrical contact model** The 2D geometrical contact model is developed in MATLAB to determine the contact properties such as,

- ‘Just-in-contact’ point: a contact positioning between wheel and rail, where the two rigid contact bodies touch each other without or with a tolerable contact gap or penetration.

- Potential contact area: the region with high susceptibility for the contact to occur. Usually, the size of the potential contact area should be prescribed to fully encompass the real contact area to guarantee the accuracy of the contact solutions.
- Local wheel rolling radius: the vertical distance from the 'Just-in-contact' point to the wheel axle centre.

These contact properties are used as an input for the FE model to apply the mesh refinement.

**CONTACT model** CONTACT is a rigorous model, of which the correctness and accuracy have been proven [93]. In this study, it is used to assess the accuracy of the developed FE model of W/R interaction via comparing the resulting shear stress, slip-adhesion area, etc.

**Field measurements** The following measurements were used for the validation of W/C model.

- 3D acceleration measurements of crossings were also performed using ESAH-M (i.e. Elektronische System Analyse Herzstijckbereich – Mobil, a track-side acceleration measurement device), by which the magnitude and position of the impact can be recorded.
- The wheel transition regions (i.e. the length of collateral running bands on the crossing rail) are measured on the track using rulers.

## 1.6 THESIS OUTLINE

Following the approach described above, the structure of this dissertation is organised below.

First, an explicit FE model of a wheel rolling over a rail is developed and presented. To improve the performance of the FE model, a novel modelling strategy, in which the 2D-geometrical contact model is employed, is devised and implemented. The effectiveness of such a modelling strategy is demonstrated. These are described in [Chapter 2](#).

Second, the effect of interface parameters on the explicit FE-based contact solutions of W/R interaction is studied. Also, the guidelines for selecting suitable W/R interface parameters are formulated in [Chapter 3](#).

Third, the verification of explicit FE model of W/R interaction against the CONTACT model is performed. The detailed procedure of FE model verification is developed. The results of the model verification are shown in [Chapter 4](#).

Fourth, the FE-based modelling study of W/C impact and experimental validation of that model is carried out. The details of the modelling study and validations are presented in [Chapter 5](#).

Finally, the main conclusions are summarised, and recommendations for future work are made in [Chapter 6](#).

## REFERENCES

- [1] S. Alfi and S. Bruni. Mathematical modelling of train–turnout interaction. *Vehicle System Dynamics*, 47(5):551–574, 2009.
- [2] C. Andersson and A. Johansson. Prediction of rail corrugation generated by three-dimensional wheel–rail interaction. *Wear*, 257(3-4):423–434, 2004.
- [3] ANSYS, Inc. Ansys user’s manual: Structural analysis guide. *ANSYS Inc*, 2013.
- [4] A. Anyakwo, C. Pislaru, A. Ball, and F. Gu. Modelling and simulation of dynamic wheel–rail interaction using a roller rig. In *Journal of Physics: Conference Series*, volume 364, page 012060. IOP Publishing, 2012.
- [5] J. Archard. Contact and rubbing of flat surfaces. *Journal of applied physics*, 24(8):981–988, 1953.
- [6] J. B. Ayasse and H. Chollet. Determination of the wheel rail contact patch in semi-hertzian conditions. *Vehicle System Dynamics*, 43(3):161–172, 2005.
- [7] A. Beheshti and M. M. Khonsari. An engineering approach for the prediction of wear in mixed lubricated contacts. *Wear*, 308(1-2):121–131, 2013.
- [8] A. Bernasconi, M. Filippini, S. Foletti, and D. Vaudo. Multiaxial fatigue of a railway wheel steel under non-proportional loading. *International Journal of Fatigue*, 28(5-6):663–672, 2006.
- [9] Y. Bezin, S. D. Iwnicki, and M. Cavalletti. The effect of dynamic rail roll on the wheel–rail contact conditions. *Vehicle System Dynamics*, 46(S1):107–117, 2008.
- [10] M. Bijak-Żochowski and P. Marek. Residual stress in some elasto-plastic problems of rolling contact with friction. *International Journal of Mechanical Sciences*, 39(1):15–32, 1997.
- [11] P. J. Bolton and P. Clayton. Rolling—sliding wear damage in rail and tyre steels. *Wear*, 93(2): 145–165, 1984.
- [12] F. Braghin, R. Lewis, R. S. Dwyer-Joyce, and S. Bruni. A mathematical model to predict railway wheel profile evolution due to wear. *Wear*, 261(11-12):1253–1264, 2006.
- [13] M. C. Burstow. Whole life rail model application and development for rssh–continued development of an rcf damage parameter. *Rail Standards and Safety Board, London*, 2004.
- [14] C. Chattopadhyay, S. Sangal, K. Mondal, and A. Garg. Improved wear resistance of medium carbon microalloyed bainitic steels. *Wear*, 289:168–179, 2012.
- [15] S. Damme, U. Nackenhorst, A. Wetzel, and B. W. Zastrau. On the numerical analysis of the wheel–rail system in rolling contact. In *System dynamics and long-term behaviour of railway vehicles, track and subgrade*, pages 155–174. Springer, 2003.
- [16] X. Deng, Z. Qian, and R. Dollevoet. Lagrangian explicit finite element modeling for spin-rolling contact. *Journal of Tribology*, 137(4):041401, 2015.
- [17] B. Dirks and R. Enblom. Prediction model for wheel profile wear and rolling contact fatigue. *Wear*, 271(1-2):210–217, 2011.
- [18] G. Donzella, A. Mazzù, and C. Petrogalli. Competition between wear and rolling contact fatigue at the wheel–rail interface: some experimental evidence on rail steel. *Proceedings of the Institution of Mechanical Engineers, Part F: Journal of Rail and Rapid Transit*, 223(1): 31–44, 2009.
- [19] A. Ekberg and J. Marais. Effects of imperfections on fatigue initiation in railway wheels. *Proceedings of the Institution of Mechanical Engineers, Part F: Journal of Rail and Rapid Transit*, 214(1):45–54, 2000.
- [20] A. Ekberg, E. Kabo, and H. Andersson. An engineering model for prediction of rolling contact fatigue of railway wheels. *Fatigue & Fracture of Engineering Materials & Structures*, 25(10): 899–909, 2002.
- [21] J. Evans and S. D. Iwnicki. Vehicle dynamics and the wheel/rail interface. 2002.

- [22] T. N. Farris, L. M. Keer, and R. K. Steele. The effect of service loading on shell growth in rails. *Journal of the Mechanics and Physics of Solids*, 35(6):677–700, 1987.
- [23] D. I. Fletcher and J. H. Beynon. Equilibrium of crack growth and wear rates during unlubricated rolling-sliding contact of pearlitic rail steel. *Proceedings of the Institution of Mechanical Engineers, Part F: Journal of Rail and Rapid Transit*, 214(2):93–105, 2000.
- [24] F. J. Franklin, I. Widiyarta, and A. Kapoor. Computer simulation of wear and rolling contact fatigue. *Wear*, 251(1-12):949–955, 2001.
- [25] S. L. Grassie. Rolling contact fatigue on the british railway system: treatment. *Wear*, 258(7-8):1310–1318, 2005.
- [26] F. J. Harewood and P. E. McHugh. Comparison of the implicit and explicit finite element methods using crystal plasticity. *Computational Materials Science*, 39(2):481–494, 2007.
- [27] H. R. Hertz. Über die Berührung fester elastischer Körper und über die Härte. *Journal für die reine und angewandte Mathematik*, 92:156–171, 1882.
- [28] N. Hu. A solution method for dynamic contact problems. *Computers & structures*, 63(6):1053–1063, 1997.
- [29] T. J. R. Hughes, R. L. Taylor, J. L. Sackman, A. Curnier, and W. Kanoknukulchai. A finite element method for a class of contact-impact problems. *Computer methods in applied mechanics and engineering*, 8(3):249–276, 1976.
- [30] I. Huněk. On a penalty formulation for contact-impact problems. *Computers & structures*, 48(2):193–203, 1993.
- [31] M. Ishida, T. Moto, and M. Takikawa. The effect of lateral creepage force on rail corrugation on low rail at sharp curves. *Wear*, 253(1-2):172–177, 2002.
- [32] S. Iwnick. Manchester benchmarks for rail vehicle simulation. *Vehicle System Dynamics*, 30(3-4):295–313, 1998.
- [33] S. Iwnicki. The effect of profiles on wheel and rail damage. *International Journal of Vehicle Structures & Systems*, 1(4):99–104, 2009.
- [34] X. Jin, Z. Wen, and K. Wang. Effect of track irregularities on initiation and evolution of rail corrugation. *Journal of Sound and Vibration*, 285(1-2):121–148, 2005.
- [35] E. Kabo, A. Ekberg, P. T. Torstensson, and T. Vernersson. Rolling contact fatigue prediction for rails and comparisons with test rig results. *Proceedings of the Institution of Mechanical Engineers, Part F: Journal of Rail and Rapid Transit*, 224(4):303–317, 2010.
- [36] J. J. Kalker. Survey of wheel—rail rolling contact theory. *Vehicle system dynamics*, 8(4):317–358, 1979.
- [37] J. J. Kalker. A fast algorithm for the simplified theory of rolling contact. *Vehicle system dynamics*, 11(1):1–13, 1982.
- [38] J. J. Kalker. The principle of virtual work and its dual for contact problems. *Ingenieur-Archiv*, 56(6):453–467, 1986.
- [39] J. J. Kalker. Contact mechanical algorithms. *International Journal for Numerical Methods in Biomedical Engineering*, 4(1):25–32, 1988.
- [40] J. J. Kalker. *Three-dimensional elastic bodies in rolling contact*, volume 2. Springer Science & Business Media, 1990.
- [41] J. Kalousek, D. M. Fegredo, and E. E. Laufer. The wear resistance and worn metallography of pearlite, bainite and tempered martensite rail steel microstructures of high hardness. *Wear*, 105(3):199–222, 1985.
- [42] E. Kassa and G. Johansson. Simulation of train–turnout interaction and plastic deformation of rail profiles. *Vehicle System Dynamics*, 44(sup1):349–359, 2006.
- [43] E. Kassa and J. C. O. Nielsen. Stochastic analysis of dynamic interaction between train and railway turnout. *Vehicle System Dynamics*, 46(5):429–449, 2008.



- [44] E. Kassa, C. Andersson, and J. C. O. Nielsen. Simulation of dynamic interaction between train and railway turnout. *Vehicle System Dynamics*, 44(3):247–258, 2006.
- [45] K. Knothe. History of wheel/rail contact mechanics: from redtenbacher to kalker. *Vehicle System Dynamics*, 46(1-2):9–26, 2008.
- [46] K. Knothe, R. Wille, and B. W. Zastrau. Advanced contact mechanics—road and rail. *Vehicle System Dynamics*, 35(4-5):361–407, 2001.
- [47] R. F. Kulak. Adaptive contact elements for three-dimensional explicit transient analysis. *Computer methods in applied mechanics and engineering*, 72(2):125–151, 1989.
- [48] N. Larijani, J. Brouzoulis, M. Schilke, and M. Ekh. The effect of anisotropy on crack propagation in pearlitic rail steel. *Wear*, 314(1-2):57–68, 2014.
- [49] Z. Li. *Wheel-rail rolling contact and its application to wear simulation*. PhD thesis, TU Delft, Delft University of Technology, 2002.
- [50] Z. Li. Numerical solution of wheel-rail rolling contact - some recent results, application and unsolved problems. In *Proceedings of 9th International Conference on Contact Mechanics and Wear of Rail/Wheel Systems*, pages 72–78, Chengdu, China, 2012. Southwest jiaotong university.
- [51] X. Liu, V. L. Markine, and Y. Ma. Dynamic behavior of a railway crossing: comparison of the results of multibody system dynamic and explicit fem models. 2018.
- [52] Y. Liu, L. Liu, B. Stratman, and S. Mahadevan. Multiaxial fatigue reliability analysis of rail-road wheels. *Reliability Engineering & System Safety*, 93(3):456–467, 2008.
- [53] Y. Ma, V. L. Markine, A. A. Mashal, and M. Ren. Modelling verification and influence of operational patterns on tribological behaviour of wheel-rail interaction. *Tribology International*, 114:264–281, 2017.
- [54] E. E. Magel and J. Kalousek. The application of contact mechanics to rail profile design and rail grinding. *Wear*, 253(1-2):308–316, 2002.
- [55] T. Makino, Y. Neishi, D. Shiozawa, S. Kikuchi, S. Okada, K. Kajiwara, and Y. Nakai. Effect of defect shape on rolling contact fatigue crack initiation and propagation in high strength steel. *International Journal of Fatigue*, 92:507–516, 2016.
- [56] N. K. Mandal and M. Dhanasekar. Sub-modelling for the ratchetting failure of insulated rail joints. *International Journal of Mechanical Sciences*, 75:110–122, 2013.
- [57] L. I. Markashova, V. D. Poznyakov, A. A. Gaivoronskii, E. N. Berdnikova, and T. A. Alekseenko. Estimation of the strength and crack resistance of the metal of railway wheels after long-term operation. *Materials Science*, 47(6):799–806, 2012.
- [58] V. L. Markine and C. Wan. Performance optimised geometry of railway crossings: Design and implementation. *The International Journal of Railway Technology*, 5(2), 2016.
- [59] V. L. Markine, M. J. M. M. Steenbergen, and I. Y. Shevtsov. Combatting RCF on switch points by tuning elastic track properties. *Wear*, 271(1):158–167, 2011.
- [60] J. Martínez-Casas, E. Di Galleonardo, S. Bruni, and L. Baeza. A comprehensive model of the railway wheelset–track interaction in curves. *Journal of Sound and Vibration*, 333(18): 4152–4169, 2014.
- [61] A. A. Mashal. Analysis & improvement of railway crossing using explicit finite element method. Master of Science Thesis, Delft University of Technology, 2016.
- [62] W. L. Oberkampf and T. G. Trucano. Verification and validation in computational fluid dynamics. *Progress in Aerospace Sciences*, 38(3):209–272, 2002.
- [63] B. A. Pålsson. Design optimisation of switch rails in railway turnouts. *Vehicle System Dynamics*, 51(10):1619–1639, 2013.
- [64] B. A. Pålsson. Optimisation of railway crossing geometry considering a representative set of wheel profiles. *Vehicle system dynamics*, 53(2):274–301, 2015.

- [65] P. Paris and F. Erdogan. A critical analysis of crack propagation laws. *Journal of basic engineering*, 85(4):528–533, 1963.
- [66] N. R. Paulson, J. A. R. Bomidi, F. Sadeghi, and R. D. Evans. Effects of crystal elasticity on rolling contact fatigue. *International Journal of Fatigue*, 61:67–75, 2014.
- [67] J. Piotrowski and H. Chollet. Wheel–rail contact models for vehicle system dynamics including multi-point contact. *Vehicle System Dynamics*, 43(6-7):455–483, 2005.
- [68] J. Piotrowski and W. Kik. A simplified model of wheel/rail contact mechanics for non-hertzian problems and its application in rail vehicle dynamic simulations. *Vehicle System Dynamics*, 46(1-2):27–48, 2008.
- [69] M. Pletz, W. Daves, and H. Ossberger. A wheel set/crossing model regarding impact, sliding and deformation - explicit finite element approach. *Wear*, 294:446–456, 2012.
- [70] P. Pointner. High strength rail steels—the importance of material properties in contact mechanics problems. *Wear*, 265(9-10):1373–1379, 2008.
- [71] C. L. Pun, Q. Kan, P. J. Mutton, G. Kang, and W. Yan. Ratcheting behaviour of high strength rail steels under bi-axial compression–torsion loadings: Experiment and simulation. *International Journal of Fatigue*, 66:138–154, 2014.
- [72] J. W. Ringsberg, M. Loo-Morrey, B. L. Josefson, A. Kapoor, and J. H. Beynon. Prediction of fatigue crack initiation for rolling contact fatigue. *International Journal of fatigue*, 22(3):205–215, 2000.
- [73] Y. Satoh and K. Iwafuchi. Effect of rail grinding on rolling contact fatigue in railway rail used in conventional line in japan. *Wear*, 265(9-10):1342–1348, 2008.
- [74] A. L. Schwab and C. M. Kalker-Kalkman. Joost j. kalker (1933-2006): A life in rolling contact. In *ASME 2007 International Design Engineering Technical Conferences and Computers and Information in Engineering Conference*, pages 1867–1869. American Society of Mechanical Engineers, 2007.
- [75] P. Shackleton and S. Iwnicki. Comparison of wheel–rail contact codes for railway vehicle simulation: an introduction to the manchester contact benchmark and initial results. *Vehicle System Dynamics*, 46(1-2):129–149, 2008.
- [76] Z. Shen, J. Hedrick, and J. Elkins. A comparison of alternative creep force models for rail vehicle dynamic analysis. *Vehicle System Dynamics*, 12(1-3):79–83, 1983.
- [77] I. Y. Shevtsov, V. L. Markine, and C. Esveld. Design of railway wheel profile taking into account rolling contact fatigue and wear. *Wear*, 265(9):1273–1282, 2008.
- [78] X. Shu, N. Wilson, C. Sasaoka, and J. Elkins. Development of a real-time wheel/rail contact model in nucars® 1 and application to diamond crossing and turnout design simulations. *Vehicle System Dynamics*, 44(sup1):251–260, 2006.
- [79] M. Sichani, R. Enblom, and M. Berg. Comparison of non-elliptic contact models: towards fast and accurate modelling of wheel–rail contact. *Wear*, 314(1-2):111–117, 2014.
- [80] R. Smallwood, J. C. Sinclair, and K. J. Sawley. An optimization technique to minimize rail contact stresses. In *Mechanics and Fatigue in Wheel/Rail Contact*, pages 373–393. Elsevier, 1991.
- [81] J. S. Sun, K. H. Lee, and H. P. Lee. Comparison of implicit and explicit finite element methods for dynamic problems. *Journal of Materials Processing Technology*, 105(1):110 – 118, 2000. ISSN 0924-0136.
- [82] T. Telliskivi. Simulation of wear in a rolling–sliding contact by a semi-winkler model and the archard’s wear law. *Wear*, 256(7-8):817–831, 2004.
- [83] T. Telliskivi, U. Olofsson, U. Sellgren, and P. Kruse. A tool and a method for fe analysis of wheel and rail interaction. *Royal Institute of Technology (KTH), Stockholm, Sweden*, 2000.

- [84] K. Van and M. H. Maitournam. Rolling contact in railways: modelling, simulation and damage prediction. *Fatigue & Fracture of Engineering Materials & Structures*, 26(10):939–948, 2003.
- [85] C. D. Van der Wekken and E. A. H. Vollebregt. Local plasticity modelling and its influence on wheel-rail friction. In *CM2018: 11th International Conference on Contact Mechanics, Delft, The Netherlands, 24 - 27 September*, 2018.
- [86] P. J. Vermeulen and K. L. Johnson. Contact of nonspherical elastic bodies transmitting tangential forces. *Journal of Applied Mechanics*, 31:338, 1964.
- [87] K. D. Vo, A. K. Tieu, H. Zhu, and P. B. Kosasih. A 3d dynamic model to investigate wheel-rail contact under high and low adhesion. *International Journal of Mechanical Sciences*, 85: 63–75, 2014.
- [88] E. Vollebregt and G. Segal. Solving conformal wheel-rail rolling contact problems. *Vehicle System Dynamics*, 52(sup1):455–468, 2014.
- [89] E. A. H. Vollebregt. Survey of programs on contact mechanics developed by jj kalker. *Vehicle System Dynamics*, 46(1-2):85–92, 2008.
- [90] E. A. H. Vollebregt. User guide for contact, vollebregt & kalker's rolling and sliding contact model, technical report TR09-03, version, 2013.
- [91] E. A. H. Vollebregt. Numerical modeling of measured railway creep versus creep-force curves with contact. *Wear*, 314(1):87–95, 2014.
- [92] E. A. H. Vollebregt and P. Wilders. Fastsim2: a second-order accurate frictional rolling contact algorithm. *Computational Mechanics*, 47(1):105–116, 2011.
- [93] E. A. H. Vollebregt, S. D. Iwnicki, G. Xie, and P. Shackleton. Assessing the accuracy of different simplified frictional rolling contact algorithms. *Vehicle System Dynamics*, 50(1):1–17, 2012.
- [94] C. Wan and V. L. Markine. Parametric study of wheel transitions at railway crossings. *Vehicle System Dynamics*, 53(12):1876–1901, 2015.
- [95] C. Wan, V. L. Markine, and I. Y. Shevtsov. Analysis of train/turnout vertical interaction using a fast numerical model and validation of that model. *Proceedings of the Institution of Mechanical Engineers, Part F: Journal of Rail and Rapid Transit*, 228(7):730–743, 2014.
- [96] C. Wan, V. L. Markine, and I. Y. Shevtsov. Improvement of vehicle–turnout interaction by optimising the shape of crossing nose. *Vehicle System Dynamics*, 52(11):1517–1540, 2014.
- [97] A. Warhadpande, F. Sadeghi, M. N. Kotzalas, and G. Doll. Effects of plasticity on subsurface initiated spalling in rolling contact fatigue. *International Journal of Fatigue*, 36(1):80–95, 2012.
- [98] Z. Wen, X. Jin, and W. Zhang. Contact-impact stress analysis of rail joint region using the dynamic finite element method. *Wear*, 258(7):1301–1309, 2005.
- [99] M. Wiest, E. Kassa, W. Daves, J. C. O. Nielsen, and H. Ossberger. Assessment of methods for calculating contact pressure in wheel-rail/switch contact. *Wear*, 265(9):1439–1445, 2008.
- [100] P. Wriggers. Finite element algorithms for contact problems. *Archives of Computational Methods in Engineering*, 2(4):1–49, 1995.
- [101] P. Wriggers and T. A. Laursen. *Computational contact mechanics*, volume 30167. Springer, 2006.
- [102] S. R. Wu and L. Gu. *Introduction to the explicit finite element method for nonlinear transient dynamics*. John Wiley & Sons, 2012.
- [103] K. E. Zaazaa and A. L. Schwab. Review of joost kalker's wheel-rail contact theories and their implementation in multibody codes. In *ASME 2009 International Design Engineering Technical Conferences and Computers and Information in Engineering Conference*, pages 1889–1900. American Society of Mechanical Engineers, 2009.
- [104] X. Zhao and Z. Li. The solution of frictional wheel-rail rolling contact with a 3D transient finite element model: Validation and error analysis. *Wear*, 271(1):444–452, 2011.

- [105] Z. Zhong. *Finite element procedures for contact-impact problems*. Oxford university press, 1993.
- [106] Z. H. Zhong and J. Mackerle. Contact-impact problems: A review with bibliography. *Applied Mechanics Reviews*, 47(2):55–76, 1994.
- [107] O. C. Zienkiewicz and R. L. Taylor. *The finite element method for solid and structural mechanics*. Elsevier, 2005.



# 2

## ENHANCED EXPLICIT FE MODEL OF W/R INTERACTION

*To improve the performance of FE simulations on W/R interaction, a novel modelling strategy is proposed. In this strategy, the 3D explicit FE analysis is coupled with the 2D geometrical contact analysis seamlessly. The contact properties in the 3D-FE analyses, such as the initial “Just-in-contact” point, the exact wheel local rolling radius, etc., that are usually a-priori unknown, are determined using the 2D geometrical contact model.*

*As a part of the coupling strategy, a technique of adaptive mesh refinement is developed. The mesh and mesh density of W/R FE models change adaptively depending on the exact location of contact areas and the local geometry of contact bodies. By this means, a good balance between the calculation efficiency and accuracy can be achieved. The last, but not least, advantage of the coupling strategy has been demonstrated in the study of the relationship between initial slips and the steady frictional rolling state. Finally, the results of simulations are presented and discussed.*

---

Parts of this chapter have been published in the Proceedings of the Institution of Mechanical Engineers, Part F: Journal of rail and rapid transit, (2017) [20].

Chapter 2 presents an explicit model of a wheel rolling over a rail developed in ANSYS LS-DYNA. Also, a study on how to improve the accuracy and efficiency of such a model is performed. It is aimed to answer the research question **Q1** presented in Chapter 1.

The outline of this chapter is as follows. First, a brief introduction of the research background of Chapter 2 is presented in Section 2.1. In Section 2.2, full attention is focused on the general descriptions of the 3D-FE model. Also, the details of FE modelling challenges, that prohibit the analysts from attaining accurate contact solutions, are presented. The strategy (referred to as ‘enhanced explicit FE-based coupling strategy’, abbreviated as ‘eFE-CS’, hereinafter), which couples the 2D-Geo model together with that of 3D-FE model, is described in Section 2.3. Following that, the effectiveness and advantages of ‘eFE-CS’ strategy are demonstrated in Section 2.4. Finally, concluding remarks are drawn.

## 2.1 INTRODUCTION

Rolling frictional contact between wheel and rail (W/R) is a highly non-linear problem involving large deformation, large rotation, material plasticity, contact, friction, etc. With the development of modern computing techniques and the availability of supercomputers, advances in the field of numerical simulations on such complex problems have been strongly boosted. Among the various numerical methods proposed [4, 5, 12, 36], the finite element (FE) method is getting more widely used, by virtue of its striking versatility (i.e. accounting for arbitrary contact geometries, material plasticity, etc.). In general, based on the different features of solution procedures, the FE methods are classified into two main categories [11, 32]: namely, implicit and explicit.

Regarding the implicit FE method, a variety of models/tools have been created for different engineering purposes [3, 23, 29, 30, 33, 41]. For instance, Wiest et al. [41] performed implicit FE analyses to predict the normal pressure of W/R impact at a crossing nose. Telliskivi and Olofsson [33] developed an implicit FE model for understanding the complex behaviour of W/R interaction. In [29], the ratcheting performance of rail steels was evaluated by Pun et al. The problem of normal contact was resolved using a quasi-static FE simulation, while the tangential shear stress distributions were calculated according to Carter’s theory [4]. In [3], the effect of wheel motions on the distribution of residual stresses was studied by Bijak et al. In [23], Mandal presented a novel sub-modelling approach for investigating the ratcheting failure of insulated rail joints. Based on the detailed stress/strain responses obtained from FE simulations, attempts were made by Ringsberg et al. [30] to predict the fatigue life of crack initiation on the rail surface. In [17], Ma et al. introduced an implicit FE tool for qualitatively evaluating the performance of different rail pre-grinding strategies. However, due to the difficulties of convergence and the inaccurate modelling of dynamic effects [11, 32], these implicit FE approaches were no longer able to meet the increasing expectations of FE-based contact models possessing higher degree of realism and better accuracy.

As an alternative problem-solving procedure (opposed to the implicit FE method), the explicit FE simulation proceeds without solving a large set of simultaneous equations at each time step and inverting the large matrix [1, 11, 13, 32]. This enables the explicit FE method to avoid certain difficulties of non-linear programming that the implicit method usually has [42]. Owing to such intrinsic advantages, explicit FE approach is getting

increasingly popular for combatting the associated problems of W/R interaction. More recently, a series of representative three-dimensional (3D) explicit FE models [28, 35, 40, 44] have been presented. In [44], Zhao et al. developed a 3D explicit FE model of W/R interaction. The model was successfully verified against CONTACT. In [40], an explicit FE tool was created to simulate the W/R contact-impact at rail insulated joint by Wen et al. It was found that the variation of axle load had stronger effects on the impact event than other operational parameters. In [28], Pletz et al. presented a dynamic wheel/crossing FE model to investigate the influence of operational parameters, such as axle loads, train speeds, material properties, etc., on the impact phenomena. In [35], the stress states and material responses under different levels of adhesions were analysed by Vo et al. It was anticipated that the rail was highly prone to the damage resulting from the ratcheting fatigue of the material.

In summary, significant progress in the field of FE simulations on W/R interaction, from which a number of valuable insights are gained, has been made. Yet, there is still much work to be done. For example, the “gaps or penetrations” between wheel and rail interfaces cause the problems of divergence in the implicit analyses [1, 42] or even an unexpected failure in the explicit FE analyses [9]. Also, due to a-priori unknown of contact location, the general experience- or visualization- based discretization on the potential contact area could always lead to a redundant, insufficient or mismatched FE mesh. As a consequence, the efficiency and accuracy of FE simulations would be adversely affected.

To address these modelling challenges (explained later in detail) and improve the performance of FE simulations, a novel coupling strategy, that couples the two-dimensional geometrical (2D-Geo) contact analysis and the three-dimensional explicit finite element (3D-FE) analysis, has been proposed. The idea of this strategy is inspired by the approach used in CONTACT (i.e. a well-established computational programme developed by Professor Kalker[15] and powered by VORtech Computing [36]). Prior to the 3D-FE analysis, the 2D-Geo contact analysis is functioning effectively as an adaptive guidance for the identification and discretization of the potential area in contact. The challenge of the coupling strategy lies in the programming efforts on how to build up the 2D-Geo and 3D-FE models as well as how to make the interface of two models work effectively. Based on the simulation results, it has been noticed that the computational problems, such as gaps/penetrations, mesh refinement, unexpected initial slips, etc., have been resolved successfully. The goal of improving the performance of FE simulations has thus been achieved with the aid of this coupling strategy.

## 2.2 W/R 3D-FE MODEL

In this section the FE model for the analysis of W/R interaction is presented. The two counterparts investigated here are the standard S1002 profile of the wheel [7] (EN13715-S1002/h28/e32.5/6.7%) with a nominal rolling radius of 460 mm and the standard (UIC) 54E1 rail. Here, ‘h28’ refers to the flange height of 28 mm; ‘e32.5’ means the flange thickness of 32.5 mm; ‘6.7%’ is the reverse slope. The drawing of wheel cross section is adopted from [14]. The inner gauge of the wheel-set is 1360 mm and the axle length is 2200 mm. The track gauge is 1435 mm. Also, the cant angle of 1/40 is considered in the model. Note that the model can easily be adjusted to account for other W/R profiles (e.g. measured worn profiles, 60E1, 75E1, etc.).



### 2.2.1 DISCRETIZED FE MODEL

A half W/R FE model shown in [Figure 2.1a-b](#), where the rail is modelled with restriction to an overall length of 1.8m, is adopted by taking advantage of the symmetrical characteristic of the track and the wheel-set. Here, the “a half W/R FE model” used here and after in this thesis means that only a half of the wheel-set and the track is accounted for. Such a W/R FE model is similar with and inspired by the ones described in [28, 40]. The wheel is set to roll from the origin of the global coordinate system  $O - XYZ$  over a short travelling distance  $d$  on the rail (See [Figure 2.1a](#)). The global coordinate system is defined as: the  $X$ -axis is parallel to the longitudinal direction along which the wheel-set travels, the  $Z$ -axis is the vertical pointing upwards, and the  $Y$ -axis is perpendicular to both  $X$  and  $Z$  directions, forming a right-handed Cartesian coordinate system.

The two ends of rail are constrained in the longitudinal and lateral directions. The bottom surface of rail is completely fixed (i.e. a rigid foundation as inspired by [44]). The reason of defining such boundary conditions is to minimize the vibration of the structure excited by the rolling of a wheel over a rail. By this means, the comparability of FE results to those of CONTACT, which focuses on the cases of steady-state contact [15, 37], can be ensured for the purpose of verification [19, 44]. The results of FE model verification with realistic W/R profiles considered are to be presented in [Chapter 4](#).

In the FE model, the wheel and rail contact bodies are discretized with 3D 8-node structural solid elements (SOLID164). Only the regions where the wheel travels are discretized with dense mesh, leaving the remaining regions with coarse mesh (See [Figure 2.1a-b](#)). A solution area is introduced and positioned in the middle of the dense meshed area. Here, the solution area is defined as a region to extract and analyse the contact properties, such as the contact patch, normal pressure, shear stress, etc. For the FE model shown in [Figure 2.1](#), the mesh size in the solution area is 1 mm, while that in the dense meshed area is 2 mm. The wheel model has 141,312 solid elements and 154,711 nodes, whereas the rail model has 117,598 solid elements and 132,177 nodes. Such a mesh refinement is to fulfil the continuity requirement of Lagrangian formulation [2, 9, 10], which is the theoretical basis of explicit FE method (See [Section 3.2](#)) in ANSYS LS-DYNA. Thus, the number of elements & nodes generated is much larger than that of FE model (only about 5000 elements of wheel model [25, 34]) using Eulerian approach. More discussion on the difference between Lagrangian and Eulerian approaches can be found in [8].

To take the primary suspension into account, a group of sprung mass blocks are lumped over the spring-damper system. [Figure 2.7b](#) shows 8 spring-dampers created, which attempt to avoid the high stress concentrations on the elements of wheel axle centre. The errors of negative volumes can thus be minimised/eliminated, which will facilitate the success of explicit FE simulations. The mass blocks that represent the weight of the loaded car body, are 10 tons. The corresponding parameters of the springs and dampers are listed in [Table 2.1](#). Linear elastic material model is used to describe the constitutive relation of W/R components.

To better simulate the process of W/R dynamic contact, an implicit-to-explicit sequential solving procedure [9] is adopted. In this procedure, the implicit solver (ANSYS Mechanical [1]) and explicit solver (ANSYS LS-DYNA [9]) work in pairs. First, the equilibrium state of the preloaded structure (e.g. under the axle-load of 100 kN) is determined

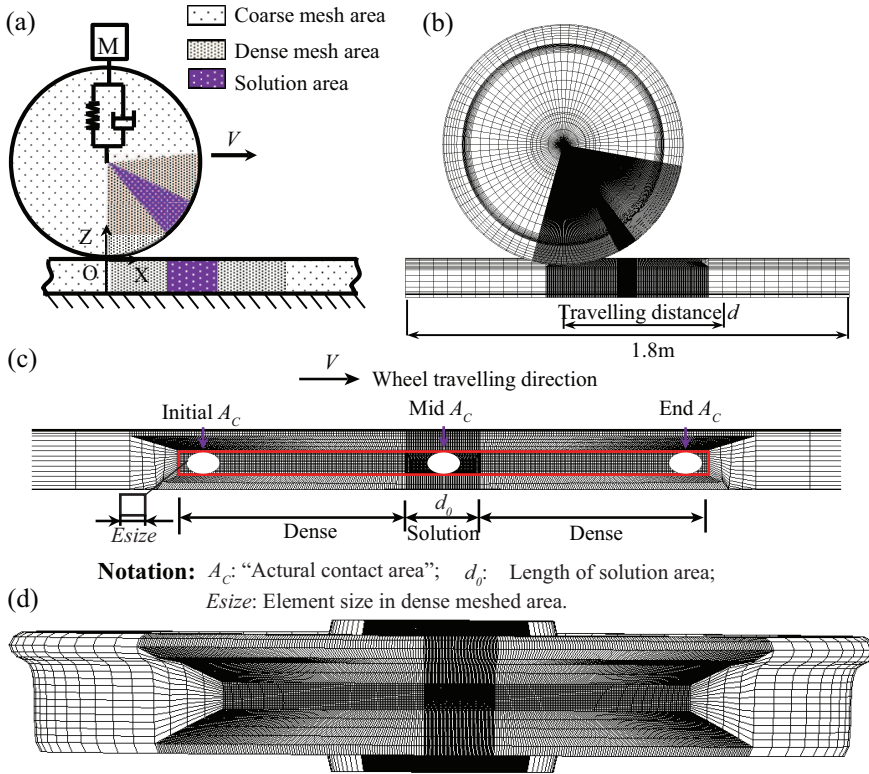


Figure 2.1: FE model of W/R interaction: (a) Schematic graph; (b) Front view; (c) Refined mesh at rail potential contact area; (d) Refined mesh at wheel potential contact area.

with ANSYS Mechanical. The displacement results of the implicit analysis are used to do a stress initialization for the subsequent transient analysis. Then, the processes of rolling frictional contact begin at time zero with a stable preloaded structure [1]. The responses of dynamic contact are further simulated with ANSYS LS-DYNA following the scheme of central difference time integration [9].

For such a typical FE analysis of dynamic contact, the basic process consists of three tasks: 1) Build the model, including prescribing the initial location of W/R, defining correct boundary conditions, performing mesh refinement, etc. 2) Apply the loads & run the simulations, involving traction application, contact definition and determination of calculation time step size; 3) Review the results, referring to the visualisation of contact properties, such as surface normal pressure, shear stresses within the actual contact patches, subsurface stress/strain responses, etc.

All the explicit FE simulations are performed on a workstation with an Intel(R) Xeon(R) @ 3.10 GHz 16 cores CPU and 32GB RAM. Also, the shared memory parallel processing capability of ANSYS LS-DYNA (High Performance Computation module) for 8 processors is used. Each simulation takes around 9 hours. The result file is approximately 45 GB.

Table 2.1: Material properties and mechanical parameters.

	Properties	Values
Wheel/rail material	Young modulus(GPa)	210
	Possion ratio	0.3
	Density ( $\text{kg}/\text{m}^3$ )	7900
Primary suspension	Stiffness (MN/m)	1.15
	Damping (Ns/m)	2500
	Friction coefficient <sup>a</sup>	0.5
Operational parameters	Traction coefficient <sup>b</sup>	0.25
	Train velocities (km/h)	140
	Lateral displacement (mm)	0.0

<sup>a</sup>: Friction is the force resisting the relative motion (i.e, slip) of contact surfaces. Coefficient of friction = Friction force/Normal force. <sup>b</sup>: Traction is the force applied to generate motion between a body and a tangential surface. The tangential traction appears only if the friction is assumed. Coefficient of traction = Traction/Normal force.

### 2.2.2 CHALLENGES OF FE ANALYSIS

As contact always occurs at a-priori unknown area, a series of obstacles will thus be encountered when performing FE-based contact simulations. In this section, the details of those obstacles are presented and discussed.

#### GEOMETRICAL GAPS OR PENETRATIONS

Figure 2.2 shows the 'gaps/penetrations' between the contacting bodies of W/R. Both the gaps and penetrations are undesired. For example, in the implicit FE analyses, too large gap may lead to the wrong identification of contact pairs, while prominent penetrations may cause the overestimation of contact forces. Consequently, it causes an unexpected failure (usually the error of divergence) of the FE simulation. For the case of explicit FE analyses, no penetrations are allowed and the gaps can increase the calculation cost significantly for eliminating the effect of initial disturbances.

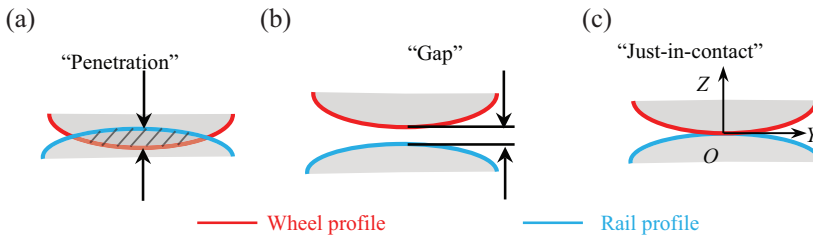


Figure 2.2: Schematic of initial contact gap and penetration.

Although there are several options (tuning the real constants and key options of contact elements independently or in combination) suggested in ANSYS to adjust the initial

contact conditions, they do not work well when the values of gaps/penetrations are large (e.g. in the order of millimetre or even larger). Also, it is challenging to manually bring the two W/R contacting bodies into the positions of “Just-in-contact” as shown in Figure 2.2c. Here the term of “Just-in-contact” refers to a contact positioning between wheel and rail, where the two bodies touch each other without or with a tolerable contact gap or penetration. Moreover, due to the complexity of W/R realistic contact geometry, it is getting even more difficult to determine where the first point of contact will occur. Thus, the gaps/penetrations appear to be inevitable and troubling.

#### PRELOAD APPLICATION

As shown in Figure 2.3, the wheel is prescribed to travel over the rail from the initial condition of pure rolling state to the steady state of partial slip. Here, the steady state [15] means that the slip-adhesion phenomenon is independent of time. To achieve the initial state of pure rolling without slip, the velocity  $V_{CP}$  of the contact point  $CP$ , should be zero. The initial translational velocity  $V_0$  and the initial angular velocity  $\omega_0$  are thus related by

$$V_0 = R_w \omega_0 \quad (2.1)$$

For the reason that the “Just-in-contact” point is a-priori unknown, the real local wheel rolling radius  $R_w$  at the point of contact  $CP$  would be difficult to predict. In case that it is wrongly predicted as  $R_w^*$ , the initial angular velocity will be derived as  $\omega_0^* = V_0/R_w^*$  and then improperly applied on the wheel. Thus, an unexpected initial slip  $\varepsilon_0$ , which is defined as [6].

$$\varepsilon_0 = (V_0 - \omega_0^* R_w) / V_0 = (1 - R_w / R_w^*) \neq 0 \quad (2.2)$$

will be introduced and exerted onto the system of W/R dynamic contact.

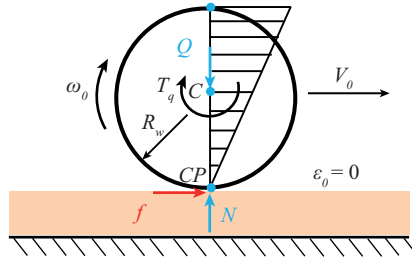


Figure 2.3: Schematic of wheel kinematics: (Note: “C” denotes the wheel centre-of-mass).

In addition, to reproduce the local phenomenon of partial slip numerically, the appropriate traction torque  $T_q$  is derived from the viewpoint of classical mechanics [38],

$$T_q = \frac{J_c + mR_w^2}{mR_w} f \quad (2.3)$$

where,  $f$  is the frictional force,  $m$  represents the mass of the wheel and  $J_c$  is the moment of the inertia of the wheel. It is obvious that any wrong estimation of the local wheel radius  $R_w$  may lead to the inaccurate application of the traction  $T_q$ .

### MESH REFINEMENT

Given that the refined element size inside the contact patch should be as small as 1000 times over the dimension of W/R components, an economic, adaptive and reliable mesh generation has always been a challenge for the analysts.

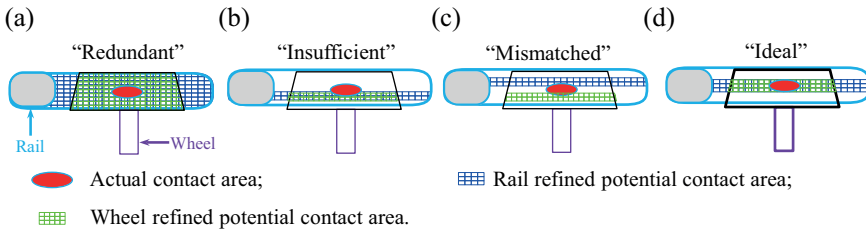


Figure 2.4: Schematic of mesh refinement at potential contact area.

However, there are no clear rules proposed for determining the size of the refined potential contact area up to now. The most commonly adopted approach is the trial-and-error method mainly depending on the researchers' experience or visualization. Using this method, the refined potential contact area can be easily overestimated or underestimated (See Figure 2.4a-b). In particular cases, the refined potential contact areas might be mismatched or deviated from each other (See Figure 2.4c). Thus, the trial-and-error method is highly prone to the inaccurate or undesired contact solutions of W/R interaction.

In addition, if the relative contact locations between the wheel and the rail vary along the track, the corresponding mesh refinement is in demand to be altered spontaneously. This brings about an even higher requirement on the flexibility of the mesh refinement approach.

As one of the main objectives of this chapter, all the three aforementioned challenges of FE-based contact modelling/analyses are to be addressed in the following sections.

## 2.3 COUPLING STRATEGY

To deal with the aforementioned challenges of FE analyses, a novel coupling strategy, that combines 2D-Geo contact analysis and 3D-FE analysis, is developed (See Figure 2.5). The purpose of the 2D-Geo simulation is to detect and determine the initial "Just-in-contact" location (CP), the contact clearance and the corresponding local wheel rolling radius at the point of contact. The obtained contact information is used as the adaptive guidance for the 3D-FE analysis (See Section 2.2).

To implement this coupling strategy, the data exchange between 2D-Geo and 3D-FE models is performed by a small external routine written in the MATLAB environment. Once the processes of 3D-FE modelling and preloading are accomplished, the dynamic simulation is performed to study the behaviour of W/R contact. The details of the 2D-Geo analysis and the interfacing scheme of the two models are briefly described in this section.

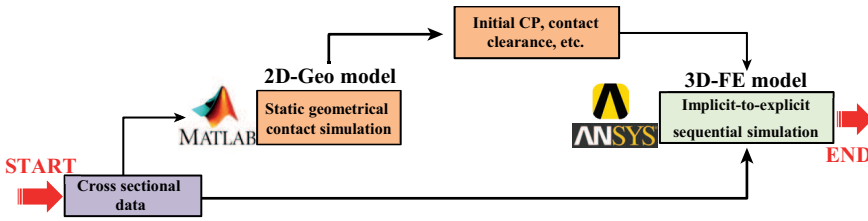


Figure 2.5: Working mechanism of coupling strategy.

### 2.3.1 2D-GEO ANALYSIS

In order to better illustrate the 2D-Geo contact model, a rigid wheel-set is positioned over a rigid track shown in Figure 2.6a. The global coordinate system  $O - XYZ$  is complementary to the one shown in Figure 2.1.  $O^t - X^t Y^t Z^t$  and  $O^w - X^w Y^w Z^w$  refer to the wheel-set- and track-based coordinate systems, respectively. Since the model is 2D, only the roll motion  $\theta$  and the lateral shifts  $\delta y$  of a wheel-set as shown in Figure 2.6a are considered.

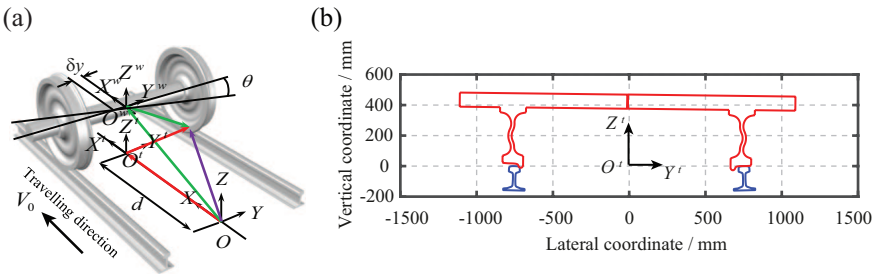


Figure 2.6: (a) W/R 3D coordinate systems; (b) “Just-in-contact” equilibrium condition of wheel-rail at lateral displacement of -10 mm.

The current 2D-Geo contact model is further developed on the basis of the previous work [17]. The initial contact points, where the two particles on the un-deformed wheel and rail coincide with each other, are determined under a given lateral displacement of the wheel-set. The solution procedure of 2D-Geo model has been improved/extended to be non-iterative by taking advantage of efficient matrix operations in MATLAB, which means that no inner and/or outer loop iterations (e.g. ‘for’ or ‘while’ loops used in [17]) of exploring the “Just-in-contact” equilibrium conditions are performed. By this means, a significant increase in the calculation efficiency (around 10 seconds) is accomplished, as opposed to the conventional iterative fashion (e.g. 2~3 minutes in [17]). More information about the contact searching schemes is given in [17, 18, 22]. Figure 2.6b shows a typical example of the 2D-Geo contact analysis, in which the wheel-set is located at the “Just-in-contact” equilibrium position with a lateral displacement of -10 mm.

### 2.3.2 COUPLED INTERFACE

Using the 2D-Geo model described above, the interface and outcome of the ‘eFE-CS’ strategy are presented below.

#### “ZERO” GAPS/PENETRATIONS & OBTAINED $R_w$

Figure 2.7a shows the results of the 2D-Geo contact analysis, through which the 2D wheel-set is positioned on the “Just-in-contact” point of the track. Depending on the lateral displacement and roll angle of the wheel-set determined by the 2D-Geo analysis, the wheel position in the 3D W/R FE model (See Figure 2.7b) has been properly adjusted. The resulting gaps or penetrations between wheel and rail can be reduced into the order of micrometer or even less. This ensures a successful FE simulation of W/R interaction by taking advantage of the suggested options in ANSYS (See Section 2.2.2).

Besides, the actual rolling radius  $R_w$  corresponding to the given lateral displacements of the wheel-set can be obtained. For example, at the lateral shift of 0 mm, the exact local wheel rolling radius  $R_w$  is 460.43 mm, which is denoted by a cyan arrow as shown in Figure 2.7a.

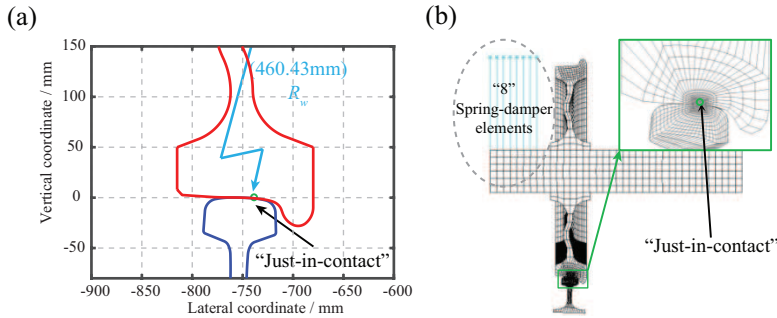


Figure 2.7: (a) “Just-in-contact” equilibrium location derived from 2D-Geo contact analysis; (b) W/R dynamic contact FE model – cross sectional view.

#### NEW ADAPTIVE MESH REFINEMENT

Considering that the refined potential contact area should completely encompass the actual contact area [15, 36] (See Figure 2.8b), the calculated contact clearance from 2D-Geo analysis is used as the adaptive guideline for the mesh refinement of W/R interface. Here, the term of “Contact clearance”  $\delta z$  used here and after in this thesis (See Figure 2.8a) is defined by the vertical distance between the wheel and rail for the undeformed contact geometry. The value of the contact clearance defines the region with high susceptibility for contact to occur (also called the potential contact area). It is assumed that the most stressed point inside the contact patch coincides with the initial contact point (‘CP’ in Figure 2.8a). The origin of the mesh refinement is designated to the initial CP. The width of the refined region  $\Delta y$  is gradually arising with the increase of the contact clearance (See Figure 2.8c-d).

For the sake of identifying the best contact clearance, it is expected to follow a guideline as follows:

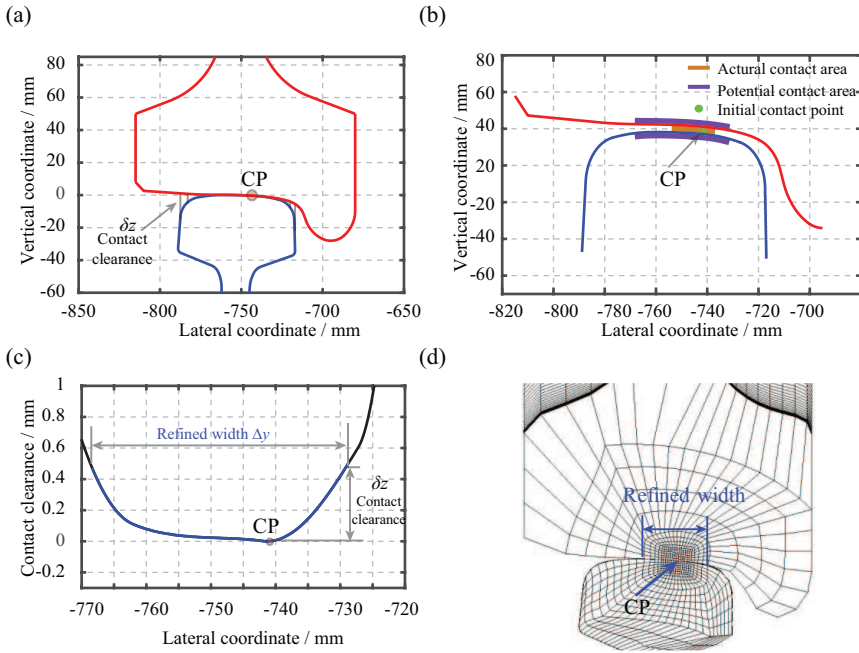


Figure 2.8: Schematic representation of novel adaptive refining approach: (a) Global view of contact clearance; (b) Schematic graph of potential and actual contact areas; (c) Close-up view on variation of contact clearance at the vicinity of initial contact points; (d) Close-up view of refined potential contact region.

- (i) The contact clearance  $\delta z$  should be small enough to constrain the size of the model and thus maintain the calculation expenses into a low level;
- (ii) The refined potential contact area determined by the contact clearance  $\delta z$  should be sufficient to encompass the resulting real contact patch obtained from the FE analysis.

Based on the selected value of the contact clearance, the mesh refinement process in these regions will be initiated. Using the proposed Nested Transition Mapped (NTM) mesh refining approach [16], the elements in the solution area are able to be refined as small as  $1.0 \text{ mm} \times 1.0 \text{ mm} \times 1.0 \text{ mm}$  (as shown in Figure 2.8d and Figure 2.10), while for the remaining out-of-contact region (Coarse mesh area), less attentions will be paid.

#### FLEXIBILITY OF THE NOVEL MESH REFINING APPROACH

To automate the common tasks and implement the coupling strategy more efficiently, both the 2D-Geo and 3D-FE models have been all coupled and parametrised using the scripting language of MATLAB and Parametric Design Language of ANSYS (APDL). The scripted and later packaged ‘eFE-CS’ modelling strategy offers great convenience and flexibility for the day-to-day analyses.

One added important feature of this adaptive mesh refining method is shown in Figure 2.9, where the patterns of these local mesh refinements change flexibly with respect



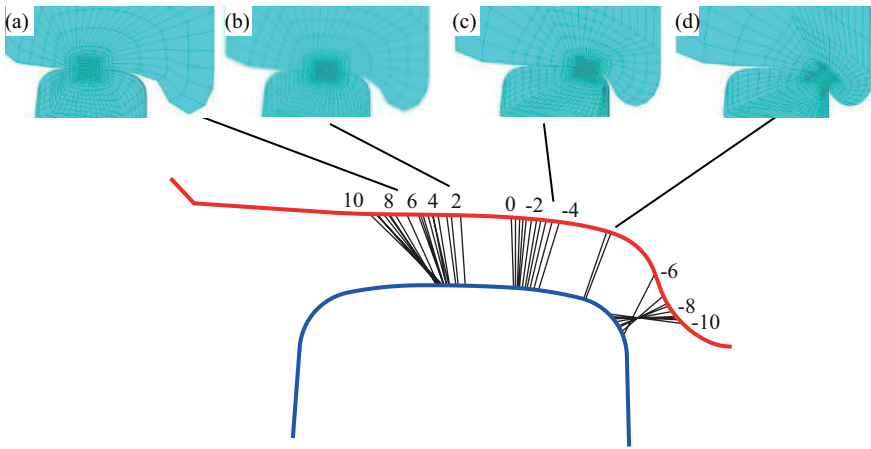


Figure 2.9: Flexibility of novel mesh refining approach w.r.t. different lateral displacements: (a) 5.5 mm; (b) 2.0 mm; (c) -3.5 mm; (d) -5.5 mm.

to different lateral displacements of the wheel-set (e.g. ranging from -5.5 mm to 5.5 mm). This means that in each simulation the position of the geometric contact point (and hence the mesh) is fixed. Owing to ‘eFE-CS’ modelling strategy created, running different simulations of different relative wheel-rail positions will cost much less or even no manual work to adapt the mesh.

For the cases of non-zero lateral displacements, the rails remain symmetric in relation to the track centre, while only the wheel and contact conditions vary. The variations of geometrical contact properties associated (i.e. locations and dimensions of refined potential contact areas) are predicted by a-priori 2D-Geo contact analysis (See [Figure 2.6b](#)). Once the FE models (with half W/R considered) are created, they are used to study the dynamic behaviour of W/R interaction. Here, the applicability of this half W/R FE modelling approach (as shown in [Figure 2.1](#)) to the cases of different lateral displacements are explained as:

- (i) A complete wheel-set and two rails are considered in the 2D-Geo contact model (See [Figure 2.6](#)). The roll angles of the wheel resulting from the variation of lateral displacements have been explicitly taken into account.
- (ii) A range of lateral displacements (i.e. [-5.5 - 5.5] mm) cover most sections of railway track (e.g. tangent, large radius curves, etc.) [31], where the yaw angles (also called attack angle) are usually small (less than 2 degrees [43]). Moreover, being aware that the wheel travels over a relatively short distance of 0.52m, which is rather short in comparison to the wavelength of yaw/Klingel motion (i.e. usually in the order of 10 to 100 meters), the variation of yaw angle would be relatively small. It is thus assumed that the neglect of yaw motion in the model presented might be acceptable.
- (iii) A comprehensive model verification against CONTACT [36] has been performed by the authors recently [19]. For the cases of different lateral displacements (i.e.

[-5.5 - 5.5] mm), the model verification shows that the half W/R FE model can produce as good results as CONTACT.

In summary, the half W/R FE model enhanced with 2D-Geo contact analysis is flexible enough to be used in the cases of different lateral displacements. However, regarding the further applicability of half W/R FE model to the sharp curves (i.e. curve radius smaller than 500m [26]), in which the yaw angle is indispensable and plays an important role, it will be explained later in Section 2.4.

### RESULTING CONTACT PAIRS

Figure 2.10a-b shows a contact pair, consisting of two master and slave segments for explicit FE analysis (TARGET 170 and CONTACT 173 elements for implicit FE analysis). It can be seen that the size of the potential contact area is controlled by the magnitude of the refined width  $\Delta y$  in the lateral direction (See Figure 2.8) and the refined length  $\Delta x$  in the longitudinal direction (See Figure 2.1). Here, potential contact areas are defined by the two curved rectangles on the outer layers of the W/R interfaces.

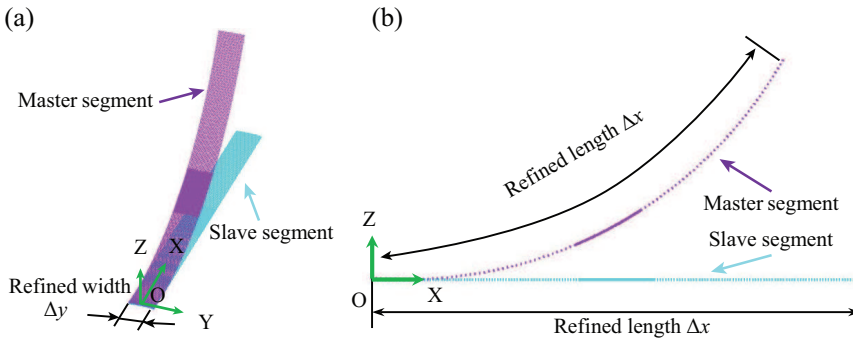


Figure 2.10: Resulting contact pair: (a) Isometric view; (b) Side view.

It has been reported in [2, 9] that contact analysis will add a significant computational cost for the overall solution, even when the ratio between the number of contact points and the number of elements is small. To limit the level of calculation expense as low as possible, the smallest and localised contacting zones are always desired to maintain the most efficient solution. Also, as discussed before, the refined potential contact areas should be large enough to encompass all the necessary contacts to maintain the accuracy of the solution. According to the coupling strategy, the refined width  $\Delta y$  is defined in the 2D-Geo analysis in terms of the contact clearance  $\delta z$ , while the refined length  $\Delta x$  is defined in terms of the travelling distance  $d$ . In the following section, the effects of corresponding geometrical parameters on the performance of FE simulations are studied.

## 2.4 FE RESULTS AND DISCUSSIONS

To demonstrate the effectiveness of the 'eFE-CS' strategy, a series of the FE simulations have been performed. The influence of the size of potential contact areas and the local wheel rolling radius on performance of 'eFE-CS' strategy are to be analysed. As the

wrongly estimated rolling radius  $R_w^*$  will result in an initial slip  $\varepsilon_0$  (See Equation 2.2), the investigation on the effect of local wheel rolling radius  $R_w$  is replaced here by the initial slip  $\varepsilon_0$ .

## 2

### 2.4.1 CONTACT CLEARANCE

Figure 2.11 shows the effect of contact clearances ( $\delta z$ ) on the FE models. Here, the contact clearance  $\delta z$  varies from 0.08 mm to 0.50 mm, while the other two parameters of travelling distance  $d$  and initial slip  $\varepsilon_0$  keep constant (See Table 2.2).

For the reason that the actual contact areas would not vary much (the same axle load is applied in both implicit and explicit FE analyses), the effect of varying contact clearances  $\delta z$  on the performance of FE models would only be analysed by the implicit FE codes (no explicit analyses are performed).

Table 2.2: Comparison of FE models w.r.t. three different refined widths.

Cases	Variables			Implicit FE simulation	
	$\delta z/mm$	$d/mm$	$\varepsilon_0$	$N^a$	$T^b/hour$
I	0.50			382543	4.73
II	0.17	660	0	323879	2.9
III	0.08			286700	2.5

<sup>a</sup>: Number of elements in FE model;

<sup>b</sup>: Calculation expense;

Figure 2.12 shows the variation of normal pressure corresponding to different contact clearances. A noticeable discrepancy of the maximum contact pressure is observed between case I (1216 MPa) and II (1041 MPa). Such a discrepancy is explainable, since the mesh sizes of FE models at the origin of wheel rotation (not the solution area, See Figure 2.1) are relatively large (around 2 mm). Also, considering that W/R contact occurs at a highly stressed area (as small as 150 mm<sup>2</sup>, See [21]), these large mesh sizes are hardly possible to capture the stress/strain gradients accurately. It can thus readily trigger the tolerable discrepancies of the maximum contact pressure. (Notation: the contact responses extracted from the solution area, where the mesh size is as small as 1 mm, are preferred.)

With respect to case III ( $\delta z = 0.08$  mm, Figure 2.12c), it can be observed that the refined potential contact area can not fully cover the one simulated by the model any more. It indicates that the accuracy of contact solution might not be guaranteed, which is attributed to the underestimation of the size of refined potential contact area.

Moreover, it can be observed from Table 2.2 that the amount of the discretized elements as well as the calculation expense reduce significantly with the decrease of the contact clearance  $\delta z$ . Taking both the calculation expenses and the accuracy into account, the contact clearance of 0.17 mm appears to be a good choice for the operational conditions as described in Section 2.3.1.

To assess the applicability of the selected contact clearance (0.17 mm) to varying axle loads, two more case studies with axle load of 120 kN and 140 kN have been performed.

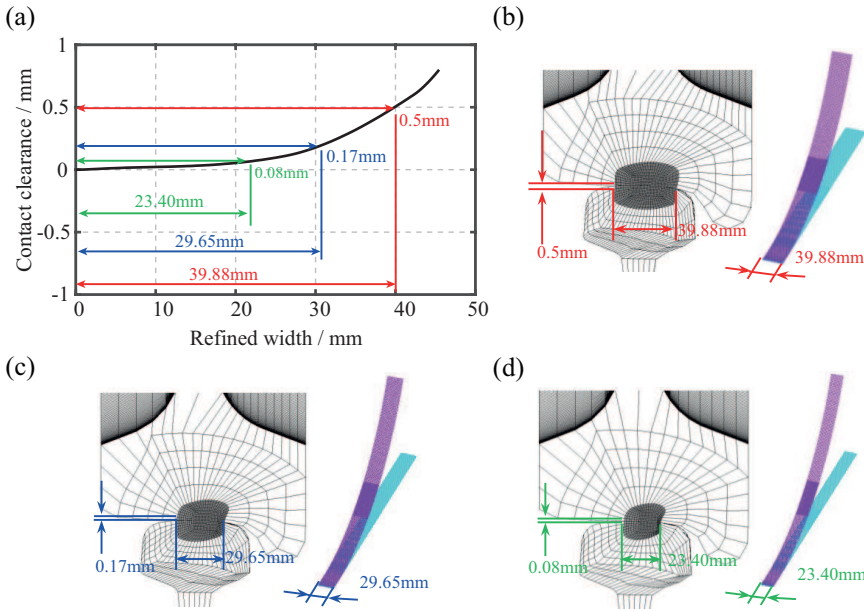


Figure 2.11: Variation of refined widths w.r.t. different contact clearances: (a) Relations between contact clearance  $\delta z$  and refined width  $\Delta y$ ; (b) Case I:  $\delta z = 0.5$  mm,  $\Delta y = 39.88$  mm; (c) Case II:  $\delta z = 0.17$  mm,  $\Delta y = 29.65$  mm; (d) Case III:  $\delta z = 0.08$  mm,  $\Delta y = 23.40$  mm.

Figure 2.13 shows the comparison of actual contact patches with respect to different axle loads. It can be seen that there is a steady increase in both the maximum contact pressure and the actual contact area in relation to the increasing axle loads. The width of refined potential contact areas determined by the contact clearance of 0.17 mm is robust enough to encompass all the real contact areas, which are resulting from the applied axle loads up to 40% (140 kN) higher than the normal one (100 kN).

Similarly, the applicability of the selected contact clearance of 0.17 mm to the varying lateral shifts of the wheel-set (See Figure 2.9) has been evaluated. The results are shown in Figure 2.14a-c. It can be seen that although the contact clearance of 0.17 mm can satisfy the case with the lateral shift of 5.5 mm (Figure 2.14c), it is insufficient for the case of -5.5 mm (Figure 2.14a), where the real contact patch tends to fall out of the refined potential contact area. Given a larger contact clearance  $\delta z$  of 0.35 mm, it is observed from Figure 2.14d that the refined potential contact area is able to better encompass the real contact area.

In summary, a contact clearance of 0.17 mm performs well at zero lateral displacement of the wheel-set. It is robust enough to apply in the cases of higher axle loads. One can further affirm that such a contact clearance is applicable to the case of different operational conditions (i.e. train velocities, friction coefficients, traction coefficients, etc.), since their influences on the size of real contact patches are insignificant in comparison to the increased axle loads. The applicability of contact clearance 0.17 mm to these varying operational patterns has been verified in the authors' recent work [19, 21].

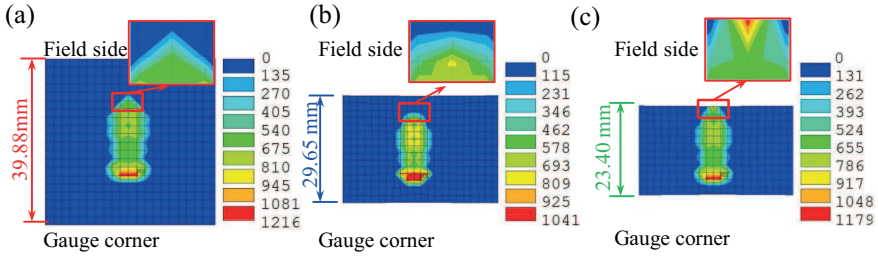


Figure 2.12: Variation of actual contact patches and contact pressure w.r.t. different refined widths: (a) Case I:  $\delta z = 0.5$  mm,  $\Delta y = 39.88$  mm. (b) Case II:  $\delta z = 0.17$  mm,  $\Delta y = 29.65$  mm; (c) Case III:  $\delta z = 0.08$  mm,  $\Delta y = 23.40$  mm.

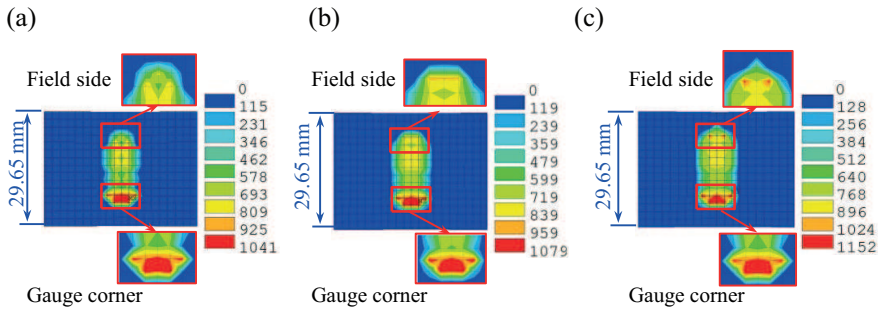


Figure 2.13: Comparison of actual contact patches and contact pressure at different axle loads: (a) 100 kN; (b) 120 kN; (c) 140 kN.

However, with respect to the cases of large (e.g.  $\delta y = -5.5$  mm, contact occurs between rail gauge corner and wheel flange root) lateral displacements of the wheel-set, this contact clearance of 0.17 mm is no longer suitable. A contact clearance of 0.35 mm is thus suggested based on the simulation results. It is more robust than that of 0.17 mm, which implies that the contact clearance of 0.35 mm has wider applicability to different geometrical, loading, operational conditions of W/R interaction.

In extreme cases (e.g. severe worn contact geometries), if the suggested contact clearance (either 0.17 mm or 0.35 mm) cannot guarantee accurate results, it is recommended to follow the above presented parametric study procedure to make a proper decision. Normally within two (maximally three) times of targeted parametric examinations of contact clearances, the best refined width of the potential contact area can be found.

#### 2.4.2 TRAVELLING DISTANCE

Apart from the contact clearance  $\delta z$ , the dimensions of the potential contact area can be changed by adjusting another important parameter: travelling distance  $d$ . The dynamic behaviour of W/R interaction is studied from an initial travelling distance of 660 mm. Note that the interface parameters (such as, contact stiffness and damping) are chosen as default.

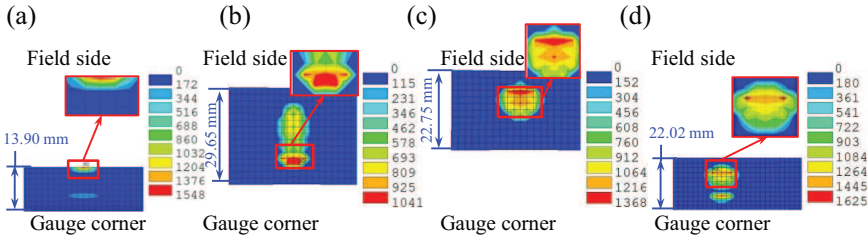


Figure 2.14: Comparison of actual contact patches and contact pressure at different lateral shifts: (a) -5.5 mm ( $\delta z = 0.17$  mm); (b) 0.0 mm ( $\delta z = 0.17$  mm); (c) 5.5mm ( $\delta z = 0.17$  mm); (d) -5.5 mm ( $\delta z = 0.35$  mm).

Table 2.3: Comparison of FE models w.r.t. different travelling distances.

Cases	Variables			FE models <sup>a</sup>	
	$\delta z$ /mm	$d$ /mm	$\epsilon_0$	$N$ <sup>b</sup>	$T$ <sup>c</sup> /hour
I		800		373511	25.3
II		660		323879	19.6
III	0.17(Best)	520	0	275043	12.5
IV		380		225033	7.7
V		240		176205	4.7

<sup>a</sup> : Implicit-to-explicit sequential solution.

<sup>b</sup> : Number of elements; <sup>c</sup> : Calculation expense;

Figure 2.15a shows the results of contact forces obtained from implicit-to-explicit FE analyses. It can be observed that the W/R mutual reactions are equal in magnitude and opposite in direction. Such observations are complementary to the classical contact theory as demonstrated in [27].

The solid lines represent the contact response in the dense meshed area, while the diamond dotted lines denotes that inside the solution area. It is observed that the vertical contact forces  $N_{Mas}$  and  $N_{Sla}$  vary around the prescribed axle load (100 kN). Here, the subscripts “Mas” and “Sla” are the abbreviations of “Master” and “Slave”, which refer to the resulting contact forces on the master and slave contact interfaces, respectively. The “saw-toothed” oscillations of  $N_{Mas}$  and  $N_{Sla}$  (as denoted by the grey elliptical box) gradually decay at the first 150 mm from the starting point. These noticeable oscillations are mainly caused by the initial conditions (i.e. the applied initial train velocities, accelerations, etc.) according to the authors’ earlier research [21]. With the increase of initial velocities, the oscillation amplitudes will increase correspondingly.

In addition, the longitudinal frictional forces of  $f_{Mas}^{Lon}$  and  $f_{Sla}^{Lon}$  grow gradually to its saturation value 25 kN, which is in line with the applied traction. Due to the constrained lateral motion of the wheel-set and small contact angle between the resultant W/R contact geometries at the lateral shift of 0 mm, the lateral force component  $f_{Mas}^{Lat}$  and  $f_{Sla}^{Lat}$  seems to make minor contribution (varying around 0 kN). Here, the subscripts “Lon” and “Lat” are the abbreviations of “Longitudinal” and “Lateral”.

In comparison with the dense meshed region (See Figure 2.15a), all the force compo-

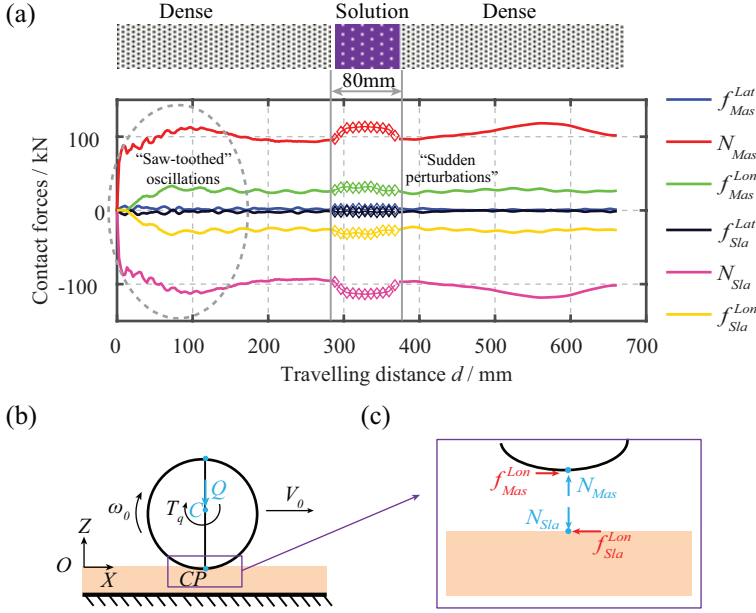


Figure 2.15: (a) Responses of W/R contact forces with a travelling distance ( $d$ ) of 660 mm; (b) Schematic graph of W/R interaction; (c) Close-up view on the reactions at contact point  $CP$ .

nents exhibit a “sudden perturbation”, as the wheel rolls and approaches the vicinity of the solution area (80 mm). The causes of these “sudden perturbations” have been studied extensively and found [21] to be the difference of the associated mesh sizes, which vary from 2 mm (the dense meshed area) to 1 mm (the solution area). For this reason, the magnitude of nodal contact stiffness  $k^{master(slave)}$ , which is expressed as [9]

$$k^{master(slave)} = \frac{\alpha \cdot K \cdot A^2}{V} \quad (2.4)$$

, is thus strongly affected. Here,  $\alpha$  denotes the penalty scale factor,  $K$  is the bulk modulus,  $V$  and  $A$  represent the volume and face area of a contact element, respectively.

Accordingly, the change of contact stiffness manifests itself in the variation of contact forces  $f$ , which are then calculated on the basis of penalty method [9],

$$f = k^{master(slave)} \cdot l \quad (2.5)$$

Here,  $l$  is the amount of penetrations between master and slave segments.

To sum up, the variation of mesh sizes implies the “sudden perturbations” of contact forces as shown in Figure 2.15a. Also, it has been reported in [21] that the problems of “sudden perturbations” can be addressed using an optimal penalty scale factor  $\alpha$  (i.e.  $\alpha = 12.8$ ), which is determined according to the criteria of contact stability [9, 21].

To investigate the sensitivity of contact solutions to the travelling distance  $d$ , five cases of travelling distance varying from 240 mm to 800 mm are selected and analysed. The information about the obtained FE models is listed in Table 2.3.

Figure 2.16a shows three of the five representative refined FE models with the travelling distance of 240, 520 and 800 mm. A close-up view on the performance of these varying travelling distances is taken by a supplemental and independent check on the resulting contact forces (as suggested by [27]). The results shown in Figure 2.16b indicate that all the resulting vertical forces are varying around the axle load (100 kN) exerted on the wheel axle. It is clear that the oscillations of contact forces (“sudden perturbations” as depicted with diamond dotted lines) occur for all the five cases of different travelling distances.

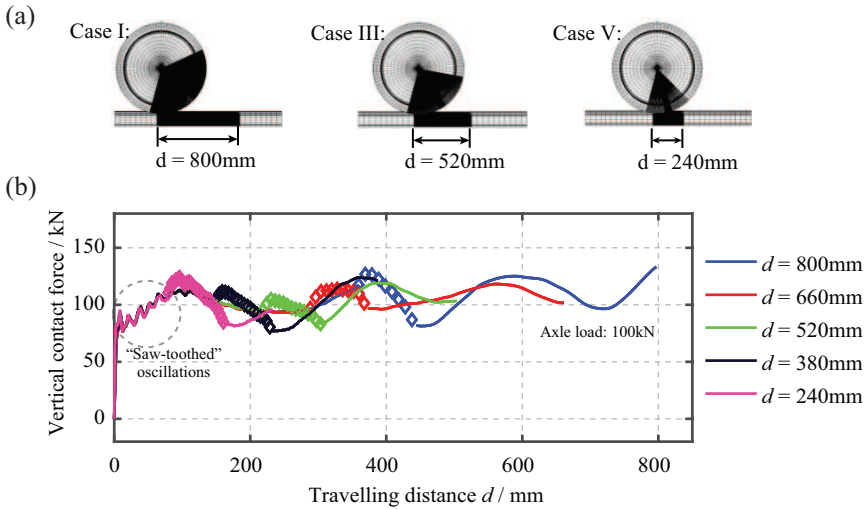


Figure 2.16: Influence of varying travelling distances on W/R dynamic contact responses: (a) Representative FE models of different travelling distances; (b) Vertical contact force w.r.t different travelling distances.

Similarly, the “saw-toothed” force oscillations, which has been explained previously, are observed in Figure 2.16b. Also, it can be seen that all the FE models take around 150 mm to completely get rid of the initial contact disturbances under the specified operational conditions as shown in Table 2.1.

Figure 2.17 shows the normal contact pressure that is extracted at the instant when the wheel travels over the middle of the solution area. It can be seen that both the magnitude and the distribution of the contact pressure vary slightly with respect to different travelling distances.

In view of the increasing calculation expense (as listed in Table 2.3) as well as the varying contact forces and pressures, it is practically necessary to build up a guideline/criterion to select the best travelling distance. Aiming to maintain the good compromise between the calculation efficiency and accuracy, the guideline is formulated as a recommendation:

- (i) The overall travelling distance should be kept short enough to save the calculation expenses;
- (ii) A distance of 150 mm before the solution area should be reserved for damping out



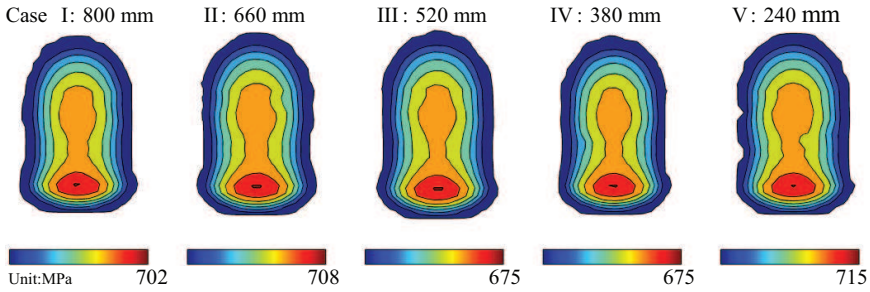


Figure 2.17: Effect of varying travelling distances on contact pressure.

the “saw-toothed oscillations”.

Following the guideline aforementioned, the most suitable travelling distance of 520 mm is suggested. This suggested travelling distance  $d$  would be used for W/R contact analysis in the rest of this chapter.

### 2.4.3 INITIAL SLIP

To study the influence of initial slips  $\varepsilon_0$  on the dynamic performance of W/R interaction, a series of FE simulations have been performed. The contact clearance  $\delta z$  (0.35 mm) and travelling distance  $d$  (0.52m) suggested are used, while the initial slips  $\varepsilon_0$  vary from -0.04 to 0.13.

Figure 2.18 shows the variation of longitudinal traction forces with respect to different initial slips  $\varepsilon_0$ . Figure 2.19 shows the effect of varying initial slips on the distribution of shear stresses. It is clear that both the traction forces and the shear stresses change significantly with respect to the initial slips, which implies the unexpected initial slip  $\varepsilon_0$  has a significant influence on the tangential solutions of W/R interaction.

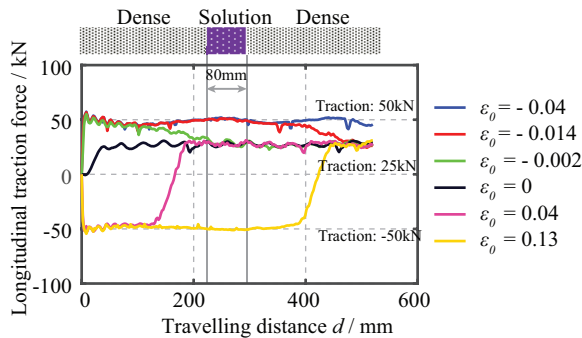


Figure 2.18: Variation of frictional forces w.r.t. different initial slips.

With the increase of initial slips  $\varepsilon_0$  from -0.04 to -0.002 (i.e. the first three cases), the magnitude of longitudinal traction forces tends to drop from 50 kN to 25 kN (See Figure 2.18). Accordingly, the distribution of shear stresses changes. For cases I ( $\varepsilon_0 =$

$-0.04$ ) & II ( $\varepsilon_0 = -0.014$ ), the shear stress is distributed parabolically all over the contact patch. Regarding case III ( $\varepsilon_0 = -0.002$ ), the “hot area” of shear stress is significantly reduced. Here, “hot area” is referred to as an area, where the amplitude of the shear stress is larger than 250 MPa. Such a “hot area” is positioned at the rear part of the contact patch.

Similar patterns of shear stress distribution occur in the other two cases of IV ( $\varepsilon_0 = 0.0$ ) & V ( $\varepsilon_0 = 0.04$ ). The reduced “hot area” of shear stress manifests itself in the small value (25 kN) of longitudinal traction forces (See, cases III, IV, V in [Figure 2.18](#)).

When the value of  $\varepsilon_0$  becomes positive (i.e. case V ( $\varepsilon_0 = 0.04$ ) & VI ( $\varepsilon_0 = 0.13$ )), negative longitudinal forces (-50 kN) are observed. These negative traction forces hold constant for a certain travelling distance or time span (i.e. the calculation time). After that, it steeply increases and then reaches a steady state, getting saturated with a positive traction force of 25 kN. The distance/time, that the negative traction forces hold, is highly related to the magnitude of initial slips. More specifically, the larger the value of  $|\varepsilon_0|$  is, the longer distance/time the wheel has to travel so as to accomplish such conversions of traction forces (See [Figure 2.18](#)).

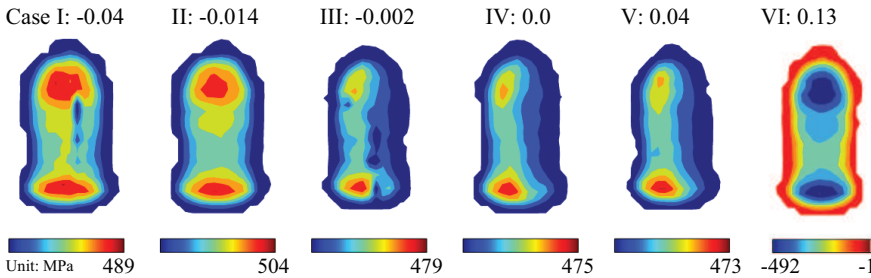


Figure 2.19: Effect of varying initial slips on surface shear stress.

Such phenomena could be explained by the wheel kinematics as shown in [Figure 2.20](#), which depicts the relationship between the frictional forces and the slip velocities. It can be seen that the directions of frictional forces are in opposite to the ones of slip velocities. This explains the conversions of traction forces from negative to position in the cases of V and VI, where the signs of initial slips are reversed in comparison to the other cases.

[Figure 2.20c](#) schematically shows the traction curve [6]. It is observed that when the magnitude of the slip (also interpreted as creepage) exceeds certain level, the regime of full slip is entered. The frictional force thus reaches its saturation value (i.e. traction bound of 50 kN). Here, the traction bound, which amounts to the product of frictional coefficient  $\mu$  and the normal load  $N$ , is determined by Coulomb's friction law. This indicates the trend in the results of traction forces shown in [Figure 2.18](#), where all the six cases tend to converge over travelling distance/time towards a steady state of partial slip. It also implies that for the cases of non-zero initial slips, the contact statuses first fall into full slip and then approach the equilibrium state of partial slip. This state, in which the expected traction forces is equal to the applied one of 25 kN (See [Equation 2.3](#)), can only be reached until the effect of the unexpected initial slip has been completely damped out.

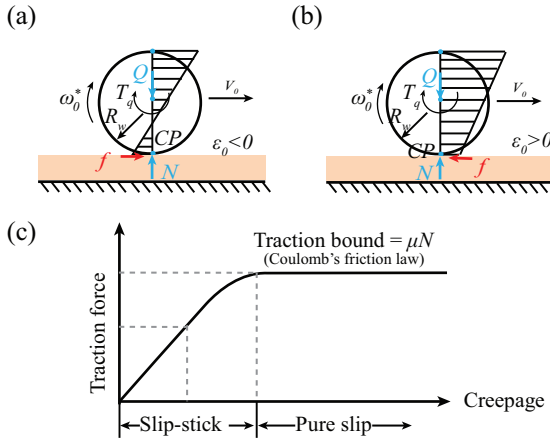


Figure 2.20: Schematic of wheel kinematics: (a) Negative initial slip  $\varepsilon_0 < 0$ ; (b) Positive initial slip  $\varepsilon_0 > 0$ ; (c) Traction curve adapted from [6].

For the case of initial slip  $\varepsilon_0 = 0$  (i.e. Case IV: initial velocities applied appropriately), the accurate tangential contact solution can be obtained within a rather short travelling distance of 50 mm. If the absolute value of initial slip is small (e.g. Case III and V), extra calculation time and travelling distances will be taken to ensure the correct solution. However, in the cases of large initial slips (e.g. I, II, VI), the results of shear stress extracted from the solution area (80 mm), are inaccurate, which may lead to wrong decisions.

To summarise, using the proposed 'eFE-CS' approach, the local wheel rolling radius  $R_w$  can be correctly estimated. No unexpected initial slips will be introduced into the FE model. Accordingly, accurate and steady tangential solutions of W/R rolling contact problems can be guaranteed. It is, thus recommended to address the issues of initial slip with the aid of this 'eFE-CS' strategy.

#### 2.4.4 DISCUSSION: PROS OF 'eFE-CS' MODEL OF W/R INTERACTION

From the results of FE simulations presented, it can be noticed that the proposed 'eFE-CS' strategy is promising enough for improving the performance of FE simulations on W/R interaction. The advantages it holds can be categorised into four groups:

- All the modelling challenges (See Section 2.2.2), from which most of 3D-FE models often suffer, can be readily addressed. Also, a good compromise between the calculation accuracy and efficiency is maintained;
- More detailed normal & tangential contact solutions than those of 2D W/R contact analysis [24, 39] are generated. These stress/strain responses are expected to contribute positively on other advanced applications (e.g. prediction of wear/rolling contact fatigue (RCF), profile design/optimisation, etc.);
- The dynamic effects, which are often neglected in the static or quasi-static 3D FE models [17] (contact constraints are enforced with Lagrange Multiplier method,

Augmented Lagrangian method, etc.), are taken into account in the present model (Penalty method). A high degree of realism is attained;

- The strategy shows good applicability to the problem of W/R interaction. As there are no special restrictions imposed upon its use, it is recommended to use for addressing other contact/impact problems (e.g. gear, bearing, metal forming, etc.) that have complex contact geometries.

## 2.5 CONCLUSIONS

Aiming to improve the performance of finite element analysis on the wheel-rail interaction, a novel 'eFE-CS' strategy, that couples the three-dimensional finite element (3D-FE) model and the two-dimensional geometrical (2D-Geo) contact model, has been presented. Prior to the 3D-FE simulations, the 2D-Geo contact analysis is performed to better define the contact properties that are in demand for FE analyses. The advantages of developed 'eFE-CS' model have been discussed. Based on the simulation results and discussions, the following conclusions are drawn:

- (i) Following the coupling procedure, the convergence problems or even a failure of the FE simulations in the presence of gaps or penetrations have been addressed by correctly placing the wheel onto a position of "Just-in-contact" over the rail;
- (ii) In order to avoid the issues of the redundant, insufficient or mismatched mesh refinement in the vicinity of the contact region, which will lead to either the prohibitive calculation expense or the inaccurate solution, an adaptive mesh refining technique based on the contact clearance has been proposed. Using this technique, the solution of W/R rolling frictional contact is able to be maintained with satisfactory accuracy and efficiency. The flexibility of this coupling approach has also been demonstrated by solving the cases of different contact locations due to various lateral shifts of the wheel-set;
- (iii) An unexpected initial slip can be introduced by mismatching the angular and translational velocity of the wheel, owing to the wrongly estimated local wheel rolling radius. Such an initial slip can cost unnecessary calculation effort to achieve the steady frictional rolling state or even lead to wrong tangential solution of W/R interaction in extreme cases. Using the coupling strategy, the value of undesired initial slip can be easily minimised. Accordingly, the accurate and efficient finite element solution can be guaranteed.

In conclusion, the proposed coupling strategy allows the proper prescription of the contact properties, which can enhance the performance of the FE analyses of W/R interaction significantly. Such a strategy is promising enough to promote the application of the FE approaches on the contact problems with more complex and irregular contact geometries (e.g. the mild or severe worn W/R interfaces, metal forming, gear, bearings, etc.).

## REFERENCES

- [1] ANSYS, Inc. Ansys user's manual: Structural analysis guide. ANSYS Inc, 2013.

- [2] D. J. Benson and J. O. Hallquist. A single surface contact algorithm for the post-buckling analysis of shell structures. *Computer Methods in Applied Mechanics and Engineering*, 78(2): 141–163, 1990.
- [3] M. Bijak-Żochowski and P. Marek. Residual stress in some elasto-plastic problems of rolling contact with friction. *International Journal of Mechanical Sciences*, 39(1):15–32, 1997.
- [4] F. W. Carter. On the action of a locomotive driving wheel. *Proceedings of the Royal Society of London A: Mathematical, Physical and Engineering Sciences*, 112(760):151–157, 1926.
- [5] A. I. El-Ghandour, M. B. Hamper, and C. D. Foster. Coupled finite element and multibody system dynamics modeling of a three-dimensional railroad system. *Proceedings of the Institution of Mechanical Engineers, Part F: Journal of Rail and Rapid Transit*, 230(1):283–294, 2016.
- [6] C. Esveld. *Modern railway track*, volume 385. MRT-productions Zaltbommel, The Netherlands, 2001.
- [7] European Committee for Standardization (CEN). EN 13715: 2006 + A1: 2010: Railway applications – Wheelsets and bogies – Wheels – Tread profile. European Standard, 2006.
- [8] J. Fayos, L. Baeza, F. D. Denia, and J. E. Tarancón. An eulerian coordinate-based method for analysing the structural vibrations of a solid of revolution rotating about its main axis. *Journal of Sound and Vibration*, 306(3-5):618–635, 2007.
- [9] J. O. Hallquist. ANSYS/LS-DYNA theoretical manual, 2005.
- [10] J. O. Hallquist, G. L. Goudreau, and D. J. Benson. Sliding interfaces with contact-impact in large-scale lagrangian computations. *Computer methods in applied mechanics and engineering*, 51(1-3):107–137, 1985.
- [11] F. J. Harewood and P. E. McHugh. Comparison of the implicit and explicit finite element methods using crystal plasticity. *Computational Materials Science*, 39(2):481–494, 2007.
- [12] L. Huang, Z. Li, L. Li, and Q. An. Methods to calculate accurate wheel/rail contact positions and static contact stress levels. *Proceedings of the Institution of Mechanical Engineers, Part F: Journal of Rail and Rapid Transit*, 230(1):138–150, 2016.
- [13] T. J. R. Hughes, R. L. Taylor, J. L. Sackman, A. Curnier, and W. Kanoknukulchai. A finite element method for a class of contact-impact problems. *Computer methods in applied mechanics and engineering*, 8(3):249–276, 1976.
- [14] International Union of Railways(UIC). UIC Leaflet 515-1 OR: Passenger rolling stock – Trailer bogies – Running gear – General provisions applicable to the components of trailers bogies. 2nd edition, 2003.
- [15] J. J. Kalker. *Three-dimensional elastic bodies in rolling contact*, volume 2. Springer Science & Business Media, 1990.
- [16] Y. Ma and V. L. Markine. A numerical procedure for analysis of w/r contact using explicit finite element methods. In *CM2015: 10th International Conference on Contact Mechanics, Colorado Springs, USA, 30 August-3 September 2015*, pages 1–10, 2015.
- [17] Y. Ma, M. Ren, G. Hu, and C. Tian. Optimal analysis on rail pre-grinding profile in high-speed railway. *Jixie Gongcheng Xuebao(Chinese Journal of Mechanical Engineering)*, 48(8):90–97, 2012.
- [18] Y. Ma, A. A. Mashal, and V. L. Markine. Numerical analysis of wheel-crossing interaction using a coupling strategy. In Pombo J., editor, *Proceedings of the 3rd international conference on railway technology: Research, development and maintenance, 5 April – 8 April*, pages 1–19, Cagliari, Italy, 2016. Civil-Comp Press, Stirlingshire, UK.
- [19] Y. Ma, V. L. Markine, A. A. Mashal, and M. Ren. Modelling verification and influence of operational patterns on tribological behaviour of wheel-rail interaction. *Tribology International*, 114:264–281, 2017. ISSN 0301-679X.

- [20] Y. Ma, V. L. Markine, A. A. Mashal, and Ren M. Improving the performance of finite element simulations on the wheel-rail interaction by using a coupling strategy. *Proceedings of the Institution of Mechanical Engineers, Part F: Journal of Rail and Rapid Transit*, 232(6):1741–1757, 2018.
- [21] Y. Ma, V. L. Markine, A. A. Mashal, and Ren M. Effect of wheel-rail interface parameters on contact stability in explicit finite element analysis. *Proceedings of the Institution of Mechanical Engineers, Part F: Journal of Rail and Rapid Transit*, 232(6):1879–1894, 2018.
- [22] Y. Ma, A. A. Mashal, and V. L. Markine. Modelling and experimental validation of dynamic impact in 1:9 railway crossing panel. *Tribology International*, 118:208–226, 2018.
- [23] N. K. Mandal and M. Dhanasekar. Sub-modelling for the ratchetting failure of insulated rail joints. *International Journal of Mechanical Sciences*, 75:110–122, 2013.
- [24] V. L. Markine, M. J. M. M. Steenbergen, and I. Y. Shevtsov. Combating RCF on switch points by tuning elastic track properties. *Wear*, 271(1):158–167, 2011.
- [25] J. Martínez-Casas, E. Di Gialleonardo, S. Bruni, and L. Baeza. A comprehensive model of the railway wheelset–track interaction in curves. *Journal of Sound and Vibration*, 333(18):4152–4169, 2014.
- [26] A. Matsumoto, Y. Sato, M. Tantomoto, Y. Oka, and E. Mtyauchi. Experimental and theoretical study on the dynamic performance of steering bogie in sharp curve. *Vehicle system dynamics*, 29(S1):559–575, 1998.
- [27] L. D. McMichael. Contact interface verification for dyna3d scenario 1: Basic contact. Technical report, Lawrence Livermore National Laboratory (LLNL), Livermore, CA, 2006.
- [28] M. Pletz, W. Daves, and H. Ossberger. A wheel set/crossing model regarding impact, sliding and deformation - explicit finite element approach. *Wear*, 294:446–456, 2012.
- [29] C. L. Pun, Q. Kan, P. J. Mutton, G. Kang, and W. Yan. Ratcheting behaviour of high strength rail steels under bi-axial compression–torsion loadings: Experiment and simulation. *International Journal of Fatigue*, 66:138–154, 2014.
- [30] J. W. Ringsberg, M. Loo-Morrey, B. L. Josefson, A. Kapoor, and J. H. Beynon. Prediction of fatigue crack initiation for rolling contact fatigue. *International Journal of fatigue*, 22(3):205–215, 2000.
- [31] I. Y. Shevtsov. *Wheel/rail interface optimisation*. PhD thesis, Delft University of Technology, 2008.
- [32] J. S. Sun, K. H. Lee, and H. P. Lee. Comparison of implicit and explicit finite element methods for dynamic problems. *Journal of Materials Processing Technology*, 105(1):110 – 118, 2000. ISSN 0924-0136.
- [33] T. Telliskivi, U. Olofsson, U. Sellgren, and P. Kruse. A tool and a method for fe analysis of wheel and rail interaction. *Royal Institute of Technology (KTH), Stockholm, Sweden*, 2000.
- [34] P. Vila, L. Baeza, J. Martínez-Casas, and J. Carballeira. Rail corrugation growth accounting for the flexibility and rotation of the wheel set and the non-hertzian and non-steady-state effects at contact patch. *Vehicle System Dynamics*, 52(sup1):92–108, 2014.
- [35] K. D. Vo, A. K. Tieu, H. T. Zhu, and P. B. Kosasih. A 3d dynamic model to investigate wheel–rail contact under high and low adhesion. *International Journal of Mechanical Sciences*, 85: 63–75, 2014.
- [36] E. A. H. Vollebregt. User guide for contact, vollebregt & kalker’s rolling and sliding contact model, technical report TR09-03, version, 2013.
- [37] E. A. H. Vollebregt, S. D. Iwnicki, G. Xie, and P. Shackleton. Assessing the accuracy of different simplified frictional rolling contact algorithms. *Vehicle System Dynamics*, 50(1):1–17, 2012.
- [38] J. D. Walker. *Fundamentals of Physics Extended*. Wiley, 2010.

- [39] C. Wan, V. L. Markine, and I. Y. Shevtsov. Analysis of train/turnout vertical interaction using a fast numerical model and validation of that model. *Proceedings of the Institution of Mechanical Engineers, Part F: Journal of Rail and Rapid Transit*, 228(7):730–743, 2014.
- [40] Z. Wen, X. Jin, and W. Zhang. Contact-impact stress analysis of rail joint region using the dynamic finite element method. *Wear*, 258(7):1301–1309, 2005.
- [41] M. Wiest, E. Kassa, W. Daves, J. C. O. Nielsen, and H. Ossberger. Assessment of methods for calculating contact pressure in wheel-rail/switch contact. *Wear*, 265(9):1439–1445, 2008.
- [42] S. R. Wu and L. Gu. *Introduction to the explicit finite element method for nonlinear transient dynamics*. John Wiley & Sons, 2012.
- [43] Y. Zhang and X. Kong. Effect of lateral displacement on elasto-plastic stress field in rail head. *Journal of Railway Engineering Society*, 16(1):17–20, 1999.
- [44] X. Zhao and Z. Li. The solution of frictional wheel–rail rolling contact with a 3D transient finite element model: Validation and error analysis. *Wear*, 271(1):444–452, 2011.

# 3

## EFFECT OF W/R INTERFACE PARAMETERS ON CONTACT STABILITY

*It is widely recognised that the accuracy of explicit FE simulations is sensitive to the choice of interface parameters (i.e., contact stiffness/damping, mesh generation, etc.) and time step sizes. Yet, the effect of these interface parameters on the explicit FE-based solutions of wheel-rail (W/R) interaction has not been discussed sufficiently in the literature. In this chapter the relation between interface parameters and the accuracy of contact solutions is studied. It shows that the wrong choice of these parameters, such as too high/low contact stiffness, coarse mesh or wrong combination of them, can negatively affect the solution of W/R interaction that manifests itself in amplification of contact forces and/or inaccurate contact responses (called here “contact instability”). The phenomena of “contact (in)stabilities” are studied using an explicit FE model of a wheel rolling over a rail. The accuracy of contact solutions is assessed by analysing the area of contact patches and the distribution of normal pressure. Also, the guidelines for selections of optimum interface parameters, that guarantee the contact stability and therefore provide an accurate solution, are proposed. The effectiveness of selected interface parameters is demonstrated through a series of simulations. The results of these simulations are presented and discussed.*

---

Parts of this chapter have been published in the Proceedings of the Institution of Mechanical Engineers, Part F: Journal of rail and rapid transit, (2017) [18]



Chapter 3 concentrates on how the choice of the four important interface parameters such as the penalty scale factor, mesh uniformity, mesh density and contact damping, affects the accuracy of the explicit FE-based contact solutions, since the default values of the interface parameters provided in the commercial FE packages are not always suitable for the modelling of W/R rolling contact. This chapter is aimed to answer the research question Q2 presented in Chapter 1.

To perform this study, the explicit FE model of a wheel rolling over a rail presented in Chapter 2 will be used. Also, the parameters such as contact clearance (0.17 mm), travelling distance (520 mm) suggested in Chapter 2, which ensure the satisfactory compromise between calculation accuracy and efficiency, will be used.

The outline of this chapter is as follows. First, a brief introduction of the research background of Chapter 3 is presented in Section 3.1. After that, Section 3.2 is focused on the theoretical background of the FE algorithms to better understand the physics of contact problems before attempting to solve it. Also, the challenges and approaches for maintaining contact stabilities are illustrated (See Section 3.3). The influence of interface parameters on the computational accuracy and contact stabilities is studied and discussed in Section 3.4. Finally, concluding remarks are drawn.

### 3.1 INTRODUCTION

When performing contact analysis, all contact forces have to be distributed over a-priori unknown area in contact. The contact pressure is another primary unknown in such a problem that has to be determined. To estimate these unknowns accurately, extensive research efforts have been made in the field of contact mechanics since the pioneering work of Hertz [8]. A number of analytical and/or semi-analytical contact solutions, such as Hertzian [8], non-Hertzian [26, 30], multi-Hertzian contact models [25], etc., have been developed and reported [12, 14, 23]. These approaches have been verified and/or validated to be effective and efficient enough for addressing the problems of wheel-rail (W/R) contact in elasticity as well as in the cases of quasi-static and/or low frequency dynamic [3, 20–22, 26, 33]. Regarding the complex problems with both realistic contact geometries and material plasticity considered, finite element (FE) method, as opposed to the aforementioned approaches, appears to be much preferable and powerful to ensure the desired solutions.

Generally, two basic methods are used in FE programmes to enforce the contact constraints, namely the Lagrange multiplier method [9, 10] and the penalty method [6, 7, 11, 13]. Due to the easy implementation, the penalty method has been always the first choice to be integrated in the explicit FE software (e.g. ANSYS LS-DYNA [6]), where the central difference method is commonly used to perform the time integration.

With the rapid development of computer power and computing techniques, many representative three-dimensional (3D) explicit FE models [27, 29, 34, 35] have been created to fulfil different engineering purposes. For instance, in [34], an explicit FE model was developed by Zhao & Li to study the behaviour of W/R frictional rolling contact. The results of verification against CONTACT [12, 30] showed that the FE model presented was a promising tool to be used in the future work. For example, as a further application of that model [34], Zhao et al. [35] assessed the performance of W/R frictional rolling contact in the presence of rail contaminants. It was reported that contact surface damages

such as wheel flats and rail burns might be caused by the presence of contaminants. In [29], the stress/strain responses of W/R interaction under high and low adhesion levels were assessed by Vo et al. It was found that the adhesion conditions were highly related to the level of damages (RCF damage, corrugation, etc.) on the rail surface. In [27], Pletz et al. introduced a dynamic wheel/crossing FE model to quantify the influence of operational parameters such as axle loads, train speeds, etc., on the impact phenomena. It was found that the contact pressure and the micro-slip were critical variables responsible for the surface damage of crossing rail. More recent modelling advances of W/R interaction, including the development of implicit FE models [20, 22, 31] (i.e., not referenced but of equal importance as those explicit FE models), can be found in [17, 23].

To summarise, significant progress in the analyses of W/R interaction using explicit FE tools has been made. However, the issue of selecting suitable interface parameters [11], as the essence of penalty-type methods [36], has not been studied sufficiently. Also, the resulting phenomena of “contact instabilities” from the improperly chosen interface parameters have not been discussed adequately. Here, the phenomenon of “contact instability” is referred to as a numerical problem of dynamic contact stability and has no physical correspondence. Detailed explanations of “contact (in)stability” are given in the later sections. The term of “interface parameters” is referred to as the key variables such as contact stiffness and damping that, if changed or varied, influence the entire operation of W/R dynamic interaction system. “Optimum” refers to the “interface parameters” employed that result in acceptable interface compatibility and maintains numerical contact stability [15].

Up to now only a few general guidelines [1, 5, 6, 11, 24] are available for making the choice of suitable interface parameters. For example, in [11], Huněk proposed that an appropriate value of contact stiffness (also called penalty stiffness) can be made considering the penalty stiffness comparable to the normal stiffness of the interface elements. Similarly, in [5, 6], Goudreau and Hallquist suggested the contact stiffness to be of approximately the same order of magnitude as the stiffness of the elements normal to the contact interface. In [1], Belytschko and Neal presented the upper bounds on the contact force in explicit calculations and showed the effect of the contact stiffness on the stable time step [11]. In [24], a coefficient of contact damping was introduced by Pifko et al. to suppress the high frequency oscillations.

Although those general guidelines are relatively helpful for identifying suitable interface parameters, it is widely recognised [9, 11, 15, 36, 37] that there are no universally applicable rules/guidelines for particular problems considered. Regarding the specific problem of W/R rolling contact, more research attention to the importance of interface parameters has to be drawn. The motivation of this study is thus summarised as follows:

- (i) To ensure accurate solutions of W/R interaction: Considering that the penalty methods enforce contact constraints approximately, the solution accuracy depends strongly on the interface parameters selected [9]. A set of arbitrary chosen interface parameters on the risk of being underestimated or overestimated may easily cause an unexpected or inaccurate solution from FE simulations.
- (ii) To formulate clear guidelines for suitable W/R interface parameters: The choice of interface parameters can affect not only the accuracy of contact solutions, but

also the stability of explicit FE time integration (i.e. central difference method is conditionally stable) [15, 36]. Thus, well-demonstrated guidelines are in high demand to address the problems of contact instabilities and to maintain the solution accuracy.

## 3.2 RECAP EXPLICIT FE THEORY

In this section, the corresponding explicit FE theories, which are highly related to the background of contact stability, are recapitulated. More generally, a solution of the unknown vector of the displacements  $\bar{\mathbf{u}}$  is to be found through the process of FE analysis. Using the Galerkin approximation method [38], the discretized equation of motion is given as [32]

$$\mathbf{M}\ddot{\mathbf{u}} = \mathbf{M}\mathbf{a} = \mathbf{F} \quad (3.1)$$

where  $\mathbf{M}$  is the mass matrix and  $\mathbf{F}$  is the force vector.  $\mathbf{a}$  is the nodal acceleration vector.

### 3.2.1 STABILITY OF CENTRAL DIFFERENCE METHOD

By taking advantage of the central difference method [6, 32, 37], the iterative scheme of the explicit time integration varying from the instant  $t_n$  to  $t_{n+1}$  becomes [6]

$$\begin{aligned} \mathbf{a}_n &= \mathbf{M}^{-1}\mathbf{F}_n \\ \mathbf{V}_{\frac{n+1}{2}} &= \mathbf{V}_{\frac{n-1}{2}} + \mathbf{a}_n\Delta t_n \\ \mathbf{u}_{n+1} &= \mathbf{u}_n + \mathbf{V}_{\frac{n+1}{2}}\Delta t_{\frac{n+1}{2}} \end{aligned} \quad (3.2)$$

where  $\Delta t_{\frac{n+1}{2}} = \frac{(\Delta t_n + \Delta t_{n+1})}{2}$ .  $\mathbf{V}$  is the global nodal velocity vector,  $n$  indicates the number of time steps. Due to the conditionally stable characteristic of the central difference method, the integration time step  $\Delta t_{calc}$  (also called calculation time step) must be small enough to maintain the numerical stability of the solution. The exact stability criterion is expressed as [6, 37]

$$\Delta t_{calc} < \Delta t_{crit} = 2/\omega_{max} \quad (3.3)$$

where  $\omega_{max}$  denotes the maximum eigenfrequency in the FE model. To satisfy this stability criteria, the explicit FE solver needs to find the maximum eigenfrequency of the whole FE dynamic system. As reported in [6, 32] that this is not practical, not only due to the computational cost but also the lack of Eigen-solver in the explicit FE programme. The alternative of Equation 3.3 is the Courant-Friedrichs-Lewy stability criterion (also called Courant criterion) [4], which states

$$\Delta t_{calc} = \min\{\Delta t_1, \Delta t_2, \Delta t_3, \dots, \Delta t_N\} \quad (3.4)$$

From Courant criterion, it can be seen that the global calculated time step  $\Delta t_{calc}$  is determined on the basis of the smallest critical time step value of all the elements within the FE model. Here,  $N$  refers to the maximum number of the element in the FE model.

### 3.2.2 PENALTY METHOD

The penalty method [7, 37] is one of the most commonly used approaches to enforce the contact constraints in the explicit FE programmes, where a list of invisible “interface spring” elements are placed between the penetrating slave nodes and the master segments (as depicted in Figure 3.1a-c). The restoring interface force vector  $\mathbf{f}_s$  [7] is aligned with the normal of the master segment  $\mathbf{n}_i$  and linearly dependent on the penetration depth  $l$ :

$$If \ l < 0, \mathbf{f}_s = -l \cdot k \cdot \mathbf{n} \quad (3.5)$$

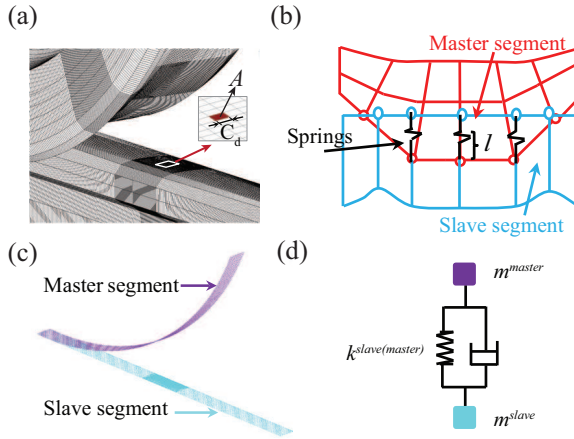


Figure 3.1: Schematic graph of penalty method: (a) Close-up view of FE model; (b) Cross-sectional view of contact segments; (c) Master-slave segments; (d) Schematic of “invisible” spring-damper-mass system.

#### CONTACT STIFFNESS

The penalty stiffness  $k$  for these “springs” is prescribed as follows [6]

$$k = \frac{\alpha \cdot K \cdot A^2}{V} = \alpha \cdot K \cdot C_d \quad (3.6)$$

where  $\alpha$  denotes the penalty scale factor.  $K$  is the bulk modulus,  $V$  and  $A$  represent the volume and face area of a contact element respectively,  $C_d$  is the side length of this element. An example of such a contact element is shown in Figure 3.1a.

Friction in LS-DYNA is based on the Coulomb formulation [2, 6]. To predict the frictional force  $f^{n+1}$  at next time step  $t_{n+1}$ , a trail force  $f^*$  calculated based on the frictional force  $f^n$  at the present time step  $t_n$  is introduced in the friction algorithm [2, 6]:

$$f^* = f^n - k\Delta e \quad (3.7)$$

where  $\Delta e$  is the relative displacement increment. The next frictional force  $f^{n+1}$  is given as:

$$f^{n+1} = \begin{cases} f^*, & \text{if } |f^*| \leq F_{yield} \\ \frac{F_{yield} f^*}{|f^*|}, & \text{if } |f^*| > F_{yield} \end{cases} \quad (3.8)$$

where  $F_{yield}$  refers to the maximum possible friction force  $\mu|\mathbf{f}|$ . As the simulation starts, the explicit FE programme predicts the frictional force iteratively using the central difference method [6].

### CONTACT DAMPING

In order to avoid undesirable oscillations in contact, a certain amount of viscous damping perpendicular to the contact surfaces is automatically included in the explicit FE software (e.g. LS-DYNA). For simplicity, a damping coefficient  $\xi$  is introduced as [6]

$$\xi = \frac{VDC}{100} \xi_{crit} \quad (3.9)$$

where  $\xi$  is given in percent of critical damping coefficient  $\xi_{crit}$  for explicit contact.  $VDC$  is the abbreviation of “viscous damping coefficient in percent of critical”. By default [6], the magnitude of  $VDC$  is 80, which means the applied damping coefficient  $\xi$  is as large as 80% of the critical damping coefficient  $\xi_{crit}$ .  $VDC$  is a control parameter that can be tuned to fit particular contact-related problems.

### 3.2.3 CONTACT STABILITY

Together with the related nodal mass  $m^{master}$  and  $m^{slave}$ , the “closed” contact segment (See Figure 3.1) becomes a “invisible” spring-damper-mass system. Here, the contact segments are the components of nodes on the outmost surface layer of the two wheel-rail contact bodies (See Figure 3.1c).  $m^{master}$  and  $m^{slave}$  are referred to as the master and slave nodal mass, respectively.

The interface spring stiffness  $k$  used in the contact algorithms [6] is based on the minimum value of the slave segment stiffness  $k^{slave}$  or master segment stiffness  $k^{master}$ . Accordingly, there are two time step sizes obtained according to the two contact stiffness (master and slave) for these invisible spring-damper contact elements. One is the contact time step size of master segment, the other is that of slave segment.

### CONTACT SURFACE TIME STEPS

Two critical time steps for the master segments  $\Delta t_{cont}^{master}$  and the slave segments  $\Delta t_{cont}^{slave}$  are defined individually as [6]

$$\begin{aligned} \Delta t_{cont}^{master} &= \frac{2}{\omega_{max}} = 2\sqrt{\frac{m^{master}}{k^{master}}} \\ \Delta t_{cont}^{slave} &= \frac{2}{\omega_{max}} = 2\sqrt{\frac{m^{slave}}{k^{slave}}} \end{aligned} \quad (3.10)$$

Taking the contact damping coefficient  $\xi$  into account, the critical time step size of contact elements  $\Delta t_{cont}^{master}$  and  $\Delta t_{cont}^{slave}$  will be reduced as [6]

$$\Delta t_{cont}^{master(slave)} = 2\sqrt{\frac{m^{master(slave)}}{k^{master(slave)}}} (\sqrt{1 + \xi^2} - \xi) \quad (3.11)$$

### CONTACT STABILITY CRITERIA

The calculation time step  $\Delta t_{calc}$  used in explicit FE software (e.g. LS-DYNA) is not allowed to be larger than the critical contact surface time step sizes [6], i.e.

$$\Delta t_{calc} < \min(\Delta t_{cont}^{master}, \Delta t_{cont}^{slave}) \quad (3.12)$$

Otherwise, the contact stability could not be guaranteed.

## 3.3 UNDERLYING CHALLENGES AND POSSIBLE SOLUTIONS

As it has been presented in Section 3.2, the FE theoretical background is rather complicated. There are several interface parameters involved in both the contact modelling and solving procedures. Thus, a number of challenges are encountered and need to be addressed.

### 3.3.1 INTERFACE PARAMETERS

To properly capture the highly non-linear contact characteristics of W/R interaction, a very dense mesh in the potential contact area is always desired. However, it is not always the case that the very dense mesh can be used in the model due to the large and complex contact geometries as well as the limited computer capability. Therefore, a non-uniform mesh (See Figure 2.1c) is introduced by making the solution area much denser than other contact regions.

It is clear that the two parameters (mesh density and mesh uniformity) shown in Figure 2.1c are to be adjusted and evaluated. By decreasing the length  $d_0$  of solution area into zero, the non-uniform mesh refinement becomes a uniform one. Similarly, the mesh density could be changed by increasing or decreasing the mesh size  $Esize$  of the element. Here, “mesh density” refers to the number of elements per unit area in the dense meshed area (not that in the solution area).

Besides, there are no standard routines on how to prescribe the magnitude of the penalty scale factor  $\alpha$  and the contact damping factor  $VDC$  embedded in Equation 3.6 and Equation 3.9. Their effects on the contact stability have not been sufficiently discussed especially in the field of FE-based simulations on W/R rolling frictional contact.

To sum up, the main challenges associated are exploring the relation between the dynamic responses of W/R interaction and the four key interface parameters: namely, 1) Penalty scale factor  $\alpha$ ; 2) Mesh uniformity  $d_0$ ; 3) Mesh size  $Esize$ ; 4) Contact damping factor  $VDC$ .

### 3.3.2 APPROACHES FOR ADDRESSING CHALLENGES

To address the aforementioned challenges, the approach of parametric study is adopted. In this section, the details of this approach are given first. Following that, the scheme on how to integrate such an approach with the FE analysis is presented.

#### PARAMETRIC STUDY

According to the general rule of a parametric study, the dynamic behaviour of the W/R interaction has to be studied by iteratively varying the values of certain interface parame-

ters, while the other parameters are fixed. Based on the parametric studies, the following questions are expected to be answered:

- (i) How does the contact instability look like? Are there any effective measures for maintaining the contact stability (if contact instability happens)?
- (ii) What are the effects of the interface parameters on the performance of the contact stability as well as on the dynamic contact responses?
- (iii) Is there a set of interface parameters that is the most suitable one for the analysis of W/R interaction ?

#### INTEGRATION WITH FE MODEL

To perform the parametric study, it has to be properly integrated with the 3D-FE model. Its basic working mechanism is shown in Figure 3.2.

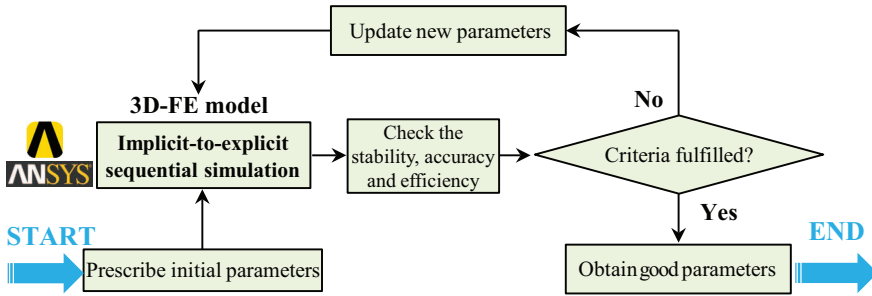


Figure 3.2: Flow chart of parametric study with 3D-FE model.

Firstly, an initial set of the interface parameters is prescribed in the 3D-FE model. Once the explicit FE simulations are completed, the statuses of the contact stability, calculation efficiency and accuracy have to be examined. The criteria are the satisfactory compromise among the contact stability, calculation efficiency and accuracy. When the criteria are fulfilled, the set of good/appropriate interface parameters is identified. If not, new parameters will be updated and tested against the 3D-FE simulations iteratively until such a compromise is reached.

### 3.4 RESULTS AND DISCUSSIONS

Following the flow chart shown in Figure 3.2, a series of explicit FE simulations are performed so as to examine the effect of the four interface parameters on the performance of W/R interaction. These interface parameters vary within certain given ranges:

- (i) Penalty scale factor  $\alpha$  (from 0.05 to 409.6);
- (ii) Mesh uniformity  $d_0$  (from 0 mm to 120 mm);
- (iii) Mesh size  $Esize$  (from 1.5 mm to 4.0 mm);
- (iv) Damping factor  $VDC$  (from 10 to 180).

It is worth noting that all these interface parameters are studied in the case of zero lateral shift of the wheel-set. To increase the calculation efficiency of this parametric study, the FE modelling procedure has been parametrised using MATLAB scripts and ANSYS Parametric Design Language (APDL) [17].

### 3.4.1 CONTACT STIFFNESS

Nine cases of penalty scale factor are selected to analyse varying from 0.05 to 102.4, while the other parameters keep constant. Due to the inversely proportional relation between the contact time steps  $\Delta t_{cont}^{slave(master)}$  and the square root of the penalty scale factor  $\alpha$  (Equation 3.6 and Equation 3.10), the increase of penalty scale factor  $\alpha$  will lead to the decrease of contact time step  $\Delta t_{cont}^{slave(master)}$ . The values of penalty scale factors are thus set to be the product of its “default” (0.1) and the  $m$ th power of 2 (i.e.  $\alpha = 0.1 \times 2^m$ ), which is to maintain the variation of  $\Delta t_{cont}^{master}$  and  $\Delta t_{cont}^{slave}$  to be approximately linear.  $m$  is chosen in the range of [-1, 10]. Here, the term of “default” means the programme suggested settings in explicit FE software LS-DYNA. By this means, the influence of penalty scale factors on the contact stability (Equation 3.12) is able to be effectively investigated.

Figure 3.3a shows the variation of vertical contact forces corresponding to different penalty scale factors  $\alpha$ . It can be seen that a “saw-toothed” force oscillation is generated and located at a distance of 150 mm from the origin. As the wheel rolls further along the rail and approaches the vicinity of the solution area ( $d_0 = 80\text{mm}$ ), a “sudden perturbation” of the contact force gets noticeable for the cases of  $\alpha = 204.8$  and  $\alpha = 409.6$  (extremely high contact stiffness) as well as those of  $\alpha = 0.05$  and  $\alpha = 0.1$  (extremely low contact stiffness).

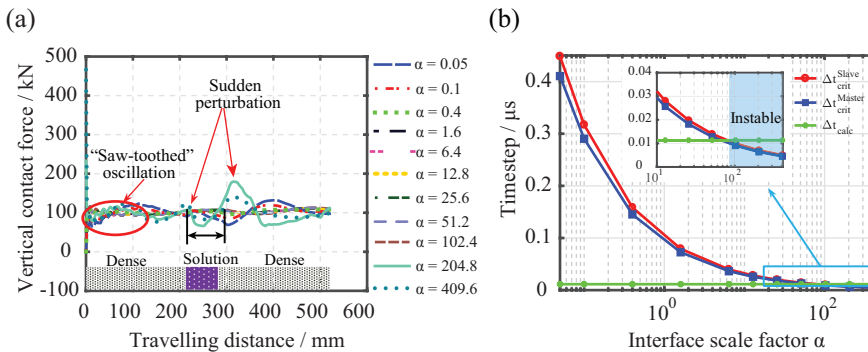


Figure 3.3: (a) Variation of vertical contact forces w.r.t. different penalty scale factors  $\alpha$ ; (b) Variation of three typical time steps.

The observed “saw-toothed oscillations” and “sudden perturbations” of the contact forces could all be interpreted as the indicators of “contact instability”. In contrast, a continuous and smooth dynamic response from the explicit FE simulations is perceived as a prognosis of the “contact stability”.

A comparison (See Figure 3.3b) of the contact time steps  $\Delta t_{cont}^{master}$ ,  $\Delta t_{cont}^{slave}$  with the calculation time step  $\Delta t_{calc}$  has been performed for all the studied cases. It shows that the two critical contact time-step sizes  $\Delta t_{cont}^{master}$  and  $\Delta t_{cont}^{slave}$  decrease significantly with



the increase of the penalty scale factor  $\alpha$ . At the region denoted by the blue block, where the penalty scale factor  $\alpha$  is larger than 100, the calculation time step  $\Delta t_{calc}$  starts to exceed the thresholds of the critical contact time steps  $\Delta t_{cont}^{master}$  and  $\Delta t_{cont}^{slave}$ . According to Equation 3.12, such a violation of the time step inequality could be hypothesised to be the main cause of the “sudden perturbation” at the solution area for the cases of  $\alpha = 204.8$  and  $\alpha = 409.6$ . With regard to the “saw-toothed oscillations”, it is hypothesised to be caused by the initial conditions (i.e. the vibration of the structure excited by the initial train velocities) of the explicit FE analysis.

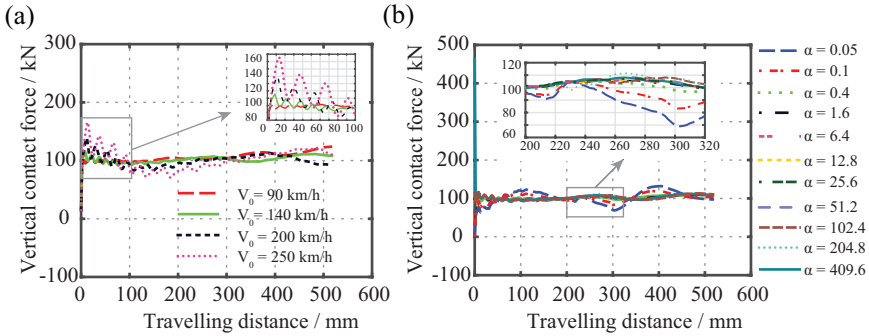


Figure 3.4: (a) Variation of vertical contact forces w.r.t. different train velocities  $V_0$ ; (b) Variation of vertical contact forces corresponding to reduced calculation time step sizes  $\Delta t_{calc}$ .

In order to verify the hypothesis of initial conditions, four FE simulations with different initial train velocities  $V_0$  ranging from 90km/h to 250km/h are performed. Here, the penalty scale factor  $\alpha$  of 12.8 is adopted. Figure 3.4a shows the variation of vertical contact forces with respect to different initial train velocities  $V_0$ . At the higher train speed levels, it can be seen that the “saw-toothed” dynamic force oscillations are getting more noticeable.

Besides, two more FE simulations for the cases of  $\alpha = 204.8$  and  $\alpha = 409.6$  have been performed, where their calculation time step sizes  $\Delta t_{calc}$  have been scaled down with a factor of 0.5 and 0.15, respectively. The corresponding variation of vertical contact forces is shown in Figure 3.4b. It can be clearly seen that the “sudden perturbations” at the vicinity of the solution area have disappeared. Thus, the two hypotheses of the time steps violations and initial conditions have been verified.

However, the calculation expenses for the tuned cases of  $\alpha = 204.8$  and  $\alpha = 409.6$ , which grow from 8.8 hours to 15.91 hours and 50.32 hours, have been significantly increased because of the reduced calculation time step size. As a consequence, the calculation efficiency is negatively affected. Moreover, it is observed from Figure 3.4b that the variation of vertical contact forces is getting converged with the increase of the penalty scale factor  $\alpha$ .

Figure 3.5 shows the distributions of normal contact pressure, which are extracted at the instant when the wheel travels over the middle of the solution area. It can be seen that both the magnitude and distribution of the contact pressure tend to converge at higher levels of penalty scale factor. Such an observation agrees well with the classical penalty theory [6, 7, 37, 38] that the larger the contact stiffness is, the more realistic the

results would be.

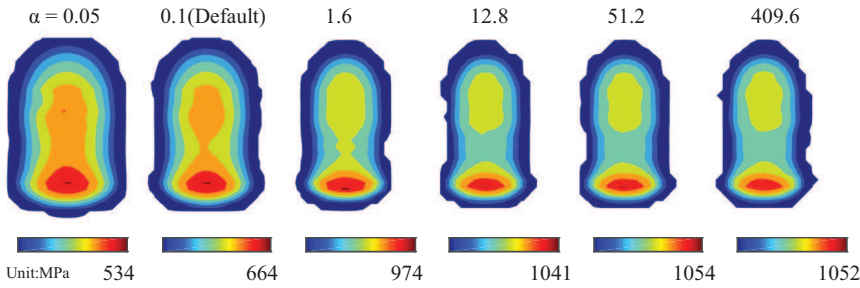


Figure 3.5: Effect of contact stiffness on contact pressure distribution.

It can be concluded from the simulation results that the default parameters (such as the default penalty scale factor  $\alpha = 0.1$ ) in LS-DYNA cannot accurately simulate the dynamic behaviour of the W/R interaction well, and the values of these parameters used in the analysis have to be justified. The guideline for selecting a suitable penalty scale factor  $\alpha$  could be formulated as follows:

- (i) To ensure a proper accuracy of the contact solution, the contact stiffness should be as large as possible, which can be achieved by increasing the penalty scale factor  $\alpha$ . For the chosen value of the penalty scale factor, the calculation time step  $\Delta t_{calc}$  should be smaller than the contact time step sizes  $\Delta t_{cont}^{slave(master)}$  so as to guarantee the contact stability as explained in Figure 3.3. The time step sizes of  $\Delta t_{cont}^{slave(master)}$  are available in the output of LS-DYNA;
- (ii) Once the calculation time step  $\Delta t_{calc}$  exceeds the thresholds of contact time steps  $\Delta t_{cont}^{slave(master)}$ , a reduced calculation time step is demanded to retrieve the stable dynamic contact response and get rid of the sudden perturbations (if it happens), but with a sacrifice of the calculation efficiency.

Based on the aforementioned guideline, a penalty scale factor  $\alpha$  of 12.8 that can maintain the good compromise of the accurate contact performance and calculation efficiency is suggested.

### 3.4.2 MESH UNIFORMITY

Figure 3.6a-b shows the FE models corresponding to different mesh uniformities. The case of  $d_0$  equal to 0 mm means the uniform mesh (See Figure 3.6d).  $d_0$  is prescribed to vary from 0 mm to 120 mm. When the length of the solution area changes from 40 mm to 120 mm, the number of the solid elements in the solution area increases from 472 to 1382.

To study the influence of the mesh uniformity on the dynamic performance of W/R interaction, the default penalty scale factor  $\alpha$  of 0.1 is chosen to be studied first, while the other parameters (except the mesh uniformity  $d_0$ ) are fixed.

Figure 3.7a shows the dynamic responses with the default penalty scale factor of  $\alpha = 0.1$ . It can be noticed that the “sudden perturbations” happen again nearby the solution

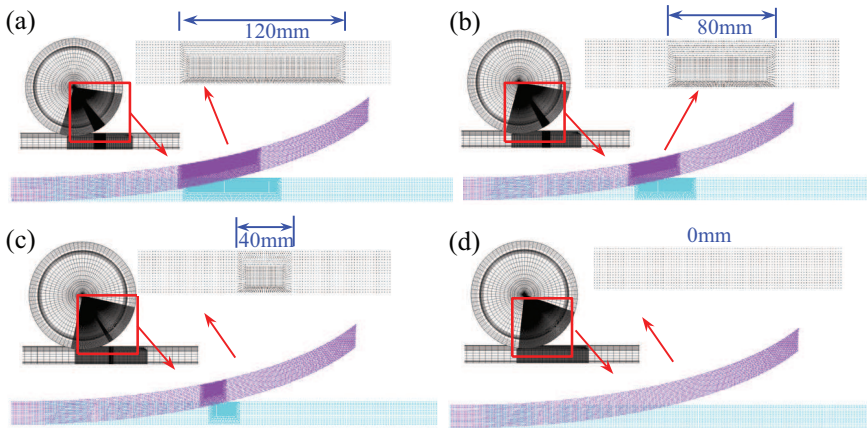


Figure 3.6: Variation of non-uniform mesh to uniform mesh: (a) 120 mm; (b) 80 mm; (c) 40 mm; (d) 0 mm - uniform mesh.

area. Taking the case of  $d_0 = 0\text{ mm}$  (uniform mesh refinement) as a reference, it can be seen that the location of the starting and ending points of the perturbation is highly related to the exact position and the dimension  $d_0$  of the solution area. Moreover, it can be observed that the curves of vertical contact forces are overlapped before the wheel entering into the solution area, while the difference is getting more pronounced after it passing over the solution area. Presumably, it is the default penalty scale factor  $\alpha = 0.1$  that is too low to compensate the drastic contact stiffness difference between the dense meshed region and the solution area of the contact bodies as shown in Figure 3.7a.

To verify the presumption of the contact stiffness difference, another four cases of FE simulations corresponding to different mesh uniformities have been performed analysed using the suggested best penalty scale factor of 12.8. The variation of vertical contact forces has been shown in Figure 3.7b. It can be seen that the “sudden perturbations” of the contact instability inside the solution area, which occur at the default penalty scale factor of 0.1 as shown in Figure 3.7a, die out. All the responses of the contact forces seem to converge into a common curve. This implies that the “sudden perturbations” introduced by mesh non-uniformity at low contact stiffness could be arrested and eliminated by specifying a high enough penalty scale factor (i.e. 12.8). In other words, the high penalty scale factor can minimise the contact stiffness difference and maintain the contact stability.

Figure 3.8 shows the variation of time step sizes corresponding to different mesh uniformities. It is clear that the calculation time step size  $\Delta t_{calc}$  decreases significantly, when the mesh pattern changes from uniform to non-uniform. For this reason, the calculation expense of the non-uniform mesh increases from 8 hours (that of uniform mesh) to more than 20 hours. Besides, it is observed that, at higher penalty scale factor of  $\alpha = 12.8$ , the gap between calculation and contact time step sizes reduces much more than that of low penalty scale factor ( $\alpha = 0.1$ ). This is complementary to the relation between contact stiffness and the time step size as derived from Equation 3.10.

It is observed from Figure 3.9 that both the magnitude & distribution of the contact

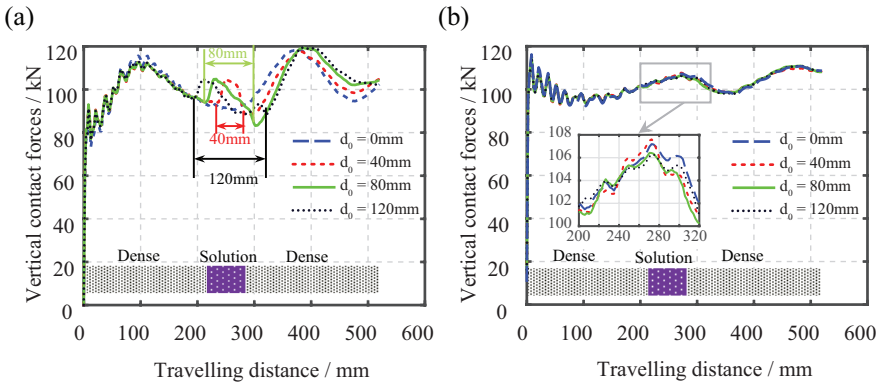


Figure 3.7: Variation of vertical contact forces w.r.t. different mesh uniformities: (a) Default penalty scale factor  $\alpha = 0.1$ ; (b) Optimal penalty scale factor  $\alpha = 12.8$ .

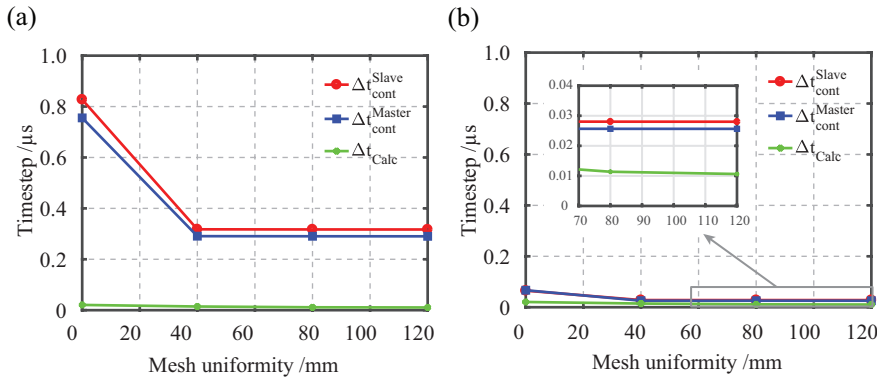


Figure 3.8: Variation of time step sizes w.r.t. different mesh uniformities: (a) Default penalty scale factor  $\alpha = 0.1$ ; (b) Optimal penalty scale factor  $\alpha = 12.8$ .

pressure obtained from the uniformly meshed FE model are quite different from those of FE simulations having non-uniform mesh patterns. The reason for that is attributed to the difference of FE mesh patterns in the solution area, where the uniformly meshed FE model is too coarse to capture the high stress gradients within the contact patch. It further demonstrates the importance of mesh non-uniformities to the contact solutions, which means the mesh non-uniformity is one necessary feature for the analysis of W/R interaction.

Despite the fact that the mesh non-uniformity can introduce a high (more than 20 hours) calculation expense compared with the uniformed mesh (8 hours), detailed contact properties are obtained. Considering that the longer the refined solution area is, the greater the amount of the elements will be created, it makes sense to adopt the length  $d_0 = 80\text{mm}$  of the solution area to make a satisfactory compromise between the calculation efficiency and accuracy. Although the mesh non-uniformity introduces contact instability, using proper (e.g.  $\alpha = 12.8$ ) contact stiffness this effect can be eliminated.

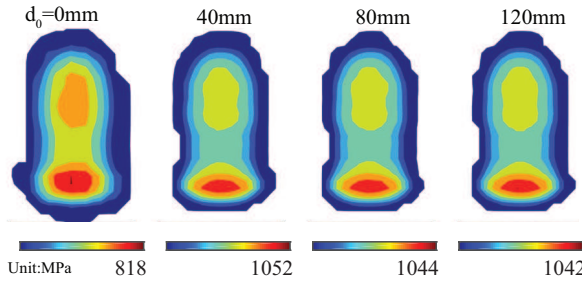


Figure 3.9: Effect of mesh uniformity on contact pressure distribution.

### 3.4.3 MESH DENSITY

In order to study the effect of mesh density on the performance of W/R interaction, six cases of mesh size varying from 1.5 to 4.0 mm are studied. The other parameters are fixed.

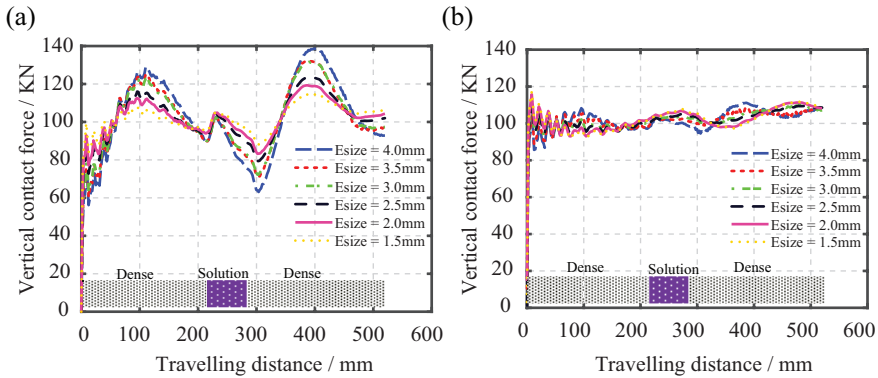


Figure 3.10: Variation of vertical contact forces w.r.t. different mesh sizes: (a) Default penalty scale factor  $\alpha = 0.1$ ; (b) Optimal penalty scale factor  $\alpha = 12.8$ .

Figure 3.10a shows the variation of vertical contact forces corresponding to different mesh sizes. It should be noted that the penalty scale factor  $\alpha = 0.1$  is in default for the present studied cases. It can be seen that the amplitude of “sudden perturbations” inside the solution area is gradually reducing with the decrease of the mesh size. It implies that the mesh density would be an alternative parameter of preventing the “sudden perturbations” in addition to the penalty scale factor  $\alpha$ .

To further evaluate the influence of mesh density at high level of contact stiffness, another six cases of varying mesh sizes are studied by increasing the penalty scale factor to the optimal one of  $\alpha = 12.8$ . Figure 3.10b shows the variation of vertical contact forces with respect to different mesh sizes. The prior insistent statement that an increased penalty scale factor could eliminate the contact instability (“sudden perturbation”), has been further verified.

The reason of this phenomenon can be attributed to the reduced element size, which

decreases from  $C_d$  to  $\lambda C_d$  in the solution area. Here,  $\lambda$  is a scale factor,  $0 < \lambda < 1$ . Given a constant penetration depth  $l$ , it derives from Equation 3.5 and Equation 3.6 that,

$$\lambda \cdot \lambda \cdot \mathbf{f}_s = -l \cdot \alpha \cdot K \cdot \lambda \cdot C_d \cdot \mathbf{n} \tag{3.13}$$

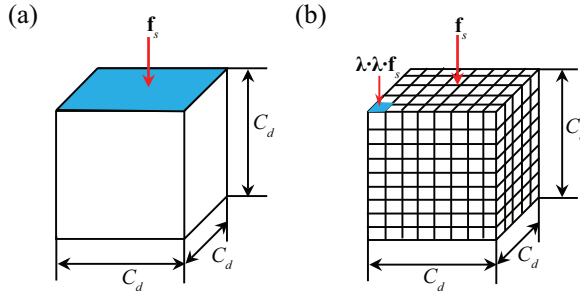


Figure 3.11: Schematic graph of mesh size variation: (a) Brick element with side length of  $C_d$  (also shown in Figure 3.1a); (b) Refined small element with side length of  $\lambda C_d$ .

From Equation 3.5 and Equation 3.13, it finds that the nodal contact stiffness  $k$  contributed by the smaller elements ( $\lambda C_d$ ) only decreases by a factor of  $\lambda$  in comparison with that of large elements ( $C_d$ ). But the overall contact stiffness (i.e. the summation of nodal contact stiffness  $\sum k$ ) increases  $\frac{1}{\lambda}$  times. For instance, if  $\lambda$  is  $\frac{1}{4}$ , the overall contact stiffness will increase 4 times.

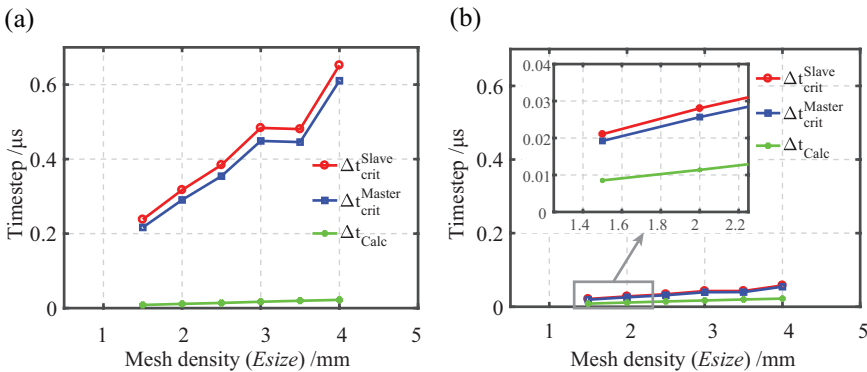


Figure 3.12: Variation of time step sizes w.r.t. different mesh sizes: (a) Default penalty scale factor  $\alpha = 0.1$ ; (b) Optimal penalty scale factor  $\alpha = 12.8$ .

Figure 3.12a-b shows the variation of time step sizes with respect to different mesh sizes. With the decrease of the element size, both the contact and calculation time step sizes tend to drop.

Figure 3.13a shows the normal contact pressure as continuous contour plots for all the nodes in contact. It can be seen that the distribution of the normal contact pressure is getting converged towards the denser mesh, which also indicates that the denser the mesh is, the better the contact solution would be ensured.

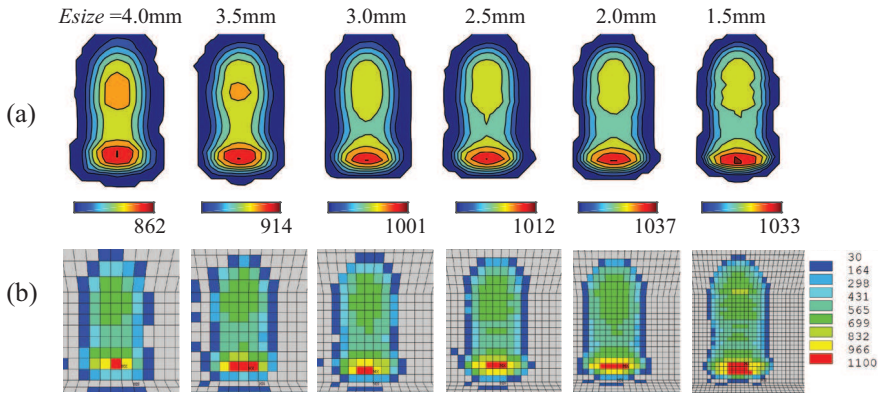


Figure 3.13: Effect of mesh size on contact pressure distribution: (a) Nodal contour plot; (b) Element contour plot.

Figure 3.13b shows the normal contact solution results as discontinuous element contours. The discontinuity between contours of adjacent elements is an indicator of the stress gradient across elements. These element contours are determined by linear interpolation within each element, unaffected by surrounding elements (i.e. no nodal averaging is performed). Following the method presented in [16], the contact statuses of these elements are determined by the normal pressure  $\sigma_n$  as:

$$\text{An element is in contact: if } \sigma_n > 0 \quad (3.14)$$

Table 3.1 lists the quantitative results in terms of the number of elements in contact and the size of the resulting contact patches. The maximum number of element in contact is 379 for the case of  $Esize = 1.5mm$ , whereas it is only 73 for  $Esize = 4.0mm$ . With the decrease of the mesh size  $Esize$ , the number of elements in contact increases significantly. Also, the size of the contact patch is getting smaller in accordance with the mesh size.

As the calculation expense would increase drastically due to the huge amount of elements generated, it is hardly possible to run the simulations with extremely small mesh size (e.g. 0.5 mm). The alternative is to run the simulation with a better selected parameter of mesh density, which could compromise between the calculation accuracy and efficiency in accordance with the criteria stated in Section 3.3. It is found that when the ratio of the contact area to the number of element in contact is around 1, the satisfactory compromise between calculation efficiency and accuracy is reached. Thus, the appropriate mesh size at the dense meshed area is suggested to be 2.0 mm (Case V, highlighted with light-grey colour, See Table 3.1), while the one in the solution area is 1.0 mm. It is worth noting that the suggested mesh size in solution area (i.e. 1.0 mm) falls within the range of 0.33 mm to 1.33 mm, which are recommended by Zhao & Li [34] to maintain an accuracy comparable to that of CONTACT and to satisfy the accuracy of engineering applications, respectively.

In summary, the mesh density can drastically influence the dynamic responses of W/R interaction when the contact stiffness is small. With the increase of the penalty

Table 3.1: Effect of mesh size on normal contact properties.

	$Esize/mm$	$A_c^a/mm^2$	$N^b$	$A_c^{mean\ c}/mm^2$
Case I	4.0	307.4	73	4.2
Case II	3.5	299.7	89	3.4
Case III	3.0	287.9	117	2.5
Case IV	2.5	277.0	154	1.8
Case V	2.0	265.8	218	1.2
Case VI	1.5	258.5	379	0.7

<sup>a</sup>: Real contact area, which is enclosed by the outmost contour line of Figure 3.12a. Note that the mesh size in this area is  $\frac{1}{2}Esize$  instead of  $Esize$  (definition See Section 3.3.1). Approximately,  $A_c$  is equal to  $N$  times the square of  $\frac{1}{2}Esize$ ;  
<sup>b</sup>: Number of elements in contact;  
<sup>c</sup>: Average contact area per element,  $A_c^{mean} = A_c/N$ .

stiffness, the dynamic response is getting less sensitive to the variation of mesh density. The denser the FE mesh is, the better the FE results can represent the reality.

### 3.4.4 CONTACT DAMPING

As similar to the parametric cases studied previously, the contact damping factor  $VDC$  varies from 10 to 180. The corresponding dynamic responses of W/R contact forces are displayed in Figure 3.14. It can be seen that when the contact damping factor is getting higher than 160, the resulting contact forces start to oscillate.

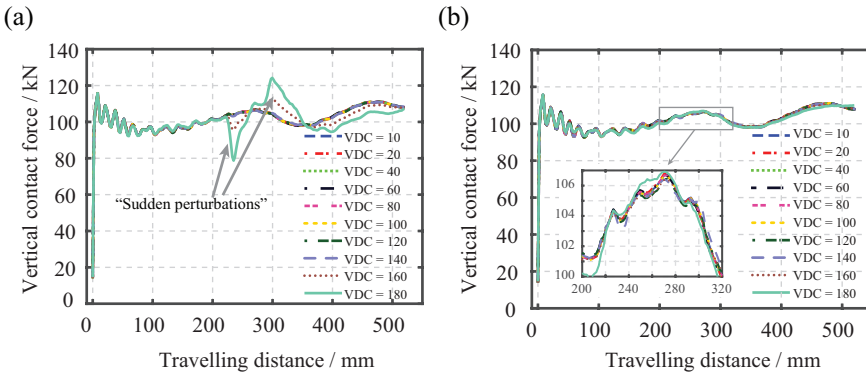


Figure 3.14: Variation of vertical contact forces w.r.t. different contact damping factors  $VDC$ : (a) Default calculation time step  $\Delta t_{calc}$ ; (b) Reduced calculation time steps  $\Delta t_{calc}$ .

According to Equation 3.11 and Equation 3.12, the “sudden perturbations” (nearly the solution area) are assumed to be caused by the fact that the value of the calculation time step size exceeds the magnitude of the reduced critical contact time step size. Attempts have been made to check the time step violations by comparing the contact



time step sizes and the calculation time step sizes. It is found that the exported contact time step size only follows Equation 3.10, which means that the influence of the contact damping as indicated by Equation 3.11 is not considered for output. As a consequence, all the contact time step size are remaining constant under different contact damping factors. Therefore, the check of time step violations such as the ones shown in Figure 3.8 and Figure 3.12 are not presented in this section. But it is still assumed that the high contact damping is the main cause of the “sudden perturbations”.

To check the validity of the assumption, the calculation time step sizes  $\Delta t_{calc}$  for the cases of  $VDC = 160$  and  $VDC = 180$  have been scaled down with two factors of 0.5 and 0.3, respectively. It is found that the variation of vertical contact forces is getting stable again (See Figure 3.14b). This re-stabilization process of contact forces implies that the contact damping would be another parameter, which can trigger the phenomenon of contact instability. The approach of retrieving the contact stability (if the phenomenon of contact instability happens) is always to reduce the calculation time step size, but with a sacrifice of the calculation efficiency.

Figure 3.15 shows the variation of the contact pressure corresponding to different contact damping factors. It can be seen that both the magnitude & distribution of the contact pressure hold almost constant, which indicates that the influence of contact damping factors on the contact pressure is insignificant. This agrees with the statement made in [6] that contact damping tends to play an important role in the analysis of impact-related problems.

In short, the contact damping is a parameter that is low sensitive to the analyses of W/R interaction. The default damping factor  $VDC$  of 80 is good enough to fulfil the criteria of contact stability.

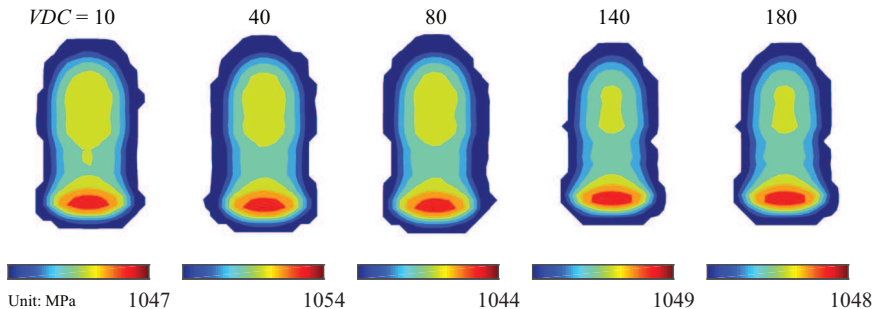


Figure 3.15: Effect of contact damping on contact pressure distribution.

As reported in [28], the sources of contact damping are relatively complex in reality, including the surface roughness, lubricant, liquid, etc. Although those over-critical damping factors (i.e.  $VDC > 100$ ) employed may not have a direct physical correspondence, it is necessary to demonstrate the low sensitive effect of contact damping to the contact instabilities. Further investigation on the modelling of contact damping with high degree of realism is part of future work.

### 3.4.5 DISCUSSION: APPLICABILITY OF SUGGESTED GUIDELINES & PARAMETERS

From the parametric results, it can be recognised that the proposed guidelines are suitable for identifying an appropriate set of interface parameters. Those guidelines are not subjected to particular geometrical and/or technical restrictions (i.e. special contact geometries, hardware configurations, programming languages, etc.). Thus, it enables the suggested guidelines to have broad applicability in the area of explicit FE-based contact modelling, especially in which the contact constraints are enforced with penalty method. It is recommended for further applications to other mechanical contact/impact systems (e.g. gear, bearing, etc.) having complex local contact geometries.

With respect to the suggested interface parameters (i.e. penalty scale factor ( $\alpha = 12.8$ ), damping factor ( $VDC = 80$ ), mesh size ( $Esiz = 2.0mm$ ) & uniformity ( $d_0 = 80mm$ )), it has reduced applicability in comparison with those guidelines. The reason is that the choice of interface parameters is strongly dependent on the level and form of the mesh discretization, which determine the magnitude of calculation & contact time step sizes and manifest themselves further in the phenomena of contact (in)stabilities.

To summarise, the applicability of the interface parameters suggested is classified as two categories:

- (i) Suggested/similar mesh patterns as shown in [Figure 2.1](#): The interface parameters suggested have wide applicability for the cases of different axle loads, train speeds, W/R profiles, etc. This can be explained by the recapitulated explicit FE theory, from which it finds that these varying operational patterns and geometrical parameters have no direct relations with the criteria of contact stability.

Taking the varying axle loads (ranging from 80 kN to 140 kN) as an example (See [Figure 3.16](#)), the interface parameters suggested are capable of suppressing the oscillations of contact forces and thus maintain the contact stability effectively. Also, with the increase of axle load, a steady growth of the area of contact patches and the magnitude of contact pressure is observed.

It has also been demonstrated in [[16](#), [19](#)] that the interface parameters suggested are suitable for the cases of varying operational patterns (i.e. varying friction and traction) and contact geometries (e.g. crossing rail).

- (ii) Different mesh patterns: When the form (uniformity) and level (density) of mesh discretization change, the magnitudes of both the calculation  $\Delta t_{calc}$  and contact  $\Delta t_{cont}^{slave(master)}$  time step sizes will be affected (See [Figure 3.8](#) and [Figure 3.12](#)). Thus, the suitable interface parameters determined based on [Equation 3.12](#) might differ from those suggested. In other words, the interface parameters suggested need to be improved to fit the changing mesh pattern.

Taking the selection of suitable penalty scale factor  $\alpha_{optimal}$  as an example, [Figure 3.17a](#) schematically shows the relation (i.e. adapted from [Figure 3.3b](#)) between the calculation and contact time step sizes. As discussed previously, the optimal penalty scale factor  $\alpha_{optimal}$  is selected at the vicinity of the unstable area (i.e.  $\Delta t_{calc} > \Delta t_{cont}^{slave(master)}$ ).

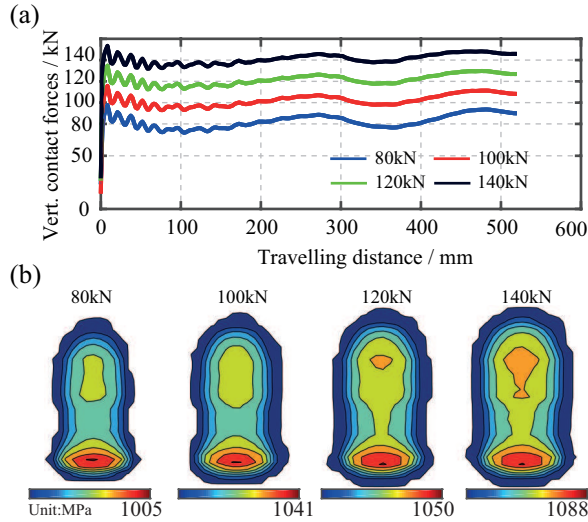


Figure 3.16: Applicability of interface parameters suggested to the cases of varying axle loads: (a) Vertical contact forces; (b) Contact pressure.

For this reason, the change of optimal penalty scale factor, alongside the varying mesh patterns, is divided into three groups:

- (1) Variation of  $\Delta t_{calc}$  (See Figure 3.17b): If the minimum side length of solid element varies, the curve of calculation time step size  $\Delta t_{calc}$  moves up and down. Accordingly, the optimal penalty scale factors  $\alpha_{optimal}$  selected have to shift.
- (2) Variation of  $\Delta t_{cont}^{slave(master)}$  (See Figure 3.17c): If the mesh size of contact elements varies, the curves of contact time step  $\Delta t_{cont}^{slave(master)}$  will offset laterally. This is complementary to the variation of contact time steps shown in Figure 3.8. Similarly, the optimal penalty scale factors selected will change.
- (3) Variation of both  $\Delta t_{calc}$  and  $\Delta t_{cont}^{slave(master)}$  (See Figure 3.17d): In this case, the optimal penalty scale factors will move both horizontally and vertically.

In summary, when the mesh patterns significantly different from that shown in Figure 2.1, it is suggested to follow the general guidelines to find the suitable interface parameters.

### 3.5 CONCLUSIONS

In this chapter the effect of W/R interface parameters on the contact stability in the explicit finite element (FE) analysis has been studied. The numerical phenomena called “contact (in)stabilities” have been presented.

Based on the results of this study, it is concluded that the interface parameters (e.g. contact stiffness, damping, mesh size etc.) strongly affect the accuracy of contact solutions and must be selected carefully. The wrong choice of these parameters (such as too

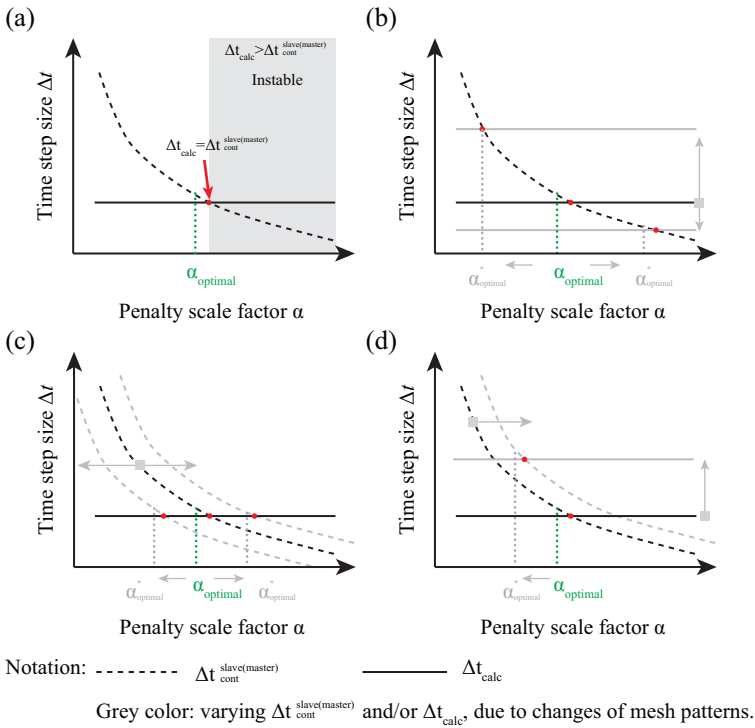


Figure 3.17: Effect of mesh patterns on selection of optimal penalty scale factor  $\alpha$ : (a) Reference case (generalised from Figure 3.3b); (b) Variation of  $\Delta t_{calc}$ ; (c) Variation of  $\Delta t_{cont}^{slave(master)}$ ; (d) Variation of  $\Delta t_{calc}$  and  $\Delta t_{cont}^{slave(master)}$ .

high/low contact stiffness and damping, course mesh or wrong combination of these parameters) can result in an inaccurate solution of the contact problem that manifests itself in amplification of the contact force or/and inaccurate contact responses (mainly due to the contact instability). The choice of these parameters used in the explicit FE analysis has to be justified.

The guideline for the selection of optimum interface parameters, which guarantee the contact stability and therefore provide an accurate solution, is proposed. According to this guideline, the time steps in the explicit analysis  $\Delta t_{calc}$  and  $\Delta t_{cont}^{slave(master)}$ , which are determined by the interface parameters, must be tuned as close as possible to each other.

An appropriate set of interface parameters is suggested (i.e. penalty scale factor (12.8), damping factor (80), mesh size (dense meshed area: 2.0 mm; solution area: 1.0mm) & uniformity (80 mm)). In comparison with the general applicability of the proposed guidelines (e.g. other mechanical contact/impact systems), the interface parameters suggested have reduced applicability.

Further research on the contact instabilities excited physically by friction or surface defects (i.e. wheel-flats, corrugation, squats, etc.) is part of future work.

## REFERENCES

- [1] T. Belytschko and M. O. Neal. Contact-impact by the pinball algorithm with penalty and lagrangian methods. *International Journal for Numerical Methods in Engineering*, 31(3):547–572, 1991.
- [2] D. J. Benson and J. O. Hallquist. A single surface contact algorithm for the post-buckling analysis of shell structures. *Computer Methods in Applied Mechanics and Engineering*, 78(2): 141–163, 1990.
- [3] Y. C. Chen and J. H. Kuang. Contact stress variations near the insulated rail joints. *Proceedings of the Institution of Mechanical Engineers, Part F: Journal of Rail and Rapid Transit*, 216(4): 265–273, 2002.
- [4] R. Courant, K. Friedrichs, and H. Lewy. Über die partiellen Differenzgleichungen der mathematischen Physik. *Mathematische annalen*, 100(1):32–74, 1928.
- [5] G. L. Goudreau and J. O. Hallquist. Recent developments in large-scale finite element lagrangian hydrocode technology. *Computer Methods in Applied Mechanics and Engineering*, 33(1-3):725–757, 1982.
- [6] J. O. Hallquist. ANSYS/LS-DYNA theoretical manual, 2005.
- [7] J. O. Hallquist, G. L. Goudreau, and D. J. Benson. Sliding interfaces with contact-impact in large-scale lagrangian computations. *Computer methods in applied mechanics and engineering*, 51(1-3):107–137, 1985.
- [8] H. R. Hertz. Über die Berührung fester elastischer Körper und über die Härte. *Journal für die reine und angewandte Mathematik*, 92:156–171, 1882.
- [9] N. Hu. A solution method for dynamic contact problems. *Computers & structures*, 63(6): 1053–1063, 1997.
- [10] T. J. R. Hughes, R. L. Taylor, J. L. Sackman, A. Curnier, and W. Kanoknukulchai. A finite element method for a class of contact-impact problems. *Computer Methods in Applied Mechanics and Engineering*, 8(3):249–276, 1976.
- [11] I. Huněk. On a penalty formulation for contact-impact problems. *Computers & structures*, 48(2):193–203, 1993.
- [12] J. J. Kalker. *Three-dimensional elastic bodies in rolling contact*, volume 2. Springer Science & Business Media, 1990.
- [13] N. Kikuchi and J. T. Oden. *Contact problems in elasticity: a study of variational inequalities and finite element methods*. SIAM, 1988.
- [14] K. Knothe. History of wheel/rail contact mechanics: from redtenbacher to kalker. *Vehicle System Dynamics*, 46(1-2):9–26, 2008.
- [15] R. F. Kulak. Adaptive contact elements for three-dimensional explicit transient analysis. *Computer methods in applied mechanics and engineering*, 72(2):125–151, 1989.
- [16] Y. Ma, V. L. Markine, A. A. Mashal, and M. Ren. Modelling verification and influence of operational patterns on tribological behaviour of wheel-rail interaction. *Tribology International*, 114:264–281, 2017. ISSN 0301-679X.
- [17] Y. Ma, V. L. Markine, A. A. Mashal, and Ren M. Improving the performance of finite element simulations on the wheel-rail interaction by using a coupling strategy. *Proceedings of the Institution of Mechanical Engineers, Part F: Journal of Rail and Rapid Transit*, 232(6):1741–1757, 2018.
- [18] Y. Ma, V. L. Markine, A. A. Mashal, and Ren M. Effect of wheel-rail interface parameters on contact stability in explicit finite element analysis. *Proceedings of the Institution of Mechanical Engineers, Part F: Journal of Rail and Rapid Transit*, 232(6):1879–1894, 2018.
- [19] Y. Ma, A. A. Mashal, and V. L. Markine. Modelling and experimental validation of dynamic impact in 1:9 railway crossing panel. *Tribology International*, 118:208–226, 2018.

- [20] N. K. Mandal. Finite element analysis of the mechanical behaviour of insulated rail joints due to impact loadings. *Proceedings of the Institution of Mechanical Engineers, Part F: Journal of Rail and Rapid Transit*, 230(3):759–773, 2016.
- [21] N. K. Mandal. Ratchetting damage of railhead material of gapped rail joints with reference to free rail end effects. *Proceedings of the Institution of Mechanical Engineers, Part F: Journal of Rail and Rapid Transit*, 231(2):211–225, 2017.
- [22] N. K. Mandal and M. Dhanasekar. Sub-modelling for the ratchetting failure of insulated rail joints. *International Journal of Mechanical Sciences*, 75:110–122, 2013.
- [23] S. Z. Meymand, A. Keylin, and M. Ahmadian. A survey of wheel–rail contact models for rail vehicles. *Vehicle System Dynamics*, 54(3):386–428, 2016.
- [24] A. B. Pifko and R. Winter. Theory and application of finite element analysis to structural crash simulation. *Computers & Structures*, 13(1):277–285, 1981.
- [25] J. Piotrowski and H. Chollet. Wheel–rail contact models for vehicle system dynamics including multi-point contact. *Vehicle System Dynamics*, 43(6-7):455–483, 2005.
- [26] J. Piotrowski and W. Kik. A simplified model of wheel/rail contact mechanics for non-hertzian problems and its application in rail vehicle dynamic simulations. *Vehicle System Dynamics*, 46(1-2):27–48, 2008.
- [27] M. Pletz, W. Daves, and H. Ossberger. A wheel set/crossing model regarding impact, sliding and deformation - explicit finite element approach. *Wear*, 294:446–456, 2012.
- [28] C. Tomberger, P. Dietmaier, W. Sextro, and K. Six. Friction in wheel–rail contact: a model comprising interfacial fluids, surface roughness and temperature. *Wear*, 271(1):2–12, 2011.
- [29] K. D. Vo, A. K. Tieu, H. T. Zhu, and P. B. Kosasih. A 3d dynamic model to investigate wheel–rail contact under high and low adhesion. *International Journal of Mechanical Sciences*, 85: 63–75, 2014.
- [30] E. A. H. Vollebregt. User guide for contact, vollebregt & kalker's rolling and sliding contact model, technical report TR09-03, version, 2013.
- [31] M. Wiest, E. Kassa, W. Daves, J. C. O. Nielsen, and H. Ossberger. Assessment of methods for calculating contact pressure in wheel-rail/switch contact. *Wear*, 265(9):1439–1445, 2008.
- [32] S. R. Wu and L. Gu. *Introduction to the explicit finite element method for nonlinear transient dynamics*. John Wiley & Sons, 2012.
- [33] W. Yan and F. D. Fischer. Applicability of the hertz contact theory to rail-wheel contact problems. *Archive of applied mechanics*, 70(4):255–268, 2000.
- [34] X. Zhao and Z. Li. The solution of frictional wheel–rail rolling contact with a 3D transient finite element model: Validation and error analysis. *Wear*, 271(1):444–452, 2011.
- [35] X. Zhao, Z. Wen, M. Zhu, and X. Jin. A study on high-speed rolling contact between a wheel and a contaminated rail. *Vehicle System Dynamics*, 52(10):1270–1287, 2014.
- [36] Z. Zhong. *Finite element procedures for contact-impact problems*. Oxford university press, 1993.
- [37] Z. Zhong and J. Mackerle. Contact-impact problems: A review with bibliography. *Applied Mechanics Reviews*, 47(2):55–76, 1994.
- [38] O. C. Zienkiewicz and R. L. Taylor. *The finite element method for solid and structural mechanics*. Butterworth-heinemann, 2005.



# 4

## MODELLING VERIFICATION AND EFFECT OF OPERATIONAL PATTERNS ON CONTACT RESPONSES

*Verification of the explicit finite element (FE) model with realistic wheel-rail profiles against the CONTACT model, which has not been sufficiently discussed before, is performed by comparing the resulting shear stress, slip-adhesion area, etc., obtained from the two models. The follow-up studies using the verified FE model on the influence of the varying operational patterns (such as different friction, traction, etc.) on the surface and subsurface tribological responses of wheel-rail interaction are accomplished through a series of simulations. It can be concluded that the results obtained from most of the explicit FE simulations agree reasonably well with the ones from CONTACT. Also, the increase of the friction and traction can bring the stress concentrations from the subsurface upwards to the surface.*



Chapter 4 focuses on how to carry out the verification of a FE model of W/R interaction. Given the fact that the realistic W/R profiles are used in the FE model developed here, attention is focused specifically on the non-Hertzian and non-planar contact problems. For such problems, the verification of the FE models has not been performed adequately so far. The main objectives of this study are to verify that FE model against CONTACT software and to explore the effect of the most influencing factors on the tribological behaviour of wheel-rail interaction through parametric studies using this model. This chapter is aimed to answer the research question Q3 presented in Chapter 1.

The same explicit FE model of a wheel rolling over a rail presented in Chapter 2 will be used. Also, all the geometrical/interface parameters such as contact clearance (0.17 mm), penalty scale factor (12.8 mm), mesh size (dense meshed area: 2.0 mm; solution area: 1.0 mm), etc. suggested in Chapter 2 and Chapter 3, which ensure the satisfactory compromise between calculation accuracy and efficiency, will be used.

This chapter is organized as follows. First, a brief introduction of the research background of Chapter 4 is presented in Section 4.1. The comparison between the results obtained using the FE model and CONTACT is highlighted in Section 4.2. Following that, the results of the parametric studies on the influence of the friction coefficient, traction force, contact point, material properties, etc., on the dynamic responses of wheel-rail interaction are presented in Section 4.3; The future work on the experimental validations is discussed in Section 4.4; Finally, concluding remarks are drawn.

## 4.1 INTRODUCTION

With the growing power of modern computers, expectations of more accurate contact models for the analysis of wheel-rail interaction have also been increased. Those models without validation or verification may generate subtle inaccuracy in the obtained results that being unnoticed, which can lead to wrong decisions [41]. Accordingly, it brings the researchers a tough challenge to justify the obtained results. In order to critically assess the confidence in the solution of a contact problem, the verified and validated contact models/algorithms have always been in high demand. Usually, validation is defined as the assessment of the computational accuracy of the numerical simulations by comparing it with the experimental data [28], while verification is performed through the comparison of the numerical results with a known solution obtained from other validated/verified models. The major difference between verification and validation lies in the relationship between the computational and the real world results (experimental data).

During the last decades, the interest in verification and validation of numerical models in the railway community has been increased significantly [1, 2, 24, 26, 31, 34–36, 42]. Usually, the validation is more difficult to perform than the verification, as the experimental methods [2, 26, 31, 34] are inherently more time consuming and expensive. Moreover, there are no well-accepted experimental methods available that can directly measure the intangible local stresses and micro-slips within the contact patches [42]. A common way of verifying a contact model is to compare its results with those from more rigorous models, of which the correctness and accuracy have been proven [39]. For example, the Kalker's exact theory implemented in his well-known computer programme CONTACT is often used for this purpose. Zhao et al. [42] developed a three dimensional

(3D) wheel-rail finite element model for the solution of rolling contact in elasticity and plasticity. Both the resulting Hertzian normal and tangential solutions agree well with the results from CONTACT. As Zhao's model was intended for studying squats that are usually found in the middle of rail top [15], it was reasonable to represent the wheel by a cylinder. Deng et al. [1] made attempts to find the solution for spin-rolling contact with a coned wheel tread. The obtained FE results were successfully verified against Kalker's exact theory (CONTACT). In [36], Vo et al. used both CONTACT [38] and Polach's models [32, 33] to verify the accuracy of their FE model through the comparison of contact forces. Both realistic rail and wheel profiles were considered in Vo's FE model. The comparison of the contact properties such as normal pressure, shear stress, slip-adhesion area, etc. with the ones of CONTACT was excluded. Wiest et al. [40] compared the normal contact pressure obtained from their FE simulations on wheel-crossing interaction with the ones from CONTACT. A novel coupling procedure between multi-body system software and FE programme was introduced. Using that procedure, the conventional complete wheel-crossing dynamic FE model is able to be simplified into a static sub-model with two small pieces (around 30mm thick) of the contact bodies considered. The normal contact pressure in wheel-crossing contact is assessed and further verified against CONTACT.

From this literature review it can be noticed that despite the significant progress in the verification of FE-based contact models against CONTACT, verification of the models with realistic wheel and rail (W/R) profiles considered has not sufficiently been performed. Therefore, the examination on the validity of FE contact models with realistic contact geometries remains in high demand. Also, the follow-up parametric studies on the influence of the operational patterns (such as the variation of friction coefficient [16, 23, 29], traction force [13], contact point [12] etc.) on the tribological behaviour of wheel-rail interaction are limited by the lack of reliable and justified FE models.

## 4.2 MODELLING VERIFICATION

To properly verify the results from the proposed FE model analysis against the ones of CONTACT analysis, a physical understanding on the background of CONTACT is necessary. Thus, some critical theoretical backbones of CONTACT are summarised first. Then, the procedure to perform the verification that integrates the CONTACT model with the developed FE model is demonstrated. Finally, the simulation results obtained using the FE model are compared with the CONTACT results.

### 4.2.1 CONTACT MODEL

The CONTACT programme is developed by Professor J.J. Kalker [11] and powered by VORtech Computing [38]. It is intended for treating the concentrated contact problems between two deformable bodies, which are assumed to have contact at one point  $O_c$  in the un-deformed state as shown in Figure 4.1. As one main function of CONTACT programme, it is able to accurately estimate the actual contact area  $A_c$ , the resulting local stresses and slips within the contact patch in the deformed state (i.e. when the wheel is shifted downwards to the rail along the direction  $O_c Z_c$ ).

CONTACT is based on the complementary energy principles of Fichera and Duvaut-

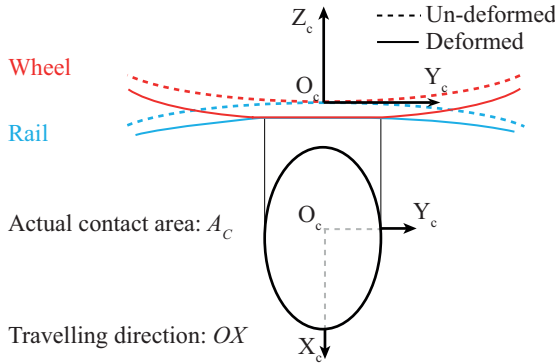


Figure 4.1: Schematic diagram of wheel-rail interaction in CONTACT.

lions [4], which are implemented in a special algorithm by Kalker [10]. In addition, the relations between the displacement  $\mathbf{u}(\mathbf{x}, t)$  and the surface traction  $\mathbf{p}(\mathbf{x}', t)$  are defined as [38]

$$\mathbf{u}(\mathbf{x}, t) = \int_{\mathbf{x}' \in A_c} \mathbf{A}(\mathbf{x}, \mathbf{x}') \mathbf{p}(\mathbf{x}', t) dS \quad (4.1)$$

where  $\mathbf{A}(\mathbf{x}, \mathbf{x}')$  is the influence function. The influence function is used to assess the effect of the surface traction  $\mathbf{p}(\mathbf{x}', t)$  applied on one particle positioned at  $\mathbf{x}'$  on the displacement  $\mathbf{u}(\mathbf{x}, t)$  of another particle placed at  $\mathbf{x}$ . In CONTACT, the following assumptions are made [38]:

- (1) The bodies are formed of linearly elastic materials and are homogeneous.
- (2) The contact area is essentially flat and small with respect to the typical dimensions of the bodies' geometries.
- (3) No sharp variations exist in the geometries of the bodies.
- (4) Inertial effects are small with respect to the contact stresses and may be ignored.

These assumptions allow for the usage of the influence function method [11, 38] (also known as half space approach). Due to the violations of the half-space assumptions, the conformal contact used to be a difficult problem to work out in CONTACT. With some FE-based adjustments on the influence function [14], the recent versions of CONTACT [37] have the option of solving the problems of conformal contact. The accuracy of CONTACT solutions has been verified/validated in [11, 39].

#### 4.2.2 INTEGRATION CONTACT WITH FE MODEL

Using CONTACT, a variety of contact problems, including the frictionless, frictional, stationary and non-stationary contact, can be addressed [38]. In order to perform the FE modelling verification against CONTACT, the CONTACT simulation has been integrated with the explicit FE analysis as shown in Figure 4.2. Such an integration is necessary to ensure that both models describe the same wheel-rail interaction process. It is worth

noting that the primary focus of this study is extending the FE model verification from the Hertzian contact problems, which have been successfully studied in [1, 42], into the common non-Hertzian contact problem due to the consideration of the realistic wheel-rail contact profiles.

Also, it should be mentioned that the proposed integration procedure is inspired a lot by the instructive analysing procedure of CONTACT [38] (i.e. the non-Hertzian contact analysis method) and the pioneering research progress made in [1, 36, 40, 42].

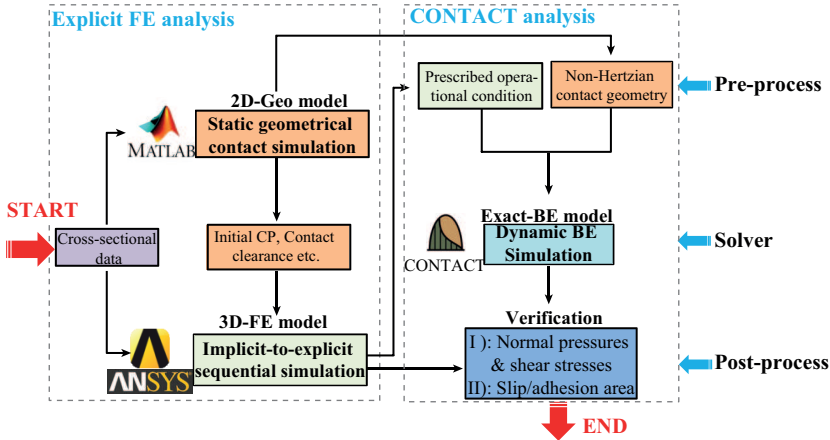


Figure 4.2: Integration procedure of CONTACT with FE model.

From Figure 4.2, it can be seen that there are three models involved in the verification process, namely, 2D-Geo model, 3D-FE model and Exact-BE model (CONTACT). Here, the abbreviation of “BE” refers to the “boundary element” method. The integration procedure consists of two parts, explicit FE analysis and CONTACT analysis. In the part of explicit FE analysis, the 2D-Geo contact analysis is performed first to determine the geometrical contact information such as the initial “Just-in-contact” location (CP), the contact clearance and the corresponding local wheel rolling radius at the point of contact. The obtained contact information is used as the adaptive guidance for the mesh refining and dynamic loading application in the 3D-FE analysis. More information of the explicit FE analysis coupled with 2D-Geo contact analysis can be found in [18–20].

In the other part of the integration procedure, there are three major steps involved in the CONTACT analysis [38]:

- (1) Pre-process: setting up the contact geometries and applying the prescribed loads;
- (2) Solver: defining the analysis type/options and running the solving processor;
- (3) Post-process: reviewing the CONTACT results with the plot routines integrated;

As the solver of CONTACT is well-established, only limited items such as defining the analysis type/options are allowed to tune. For the Pre-process and Post-process, more preparations are needed for accurately performing the CONTACT analysis.

For instance, in the pre-process, the same input of the non-Hertzian contact geometries that are defined in the coupled 2D geometrical contact analysis (a part of the FE model) is used in both models (FEM and CONTACT) (See Section 4.2.1). The operational conditions such as the contact loadings, train velocities, etc., in CONTACT are prescribed by the ones of the FE outputs (See Section 4.2.2). The same linear elastic constitutive law is used to describe the material behaviour of the two contact bodies of wheel and rail. By this means, the consistency between the explicit FE analysis and CONTACT analysis can be guaranteed. Also, the correctness of the verification procedure can be assured.

In the post-process, the outputs of normal contact pressure, shear stress and slip/adhesion area, etc., exported from FE simulations are compared with the ones obtained from CONTACT analysis. In the following two sub-sections, the approaches of the Pre-process would be detailed. For the Post-process, it will be discussed in Section 4.2.3.

## 4

## NON-HERTZIAN CONTACT GEOMETRY

According to the integration procedure displayed in Figure 4.2, the non-Hertzian contact geometry has to be characterized first. The general operational steps [38] for such a characterization is demonstrated in Figure 4.3.

- (1) The calculation starts by defining the coordinate systems that are used. Figure 4.3a shows the un-deformed state of the contact geometry in the track-based coordinate system  $O^t - X^t Y^t Z^t$ , which has its origin at the track centre-line in the plane resting on top of the rails. Figure 4.3b presents a close-up view of W/R profiles at the contact-based coordinate system in which  $Z$ -direction  $O'_c Z'_c$  is normal to the contact plane. The origin  $O'_c$  is positioned in the initial contact point and the  $Y'_c$  axis is parallel to the  $Y_t$ -axis of the track-based coordinate system.
- (2) It is seen from Figure 4.3a that the calculation of the initial contact points on left and right wheels are accomplished based on the 2D-Geo contact model.
- (3) Rotating the W/R profiles according to the resulting contact angle  $\delta$  at the detected initial contact point  $O_c$  (See Figure 4.3b), the new W/R profiles will be obtained in a tuned contact based coordinate system  $O_c - X_c Y_c Z_c$ .
- (4) Interpolating the new rotated W/R profiles with respect to a common set of lateral coordinates  $\mathbf{Y}$ , and then assessing the un-deformed distance between wheel and rail profiles. Here, the un-deformed distance is referred to as the contact clearance  $\delta z$ . The obtained contact clearance shown in Figure 4.3c is one required contact property for CONTACT. Using the obtained contact clearance, a potential contact area that encompass the real contact area could thus be identified and further used as an input for the CONTACT solving procedure.

It has to be mentioned that the integration of 2D-Geo model with CONTACT is seamlessly programmed. The W/R contact geometries (solid lines as shown in Figure 4.3a and dash lines as shown in Figure 4.3b) have been substituted for the contact clearance curve to prescribe the potential contact area.

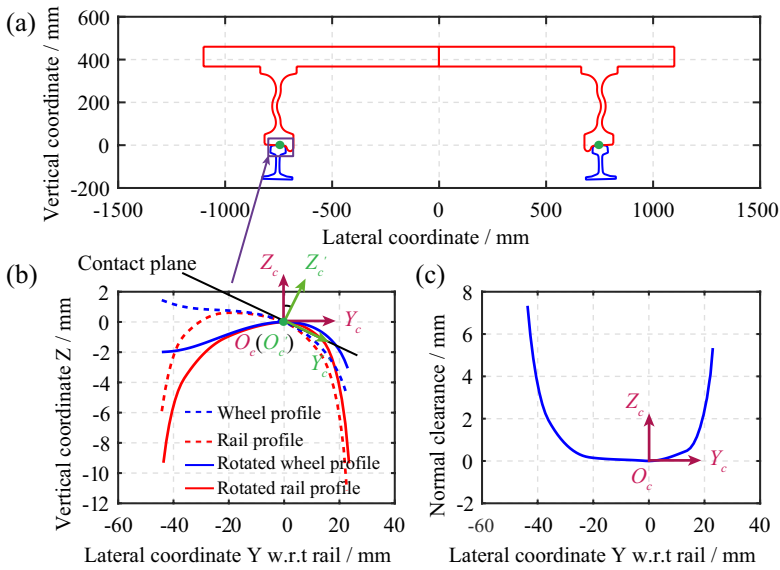


Figure 4.3: (a) Wheel-rail contact geometry at track-based coordinates  $O^t - X^t Y^t Z^t$ ; (b) Close-up view of the wheel-rail profiles at two contact based local coordinate systems  $O_c - X_c Y_c Z_c$  and  $O'_c - X'_c Y'_c Z'_c$ ; (c) The resulting normal clearance at lateral displacement  $\delta y = 0$  mm (Notation: green solid circle refers to the initial contact point).

**PRESCRIBED OPERATIONAL CONDITIONS**

To maintain the consistency between the FE simulations and CONTACT, the same elastic material properties, friction coefficients and the track geometries are used for both cases. They are shown in Table 2.1.

With respect to kinematic parameters, the prescribed total forces have to be specified according to the results obtained from the dynamic FE analysis ( See Figure 4.4 ). The resulting force components in the  $MidA_c$  area, which are extracted at the moment when the wheel passes through the middle of the solution area, are used as the prescribed loading conditions in CONTACT.

**4.2.3 VERIFICATION RESULTS**

Following the Post-process of the CONTACT analysis as demonstrated in Section 4.2.2, the FE results (such as the normal pressure, shear stress, the slip-stick area within the contact patch etc.) are compared with the ones obtained from the CONTACT simulations in this verification.

**NORMAL PRESSURE**

As indicated by the method presented in [42], the contact patches from both the FE and CONTACT analyses are determined according to the normal contact pressure as follows:

$$\text{A node is in contact , if } |\sigma_n| > 0 \tag{4.2}$$

where  $\sigma_n$  is the nodal pressure in the direction normal to the local contact surface.

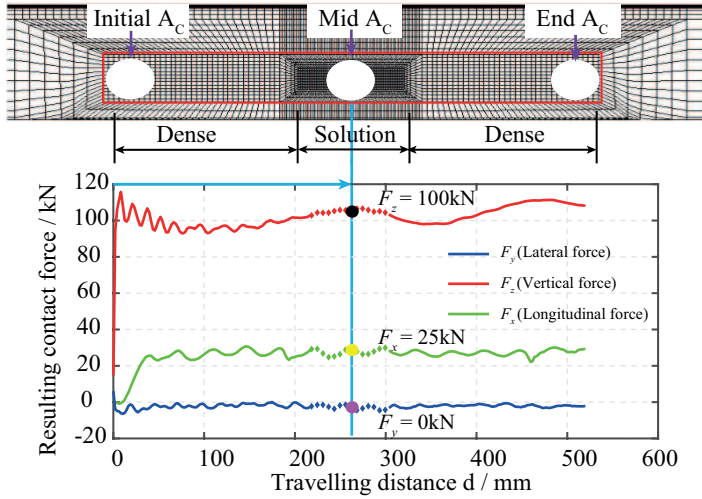


Figure 4.4: Variation of contact forces w.r.t. rolling distance.

Figure 4.5a-b shows the normal pressure distribution calculated from the FE programme. In order to better demonstrate the resulting surface pressure distribution, the compressive normal pressure here is treated as positive. The results obtained from CONTACT are shown in Figure 4.5c-d. All the resulting contact patches are non-elliptical. The reason of the non-elliptical contact patch can be attributed to the changing radius of the curvature of the realistic wheel/rail local contact geometries as well as to the rail inclination angle (1/40) considered in the model.

Also, it is observed that these contact areas are shorter in the rolling direction than the length in the lateral direction. In addition, the contact patches are approximately symmetrical with respect to the vertical-lateral plane. The peak of the contact pressure is located at the vicinity of the initial contact point. The distribution of the contact pressure has a similar pattern, i.e. the higher contact pressure is positioned at a region that is much closer to the side of gauge corner (G.C.) than to the field side (FS).

Table 4.1 lists the quantitative results in terms of the maximum normal pressure and the contact patches. The maximum length of the contact patch in lateral direction is 22.91 mm in the FE solution, whereas in CONTACT it is 20.48 mm. That has resulted in the relative difference between the area of the contact patch in both solutions of 28.23% as it can be seen from Table 4.1 (256.5 mm<sup>2</sup> in the FE solution and 200.02 mm<sup>2</sup> in the CONTACT solution). Besides, the maximum normal contact pressure, which amounts to 1226 MPa, is obtained in CONTACT that is 13.95% higher than the FE solution.

It can be seen that although the percentage deviations of contact pressure exist, the FE results agree reasonably well with the ones from CONTACT simulations. The sources of these discrepancies can be categorised into three groups, namely, the different analysis types, the FE penalty approximation and the tangent contact planes.

- (1) Analysis types: CONTACT uses a quasi-static approach [38], while the FE analysis type is transient. It can be observed from the FE simulation results (See Figure 4.4)

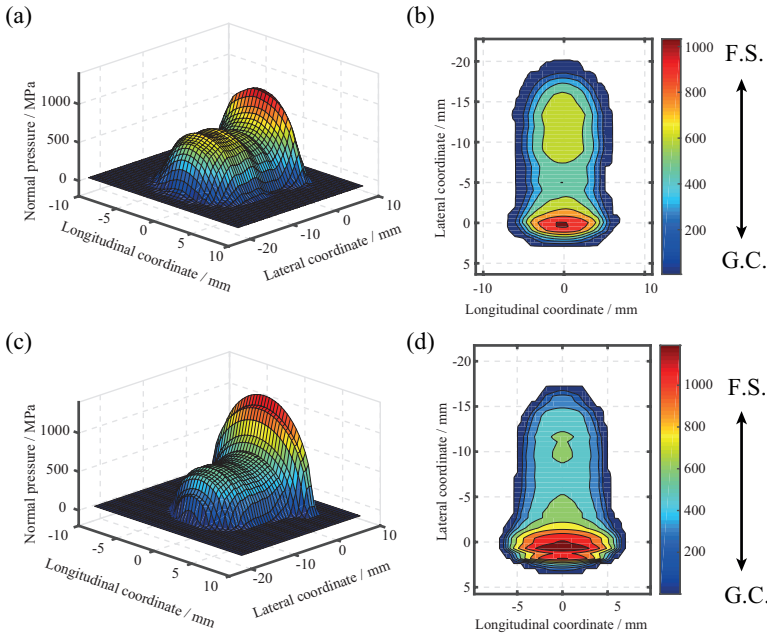


Figure 4.5: Normal pressure distribution: (a) FE surface plot; (b) FE contour plot; (c) CONTACT surface plot; (d) CONTACT contour plot. (Note: G.C. means the gauge corner, F.S. means the field side).

that both the vertical and longitudinal forces are varying with respect to travelling distances. Since these varying resultant contact forces are composed of the nodal resistive contact pressures/stresses, the transient behaviour of the explicit FE analysis would manifest itself in the discrepancies of the normal contact pressure and the actual contact patch shown in [Table 4.1](#).

- (2) Penalty approximation: It is known that penalty method (See [Section 4.2](#)) is used to satisfy the contact conditions approximately [8, 9] in the explicit FE analysis. Moreover, the penalty method can also affect the stability of the explicit time integration procedure, since the central difference method is conditionally stable [43]. In the penalty method, the choice of the interface parameters (contact stiffness, damping, etc.) should be made depending on the particular problems considered in order to obtain the accurate results. Therefore, the study on the influence of the wheel-rail interface parameters on the contact stability and accuracy of the results had been done by the authors recently [22]. In this chapter, the optimal set of the interface parameters as proposed in [22] has been used. But still, this approximate contact constraint enforcement may influence the FE results and ultimately cause the discrepancies between FE and CONTACT solutions.
- (3) Tangent contact planes: It can be seen from [Section 4.2.2](#) that the potential contact area in CONTACT is prescribed on the basis of the contact clearance, which is determined by the local tangent contact planes (involving the parameters such as



Table 4.1: Comparison of the normal solutions of the two approaches.

Approach	$\sigma_{max}^a/MPa$	$d_{lat}^b/mm$	Contact patch	
			$d_{lon}^c/mm$	Area /mm <sup>2</sup>
CONTACT	1226	20.48	13.33	200.02
FE	1055	22.91	14.08	256.5
Difference w.r.t. CONTACT	-13.95%	11.87%	5.63%	28.23%

<sup>a</sup> : Maximum normal pressure;    <sup>b</sup> : Maximum length in lateral direction;  
<sup>c</sup> : Maximum length in longitudinal direction.

the initial contact point, contact angle, etc.) obtained from the home-made 2D-Geo contact simulation. These tangent contact planes are calculated under the static, un-deformed state, which would be different from the ones at the dynamic, deformed state in reality. Also, the choice of the input resulting contact clearance curve would influence the actual contact patch and the pressure distribution obtained using the CONTACT programme.

The detection of the potential contact area in the FE analysis is much different. Two large enough potential master and salve contact segments are prescribed respectively (See Figure 3.1). As it has been discussed in Section 2.2, the contact forces are predicted iteratively using central difference method. No local tangent contact planes are needed to be predefined in the FE simulation.

**SURFACE SHEAR STRESS**

Figure 4.6a-b shows the surface shear stress distribution calculated from FE programme, while Figure 4.6c-d presents the one obtained from CONTACT programme.

It can be seen that the shear stress distribution of the FE solution is comparable with the one of CONTACT solution. The major portion of the shear stress is located at the rear part of the contact patch. The maximum surface shear stress of FE solution and CONTACT solution amount to 459.8 MPa and 486.6 MPa respectively.

In order to create a cross-sectional view of the 3D surface shear stress, two orthogonal sliced planes, namely “AA” and “BB”, are introduced as shown in Figure 4.6b & Figure 4.5d. “AA” is sliced at the initial contact point along a longitudinal-vertical plane, while “BB” is cut at the same point but along a lateral-vertical plane.

Figure 4.7 displays 2D surface shear stress sliced at the “AA” plane. It is observed that the shear stress is limited by a traction bound (denoted by solid red and blue curves), which is the product of the normal pressure and the friction coefficient . Thus, the difference between the normal pressure as shown in Figure 4.5 also manifests itself in the discrepancies between traction bounds as well as the shear stresses obtained from FE and CONTACT analysis.

It is also observed that the shear stress curves from CONTACT are much smoother and more disciplined than the ones obtained from FE simulations. Such a phenomenon could be explained by the difference of the contact solving procedures between CONTACT and FEM. In CONTACT [11], the normal and tangential friction problems are solved

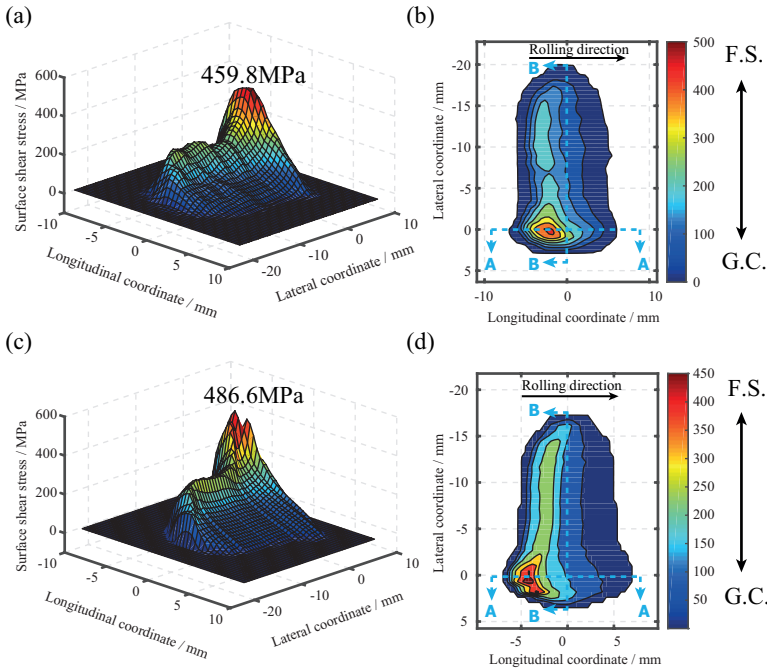


Figure 4.6: Surface shear stress distribution: (a) FE surface plot; (b) FE contour plot; (c) CONTACT surface plot; (d) CONTACT contour plot. (Notation: blue dash lines refer to the cutting planes, namely “A” and “BB”).

sequentially. The tangential traction are to be calculated until the normal pressure is known.

For the case of explicit FE analysis, Coulomb formulation [6, 7] is used to predict the tangential frictional force. The normal and tangential problems are calculated simultaneously for all the cases of contact problems. Using the central difference method [6, 41, 43], all the nodal forces including both the tangential and normal ones are calculated iteratively from the present time step to the next one.

#### SLIP-ADHESION

Based on the calculated normal pressure and surface shear stress, the slip-adhesion phenomenon can be further explored using the following equation adapted from [42]:

$$\text{The node is in adhesion, if } \mu |f_{n\_N}| - |f_{n\_T}| > \varepsilon_T \quad (4.3)$$

where  $f_{n\_N}$  is the nodal normal force,  $f_{n\_T}$  is the nodal tangential force in the longitudinal direction, and  $\varepsilon_T$  is the tolerance for distinguishing the slip and stick areas. The magnitude of  $\varepsilon_T$  is prescribed to be the 10% of the maximum traction bound force ( $\mu |f_{n\_N}|$ ).

It has to be mentioned that the tolerance used here is not as rigorous as the one in [42], since the present tolerance is applied on the contact patches resulting from the realistic wheel/rail geometries.

Figure 4.8a-b shows the slip-stick area distributions in the contact patches based on the criteria stated in Equation 4.3. As it can be observed, the leading edge of all the con-

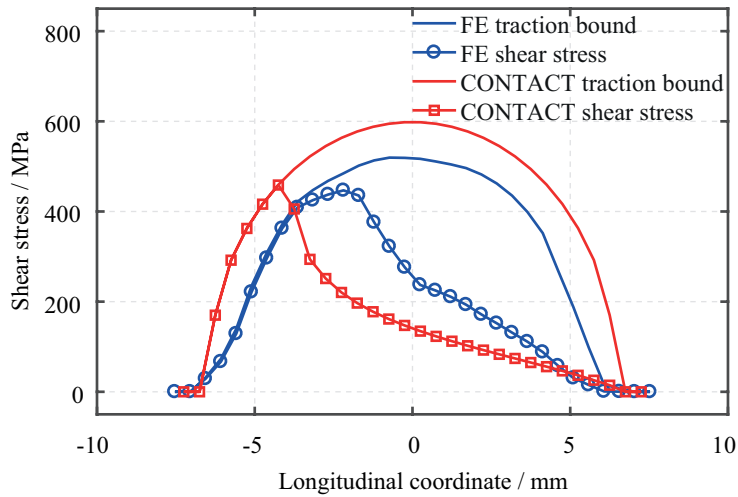


Figure 4.7: 2D surface shear stress slice plot.

tact patches is in stick, whereas the trailing edge is in slip. Such an observation conforms well with the classical rolling contact theory [11]. In addition, it can be seen from the FE result (Figure 4.8a) that some of the “stick” grids seems to be misplaced inside the “slip” zone, while the CONTACT result (Figure 4.8b) tends to be much disciplined and ordered.

From Equation 4.3, it is observed that the slip-stick area is strongly dependent on the relationship between normal pressure and shear stress. The tolerable differences of normal pressure and shear stress have been explained in the previous two sub-sections. Also, the tolerance  $\varepsilon_T$  for identifying slip-stick area is much larger than the one in CONTACT (zero tolerance). Thus, it is reasonable to see the difference in the slip-stick areas obtained from CONTACT and FE analysis.

From the results and discussions, it can be noticed that the developed FE model is able to simulate the wheel-rail interaction effectively. The obtained FE results are comparable with the ones of CONTACT. The discrepancy between the results of CONTACT and FEM simulations is reasonable enough for the developed FE model to be used in the future research. However, as one major disadvantage of the FE analysis, it has to be mentioned that the computational expenses of the FE simulation (around 9 hours) are much higher than the ones of CONTACT simulation (2~3 minutes).

### 4.3 PARAMETRIC STUDY

The knowledge on the influence of operation patterns on the tribological behaviour of W/R interaction is always in high demand for formulating the appropriate operational strategies (increasing/decreasing friction/traction, etc.) to improve the performance of railway system. To enhance such knowledge, the following parameters are varied to conduct the parametric study starting from the reference case (See Table 2.1):

- (1) the friction coefficient (changing from 0.0 to 0.8);

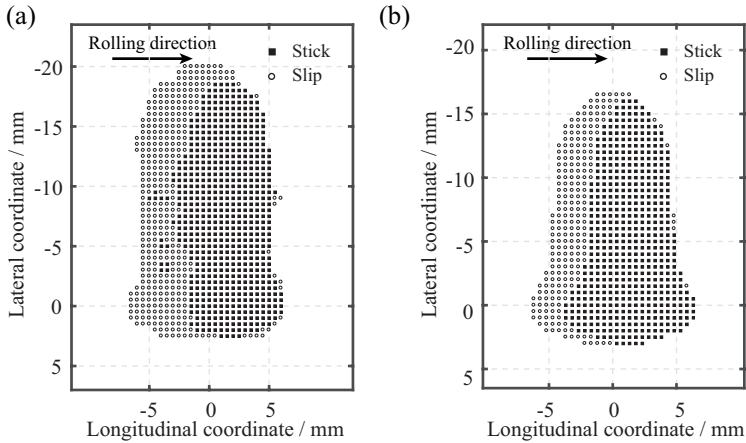


Figure 4.8: Slip-stick area plot: (a) FE result; (b) CONTACT result.

- (2) the traction forces (varying from braking to accelerating);
- (3) the lateral position of the wheel (shifting from -5.5 mm to 5.5 mm);
- (4) the material properties, by varying the yield strength limit from 280 MPa to 680 MPa.

It is worth noting that all the results of the parametric study are presented for the purpose of model verification, and are obtained by considering a linear elastic constitutive law for both the wheel and the rail, except for that presented in [Section 4.3.4](#). The corresponding results and discussions are presented below.

#### 4.3.1 FRICTION COEFFICIENT

To study the resulting stress states and contact properties under different frictional levels, nine sets of FE simulations have been performed with the friction coefficient ranging from 0.0 to 0.8. In [Figure 4.9](#), the dynamic response of the resulting longitudinal friction forces with different friction coefficients are presented. From this figure, it can be seen that the change of friction coefficient can bring about a dramatic influence on the variation of the longitudinal force.

At zero friction coefficient, no longitudinal forces are observed. When the friction coefficient is increased, the resulting contact patches start to transfer the traction for the wheel to accelerate. For the cases of friction coefficient varying from 0.1 to 0.3, the stair-type growth trend of longitudinal force is observed. With the friction coefficient increasing steadily over 0.3, the longitudinal friction forces reach to its saturated value 25kN and remain the same. This phenomenon is due to the fact that the applied traction is determined (traction coefficient  $T=0.25$ ) for all the cases of varying friction coefficient. As a result, the higher the friction coefficient is, the larger the longitudinal friction force within a upper bound of 25kN occurs. It can also be seen that all the resulted longitudinal friction forces are varying with respect to the travelling distance. These variations are

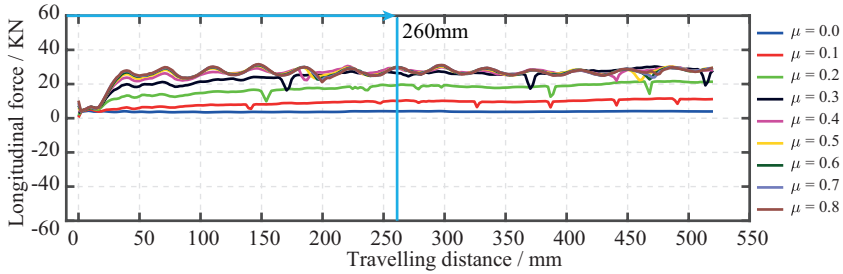


Figure 4.9: Resulting longitudinal friction forces from the variation of friction coefficient. (Note: the intersecting point between the blue dashed line and the curves of the longitudinal forces indicates the position in which the contact properties are extracted.)

4

getting more noticeable at high friction levels than the ones at low friction levels, even the studied W/R interfaces are flat and have no defect. It is observed that the oscillation of the longitudinal friction force is highly related to the magnitude of  $\kappa$ , which is the ratio of the traction coefficient  $T$  to the friction coefficient  $\mu$ . The smaller the magnitude of  $\kappa$  is, the more noticeable the oscillations of the frictional forces are. Also,  $\kappa$  is an index to assess the contact status:

$$\text{The contact is in partial slip, if } \kappa < 1 \tag{4.4}$$

Thus, the noticeable oscillations at high friction levels means that the corresponding contact statuses are partial slip. In other words, the friction forces in partial slip tend to introduce more oscillations than the ones in full slip.

Figure 4.10 shows the influence of the oscillatory longitudinal forces on the shear stress distributions at the friction coefficient  $\mu$  of 0.8. Four time moments ranging from A to D are selected from the curve of the oscillatory longitudinal force. The corresponding shear stress distributions at selected moments are shown in Figure 4.10. It can be seen that the local minimum longitudinal force located at “A” is approximately 24kN, whereas at “D” the local maximum longitudinal force amounts to 30kN. This has resulted in the relative difference of approximately 25% between the maximum shear stresses in both “A” and “D”.

As the CONTACT calculations are made for the same time moment as FEM, the magnitudes of the resulting longitudinal forces obtained from FE simulations are used as an input in the CONTACT analysis. This makes the operational/loading conditions to be consistent for both CONTACT and FEM simulations. Therefore, the influence of the oscillatory variation of the longitudinal force on the lateral verification process would be insignificant.

The distributions of the surface shear stress are shown in Figure 4.11. These contact properties are extracted at a distance of 260 mm from the starting point (See Figure 4.9). It can be further seen that both the FE solution (Figure 4.11a) and the CONTACT solution (Figure 4.11b) demonstrate the gradual change of the surface shear stress as the friction coefficient is changing. Figure 4.12 shows the slice plot of the surface shear stress sliced at the initial contact point along the longitudinal direction. It is observed that the shear stress responses of both FE and CONTACT results exhibit the similar pattern.

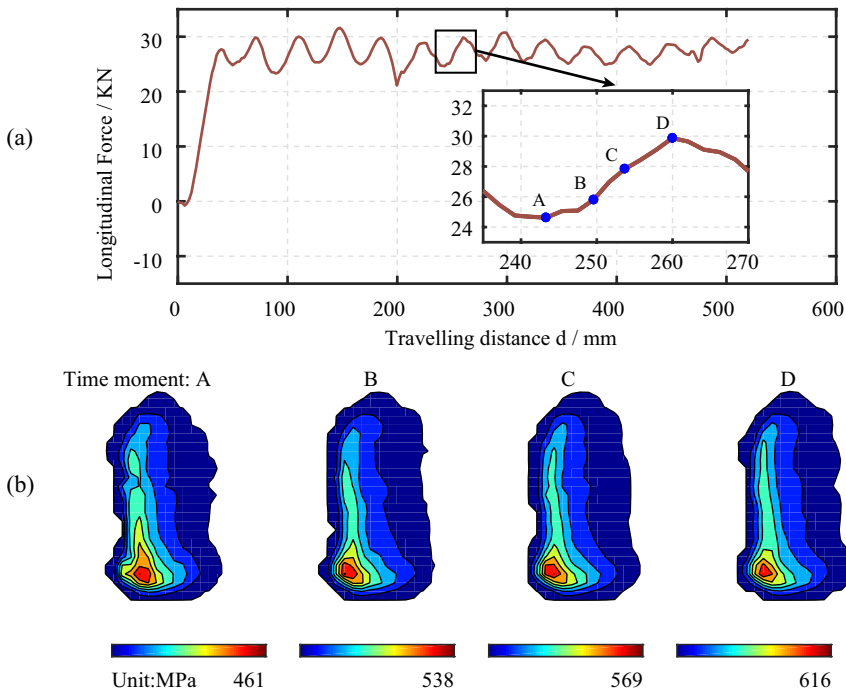


Figure 4.10: Effect of the oscillatory longitudinal force on the shear stress distribution: (a) Longitudinal friction force at high friction level of  $\mu = 0.8$ ; (b) The corresponding shear stress variation at specified time moment.

Figure 4.13 presents the slip-adhesion area variation for the different friction coefficients. It can be noticed that when the friction coefficient is lower than 0.3, saturation is reached in which full slip condition covers almost the whole contact patch.

With the increase of friction coefficient from 0.3 to 0.8, the slip area is getting smaller and smaller in comparison with the stick area. The slip-adhesion areas obtained from FE solutions agree well with the ones from the CONTACT solutions.

Using the “AA” cutting plane as demonstrated in Figure 4.6, the variation of the sub-surface stress response is presented. It is clearly seen from Figure 4.14a that the maximum Von-Mises stress is shifting from sub-surface to surface with the increase of the friction coefficients, while for the shear stress distribution shown in Figure 4.14b, the tensile stress moves upward as well.

The results correlate well with the surface shear stress distribution shown in Figure 4.11, in which the higher friction coefficient will lead to smaller slip area and higher surface pressure causing that the higher shear and Von-Mises Stress (VMS) shift upward to the surface. It has been confirmed by the research from [3] that when the friction coefficient is larger than 0.45, surface damage such as head check is getting dominant.

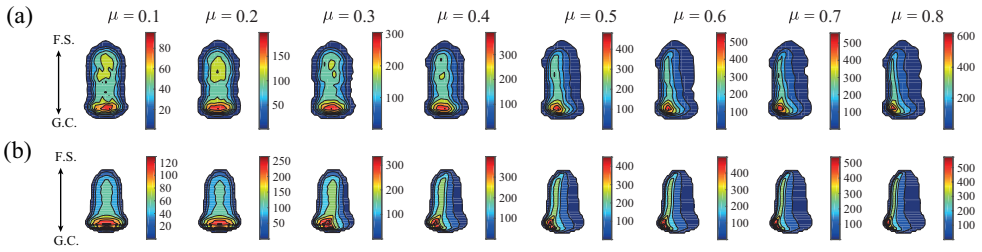


Figure 4.11: Shear stress distribution (Unit: MPa): (a) FE solution; (b) CONTACT solution.

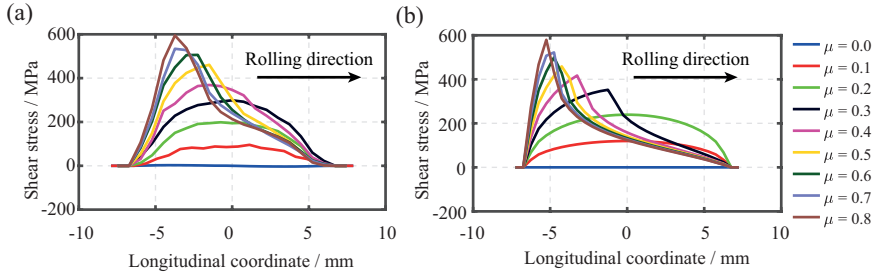


Figure 4.12: 2D Shear stress sliced plot: (a) FE solution. (b) CONTACT solution.

### 4.3.2 TRACTION FORCE

When the vehicle travels along the track, three typical operational conditions can occur, namely accelerating, free rolling and braking, which are schematically shown in Figure 4.15. For the case of free rolling, no traction forces will be applied and the translational velocity is proportional to the angular velocity, while for the braking and accelerating operations the direction of the driving torques are in opposite.

In order to study the influence of the train operations on the contact properties, a series of FE simulations has been performed. The corresponding results and interpretations would be reported in this section.

Figure 4.16 depicts the variation of the resulting longitudinal contact forces with different traction forces ranging from -50kN to 50kN. As it can be seen that, with the change of the operational conditions from accelerating to braking, the resulting longitudinal force starts to alternate its direction from positive to negative. The stair-type growth trend of traction forces is getting even more pronounced than the cases shown in Figure 4.9, when the traction coefficient  $T$  is increasing from -0.5 (braking) to 0.5 (accelerating).

It can also be seen that the force oscillations are being greatest at the medium traction force transmission levels. As the ratio  $\kappa$  of traction coefficient ( $T = -0.5 \sim 0.5$ ) to friction coefficient ( $\mu = 0.5$ ) is smaller than 1 at medium traction force transmission levels ( $|T| = 0.25$ ), the corresponding contact status is partial slip. As a result, there are more force oscillations observed.

Figure 4.17a-b shows the distribution of the resulting surface shear stress. For the CONTACT solutions, when they are compared between the braking and accelerating op-

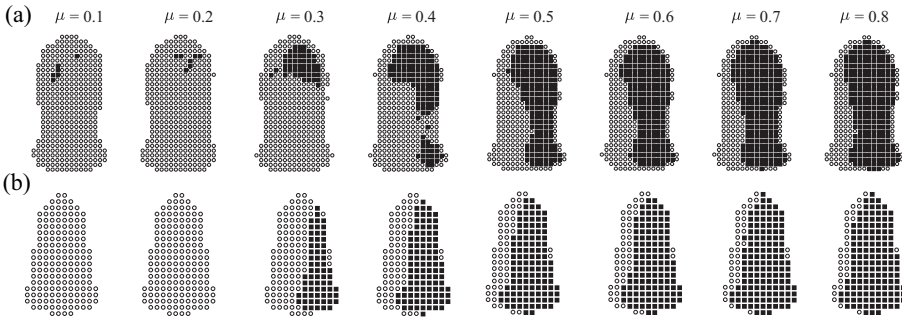


Figure 4.13: Slip-adhesion plot. (a) FE solution; (b) CONTACT solution. (Note: ○ refers to slip, ■ denotes stick).

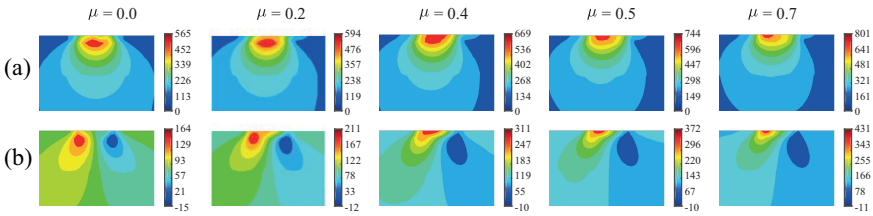


Figure 4.14: Sub-surface stress distribution (Unit: MPa): (a) Von Mises stress; (b) Shear stress.

erations with the same traction amplitude, the shear stresses exhibit the same amplitudes but opposite signs. Also, it can be seen that the “focusing point” of the shear stress is always located at the side close to the gauge corner (G.C.). Here, the “focusing point” defined as the most stressed point.

Regarding the case of the FE solutions as shown in Figure 4.17a, the “focusing point” of the shear stress is much concentrated on the field side (F.S.) when the wheels are at braking ( $T = -0.125 \sim -0.25$ ), while the accelerating operation ( $T = 0.125 \sim 0.25$ ) pushes the “focusing point” of the shear stress towards the side of the gauge corner (G.C.). Generally, the magnitude of the shear stress from FE solution is lower than the one from CONTACT solution.

Such a movement of “focusing point” observed from FE results could be caused by the special “conical” wheel contact geometry. As a result, the resulting tangent contact plane has a inclined angle with the horizontal plane. This inclined tangent contact plane would lead to the local wheel rolling radius difference between the two areas of field side and gauge corner. When the wheel rolls over the rail under accelerating operations, the large local wheel rolling radius would bring much local slip to the side of the gauge corner. Yet, the small local wheel rolling radius would generate much local slip to the side of the field side under braking operations.

As it has been discussed in Section 4.2.2 and Section 4.2.3, the tangent contact planes are determined by the 2D-Geo contact analysis. Also, the choice of these tangent contact planes may influence the imported contact clearance curve (non-Hertzian contact geometry) and ultimately the CONTACT solution. To minimise such an influence, more



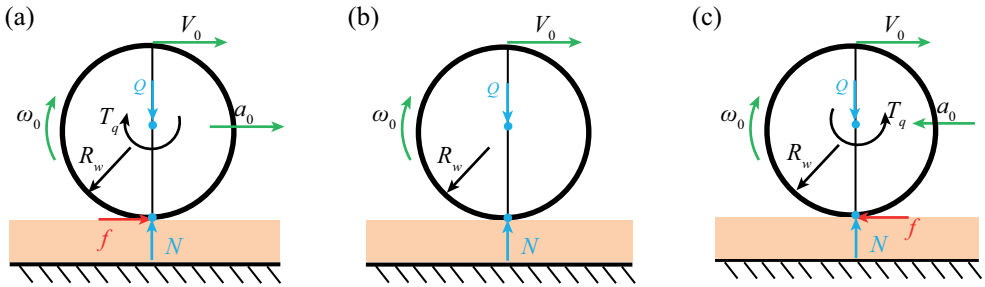


Figure 4.15: Schematic graph of train operations: (a) accelerating; (b) free rolling; (c) braking.

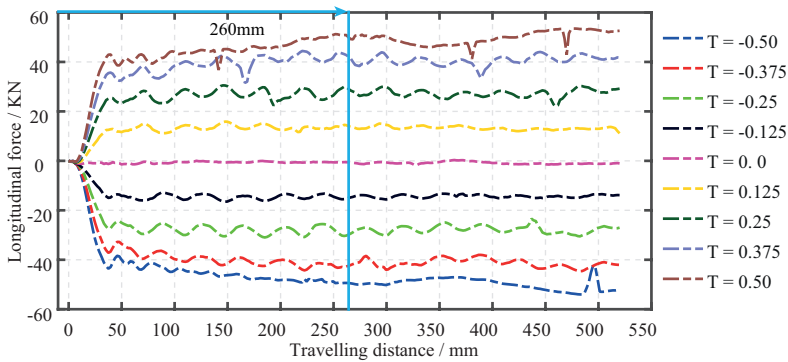


Figure 4.16: Resulting longitudinal contact forces from the variation of traction forces. (Note: the intersecting point between the blue dashed line and the curves of the longitudinal forces indicates the position in which the contact properties are extracted.)

research efforts are required to improve the functionality of the present 2D-Geo contact model. By this means, the change of the local wheel rolling radius resulting the movement of the “focusing point” is able to be considered in the improved 2D-Geo contact model. This explains the difference of the CONTACT and FE simulations results under accelerating and braking operations.

Figure 4.18 shows the 2D slice plots of the surface shear stress distribution at “AA” cutting plane. The shear stress is almost equal to zero under free rolling, while for the accelerating and braking operations, the shear stresses exhibit completely opposite behaviour, which further confirmed the afore observations. Also, a large spike is observed at the traction coefficient of 0.125. This spike also manifest itself in the discontinuities of the corresponding contour plot as shown in Figure 4.17a ( $T = 0.125$ ). Since the traction force is very small, the shear stresses are distributed at a rather narrow strip. The insufficient mesh grids within the strip may cause the spike oscillation. In the simulation with refined mesh, the spike has been considerably reduced.

According to the shear stress distribution presented above, the distribution of the slip-adhesion areas are presented in Figure 4.19a-b. It is apparent from Figure 4.19a that much slips obtained from FE solutions are shifted to field side for braking operation and to gauge corner for accelerating, respectively. The “focusing point” movement of the

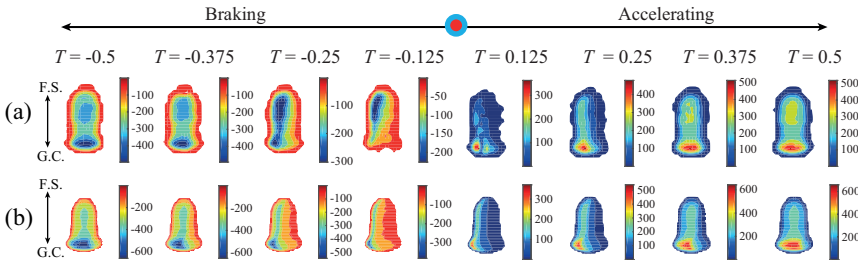


Figure 4.17: Surface shear stress distribution (Unit: MPa): (a) FE solution; (b) CONTACT solution.

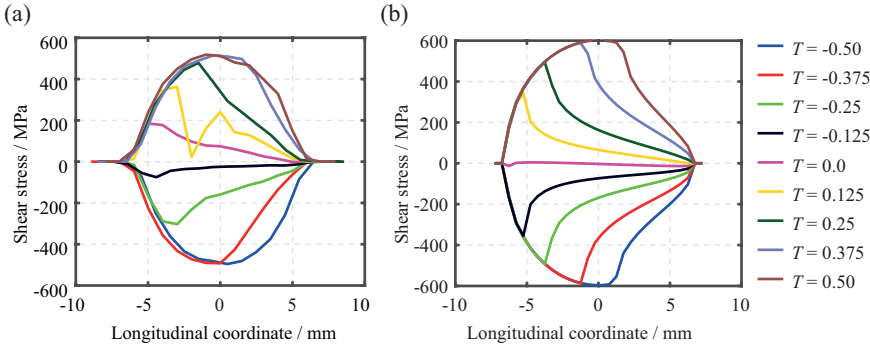


Figure 4.18: 2D surface shear stress sliced plot: (a) FE solution; (b) CONTACT solution.

shear stress as shown in Figure 4.17 also manifests itself in the slip-stick are distribution. The pattern of the slip-adhesion distribution obtained from the FE solutions agrees relatively well with the ones from CONTACT solutions.

Figure 4.20 shows the sliced plots of the sub-surface stress responses obtained from FE simulations under three typical operational conditions at the “A-A” cutting plane. In the free rolling processes, the shear stresses are distributed almost symmetrically to a distinguishable axis. In the accelerating process, the VMS stress distribution on the surface was extended to the right – ( in front of the wheel ) the positive shear stress was dominant on the top rail surface. For the braking operation, the VMS stress distribution on the surface was stretched to the left (behind the wheel ) and the negative shear stress was dominant on the top rail surface.

It is obvious that the solutions of the contact properties obtained from these two approaches are relatively well in accordance with each other, in spite of the occurrence of the deviations, such as the change of “focusing point”, the variation of the shear stress amplitudes, etc. From the parametric studies on traction forces, it can be concluded that the developed FE tool can produce as good results as CONTACT.

### 4.3.3 CONTACT POINT

The contact point distribution under different wheelset lateral shifts was determined using the 2D-Geo model. As it can be seen from Figure 2.9 the refined mesh region is

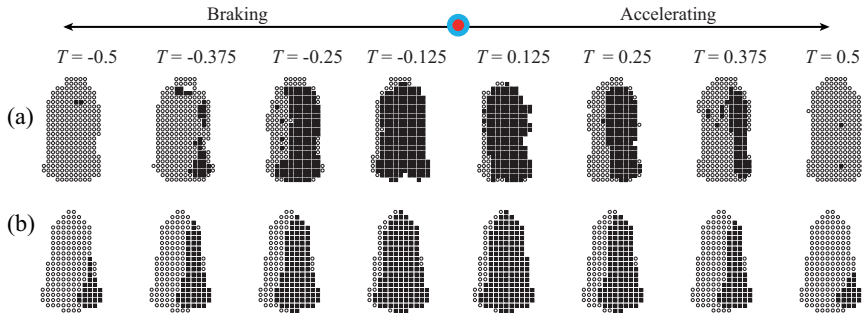


Figure 4.19: Slip-adhesion plot: (a) FE solution; (b) CONTACT solution. (Note:  $\circ$  refers to slip,  $\blacksquare$  refers to stick)

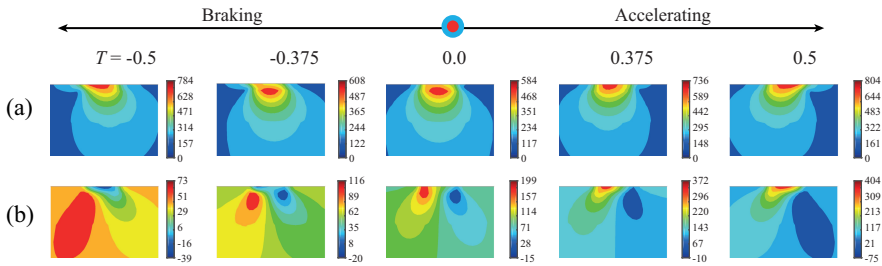


Figure 4.20: Sub-surface stress distribution in AA-plane (Unit: MPa): (a) Von Mises stress; (b) Shear stress.

automatically adjusted according to the location of the contact point. Based on the developed FE models, the influence of the contact point variation due to the various lateral shifts of the wheel set (-5.5, -3.5, -2, -1, 0, 1, 2, 3.5, 5.5 mm) on the wheel-rail contact behaviour is analysed in this section.

Figure 4.21 shows the two solutions of the contact area evolvement as the wheel is displaced over the rail with different lateral shifts. It can be seen that the non-elliptical contact patches prevail again. The reason of that is attributed to the fact that the radii of the curvature of both wheel and rail change significantly within the area of contact. Moreover, it is observed from FE solution (Figure 4.21a) that the magnitudes of the maximum normal pressure are on a steady decline from the lateral displacement of -5.5 mm (2311 MPa) to 0.0 mm (1518 MPa), while they switch into another trend of slight increase for the rest cases varying from 1.0 mm (856 MPa) to 5.5 mm (1191 MPa). From Figure 4.21b, it can also be seen that the trends of the CONTACT solution are similar to that of the FE solution. Regarding the magnitude of the normal pressure, the CONTACT results seem to have a higher value than the FE results in most cases.

For the lateral shift of -5.5 mm, contact between the wheel flange root and rail gauge corner occurs (See Figure 2.9d), there is a drastic difference in terms of the resulting contact area as well as the magnitude of the normal pressure between the two solutions. It can be interpreted by the fact that the W/R contact geometries are getting much curved and non-planar in this case. Thus, the identification of the potential contact area (i.e. the contact clearance curve) and the accurate tangent contact plane using the 2D-Geo

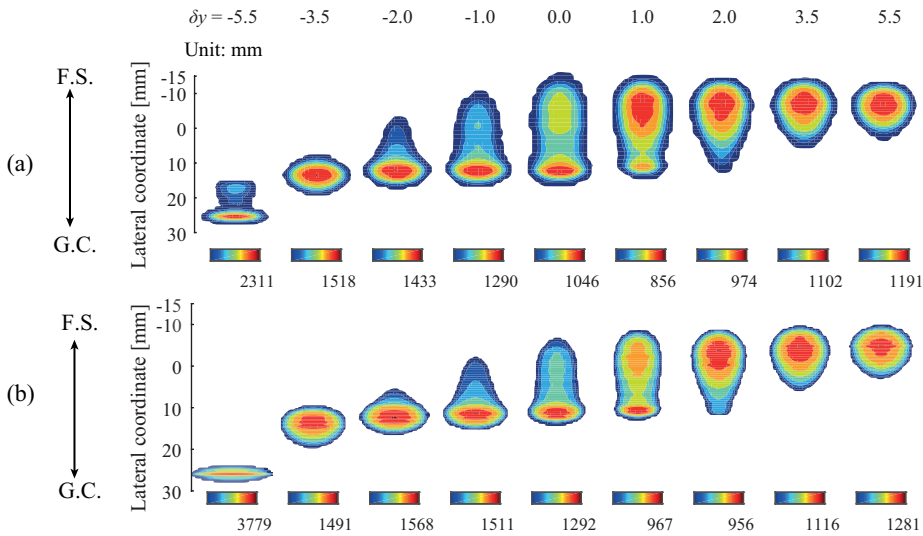


Figure 4.21: Normal pressure distribution (Unit: MPa): (a) FE solution; (b) CONTACT solution.

contact model would be influenced. As it has been mentioned in Section 4.3.2, more research efforts are required to improve the functionality of the 2D-Geo contact model so as to minimise the negative influence that it brings to the CONTACT solution.

Figure 4.22 shows the two solutions of the associated surface shear stress at different lateral displacements. As the traction force is fixed, the distribution of the shear stress is directly linked with the distribution of normal pressure as illustrated in Figure 4.21. Similar contact patches as well as discrepancies of magnitude have been observed from the two compared solutions.

Figure 4.23 shows the quiver plot of the surface shear stress at the lateral shift of -5.5 mm, in which the large shear stress components towards to the lateral direction is observed. The reason is that the angle between the contact plane and the horizontal plane in the contact point is large enough to introduce a large lateral force, and such a lateral force component starts to play a much important role in the wheel-rail interaction. The green boxes indicate the boundary of the actual contact area obtained from the two approaches.

Furthermore, the distribution of the subsurface VMS stress and shear stress along the “BB” cutting planes for the lateral shifts of 5.5, 2.0, 0.0, -2.0, -5.5 mm are presented in Figure 4.24. If the stress distribution of the lateral shift 0.0 mm was used as a reference, it can be noticed that the maximum shear and VMS stresses are shifting from field side to the gauge corner with the decrease of  $\delta y$  from 5.5 mm to -5.5 mm. When the contact occurs at the region of the gauge corner (-5.5 mm), both the magnitude of the VMS stress and the shear stress exhibit a substantial increase of 1653 MPa and 393 MPa, respectively. Such a highly-stressed subsurface cross-sectional observation from the FE simulations also indicates a satisfactory agreement with the field observations, which states that the high contact stresses at gauge corner make main contribution for the initiation of the

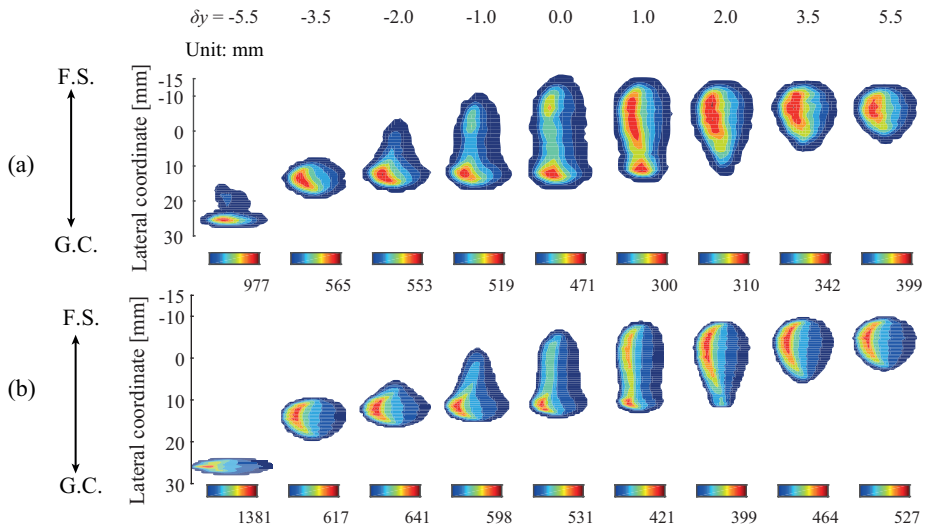


Figure 4.22: Shear stress distribution (Unit: MPa): (a) FE solution; (b) CONTACT solution.

rail defects called head checks.

It can be further seen that both the surface and the subsurface stress responses, namely the distributions and magnitudes, are drastically influenced with the change of the contact points. These FE results can be used as a good basis for studying and interpreting the phenomenon of the crack initiation or propagation at different contact points. It can be concluded that the developed FE tool is flexible, effective and reliable enough to simulate the cases of the contact point shifts.

#### 4.3.4 MATERIAL PROPERTY

Four sets of numerical simulations have been carried out to study the effect of material properties on the resulting contact properties. Among them, one set of simulations consists of the elastic wheel-rail material with the Young modulus  $E$  and Poisson ratio  $\nu$  kept constant at 210GPa and 0.3, respectively.

The other three sets consist of varying the material properties from the pure elastic to elastic-to-plastic ones. The yield strength  $\sigma_y$  for the elastic-to-plastic material is varying from 280 MPa to 680 MPa, whereas all the tangent modulus  $E_t$  is 21GPa. Here, Young modulus  $E$  represents the ratio of stress versus strain (slope) in the elastic range (See Figure 4.25). The Tangent modulus  $E_t$  refers to the slope of the stress-strain curve in the plastic range, which quantifies the “softening” of material that occurs when it begins to yield. The yield strength  $\sigma_y$  denotes the turning point in the stress-strain curve at which the stress-strain curve levels off and plastic deformation starts to occur.

It should be noted that for all the FE simulations that consider a bi-linear elastic-plastic material here and after in this thesis, the residual stresses resulted from previous wheel passages are assumed to be zero at the start of the FE calculation. Thus, in the future work, more attention needs to be paid on the effect of the accumulation of the residual stresses on the dynamic responses of W/R interaction.

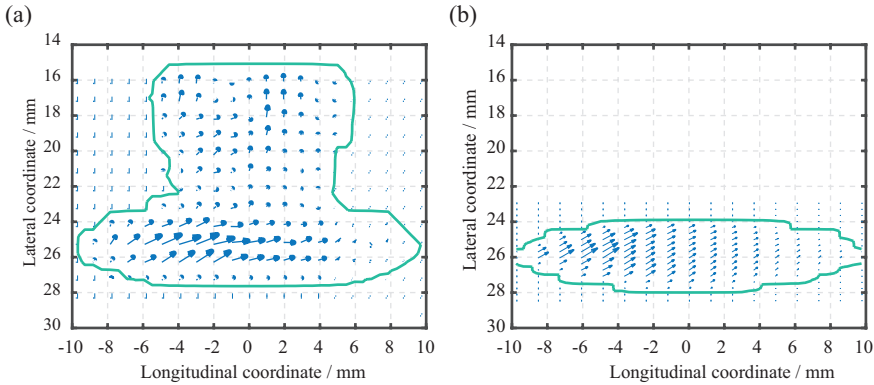


Figure 4.23: Surface shear stress quiver plot at the lateral shift of -5.5 mm. (a) FE solution; (b) CONTACT solution.

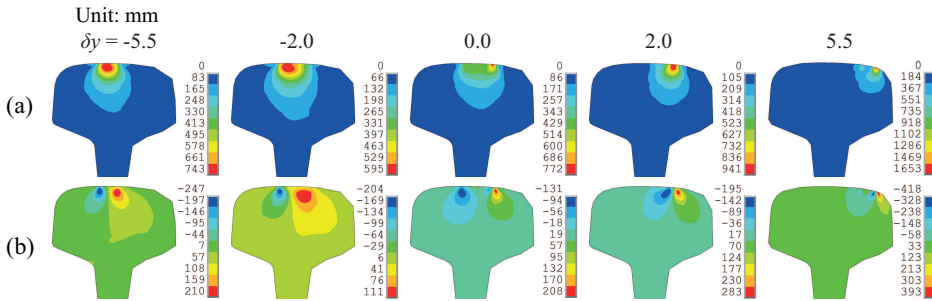


Figure 4.24: Sub-surface stress distribution of FE solution in BB-plane (Unit: MPa): (a) Von Mises stress; (b) Shear stress;

From the contour plots displayed in Figure 4.26a-d, it is observed that the pattern of the contact patch is changing from symmetry to non-symmetry. Due to the redistribution of stresses over a larger contact area obviously when using plastic materials in the case of the 280 MPa yield strength, the magnitude of the maximum normal pressure (720 MPa) is reduced up to 31.8% compared with the elastic materials (1056 MPa).

The surface shear stresses, which are transferring the traction forces over the contact areas, are shown in the Figure 4.27. Also, it can be seen that the maximum shear stress obtained from simulations with elastic-to-plastic materials in the case of the 280 MPa yield strength (500 MPa) was 55% lower in comparison with the elastic case (225 MPa).

Figure 4.28 shows the residual VMS stress distribution along the path the wheel runs. For the material with high yield strength (See Figure 4.28a-b), there is no residual stress observed. However, when there were a lower yield strength limit adopted in the material model such as the cases shown in Figure 4.28c-d, a noticeable band highlighted with relatively high residual stress was observed. It can be observed that the remained running band is increasing from three or four millimetres in the case of the 480 MPa yield strength to more than twenty millimetres with a yield strength of 280 MPa.

Figure 4.29 depicts the sliced plots at “AA” cutting planes, where the residual stresses

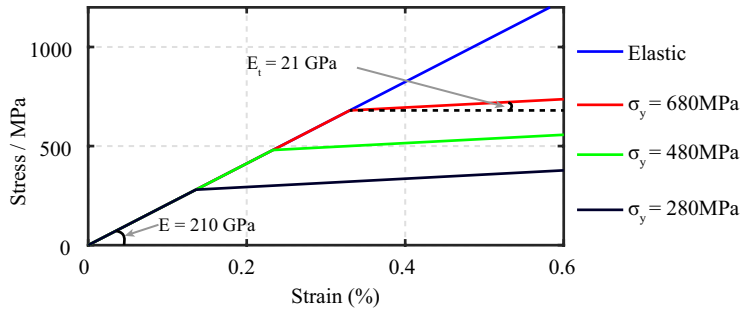


Figure 4.25: Schematic graph of the resulting bilinear elastic-plastic material model from the varying yield strength  $\sigma_y$ .

4

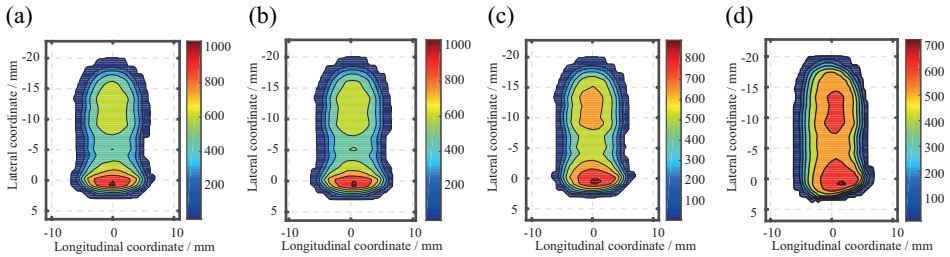


Figure 4.26: Normal pressure variation (Unit: MPa): (a) infinite; (b) 680 MPa; (c) 480 MPa; (d) 280 MPa.

located on the sub-surface are witnessed. The depth of the stressed zone is increasing from null at the case of elastic material to one or two millimetres when the yield limit is reduced to 280 MPa. It should be noted that the plots are captured at the moment when the wheel runs to the end of the refined potential contact area along the rail. The regions with high stress concentration at the right side of each plot shown in Figure 4.28 and Figure 4.29 are the area, where the wheel is standing on the top of the rail.

It can be concluded from the results that the width and depth of the remained residual stress zone maintains a steady rise with the decrement of the yield strength. The advantage of the FE approach, which can completely consider the plasticity of the material response, has been further demonstrated by the parametric study on the material properties.

#### 4.4 DISCUSSIONS: EXPERIMENTAL VALIDATIONS

The verification of the FE model against CONTACT has been presented in the previous sections. As there are no experimental validations reported, the future work on how to validate the proposed approach is discussed in this section.

Due to the relatively small size of the contact patch (around  $100 \text{ mm}^2$ ) and extremely high contact stresses, it is still a challenge to measure the contact properties experimentally [42] and further validate the FE model.

To address such a challenge, considerable efforts have been made on devising new

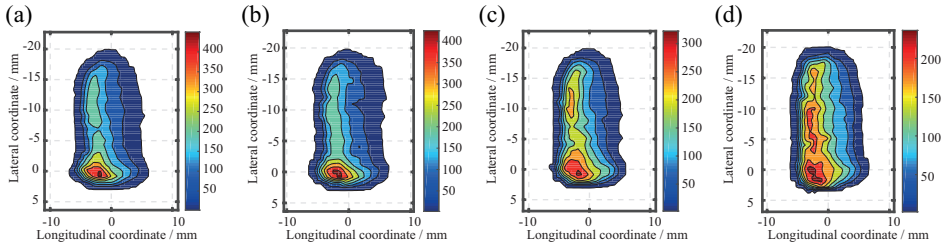


Figure 4.27: Surface shear stress distribution (Unit: MPa): (a) infinite; (b) 680 MPa; (c) 480 MPa; (d) 280 MPa.

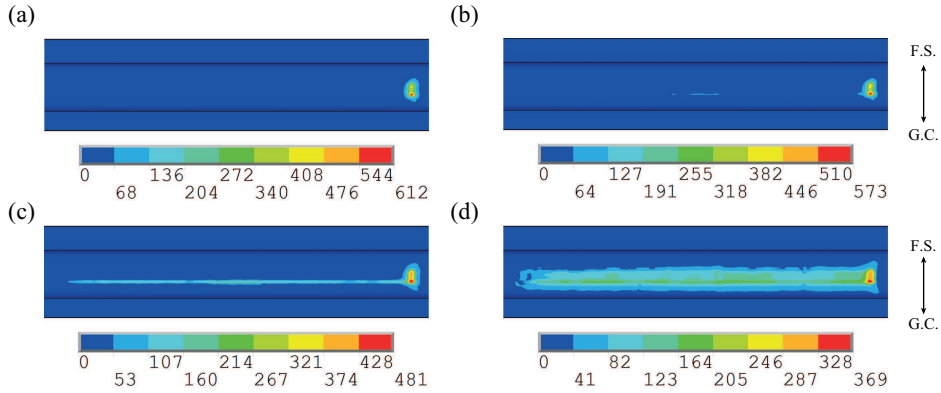


Figure 4.28: Top view of the rail running band variation (Unit: MPa): (a) Infinite; (b) 680 MPa; (c) 480 MPa; (d) 280 MPa.

methods/devices during the last decades. For instance, in [25, 30, 31], an ultrasonic non-invasive method was successfully used to estimate the dimension of the contact patch and the resulting normal pressure in the laboratory test. Also, several on-board [5, 26, 27] and track-side [17] field measurement devices were developed to predict the wheel-rail contact forces and/or the accelerations. These experimental devices were mounted onto the wheel, bogie, axle box or rail to record the real-time signal as the wheel travelling over the rail.

In future work, there are two ways of validating the proposed FE model experimentally as inspired by the above-mentioned research progress, namely:

- (1) Laboratory test: using the ultrasonic technique to validate the normal contact properties (i.e. contact patch and pressure) obtained from FE simulations against the measured ones;
- (2) Field measurement: using the on-board and/or track-side measurement systems to compare the dynamic contact forces and/or the accelerations [27] of the wheel/rail with the ones obtained from FE simulations.



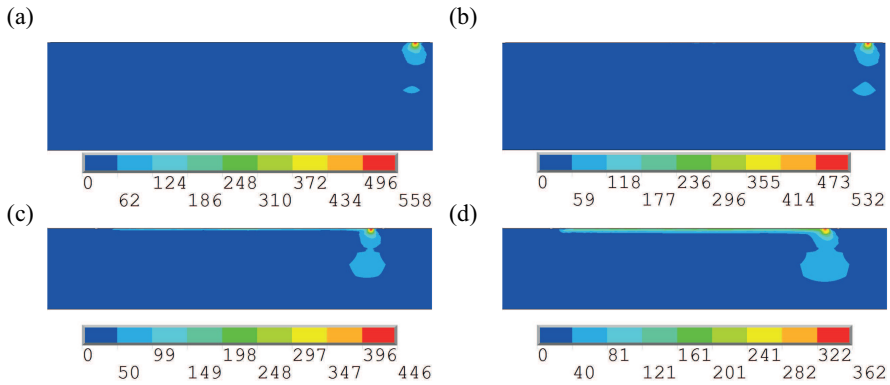


Figure 4.29: Sub-surface stress sliced plots at AA cutting plane (Unit: MPa): (a) Infinite; (b) 680 MPa; (c) 480 MPa; (d) 280 MPa.

## 4.5 CONCLUSIONS

In this chapter the accuracy of the developed explicit FE model has been verified. Also, the effect of the operational patterns such as the friction coefficients, traction forces, contact points, etc. on the tribological behaviour of the wheel-rail interaction has been studied. The future work on the experimental validations has been discussed. Based on the results and discussions of this study, the following conclusions have been drawn:

- (1) The integrating procedure of FE modelling verification against CONTACT have been introduced with application to the analysis of wheel-rail interaction. Using this procedure, the same conditions used in both FE and CONTACT simulations can be assured. Also, the correctness of the verification can be guaranteed. The usefulness and flexibility of such an integrating procedure have been demonstrated in the parametric study with different operational patterns (such as friction coefficient, traction force, contact point, etc.).
- (2) The results obtained from the CONTACT and FE analysis, including the contact pressure, shear stress, etc. agree well. Yet, tolerable discrepancies between these results still exist. The sources of the discrepancies have been explained and categorised into different groups, such as the different analysis types, solving procedures, etc. The main result of this verification is that the discrepancy between the results of CONTACT and FEM is reasonable enough for the FEM to be used in the future research. However, as one major disadvantage of FE analysis, it should be mentioned that the computational expenses of the present FE simulation (around 10 hours) are much higher than the ones of CONTACT simulation (2~3 minutes). As for the cases of contact model verification (e.g. newly developed FE model or other sophisticated models), the programme of CONTACT is recommended.
- (3) The changes of the friction coefficient, the braking and accelerating operation as well as the location of the contact point can bring about a significant influence on the tribological response in the W/R interaction, such as the distribution of normal

pressure, shear stress, slip-adhesion area as well as the subsurface stress. The accuracy of the corresponding FE simulations under varying operational parameters has been verified by comparing it with the one of CONTACT.

- (4) As one of the most pronounced advantages of the FE method, the consideration of plasticity in the material models will drastically reduce the magnitude of the shear stress and contact pressure. Also, the residual stress zone is observed at the distance of 1~2 mm (friction coefficient  $\mu = 0.5$ ) under the surface along wheel travelling path. The lower the material yield strength limit is, the wider and deeper the residual stress zone will be.

## REFERENCES

- [1] X. Deng, Z. Qian, and R. Dollevoet. Lagrangian explicit finite element modeling for spin-rolling contact. *Journal of Tribology*, 137(4):041401, 2015.
- [2] H. Doi, T. Miyamoto, Y. Nishiyama, S. Ohe, and H. Kamachi. A new experimental device to investigate creep forces between wheel and rail. *Wear*, 271(1):40–46, 2011.
- [3] R. Dollevoet. *Design of an Anti Head Check profile based on stress relief*. University of Twente, 2010.
- [4] G. Duvaut and J. L. Lions. Les inéquations en mécanique et en physique. *Travaux et Recherches Mathématiques*, 21, 1972.
- [5] P. Gullers, L. Andersson, and R. Lundén. High-frequency vertical wheel–rail contact forces—field measurements and influence of track irregularities. *Wear*, 265(9):1472–1478, 2008.
- [6] J. O. Hallquist. ANSYS/LS-DYNA theoretical manual, 2005.
- [7] J. O. Hallquist, G. L. Goudreau, and D. J. Benson. Sliding interfaces with contact-impact in large-scale lagrangian computations. *Computer methods in applied mechanics and engineering*, 51(1-3):107–137, 1985.
- [8] N. Hu. A solution method for dynamic contact problems. *Computers & structures*, 63(6): 1053–1063, 1997.
- [9] I. Huněk. On a penalty formulation for contact-impact problems. *Computers & structures*, 48(2):193–203, 1993.
- [10] J. J. Kalker. Contact mechanical algorithms. *International Journal for Numerical Methods in Biomedical Engineering*, 4(1):25–32, 1988.
- [11] J. J. Kalker. *Three-dimensional elastic bodies in rolling contact*, volume 2. Springer Science & Business Media, 1990.
- [12] H. Kanehara and T. Fujioka. Measuring rail/wheel contact points of running railway vehicles. *Wear*, 253(1):275–283, 2002.
- [13] S. R. Lewis, R. Lewis, and U. Olofsson. An alternative method for the assessment of railhead traction. *Wear*, 271(1):62–70, 2011.
- [14] Z. Li. *Wheel-rail rolling contact and its application to wear simulation*. PhD thesis, Delft University of Technology, 2002.
- [15] Z. Li, X. Zhao, C. Esveld, R. Dollevoet, and M. Molodova. An investigation into the causes of squats—correlation analysis and numerical modeling. *Wear*, 265(9):1349–1355, 2008.
- [16] X. Liu and P. A. Meehan. Investigation of the effect of relative humidity on lateral force in rolling contact and curve squeal. *Wear*, 310(1):12–19, 2014.
- [17] X. Liu, V. L. Markine, and I. Shevtsov. Dynamic experimental tools for condition monitoring of railway turnout crossing. In *Proceedings of the second international conference on railway technology: research, development and maintenance*, pages 1–9, 2014.

- [18] Y. Ma and V. L. Markine. A numerical procedure for analysis of w/r contact using explicit finite element methods. In *CM2015: 10th International Conference on Contact Mechanics, Colorado Springs, USA, 30 August-3 September 2015*, pages 1–10, 2015.
- [19] Y. Ma, M. Ren, G. Hu, and C. Tian. Optimal analysis on rail pre-grinding profile in high-speed railway. *Jixie Gongcheng Xuebao(Chinese Journal of Mechanical Engineering)*, 48(8):90–97, 2012.
- [20] Y. Ma, A. A. Mashal, and V. L. Markine. Numerical analysis of wheel-crossing interaction using a coupling strategy. In Pombo J., editor, *Proceedings of the 3rd international conference on railway technology: Research, development and maintenance, 5 April – 8 April*, pages 1–19, Cagliari, Italy, 2016. Civil-Comp Press, Stirlingshire, UK.
- [21] Y. Ma, V. L. Markine, A. A. Mashal, and M. Ren. Modelling verification and influence of operational patterns on tribological behaviour of wheel-rail interaction. *Tribology International*, 114:264–281, 2017. ISSN 0301-679X.
- [22] Y. Ma, V. L. Markine, A. A. Mashal, and Ren M. Effect of wheel-rail interface parameters on contact stability in explicit finite element analysis. *Proceedings of the Institution of Mechanical Engineers, Part F: Journal of Rail and Rapid Transit*, 232(6):1879–1894, 2018.
- [23] E. E. Magel and Y. Liu. On some aspects of the wheel/rail interaction. *Wear*, 314(1):132–139, 2014.
- [24] N. K. Mandal and M. Dhanasekar. Sub-modelling for the ratchetting failure of insulated rail joints. *International Journal of Mechanical Sciences*, 75:110–122, 2013.
- [25] M. B. Marshall, R. Lewis, R. S. Dwyer-Joyce, U. Olofsson, and S. Björklund. Experimental characterization of wheel-rail contact patch evolution. *Journal of tribology*, 128(3):493–504, 2006.
- [26] A. Matsumoto, Y. Sato, H. Ohno, M. Tomeoka, K. Matsumoto, J. Kurihara, T. Ogino, M. Tanimoto, Y. Kishimoto, and Y. Sato. A new measuring method of wheel–rail contact forces and related considerations. *Wear*, 265(9):1518–1525, 2008.
- [27] M. Molodova, Z. Li, A. Núñez, and R. Dollevoet. Validation of a finite element model for axle box acceleration at squats in the high frequency range. *Computers & Structures*, 141:84–93, 2014.
- [28] W. L. Oberkampf and T. G. Trucano. Verification and validation in computational fluid dynamics. *Progress in Aerospace Sciences*, 38(3):209–272, 2002.
- [29] E. Olsson and P. L. Larsson. On the tangential contact behavior at elastic–plastic spherical contact problems. *Wear*, 319(1):110–117, 2014.
- [30] M. Pau and B. Leban. Ultrasonic assessment of wheel–rail contact evolution exposed to artificially induced wear. *Proceedings of the Institution of Mechanical Engineers, Part F: Journal of Rail and Rapid Transit*, 223(4):353–364, 2009.
- [31] M. Pau, F. Aymerich, and F. Ginesu. Distribution of contact pressure in wheel–rail contact area. *Wear*, 253(1):265–274, 2002.
- [32] O. Polach. A fast wheel-rail forces calculation computer code. *Vehicle System Dynamics*, 33:728–739, 2000.
- [33] O. Polach. Creep forces in simulations of traction vehicles running on adhesion limit. *Wear*, 258(7):992–1000, 2005.
- [34] C. L. Pun, Q. Kan, P. J. Mutton, G. Kang, and W. Yan. Ratcheting behaviour of high strength rail steels under bi-axial compression–torsion loadings: Experiment and simulation. *International Journal of Fatigue*, 66:138–154, 2014.
- [35] C. L. Pun, Q. Kan, P. J. Mutton, G. Kang, and W. Yan. An efficient computational approach to evaluate the ratcheting performance of rail steels under cyclic rolling contact in service. *International Journal of Mechanical Sciences*, 101:214–226, 2015.

- [36] K. D. Vo, A. K. Tieu, H. T. Zhu, and P. B. Kosasih. A 3d dynamic model to investigate wheel–rail contact under high and low adhesion. *International Journal of Mechanical Sciences*, 85: 63–75, 2014.
- [37] E. Vollebregt and G. Segal. Solving conformal wheel–rail rolling contact problems. *Vehicle System Dynamics*, 52(sup1):455–468, 2014.
- [38] E. A. H. Vollebregt. User guide for contact, vollebregt & kalker’s rolling and sliding contact model, technical report TR09-03, version, 2013.
- [39] E. A. H. Vollebregt, S. D. Iwnicki, G. Xie, and P. Shackleton. Assessing the accuracy of different simplified frictional rolling contact algorithms. *Vehicle System Dynamics*, 50(1):1–17, 2012.
- [40] M. Wiest, E. Kassa, W. Daves, J. C. O. Nielsen, and H. Ossberger. Assessment of methods for calculating contact pressure in wheel-rail/switch contact. *Wear*, 265(9):1439–1445, 2008.
- [41] S. R. Wu and L. Gu. *Introduction to the explicit finite element method for nonlinear transient dynamics*. John Wiley & Sons, 2012.
- [42] X. Zhao and Z. Li. The solution of frictional wheel–rail rolling contact with a 3D transient finite element model: Validation and error analysis. *Wear*, 271(1):444–452, 2011.
- [43] Z. Zhong and J. Mackerle. Contact-impact problems. a review with bibliography. *Applied Mechanics Reviews*, 47(2):55–76, 1994.



# 5

## MODELLING AND EXPERIMENTAL VALIDATION OF WHEEL-CROSSING IMPACT

*To improve the understanding of dynamic impact in 1:9 crossing panel, which is suffering from rapid surface degradation, detailed modelling and experimental studies are performed. A three-dimensional explicit finite element (FE) model of a wheel rolling over a crossing rail, that has an adaptive mesh refinement procedure coupled with two-dimensional geometrical contact analyses, is developed. It is demonstrated that this modelling strategy performs much better than the 'conventional' FE modelling approach. Also, the experimental validations show that the FE results agree reasonably well with the field measurements. Using the validated FE model, the tribological behaviour of contact surfaces is studied. The results indicate that the proposed modelling strategy is a promising tool for addressing the problems of wheel-crossing dynamic impact.*

Chapter 5 demonstrates how to extend/upgrade the verified FE model of W/R interaction presented in Chapter 2 and Chapter 4 to a new level for analysing the wheel-crossing (W/C) interaction, and how to validate this model experimentally. It is aimed to answer the research question Q4 presented in Chapter 1.

A new explicit FE model of a wheel rolling over a crossing rail is developed in this study. Also, following the guidelines presented in Chapter 2 and Chapter 3, the geometrical/interface parameters that are suitable for the analysis of W/C interaction are selected.

The structure of this chapter is as follows. First, a brief introduction of the research background of Chapter 4 is presented in Section 5.1. In Section 5.2, the attention is focused on the general description of 3D FE model. Also, the specific modelling difficulties that prohibit an accurate solution of W/C dynamic impact are emphasized. The detailed working mechanisms of the coupling strategy are presented. The effectiveness of 'eFE-CS' model is assessed through a comparison with the 'conventional' FE model. In Section 5.3, experimental studies are performed to validate the accuracy of the proposed FE model. In Section 5.4, the results of surface and subsurface material responses obtained from the FE analysis are presented. The future work and further applications of the 'eFE-CS' model are discussed. Finally, concluding remarks are drawn.

## 5.1 INTRODUCTION

Switches & crossings (S&C, also called 'turnouts', See Figure 5.1) are key operating devices on the railway network to manage the traffic flow effectively. As one of the three major components (namely, switch, closure and crossing panels, See Figure 5.1a), the crossing panel is specially designed to enable the wheel successfully travelling from the wing rail to the nose rail or the other way around. By this means, the vehicles are capable of safely switching from through/diverging routes in either facing or trailing directions (See Figure 5.1a). However, due to the natural geometrical discontinuity of the rail and the resulting gaps at the transition region (See Figure 5.1a and Figure 5.1c), highly concentrated impact loads on the crossing rail are induced and amplified from the passing vehicles. These repeated high impact loads would lead to the rapid degradation of contact interfaces (e.g. accumulated plastic deformations) and/or the initiation of micro-cracks on the rail surface/subsurface. The small cracks might further deteriorate into the spalling damage (See Figure 5.1d) or even lead to the sudden fracture of the crossing rail. Nowadays, the Dutch railway network is severely suffering from these problems according to [39], where it has been reported that a typical crossing (e.g. the one shown in Figure 5.1b-d) needs to be repaired urgently every half year. Thus, the crossing panel is being one of the most maintenance demanding components in the Dutch railway infrastructure.

During the last decades, extensive research resources [1, 4, 10, 14–16, 21, 23, 29, 30, 33, 38–40, 43, 45] have been devoted to the subject of dynamic impact at S&C for the purpose of finding effective strategies to address the aforementioned impact-induced problems. Usually, these dynamic impact problems are studied experimentally [4, 15, 16, 21] and/or numerically [1, 10, 23, 29, 30, 33, 38–40, 43, 45]. Both approaches are very helpful to improve the understanding of the dynamic impact phenomena. However, experimental studies are often time-consuming and considerably expensive [47]. As a conse-

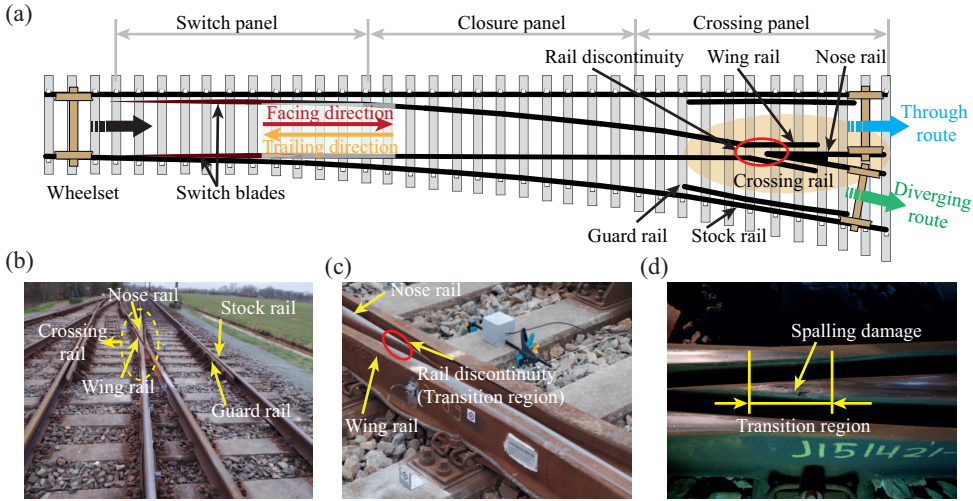


Figure 5.1: (a) Schematic of railway switches & crossings (adapted from [4], re-drawn by A. A. Mashal and then presented firstly in [23]); (b) 1:9 crossing panel on Dutch railway network (photo taken by V. Markine); (c) Close-up view of this crossing panel (photo taken by V. Markine); (d) Spalling damage on crossing nose (photo taken by Y. Ma).

quence, the use of numerical simulations is much preferable, since it allows to repeat “experiments” easily [36], thus to assess the effect of all/selected parameters (e.g. operational, contact geometrical, track, vehicle parameters, etc.) on the performance of wheel-crossing (W/C) interaction separately/integrally [2, 13, 14, 28, 38], even to improve the local design of S&C contact geometry [26, 27, 39] or tune the elastic track properties through optimisation [6, 22, 40]. Among the aforementioned numerical simulations, Hertzian [8], non-Hertzian [12], multi-Hertzian [3] contact theories are often adopted for the calculation of normal contact forces, whereas fast and approximate frictional contact algorithms, such as FASTSIM [12], FASTSIM2 [37], Polach’s method [31] and table-lookup schemes [12] are commonly used to get the tangential contact forces. These different types of normal/tangential contact models are well established and successfully integrated with many MBS (Multi-body Dynamic System) software (e.g. Adams VI-Rail, Vampire, Simpack, etc.). For the MBS simulations, all the components of vehicle & track are simplified/modelled as rigid bodies. The associated contact models are usually based on the assumptions of elastic (i.e. no material plasticity considered) half-space [12].

With the increase of expectations on the contact models for higher degree of realism and better accuracy, advanced computer programmes (such as CONTACT [12, 35], Finite Element (FE) method [44], etc.) are necessitated as alternatives for more detailed studies on the dynamic contact-impact phenomena [36]. Among the advanced numerical methods, the FE approach is more frequently used because of its striking versatility (i.e. the use of sophisticated elasto-plastic material models as well as the consideration of realistic/generic contact geometries). FE method, as opposed to the MBS method, is known as a powerful tool to determine the stresses/strains at the regions of interest with



the assumption that the bodies are deformable. Yet, the FEM simulations usually demand more computational power than that of MBS due to the large number of elements discretized. During the last decades, the growing computer power and the development of computing techniques (i.e. parallel processing) significantly boost the FE modelling studies on the W/C dynamic impact. Thus, a number of pioneering research progresses [10, 23, 29, 30, 41–43, 45] have been made. For instance, Pletz et al. [29] were among the first to simulate the dynamic impact between a wheel and a full-scale crossing rail using explicit FE method. The effects of operational parameters (such as, train velocities, axle loads, etc.) on the behaviour of dynamic impact were studied thoroughly [29, 30]. The developed FE model was well verified against the MBS model. In [43], Wiest et al. developed a novel coupling procedure between MBS and FE programmes. Using that procedure, the full-scale W/C dynamic FE model was able to be simplified into a static sub-model with two small pieces (around 30 mm thick) of the contact bodies considered. The contact pressure was assessed and further compared with that of CONTACT analysis. In [45], Xin and Markine developed a complete FE model, in which both the full-scale wheel-set and the complete crossing panel were modelled. The accuracy of their model was evaluated through comparisons with the field measurements. Also, a thorough parametric study on the effect of major operational parameters (such as, axle loads, train velocities, etc.) on the dynamic impact phenomena was performed. In [41], Wei et al. presented a similar complete FE model. The simulated dynamic response was validated through comparisons with the in-situ measurements of axle box acceleration (ABA). A good agreement between the measured and simulated acceleration signals was found. The contact properties (e.g. normal pressure, shear stress, etc.) obtained were further used as an input to simulate the plastic deformation and wear on the surface of crossing rail. More recently, Wiedorn et al. [42] introduced a simplified finite element model for studying the impact of a wheel on a crossing. It was intended to improve the calculation efficiency of FE simulations by simplifying the contact geometries. The simulation results agreed reasonably well with the ones of full-scale FE model [29, 30].

In summary, the detailed knowledge on the W/C dynamic impact has been enhanced significantly with these various and valuable FE-based numerical studies (and experimental validations). Yet, there is still much work to be done to address the following issues:

- Demanding research on 1:9 crossing: Most of the aforementioned studies are focused on the impact phenomena of 1:15 crossing panels [10, 29, 30, 42, 43, 45]. Only few research interests [41] are in 1:9 crossing panel, which is currently suffering from stronger impact and rapider degradation (as described in Figure 5.1) than the one of 1:15, due to its bigger crossing angle ('1:n' is referred to as the crossing angle of the turnout, 'n' is also called the crossing number) and the reduced transition distance (i.e. the length of collateral running bands on the crossing rail, See Figure 5.1d). Also, the material (i.e. manganese steel) of 1:9 crossing rail is prone to the issues of surface degradation.
- Contact/impact-modelling difficulties: a) General challenges: Contact/impact always occurs at a-priori unknown area until the problem is resolved. This unknown can bring about many challenges for the general cases of FE-based con-

tact/impact modelling [18], such as the geometrical “gaps or penetrations”, mismatched/insufficient mesh refinement, unexpected initial slips, etc. If these challenges are not addressed properly, the accuracy and efficiency of the corresponding FE simulations will be adversely affected [18]; b) Specific challenges: Regarding the modelling of W/C impact, the special modelling difficulties, such as, the ‘discontinuous’ mesh refinement, the prohibitive amount of elements & the low calculation efficiency, etc., are further increased due to the much complex local contact geometries at the crossing panel. More details about these modelling difficulties/challenges will be given later in [Section 5.2.1](#).

- Well-established experimental validations: Due to the complexity of W/C interaction and relatively small size of contact patches (around 150–200 mm<sup>2</sup>, See [23]), it remains challenging to measure the local contact properties within the contact patches [46]. Therefore, well-established experimental validations for the presented FE-based contact models are still in high demand. Usually, the experimental devices (e.g. strain gauges, accelerometer, etc.) are instrumented onto the wheel, bogie, axle box (train-borne/on-board) [24, 41] or rail (track-side/wayside) [4, 16, 21, 23, 45]. The acquired real-time strain/acceleration signals are preprocessed and then compared with the FE simulated results. By this means, the accuracy of the presented FE contact models is assessed indirectly [17]. However, these experimental validations are mostly focused on the single selected measurement instead of validating from the statistical/stochastic perspectives [14, 30]. In short, the problem of the experimental validations in terms of the FE-based contact models are still open to be addressed.
- Detailed stress/strain solutions of dynamic impact problems at S&C: It has been reported in [23, 29, 45] that the impact loadings will lead to the greatly increased contact stresses, which are far beyond the yield strength of typical steels. In reality, the accumulation of plastic deformation will manifest itself in the rather high levels of surface/subsurface damage (i.e. wear, RCF, etc.). To accurately quantify the wear/RCF resistance of typical materials and assess the long-term behaviour of S&C components, the detailed stress/strain solutions for this dynamic impact problem are, thus, practically needed. More discussion about the results of stress/strain will be presented in [Section 5.4](#).

In order to enrich the detailed knowledge of W/C dynamic impact at 1:9 crossing panel, an explicit finite element model of a wheel rolling over a crossing rail is developed, which includes an effective and efficient modelling procedure through the coupling with two dimensional (2D) geometrical contact analyses [18]. Such a modelling strategy is originated and further extended from the authors’ former work [17–19], which is focused on the normal wheel-rail interaction. The strategy (referred to as ‘enhanced explicit FE-based coupling strategy’, abbreviated as ‘eFE-CS’, hereinafter) has been described thoroughly in [17–19]. Its performance (refers to the accuracy, efficiency and flexibility) has been demonstrated through a number of numerical simulations with varying interface parameters and operational patterns [17, 19]. The effectiveness of this coupling strategy on addressing the general modelling challenges (such as ‘gaps and/or penetrations’, targeted mesh refinement, etc.) has been successfully proved. In this study, the approach

on how to address both the general and specific modelling challenges of W/C dynamic impact is presented. Also, the performance of this extended 'eFE-CS' model is examined through the comparison with the 'conventional' FE modelling approach. Here, the 'conventional' means that the coupling strategy is not used.

As it is motivated to make this 'eFE-CS' contact model reliable and useful based on its own advantages, two procedures of experimental validations are introduced and described in this chapter. The first procedure is based on the location of 'transition region' (See [Figure 5.1d](#)), which is referred to as the collateral zone of the two separate running bands. At this region, the change of wheel motion directly contributes to the subsequent impact responses according to [39]. The transition region has thus been suggested and used as an indication of the potential damage locations on the crossing rail [38]. Considering the great importance of the transition region, it is inspired to compare the FE predicted transition region with the field measured ones, through which the accuracy of 'eFE-CS' model can be assessed.

On the other hand, the crossing accelerations induced by the impact event are collected by a real-time measuring system called ESAH-M (Elektronische System Analyse Herzstijckbereich – Mobil). Such a measurement device has been successfully used to monitor the structural health conditions of 1:15 crossing panel [21, 45]. For the studied 1:9 crossing panel, the measured accelerations are used to compare with those obtained from the FE simulations. To address the aforementioned open challenges of the experimental validations, the current validation is performed from a statistical perspective. A great number of measured acceleration signals (recorded from 21 train passages, around 400 W/C impacts) are collected and compared with the FE acceleration signal statistically both in the time and frequency domains. It shows that the modelling results agree reasonably well with the field measurements. Also, it implies that the presented 'eFE-CS' model can represent the real system of W/C interaction reasonably and is reliable & accurate enough to be used in the future work.

Using the validated 'eFE-CS' model, the corresponding FE results of the global dynamic contact forces as well as the detailed knowledge about the local surface contact properties (i.e. sliding-adhesion area, normal/shear stresses, etc.) within the contact patches are presented. At the same time, special research interests are focused on the subsurface stress responses. The relations between greatly increased contact stresses and the causes of rapid surface degradations are discussed.

## 5.2 MODELLING OF W/C IMPACT

In this section, the modelling approach/strategy for the analyses of W/C dynamic impact is described. The two investigated counterparts are the standard S1002 wheel (EN13715 [5]) with a nominal rolling radius of 460mm and the 1:9 crossing rail (See [Figure 5.1a-d](#) and [Figure 5.2a-c](#)) used on a monitoring site near Meppel in the Netherlands.

The drawing of wheel cross-section is adopted from [25]. The inner gauge of the wheel-set is 1360 mm. The axle length is 2200 mm. The crossing rail is cast of manganese steel and prefabricated as a single unit according to the standard drawing shown in [Figure 5.2a-c](#). There is a group of characteristic cross-sections, ranging from AA to GG, specifically used to describe the whole crossing rail geometry. The overall length of this 1:9 crossing rail is 2950 mm. The nominal track gauge is 1435 mm.

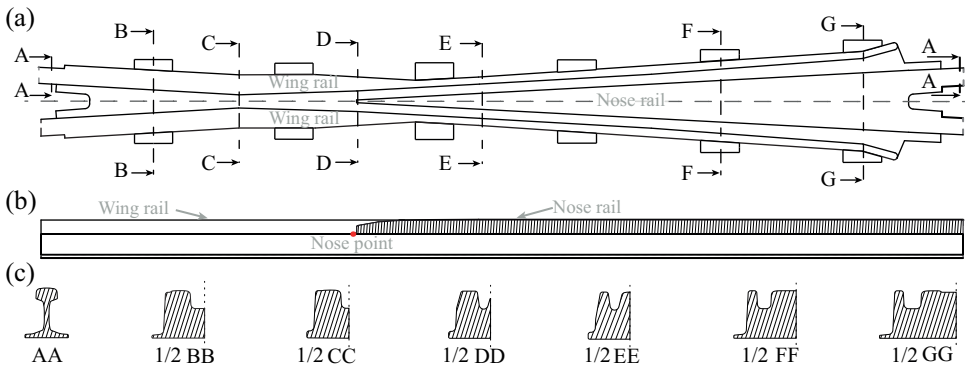


Figure 5.2: Drawing of crossing rail: (a) Global top view; (b) Vertical-longitudinal cross-sectional view; (c) Vertical-lateral cross-sectional view.

It can be seen from [Figure 5.2a](#) and [Figure 5.2c](#) that the lateral width of the wing rail head remains the same until CC cross-section. Then, it begins to shrink gradually in the lateral direction and stops at end of the wing rail (GG cross-section). For the nose rail (See [Figure 5.2a-b](#)), both the width (lateral) and height (vertical) of the rail head expand remarkably along the longitudinal path from DD to GG. Following that, it splits into two normal rails. At the two ends of the crossing rail, standard UIC54 normal rails (cross-section AA) are secured by stainless welds.

### 5.2.1 3D W/C FE MODEL

As a major component of the coupling strategy, the 3D W/C FE model is described firstly. Following that, the reasons (mainly due to the FE modelling challenges) of adopting the 'eFE-CS' modelling strategy are explained.

#### MODEL DESCRIPTIONS

A W/C FE model shown in [Figure 5.3a-b](#) is developed, where the crossing rail is modelled with restriction to an overall length of 7.45m. This finite length has been examined and confirmed in the previous research [23] that it is long enough to minimise the influence of the boundary conditions (at the two ends of the crossing rail) on the dynamic impact. The idea of constructing such a W/C FE model (single wheel considered) is inspired by the models described in [30, 46].

Only the solution regions where the wheel travels are discretized with fine mesh, leaving the remaining regions with coarse mesh. Here, the solution region (fine mesh area) is an area to extract and analyse the contact properties, such as the resulting contact patch, normal pressure, shear stress, etc. In this region, the mesh size is as small as 1.0 mm (See [Figure 5.3](#)), which is prescribed for the purpose of capturing the accurate and high stress/strain gradients inside the contact patch. This mesh size (1.0 mm) is 33% smaller than that of 1.33 mm, which can ensure the good accuracy of contact solutions according to [46]. Moreover, the type of 3D 8-node brick (i.e. hexahedral) element (SOLID164) with reduced (one point) integration is adopted so as to save the computational cost and enhance the robustness in cases of large deformations [7].

Table 5.1: Material properties and mechanical parameters.

	Properties	Values
Wheel/rail material <sup>a</sup>	Young modulus(GPa)	210
	Tangent modulus(GPa)	21
	Yield strength (MPa)	480
	Possion ratio	0.3
	Density ( $kg/m^3$ )	7900
Primary suspension	Stiffness (MN/m)	1.15
	Damping (Ns/m)	2500
	Coefficient of friction	0.5
Operational parameters	Coefficient of traction	0.25
	Train velocities (km/h)	140
	Lateral displacement (mm)	0.0
Sleeper	Mass(kg)	244
Rail pad	Stiffness (MN/m)	1300
	Damping (kNs/m)	45
Ballast	Stiffness (MN/m)	45
	Damping (kNs/m)	32

<sup>a</sup> : Bilinear (elasto- plastic) isotropic hardening law, more information about this model can be found in [17].

To take the primary suspension into account, a group of sprung mass blocks are lumped over the spring-damper system. The mass blocks, which are used to represent the weight of the loaded car body, are 10 tons. The substructures (i.e. rail-pad, ballast, etc.) are modelled as spring and damping elements as well. The sleepers are simplified by mass elements. The wheel and crossing rail are of the same material, which is considered to be bilinear isotropic hardening in ANSYS [9]. The values of the material/mechanical parameters are listed in Table 5.1. The position of the sleepers (60cm spacing) follows the schematic shown in Figure 5.3a.

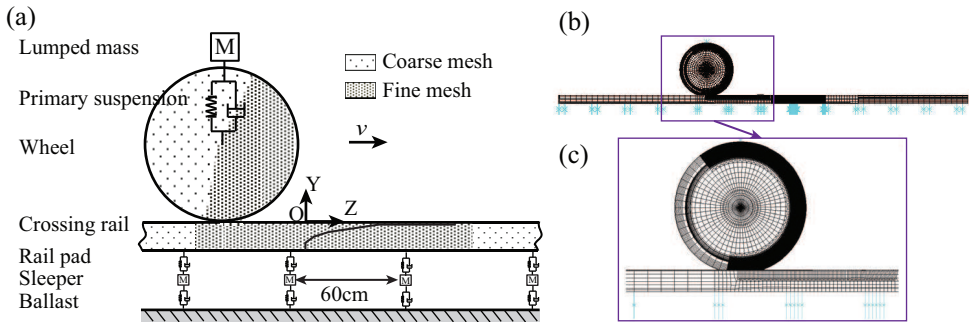


Figure 5.3: Explicit FE model of W/C dynamic impact: (a) Schematic of FE model; (b) FE model – global view; (c) FE model – close-up view.

The wheel is set to roll on the crossing rail from the origin of the global coordinate system  $O$ - $XYZ$  over a short travelling distance of 1.2m (See Figure 5.3a), which is long enough to ensure that the wheel can travel over the transition region completely. The initial train speed is 140km/h. The rotations of the wheel around the  $Z$ -axis are disabled

(i.e. turned off or prevented from occurring), since it is assumed that variations of the wheel-set's yaw angles are small over a short rolling distance (i.e. 1.2m).

To better simulate the W/C dynamic impact process, an implicit-to-explicit sequential solving procedure [7] is used. In this procedure, the implicit solver (ANSYS Mechanical) and explicit solver (ANSYS LS-DYNA) work in pairs. First, the equilibrium state of the preloaded structure (i.e. axle-load 100 kN applied) is determined with ANSYS Mechanical. The displacement results of the implicit analysis are adopted to do a stress initialization for the subsequent transient analysis. Then, the dynamic impact processes begin at time zero with a stable preloaded structure [9]. The impact responses are further simulated with ANSYS LS-DYNA using the central difference time integration scheme [7]. Also, double precision LS-DYNA [7] is used so as to ensure good accuracy of the contact solutions.

### MODELLING CHALLENGES

When performing the contact/impact-related analyses, all contact forces have to be distributed over a-priori unknown contact area. Also, the distribution of contact forces is another primary unknown to be determined. These unknowns bring about many FE modelling difficulties. In this section, both the difficulties for the general FE-based contact/impact models and the specific W/C model are discussed.

#### General modelling difficulties

- (1) Unwelcome “gaps and/or penetrations”: Small geometrical “gaps and/or penetrations” between the contact bodies are easy-induced and ‘unavoidable’ at the start of the contact modelling, because of the unknown first point of contact, the misaligned contact positions, the numerical round-off [9], etc. If these “gaps and/or penetrations” are not treated appropriately, they can proactively trigger the problem of divergence in the implicit FE analyses as well as the undesired failure of the explicit FE analyses [18];
- (2) Lack of targeted mesh refinement: Usually, the undeformed contact bodies are discretized and further refined at the vicinity of the potential contact areas according to the analysers' experience or visualisation [19]. Thus, the sizes of these areas can be easily overestimated or underestimated, which will lead to either prohibitive computational expense or inaccurate contact solutions. Considering that the desired mesh size within the potential contact area (no less than 1.3 mm to ensure the engineering accuracy according to [46]) is 1000 times smaller than the typical dimension of the wheel and rail components (usually in the meter-scale), an economic (efficiency), adaptive (flexibility) and reliable (reliability) mesh refinement has always been a strong challenge for researchers and engineers;
- (3) Demand for effective mesh transition: The surface-based tie constraints (similar as bonded contact, constraint equations, etc.[9]), which can bond together two regions having dissimilar mesh patterns (See Figure 5.4b-c), are commonly used in the contact/impact FE models. As the tie constraints might adversely affect the

overall integrity/stiffness of the contact bodies and thus the accuracy of FE simulations [19], the applicability of tie constraints is doubted if they are used without careful examinations.

### Specific modelling difficulties

Regarding the W/C model, special FE modelling difficulties (apart from the general ones) will be encountered. These special challenges are mainly induced by the varying contact geometries of the crossing rail, in which two separated running bands shaded with the yellow and diagonal patterns can be observed (See [Figure 5.4a](#)). One of the running bands lies on the wing railhead, while the other one locates on the nose railhead. To have a better insight on the specific modelling difficulties, they are collected and illustrated as follows:

- (1) To identify the potential contact areas: The best identified potential contact areas should be slightly larger than the actual ones, which will enable the satisfactory compromises between calculation accuracy and efficiency. In order to maintain the compromises and further facilitate FE modelling process, the exact locations of the potential contact areas (e.g. the starting and ending positions, the lateral width of the area, etc., See [Figure 5.4a](#)) are practically necessary.
- (2) To accomplish the 'separate' & 'dependent' mesh transitions: Here, 'separate' means that the mesh refinements at the railhead (including both the wing and nose rail) are to perform and function independently in the longitudinal direction (i.e. travelling direction)(See [Figure 5.4a](#)). The meaning of 'dependent' are twofold: a) In the vertical direction, the bonds between the coarse mesh at the rail-bottom (namely, the rail web and rail foot) and the fine mesh at the railhead are to be secured by a group of solid elements (the mesh sizes are in a descending order) instead of the artificial tie constraints (See [Figure 5.4b](#)); b) In the lateral direction, the rail-bottom mesh refinements on the wing and nose rails have to match with each other (See [Figure 5.4c](#)).

In summary, both the wing and nose rails need to be modelled carefully and further discretized properly so as to fully encompass the double points of contact in the transition region. More information of addressing these modelling (i.e. mesh refining) challenges are given in [Section 5.2.2](#).

### 5.2.2 COUPLING STRATEGY

To address the aforementioned FE modelling challenges of W/C dynamic impact analysis, a coupling strategy that combines the two dimensional geometrical (2D-Geo) contact analyses and 3D-FE analyses, is used.

The basic working mechanism of this strategy is shown in [Figure 2.5](#) (See [Chapter 2](#)). The 2D-Geo simulation is performed first to detect the initial "Just-in-contact" point (CP) and the "Contact clearance"  $\delta z$ . Here, the term "Contact clearance ( $\delta z$ )" is referred to as the vertical distance between the un-deformed contact geometries of wheel and crossing rail (See [Figure 5.6a1-a2](#)). The contact information obtained is used as a helpful guidance to identify the single point and double points of contact, which are then used in

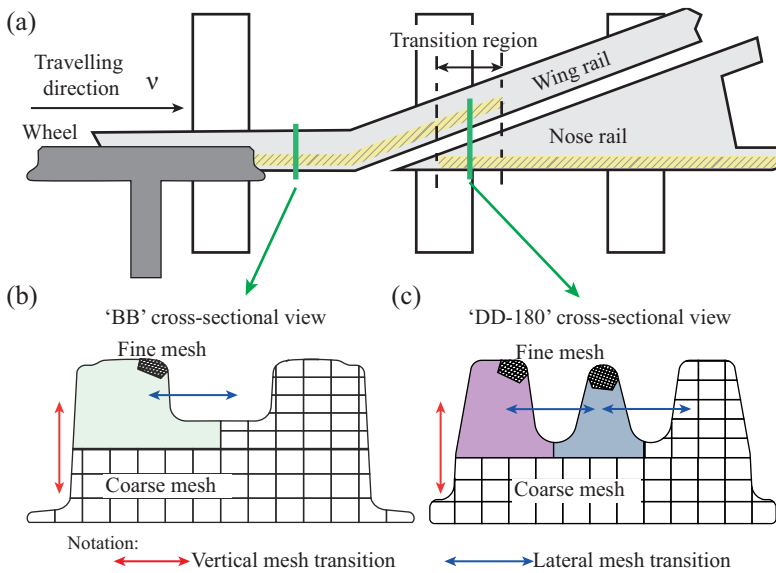


Figure 5.4: Schematic of mesh refining difficulties: (a) Top view of mesh transition (Notation: regions shaded with yellow colour & diagonal pattern indicate potential contact areas); (b) Mesh transition at 'BB' cross-section; (c) Mesh transition at 'DD-180' cross-section.

the FE mesh refinement. To make this strategy perform well, the data exchange between 2D-Geo and 3D-FE models is accomplished through an external MATLAB routine. Once the 3D-FE modelling and preloading processes are accomplished with the aid of the 2D-Geo model, the implicit-to-explicit sequential FE simulations are performed to analyse the contact behaviour of W/C dynamic impact. The details of the 2D-Geo analyses and the interfacing schemes of the coupling strategy are described in the later sections.

### 2D-GEO CONTACT MODEL

To better illustrate the 2D-Geo model, a 3D rigid wheel-set is given and positioned over a 3D solid crossing panel as shown in Figure 5.5a. The global coordinate system  $O$ -XYZ is consistent with the one shown in Figure 5.3.

The initial contact points, where the two particles on the un-deformed wheel and crossing rail coincide with each other, are determined under given lateral displacements ( $\delta y$ ) of the wheel-set. The contact searching procedure is non-iterative (i.e. no 'for/while' loops used) by taking advantage of efficient matrix operations in MATLAB. Figure 5.5b shows an example of the 2D-Geo contact analyses, in which the wheel-set is located at the "Just-in-contact" point with a lateral wheel displacement ( $\delta y$ ) of -10 mm.

### COUPLED INTERFACE & OUTCOME

Based on the 2D-Geo model and 3D-FEM model described above, the interface and outcome of the coupling strategy are presented below.

#### Refined area identification



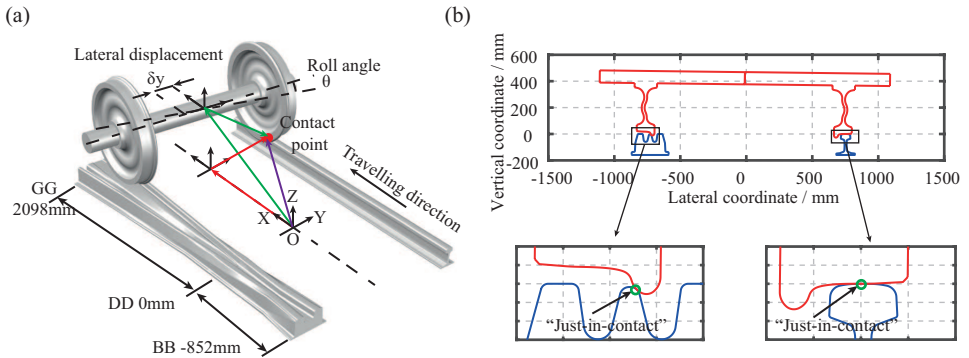


Figure 5.5: (a) 3D coordinate systems of W/C interaction; (b) “Just-in-contact” equilibrium condition of wheel and DD-180 cross-section at a lateral displacement of -10 mm.

Taking the cross-section DD-180 as an example, which is subject to a zero lateral displacement of the wheel-set (See Figure 5.6a1), the resulting contact clearance is shown in Figure 5.6a2.

Figure 5.6a1–a2 shows the double point contact, where the value of the contact clearances at the point of contact is almost zero. In order to implement the adaptive mesh refining technique, it is assumed that the most stressed area coincides with the initial contact point (CP). Moreover, the refined region on the contact bodies as indicated by the green highlights (See Figure 5.6b1–b3), is defined to start from the initial CP and expand to the two ends with a specified contact clearance, e.g. 2 mm.

Following the same working procedure as the case of cross-section DD-180, the refined regions of the other characteristic crossing profiles (See Figure 5.7a) are identified. The varying contact clearances, ranging from 0.5 mm to 2.0 mm, are prescribed on the basis of local contact geometries. The reason of selecting different contact clearances is to make the size of the potential contact areas wide enough to encompass the actual contact areas, which are strongly influenced by the varying local contact geometries and the amplified impact forces.

Figure 5.7b shows the 3D potential contact areas, which are located on the top of the crossing rail surface. The known relative position between the potential contact area and the crossing rail surface will lead to several separated solid volumes, which are further discretized by sweeping the mesh from adjacent areas through the volume as shown in Figure 5.7c. Figure 5.7d shows the cross-sectional view of the refined contact regions.

Regarding the mesh refinement on the wheel, it can be observed from Figure 5.8a that the regions on the 2D wheel profiles are varying correspondingly from the field side to the flange root, when the wheel is travelling from the characteristic cross-section BB to GG. Using the present FE modelling and meshing techniques, it is still challenging to generate a flexible 3D mesh refinement along the circumferential path of the wheel according to the varying refined regions. Thus, it is simplified into a uniform mesh, starting from the field side and ending up to the flange root as shown in Figure 5.8b. By this means, the wheel FE model (See Figure 5.8c) is capable of encompassing all the green highlighted potential contact areas.

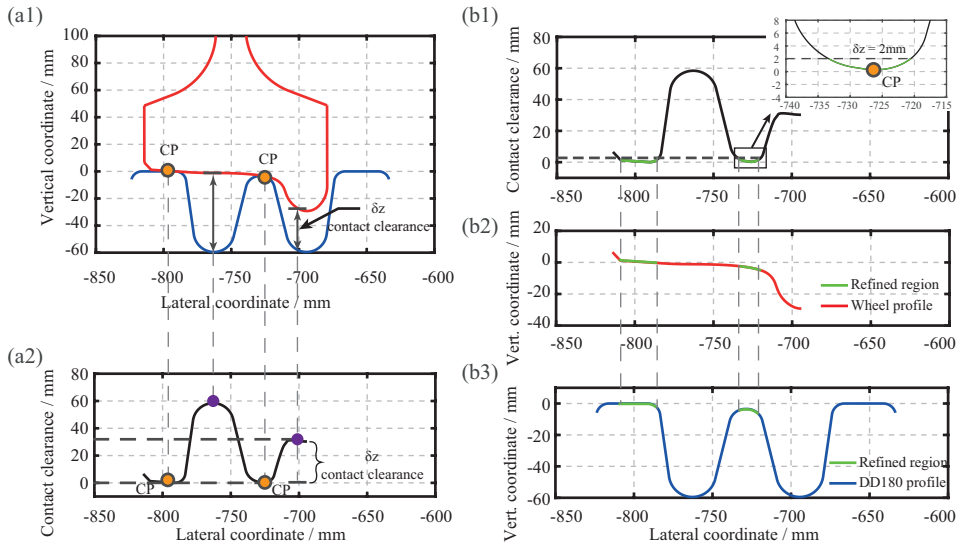


Figure 5.6: Working procedure of identifying refined potential contact area based on contact clearance: (a1) “Just-in-contact” equilibrium condition of wheel and cross-section DD-180 at a lateral displacement of 0 mm; (a2) Variation of contact clearance; (b1) Distribution of contact clearance ( $0 \text{ mm} \leq \delta z \leq 2 \text{ mm}$ ); (b2) Refined region on wheel profile; (b3) Refined region on rail cross-section DD-180.

Moreover, [Figure 5.7d](#) and [Figure 5.8b](#) show that the difficulties of transitions between the coarse and fine mesh patterns are addressed successfully. The coarse elements are split into three fine elements smoothly using the technique of “Local element refinement” [9].

### Resulting contact pair

For the explicit FE simulations (ANSYS LS-DYNA), a pair of contact segments, namely, master and slave segments for explicit FE analysis (target 170 and contact 173 elements for implicit FE analysis, See [Figure 5.9](#)), are required to track the kinematics of the deformation process. Here, the contact segments are the components of nodes on the out-most surface layer of the W/C contact bodies. The penalty method [7] is used to enforce the contact constraints, where a list of invisible “interface spring” elements are placed between all the penetrating slave segments and the master segments. Friction in LS-DYNA is based on the Coulomb formulation [7]. More information about the contact algorithms can be found in [7, 17].

### 5.2.3 EFFECTIVENESS OF ‘EFE-CS’ MODEL

In this section, the effectiveness of this ‘EFE-CS’ modelling approach is to be investigated. A comparative study on the performance of the two modelling approaches (i.e. ‘EFE-CS’ and ‘conventional’ model, See [Figure 5.10a-b](#)) is performed. The results of this comparative study are presented and discussed.

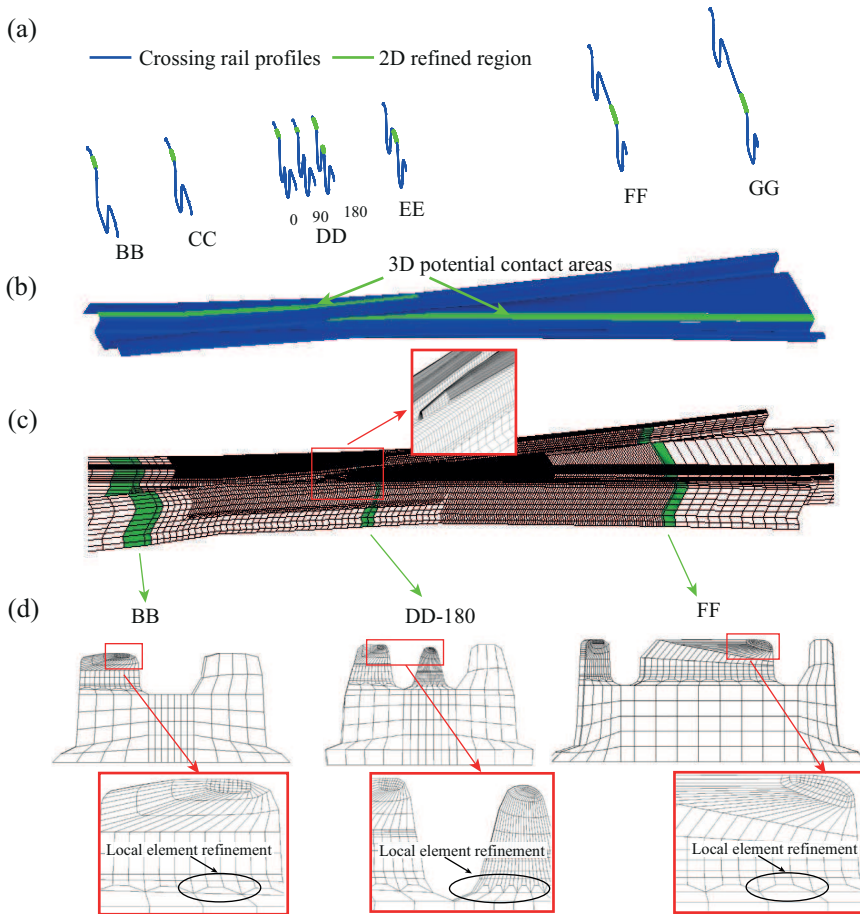


Figure 5.7: Adaptive mesh refinement on crossing rail: (a) Refined regions of 2D profiles; (b) Refined areas of 3D crossing surface; (c) Refined 3D FE model; (d) Cross-sectional view of refined contact regions.

#### SETUP OF COMPARATIVE STUDY

In the ‘conventional’ model (used as a reference case), the size of refined regions are selected in another way in comparison to the ‘eFE-CS’ model. Figure 5.10b shows that considerably large areas of contact surfaces are refined. Also, the advanced technique of ‘local element refinement’ is not used. The 3D FE models are generated through simple extruding and/or rotating operations on the 2D meshed cross-sectional areas. Such a conventional mesh refining technique is easy to implement and often used in the literature. The major difference between the ‘eFE-CS’ and conventional models lies in their performances (i.e. calculation efficiency, accuracy, flexibility of mesh refinement, etc.).

Both the same crossing rails (1:9–54E1) and the same wheel profiles (S1002) are used in the two models. Also, the same material properties of track components listed in Table 5.1 are adopted. The wheels are prescribed to run over the same rolling distance of 1.2m. The mesh sizes on the wheel and rail interface in the vicinity of the potential

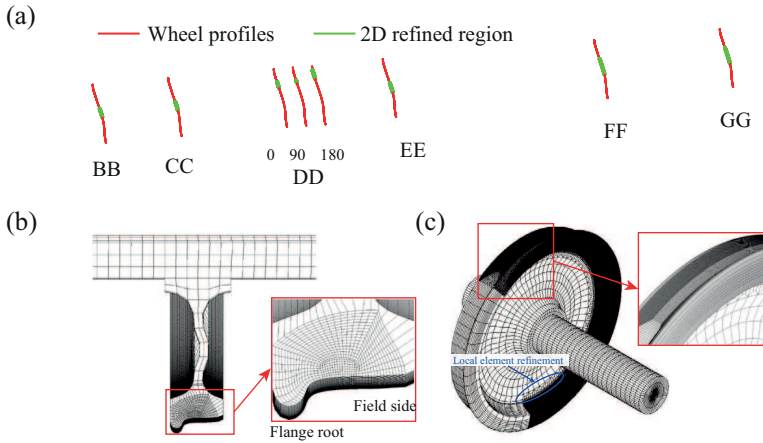


Figure 5.8: Adaptive mesh refinement on the wheel: (a) Refined regions of 2D wheel profiles; (b) Cross-sectional view of wheel mesh refinement; (c) Wheel mesh refinement along circumferential path.

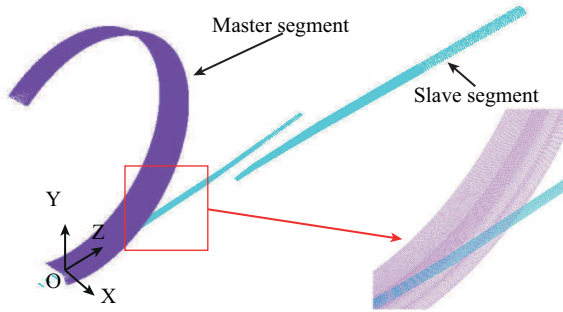


Figure 5.9: Isometric view of contact pair.

contact area are all limited to 1.0 mm.

The simulations are performed on a workstation with the same configuration as discussed in [Chapter 2](#). Such a setup of comparative study is to ensure that both models work in the same operational conditions.

### COMPARISON OF FE MODELS

Under the same modelling and/or operational conditions, the quantitative results of the two models are listed in [Table 5.2](#). It can be seen that the number of elements of 'eFE-CS' model is only 1,108,285, while the 'conventional' model has an increase of 33.8%. In the 'conventional' model, many warning/poor elements are induced by the mesh concentration at the wheel axle centre due to the rotating mesh operations (See [Figure 5.10b](#)). The amount of the poor elements are 12.62% more than that of 'eFE-CS' model. The minimum side length of the poor elements in the 'conventional' model is 0.12 mm, which makes the calculation time step size  $\Delta t_{calc}$  to be as small as  $2.45e-9$  second. It should be noted that the calculation time step size  $\Delta t_{calc}$  in ANSYS LS-DYNA is determined ac-

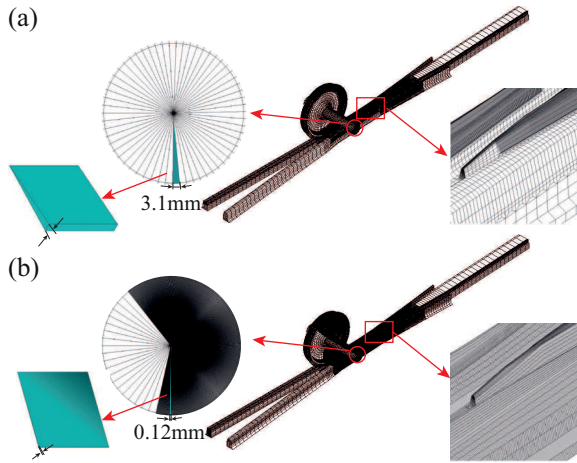


Figure 5.10: Comparison of FE models: (a) 'eFE-CS' model; (b) Conventional model (reference case).

5

ording to the minimum side length of the elements [7]. Such a calculation time step size  $\Delta t_{calc}$  is 5.93 times smaller than that of the 'eFE-CS' model. Consequently, the small calculation time step  $\Delta t_{calc}$  of the 'conventional' modelling approach manifests itself in the resulting prohibitive calculation expense  $T_{calc}$  (1128 hours), which is almost 16.63 times higher than that of 'eFE-CS' model (only 64 hours).

Table 5.2: Comparison of FE models.

Models	Number of elements	Warning/error elements	$\Delta t_{calc}$ <sup>a</sup> (/second)	$T_{calc}$ <sup>b</sup> (/hour)
'eFE-CS'	1,108,285	4.73%	1.7e-8	64
'Conventional' (reference case)	1,673,507	17.35%	2.45e-9	1128
Relative difference (w.r.t. 'conventional')	<b>-33.8%</b>	<b>-12.62%</b>	<b>5.93</b>	<b>-94.3%</b>

<sup>a</sup> : Calculation time step size; <sup>b</sup> : Calculation expense;

### COMPARISON OF IMPACT RESPONSES

Figure 5.11a-b show the vertical and longitudinal contact forces obtained from the FE simulations of the two models presented above. These dynamic contact forces are plotted versus the wheel travelling distance. It can be seen that the vertical contact forces vary around the applied axle load (100 kN) and hold constant on the straight path (around 100 mm long from the starting point of the wheel motion). After that, a noticeable force oscillation is observed. The reason of this force oscillation can be attributed to the geometrical change of the wing rail, which starts to diverge from a straight path to an inclined path (See Figure 5.11c). For the wheels of conical/worn treads, this causes vertical, downward movements of the wheels, which subsequently induce the oscillations of the contact forces. Taking the wheel contact position at CC cross-section (denoted by a

green line) as a reference, it can be clearly seen that the wheel starts to dip downward gradually with a couple of centimetres as it runs further on the inclined wing rail. The downward movement of the wheel (See [Figure 5.11c-d](#), according to the 2D-Geo contact analyses) leads to the oscillations of contact forces. It is shown in [Figure 5.11a-b](#) that the amplitudes of these contact forces are reducing within the next metre, which are mainly caused by energy dissipation in the vertical damping elements of the wheel and the crossings bedding [30].

As the wheel gets into the location of 180 mm away from the nose point, it can be observed from [Figure 5.11c-e](#) that the wheel dips downward into its maximum (1.782 mm). After that, the wheel starts to climb upward onto the nose rail, where the sudden strike of the wheel on the crossing rail occurs. The dynamic impact force (around 216 kN) is amplified to almost 2.2 times larger than the applied wheel load (100 kN). It can be noticed that the change of the dynamic forces agrees reasonably well with the change of the vertical wheel movement. In other words, the wheel ‘sink-lift’ movement [1] implies the dynamic force oscillations. Such dynamic impact phenomena observed agree reasonably well with the results presented in [22, 30], where it find more that both the wheel dip depth and angle can strongly influence the impact event.

It can also be seen from [Figure 5.11a-b](#) that the variation of the dynamic contact forces obtained from the two simulations are similar to each other. The impact events manifest themselves with a peak value on contact forces at the same location. The value of the maximum impact forces obtained is 216.3 and 195.9 kN respectively (See [Table 5.3](#)). The maximum impact force estimated by ‘eFE-CS’ model is 10.4% higher than that of ‘conventional’ FE model.

[Figure 5.12](#) shows the distribution of Von-Mises stress at the location, where the maximum impact force occurs. It can be seen that the contact patch firstly runs only on the wing rail and then it starts to shift onto the nose rail. Two discontinued residual stress areas are left on both the wing and nose rails, which implies the on-site running bands (more discussion in [Section 5.3.1](#)). Also, the distribution of the Von-Mises stress obtained using the two modelling approaches shows similar pattern. The maximum value of the Von-Mises stress is 1199 and 1044 MPa, respectively. The relative difference of the maximum Von-Mises stress is 14.8% (See [Table 5.3](#)).

These differences shown in the results might be attributed to two factors:

- Different calculation time step sizes (See [Table 5.2](#)): For the transient dynamic analyses, it is widely recognised [9] that the accuracy of solution depends on the calculation time step: the smaller the time step, the higher the accuracy. From this point of view, the accuracy of FE results obtained from the ‘conventional’ model ( $\Delta t_{calc} = 2.45e-9$ ) should be higher than that of ‘eFE-CS’ model ( $\Delta t_{calc} = 1.7e-8$ ). However, it is not always the case to have the small time step size, since exceedingly small time step size (e.g. that of ‘conventional’ model) wastes valuable computer resources and causes numerical difficulties. Moreover, it is worth noting that the accuracy of the results would not increase any more with decreasing time step sizes, if the time step size is sufficiently small.
- Presence of poor-quality elements (due to the effect of mesh discretization, See [Figure 5.10](#)): The element shape checking (See [Table 5.2](#)) shows that the ‘conven-

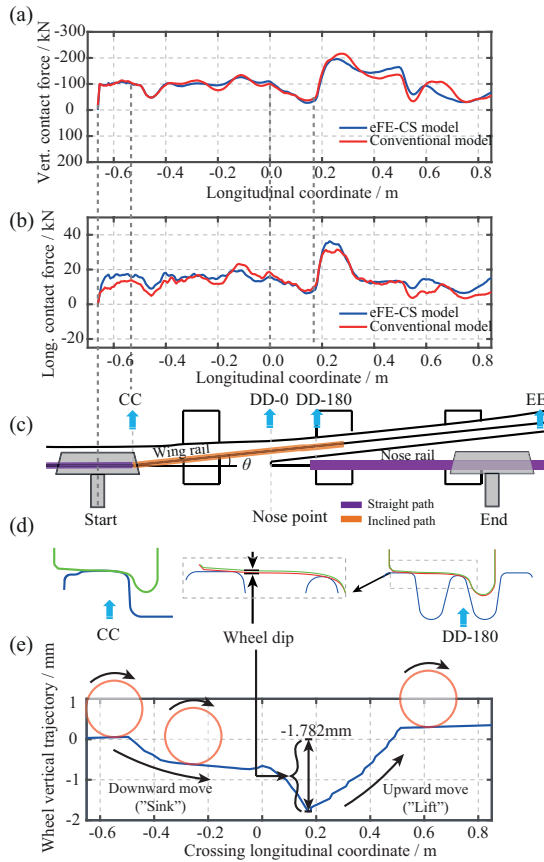


Figure 5.11: Comparison of contact forces: (a) Variation of vertical contact force w.r.t rolling distances; (b) Variation of longitudinal contact force w.r.t rolling distances; (c) Schematic of W/C interaction; (d) Close-up view of ‘wheel-dip’; (e) Vertical wheel trajectory determined by 2D-Geo contact analyses.

ventional’ model has a much bigger (17.35%) population of poor/warning elements than the ‘eFE-CS’ model (only 4.73%). The presence of those “badly shaped” elements might adversely affect the accuracy of FE simulations and thus cause the discrepancies in the results.

Considering the prohibitive calculation expense of ‘conventional’ modelling approach (due to the exceedingly small time step size, See Table 5.2), it can be summarised that the ‘eFE-CS’ modelling approach performs better than the ‘conventional’ one.

#### 5.2.4 DISCUSSION: PROS OF ‘EFE-CS’ MODEL OF W/C IMPACT

The two computational models/programmes (namely, 2D-Geo contact model and 3D FE model), which are often used separately to fulfil different engineering purposes, are seamlessly coupled together. The presented coupling strategy does not simply refer to the two programmes themselves, but more means the data exchange and interfacing

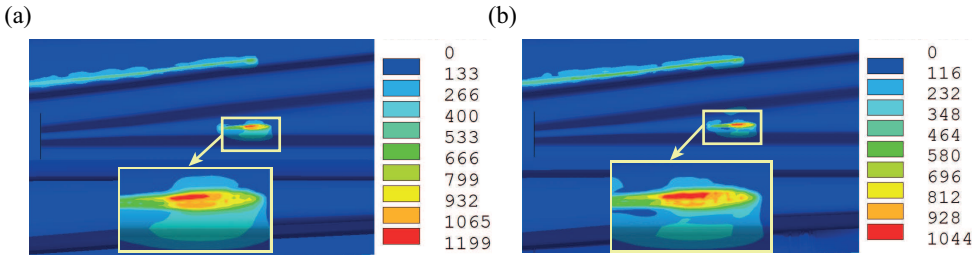


Figure 5.12: Comparison of Von-Mises stress (Unit: MPa) at most 'impact' moment: (a) 'eFE-CS' model; (b) Conventional model.

Table 5.3: Comparison of impact responses from two models.

Models	$F_{impact}^{max}$ <sup>a</sup> kN	$\sigma_{vms}^{max}$ <sup>b</sup> MPa
'eFE-CS'	216.3	1199
'Conventional' (reference case)	195.9	1044
Relative difference (w.r.t. 'conventional')	<b>10.4%</b>	<b>14.8%</b>

<sup>a</sup> : Maximum impact forces; <sup>b</sup> : Maximum Von-Mises stress;

mechanism between them. The effectiveness of the developed 'eFE-CS' model has been demonstrated through a comparative study. Based on the outcome of those coupling operations and the FE simulation results, the advantages of this coupling strategy are summarised as follows:

- General modelling challenges (See Section 5.2.1): The unwelcome "Gaps / Penetrations" at the beginning of the W/C contact modelling have been significantly reduced into a tolerable level by positioning the wheel exactly onto the "Just-in-contact" point of the crossing rail. It can be learned that the 'eFE-CS' strategy can work not only well for the cases of wheel-rail interaction [17–19] but also effectively for the analyses of dynamic impact between wheel and crossing.
- Specific modelling difficulties (See Section 5.2.1): Using this coupling strategy, the two 'separate' potential contact areas on both the wing and nose rails are identified and refined properly. Also, the "Local element refinement" enables the smooth transitions between the bonds of coarse and fine mesh in both the lateral and vertical directions.
- Improved calculation efficiency: The number of FE elements in the 'eFE-CS' model has been significantly reduced in comparison with that of the 'conventional' model, which can greatly save the memory space. The minimum side length of the elements has been increased a lot, which will maintain a relatively large calculation time step. Thus, the calculation efficiency has been significantly improved.
- Good calculation accuracy: The deviations of FE simulation results obtained from the two models are relatively small. It implies that the 'eFE-CS' model can produce as accurate results as the 'conventional' FE model. Also, the amount of the



poor/warning elements is reduced and the elements having good quality are guaranteed.

To sum up, the 'eFE-CS' modelling approach with application to the analysis of dynamic impact in a 1:9 railway crossing panel is effective. The proposed coupling strategy is a nice assistant in advancing the FE modelling of W/C dynamic impact. Also, the 'eFE-CS' strategy is not limited to contact modelling in the railway community, but also recommended to use in other mechanical contact/impact systems having complex local contact geometries (e.g. gear, worn bearing, etc.). The limitations/cons of the present 'eFE-CS' model and its further improvement are discussed later in [Chapter 6](#).

### 5.3 EXPERIMENTAL VALIDATIONS

In this section, the transition regions (Definition, See [Section 5.1](#)) estimated by the 'eFE-CS' simulations are compared firstly with the field measured ones, which are further extended from the authors' former work [23]. Furthermore, the crossing accelerations determined by the FE simulations are compared with the measured ones using the on-site acceleration measurement device.

#### 5.3.1 MODEL VALIDATION VIA TRANSITION REGIONS

To evaluate the accuracy of the transition region predicted by the 'eFE-CS' model, the transition regions measured from the field are collected and compared. Also, the transition region estimated by the 2D-Geo contact analyses is used for comparison.

##### FIELD MEASURED TRANSITION REGIONS

[Figure 5.13a-b](#) show the measured transition regions at the field. It can be seen from [Figure 5.13a](#) that the transition process starts at 180 mm away from the nose point and ends at 300 mm. The overall length of the transition region (also called transition distance) is approximately 120 mm. After more than one year's service, the start point of the transition region shifts around 20 mm towards the nose point, while the end point moves 20 mm away from its original location. The resulting transition distance expands to 160 mm long. It should be noted that during the period between measurement 1 and 2, there are several operations of welding and grinding performed to eliminate the surface defects (e.g. the one shown in [Figure 5.1d](#)) on the crossing rail.

##### FE SIMULATED TRANSITION REGION

To predict the transition region, the areas of residual Von-Mises (also called 'equivalent/effective') stress/strain are suggested to use as an indicator. Here, the term of 'residual' is referred to as the stresses/strains that are locked/frozen in the W/C contact bodies after the original cause of contact stresses has been removed (i.e. the wheel has rolled over the crossing rail).

The choice of Von-Mises stress/strain (as opposed to many other potential important stress/strain measures) is based on the complexity of contact loadings, which are multi-axial (i.e. mix of large normal and shear stresses) and non-proportional. Only one independent component of stresses/strains (e.g. contact pressure, shear stress, etc.) might

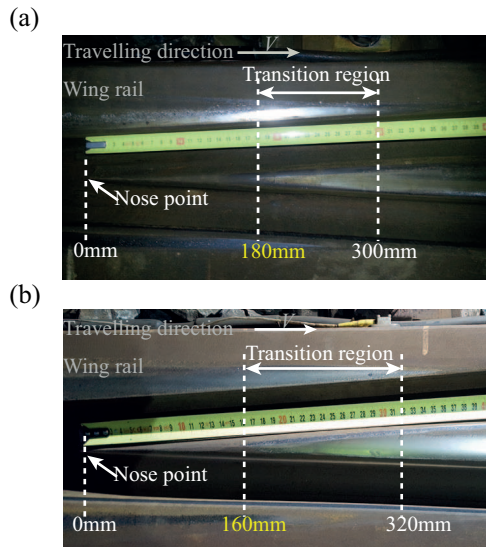


Figure 5.13: Field measured transition regions (photos taken by Y. Ma): (a) Measurement 1 (14/December/2015); (b) Measurement 2 (around one year later, 06/February/2017).

be insufficient to represent such loading conditions and to ensure the accurate prediction of transition regions.

It should be noted that this suggested area of residual Von-Mises stresses/strains might not always yield the perfect indication of transition regions for all kinds of loading conditions (e.g. at low contact load, no yield or plastic deformation occur but wear still exists). But it suits well to the study of dynamic impact at 1:9 crossing panel, since the resulting stresses substantially exceed the yield strength of the material (See Section 5.4).

Figure 5.14 shows the distribution of Von-Mises stress and plastic strain, which are determined by the 'eFE-CS' simulations. The two plots are captured at the same moment. The regions at the far right side of each plot indicate that the wheel is standing on the top of the crossing rail. The remained areas show the distribution of residual stresses/strains.

The transition region begins at approximately 180 mm far from the nose point. After 43 mm away from the starting point, the transition region ends. The maximum value of the plastic strain is as large as 3.5%, while the maximum residual stress is 825 MPa.

#### 2D-GEO ESTIMATED TRANSITION REGION

Figure 5.15a shows a number of crossing rail profiles, which are located at arbitrary locations along the track. They are generated by longitudinally interpolating the two adjacent characteristic cross-sections (as shown in Figure 5.2). Based on the interpolated profiles of crossing rail, the transition region can also be predicted using the 2D-Geo contact model (as described in Section 5.2.2).

Figure 5.15b shows that the transition region also starts at a point which is 180 mm far away from the nose point. The estimated transition distance is as short as 25 mm.

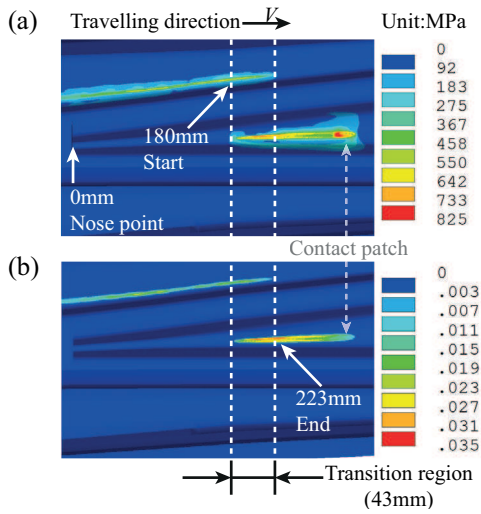


Figure 5.14: Variation of transition region determined by explicit 3D FE analysis: (a) Von-Mises stress; (b) Von-Mises plastic strain.

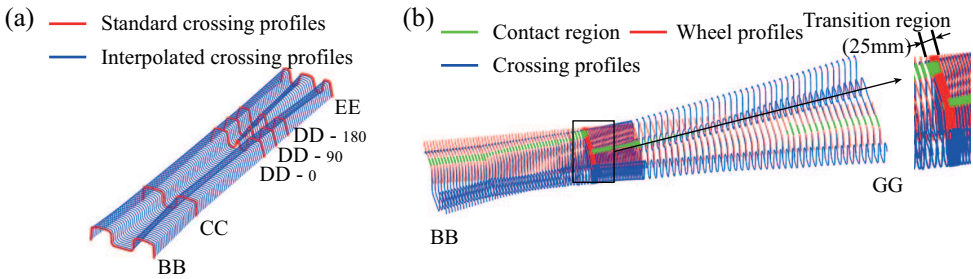


Figure 5.15: Variation of transition region determined by 2D-Geo contact analyses: (a) Interpolated cross-section profiles between characteristic cross-sections; (b) Close-up view of transition region.

COMPARISONS AND DISCUSSIONS

Table 5.4 lists the results of comparison of the transition regions. A good agreement on the estimated start points of the transition region is observed. However, for the end position of the transition region, the FE result deviates much from both the 2D-Geo estimated results and the field measurements. It ends later than the estimation of 2D-Geo analyses, but much earlier than the field measurement.

The discrepancies between the FE-estimated transition region and the corresponding field measured data are explainable, since the present ‘eFE-CS’ simulations are only focusing on standard and undeformed wheel & crossing rail profiles. Also, no lateral shifts and yaw motions of the wheel are considered in the FE model.

However, in reality, the wheel/crossing rail profiles of different conditions (i.e. degraded, improved/repared, newly replaced interfaces, etc.) are in use. The relative positions of the wheel-sets vary commonly during the process of W/C dynamic impact. In addition, the field measured transition regions are formed after multiple wheel passages,

Table 5.4: Comparison of transition regions.

	Transition region <sup>*</sup> /mm		Transition distance /mm
	Start	End	
'eFE-CS' simulation	180	223	43
Measurement 1	180	300	120
Measurement 2	160	320	160
2D-Geo estimation	180	205	25

<sup>\*</sup>: 0 mm is referred to as the nose point.

while the FE prediction only represent one wheel passage. All these uncertainties and/or variabilities can proactively affect the evolution of the contact patch and further on the transition region.

With respect to the prediction of 2D-Geo contact analyses, the discrepancies to the FE-estimated transition region are small but still distinguishable. In the 2D-Geo contact analyses, two contact bodies are assumed to be rigid (i.e. no elastic and/or plastic deformations). The double point contact, which indicates the transition region, is determined on the basis of the prescribed tolerance (i.e. as small as 0.1 mm). Regarding the 3D-FE contact analysis, the elastic-to-plastic material behaviour is considered. Also, the transition region is indicated by the area of residual stress. Such differences explain the discrepancies observed.

The comparative study shows that the FE-predicted transition region is in good correlation with that of measurement. It demonstrates that the proposed 'eFE-CS' model is capable of simulating the W/C dynamic impact accurately.

### 5.3.2 MODEL VALIDATION VIA CROSSING ACCELERATIONS

In this section, a general introduction of the acceleration measurement device is given first. Following that, a detailed comparison between the field measured and FE simulated accelerations is made.

#### MEASUREMENT DEVICE: ESAH-M

Figure 5.16 shows the general working scheme of the measurement device ESAH-M (Elektronische System Analyse Herzstijckbereich – Mobil) in the field. Basically, there are four main components involved [21, 32]:

- (1) Two inductive sensors (called 'BERO'): to detect the number of running wheel axles and determine the associated train velocities;
- (2) One magnetic triaxial acceleration sensor: to measure the accelerations of the crossing rail in three dimensions;
- (3) One sleeper displacement sensor (Optional): to record the vertical displacements of a sleeper optionally;
- (4) One main battery powered unit: to process (i.e. receive, synchronise, save and transit) all the acquired field data (including the train velocities, sleeper displacements, crossing accelerations, etc.).

The measurement range of the accelerometer is 500g. The sampling frequency of acceleration measurement device is 10kHz. To make a reasonable comparison of the FE acceleration signal with the measured acceleration signals (400 axle of 21 trains), only the cases of regular contact are studied. The remaining cases of irregular contact are excluded from current comparison, since the present FE model focuses on the cases of regular contact. The statuses of regular and irregular contact (See more information in [16, 21, 32]) are detected according to the direction and the magnitude of the measured accelerations.

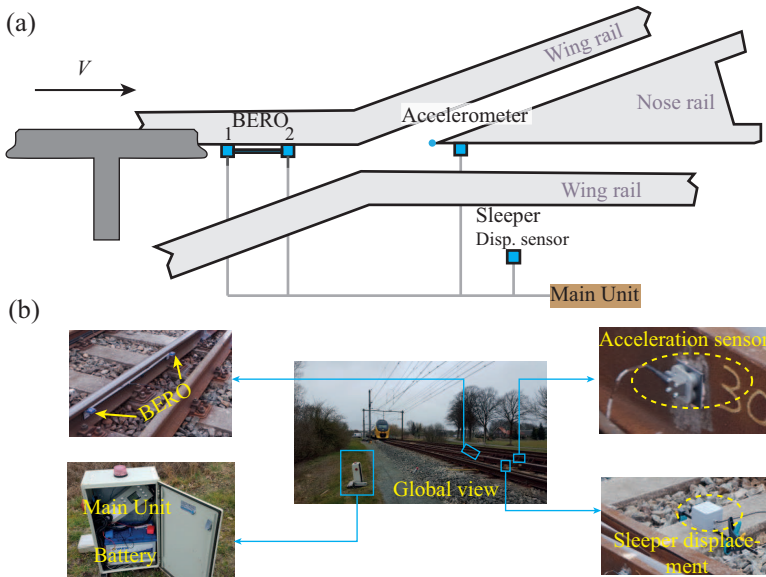


Figure 5.16: (a) Schematic of ESAH-M acceleration measurement; (b) Global and close-up views of ESAH-M measuring device at the field (photos taken by V. Markine, the one of 'global view' is shared by X. Liu).

#### FE SIMULATED ACCELERATION

Figure 5.17 shows an example of FE simulated crossing acceleration. The FE-based accelerations are extracted from a group of selected nodes (See Figure 5.17a), which are located at the same position as the acceleration sensor of ESAH-M (See Figure 5.17b). This ensures the comparability of acceleration sources.

To accurately describe the FE acceleration signal, 2000 sampling time points are selected. The resulting sampling frequency, which is the ratio between the number of the sampling points (2000) and the calculation time (0.044s), is around 45kHz. The maximum acceleration amplitude is around 38g.

#### RESULTS OF COMPARISON

Figure 5.18 shows the comparison of the FE simulated accelerations with those measured from the field. The measured accelerations of more than 85% axles (169 out of 197), which are in regular contact, are plotted in grey. The reason of not using all the measured acceleration signals of regular contact is to exclude the faulty signals [32], which

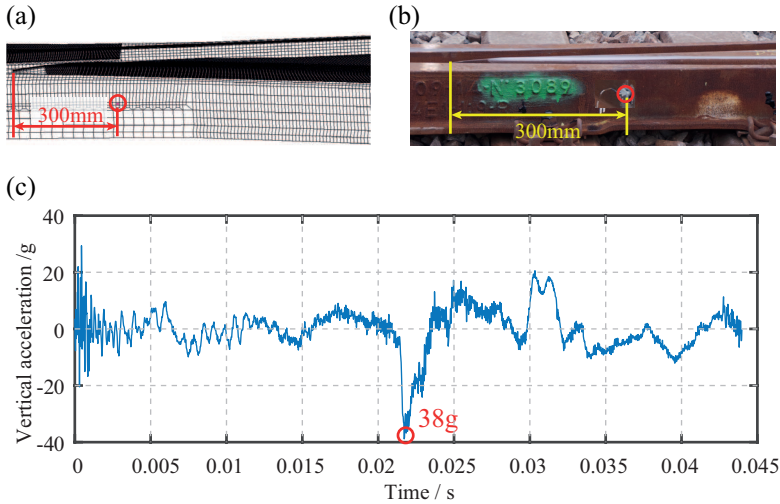


Figure 5.17: Example of FE simulated acceleration: (a) Nodes to extract FE simulated accelerations; (b) Location of acceleration sensor at the field; (c) FE simulated vertical acceleration.

are automatically detected by the ESAH-M programme itself. The measured mean acceleration is plotted in green. It can be seen that the variations of both the measured and FE simulated accelerations follow the “V” pattern. Such a “V” pattern is in good relation with the ‘sink-lift’ movement of the wheel vertical trajectory (See Figure 5.11e) as well as the oscillation of vertical contact forces (See Figure 5.11a).

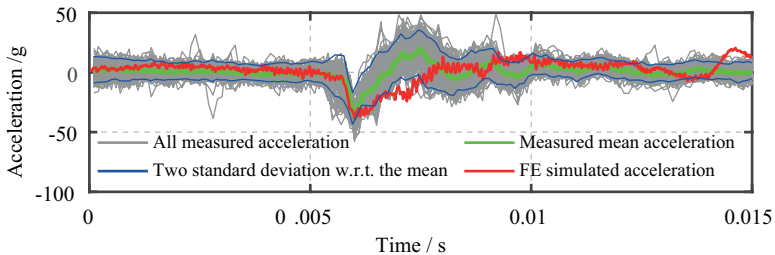


Figure 5.18: Comparison of FE simulated acceleration with measured ones in time domain.

Figure 5.19a shows the results of the statistical analysis on the maximum amplitudes of the measured accelerations. The number of the occurrences of maximum accelerations is plotted at an interval of 1g (e.g. 20g-21g, 21g-22g, and so on). Ultimately, all these measured accelerations are categorised and visualized by bars in a histogram.

The resulting histogram has a normal distribution (bell-shape) as shown in Figure 5.19a-b. The mean  $\mu$  of this normal distribution is 37.89g, while the standard deviation  $\sigma$  is 7.61g. In Figure 5.19b, the area of dark blue-grey implies one standard deviation from the mean, which accounts for 68.3% of this sampling population. The area of two standard deviations with respect to the mean accounts for 95.5%. Figure 5.18 shows the measured

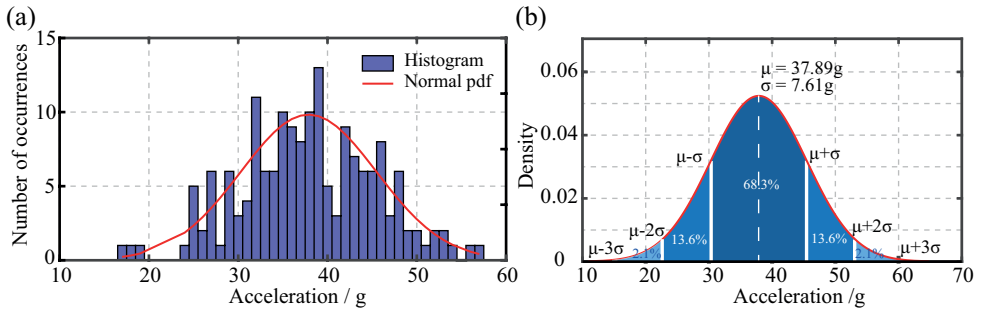


Figure 5.19: Statistical analysis on maximum amplitudes of measured accelerations: (a) Histogram; (b) Normal distribution.

mean and a band representing two standard deviations from the mean. It can be noticed that the magnitude of the FE simulated acceleration (38g, See [Figure 5.17c](#)) exactly falls within the range of the two standard deviation from the measured mean. To summarize, the FE simulated acceleration agrees reasonably well with the ones from acceleration measurements.

5

#### DISCUSSION: SOURCE OF DISCREPANCIES

The sources of these discrepancies might be categorised into three groups, namely the different operational patterns, track parameters and FE model capability:

- (1) Operational patterns: The FE simulation is performed with a nominal operational pattern (i.e. train speed, axle load, traction, etc.), in which these operational parameters are prescribed to determined values as shown in [Table 5.1](#). In reality, the operational patterns are uncertain. The parameters such as, train speeds, axle loads, traction forces, wheel profiles, etc. strongly depends on the type/condition of vehicles. The difference of operational patterns might change the distribution of transition regions and cause the variation of accelerations.
- (2) Track parameters: The degradation and/or maintenance (i.e. grinding, welding, etc.) of W/C interfaces will change the local contact geometries. The components of substructure will degrade (e.g. sleeper, ballast settlement, gaps between sleepers and ballast, etc.) and have to be maintained in time. The variation of track properties (i.e. mass, stiffness, damping, etc.) will lead to the distinguishable discrepancies.
- (3) FE model capability: The present FE model is capable of simulating the single wheel-crossing interaction. But it is still far from the real case of complete vehicle-track interaction. As a result, the influence of the second wheel (i.e. the one on the stock rail) and bogies on the impact phenomenon might not be fully considered.

Although the tolerable deviations of the impact signals exist, the FE simulations results agree reasonably well with ESAH-M measurements. It also implies that the FE model is promising to be used to simulate the W/C dynamic impact.

## 5.4 FE SIMULATION RESULTS AND DISCUSSIONS

Using the validated FE model, a series of FE simulations are performed. In this section, the FE results including both the surface and subsurface contact properties are presented. These contact properties are usually captured at a relatively large number (e.g. 2000) of time points all through the explicit FE simulation. Here, the term ‘time points’ relates to the variation of contact locations along the crossing rail. Figure 5.20 shows the variation of contact forces with respect to different time points (i.e. the equivalent of different contact locations). It can be seen that only the contact properties at the specified time points ranging from “A” to “H” are extracted, since the corresponding impacts are most significant at the vicinity of the transition region.

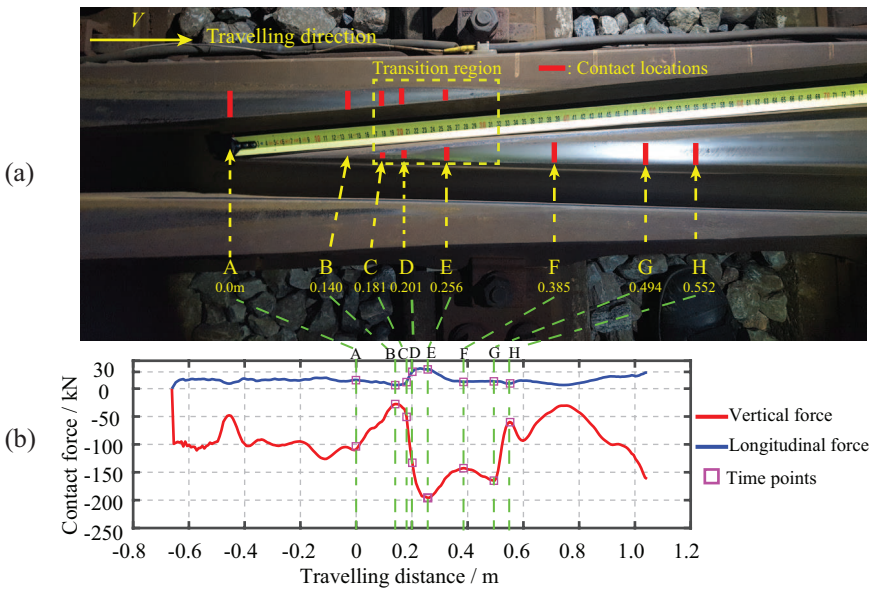


Figure 5.20: Schematic of time points (i.e. contact locations ranging from ‘A–H’) to extract contact properties: (a) Corresponding contact locations on crossing rail; (b) Variation of contact forces at specific time points.

### 5.4.1 SURFACE STRESS RESPONSE

As mentioned above, the surface contact properties are only extracted at the specified time points shown in Figure 5.20. The distribution of normal pressure, shear stress, slip-adhesion areas, etc., is presented.

#### NORMAL PRESSURE

The contact patches from the FE analyses are determined according to the normal contact pressure [46]:

$$\text{A node is in contact if: } \sigma_n > 0 \quad (5.1)$$

where  $\sigma_n$  is the nodal pressure in the direction normal to the local contact surface. Figure 5.21 shows the contour plots of the normal pressure distribution at the selected time



points. In order to better demonstrate the distribution of surface contact pressure, the compressive pressure is treated as positive. It can be seen that all the resulting contact patches are non-elliptical. Also, at the time points of “C” and “D”, double contact patches are observed, which manifest themselves in practice as the collateral running bands on both the wing and nose rails.

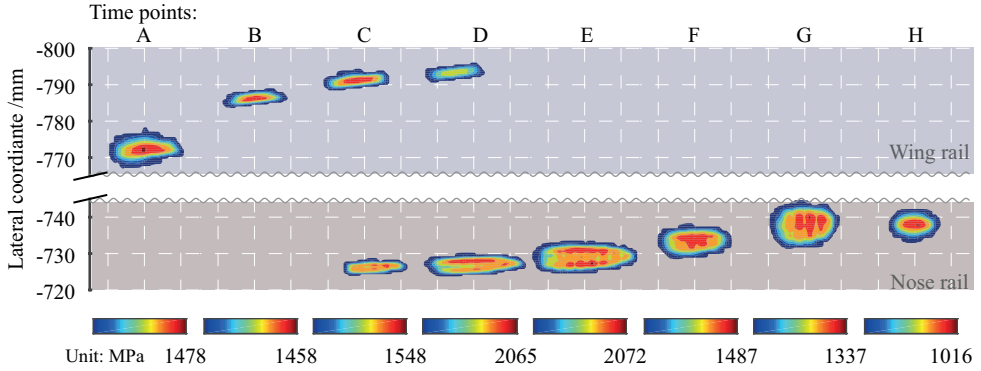


Figure 5.21: Surface normal pressure distribution.

Table 5.5 lists the results of the normal pressure and the contact patches. The maximum normal pressure obtained at the time point “E” amounts to 2072 MPa. That is 96.4% higher than the one in the case of normal wheel-rail interaction [17].

Table 5.5: Comparison of the contact solutions at different time points.

	W/C impact at different time points								Normal W/R interaction[17]
	A	B	C	D	E	F	G	H	
Contact status <sup>a</sup>	1	1	2	2	1	1	1	1	1
$\sigma_n^{max}$ / MPa <sup>b</sup>	1478	1458	1548	2065	2072	1487	1337	1016	1055
$\tau^{max}$ / MPa <sup>c</sup>	326	423	460	542	451	279	262	278	260
$A_c$ / mm <sup>2</sup> <sup>d</sup>	156.2	64.8	154.3	298.5	215.2	154.8	202.0	105.0	256.5

<sup>a</sup>: Number of contact patches; <sup>b</sup>: Maximum normal pressure; <sup>c</sup>: Maximum shear stress; <sup>d</sup>: Area of contact patch.

Under such a high impact loading condition, it is found that the relative difference of the contact area between the solutions of normal wheel-rail and wheel-crossing interaction is also big (See Table 5.5 -74.7% in the time point “B” and 16.4% in the time point “D”). This clearly shows the effect of varying crossing geometry on the contact properties.

**SHEAR STRESS**

Once the normal contact is established, the imposed driving (or braking) torque leads to the relative difference between the rolling velocity and longitudinal velocity. Accordingly, the wheel exhibits a slip in the direction opposite (or parallel if braking) to the travel of vehicle. The friction in the tangential direction builds up to resist the relative motion between two contact bodies.

Depending on the magnitude of the applied traction (i.e. driving torque), the statuses of contact can be classified into partial slip (or slip-adhesion) and full slip (sliding). In the state of partial slip, the applied traction is smaller than the frictional force. With the increase of the applied traction, the slip region spreads forwards from the leading edge of the contact patch until the slip zone reaches the leading edge and full slip occurs [11]. At the point of transition from partial slip to full slip, the traction is equal to the frictional force. In general, the traction is limited by the friction and is sometimes called the utilized friction [34]. To focus the attention on the partial slip contact (i.e. commonly occur in the process of wheel-rail interaction), the coefficient of friction is assumed to be 0.5 and the coefficient of traction is 0.25. The value of these two operational parameters is adapted from [36, 46], where the maximum tractive effort of the locomotives is considered. Note that the model can easily be adjusted for other operational parameters (See [17]). More information about the friction coefficient and the applied traction can be found in Table 5.1.

Figure 5.22 shows the distribution of shear stress on the surface of crossing rail. These shear stresses are captured at the same moment as the contact pressure. For both cases, the major portion of the shear stress is located at the rear part of the contact patch.

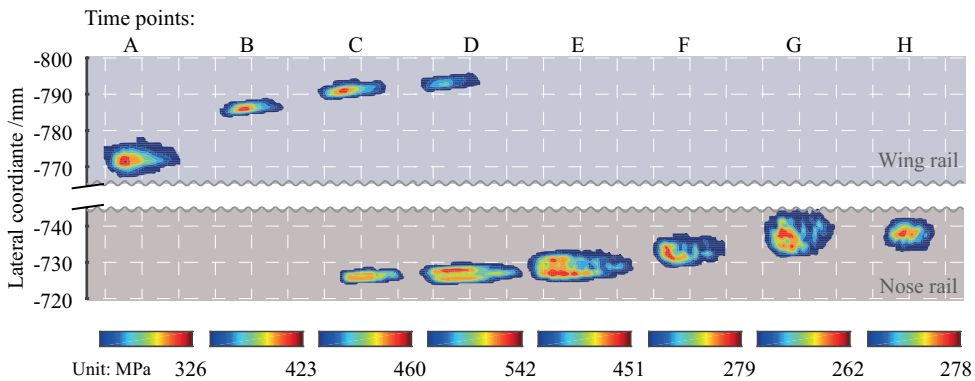


Figure 5.22: Surface shear stress distribution.

The maximum shear stress is 542 MPa (Time point: 'D'), which is 108.5% higher than the one in the case of wheel-rail interaction (260 MPa) [17]. These high shear stresses indicate the high risk of surface damages on the crossing rail (See Figure 5.1).

#### SLIP-ADHESION PHENOMENA

Under the condition of partial slip, the contact area is divided into two regions of slip and adhesion [12]. However, the division of contact area is not known in advance and must be found by trial [11]. Following the well-established criterion described in [35, 46],

$$A \text{ node is in adhesion if } : \mu |f_{n_N}| - |f_{n_T}| > \varepsilon_T \quad (5.2)$$

the phenomena of slip-adhesion can be explored. Here,  $f_{n_N}$  is the nodal normal force,  $f_{n_T}$  is the nodal tangential force in the longitudinal direction, and  $\varepsilon_T$  is the tolerance

for distinguishing the slip and adhesive areas. The magnitude of  $\varepsilon_T$  is prescribed to be the 10% of the maximum traction bound force [17].

It should be noted that the effectiveness of the tolerance suggested has been assessed in the authors' previous work [17], where verifications of varying operational patterns (i.e. applied traction, friction coefficient, etc.) against CONTACT have been performed extensively. The results show that such a tolerance fits well to the case of FE-based W/R contact analysis under the consideration of realistic profiles.

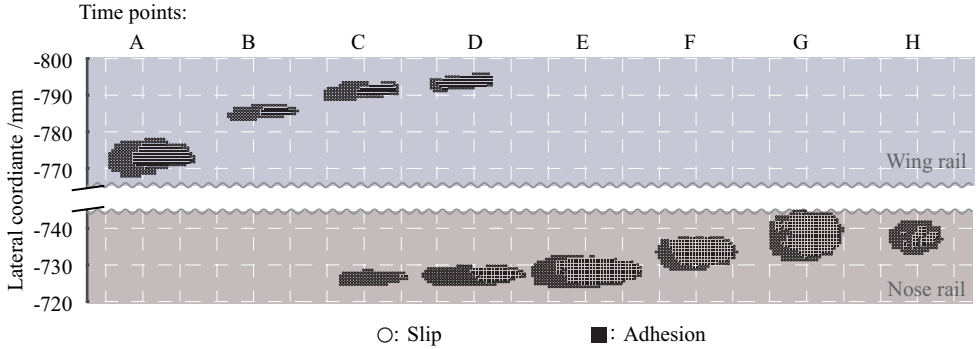


Figure 5.23: Slip-adhesion area plot.

Figure 5.23 shows the distribution of slip-adhesion area according to Equation 5.2. As it can be observed, the leading areas of all the contact patches are in adhesion, whereas the trailing areas are in slip. Such an observation conforms well with the classical frictional rolling contact theories [11, 12]. The relationship between the obtained contact properties and surface degradation will be discussed later in Section 5.4.3.

#### 5.4.2 SUBSURFACE STRESS RESPONSE

To check the stress responses on the sub-surface, two orthogonal sliced planes, namely “AA” and “BB”, are introduced as shown in Figure 5.24b & Figure 5.25b. “AA” is sliced at the initial contact point along a longitudinal-vertical plane, while “BB” is located at the same point but along a lateral-vertical plane. The stresses mapped on the two cutting surfaces are presented in this section.

##### VON-MISES STRESS

Generally, Von-Mises stress is adopted as a measure of material performance assessment under specific contact conditions for elastic-plastic material. Thus, the most critical moment, when the Von-Mises stress reaches peak value (Time point: ‘E’) at a distance of 223 mm away from the crossing nose point, is examined as shown in Figure 5.24a-b.

It can be seen that the maximum Von-Mises stress of 1197 MPa is far above the yield limit (480 MPa) of the materials. Such a high stress concentration is attributed to the relatively small size of the contact patch as well as the amplified impact loads. Figure 5.24c-d show that the maximum Von-Mises stress is concentrated at a small volume of material, which is ranging from the rail top surface to 2.0 mm beneath.

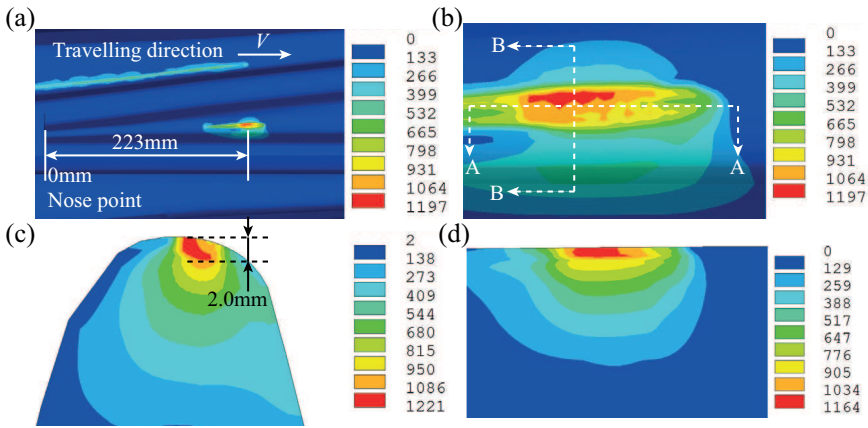


Figure 5.24: Distribution of subsurface Von-Mises stress (Unit: MPa): (a) Global view; (b) Close-up view; (c) Von-Mises stress on cutting plane “BB”; (d) Von-Mises stress on cutting plane “AA”.

SHEAR STRESS

Figure 5.25a-b show the global view and close-up view of the shear stress in the longitudinal direction. As the wheel rolls, it can be seen from “AA” cutting plane as shown in Figure 5.25d that tensile shear stresses are created at the rear of the contact patch and compressive shear stresses at the front of the contact patch. For the shear stress mapped on the “BB” cutting plane as shown in Figure 5.25c, the shear stress is more concentrated on the right side of the nose rail than on the left side. This phenomenon can be caused by the unsymmetrical contact angle between wheel and crossing contact geometries.

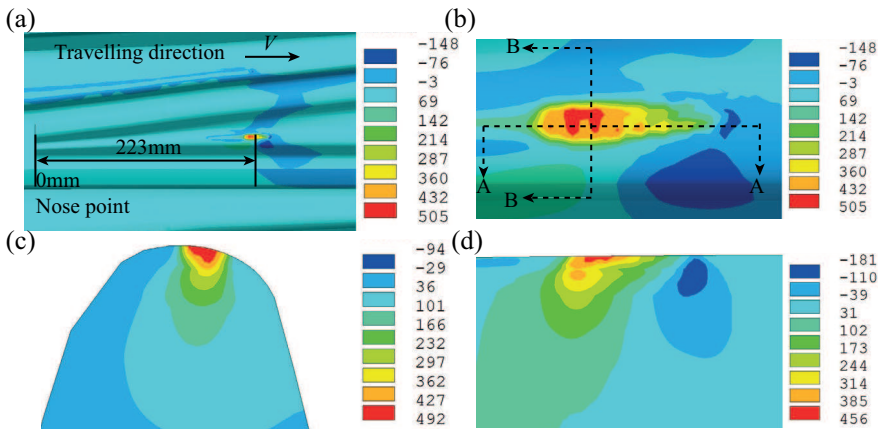


Figure 5.25: Distribution of subsurface shear stress (Unit: MPa): (a) Global view; (b) Close-up view; (c) Shear stress on “BB” cutting plane; (d) Shear stress on “AA” cutting plane.

### 5.4.3 DISCUSSIONS OF RESULTS

The studies on the surface & subsurface stress responses demonstrate the influence of the dynamic impact on the material responses. Based on the FE simulation results, the causes of the rapid crossing surface degradation are discussed.

#### CAUSES OF RAPID SURFACE DEGRADATION

The surface degradation is referred to as wear, plastic deformation, RCF cracks (e.g. spalling damages, See [Figure 5.1](#)), etc., which are commonly observed on the crossing rail.

From the results of contact forces (See [Figure 5.20](#)), it can be seen that the nominal axle load (100 kN) has been drastically amplified more than 2 times (around 216.3 kN). Accordingly, both the maximum local contact normal (2072 MPa) and shear stresses (542 MPa) (See [Figure 5.21](#) and [Figure 5.22](#)) are increased accordingly around 2 times, in comparison to the case of normal wheel-rail interaction [17] (See [Table 5.5](#)). These impact-induced stresses (See [Section 5.4.1](#) and [Section 5.4.2](#)) exceed the yield limit of the material (480 MPa) greatly.

Considering the severe loading condition over one cycle, one might imagine that the processes of wear/RCF damage initiate in the microscopic scale. Under such cyclic loading condition, localized plastic deformation and/or cracks propagate proactively in the macroscopic scale. As a consequence, the rapid surface degradation in 1:9 crossing panel occurs.

## 5.5 CONCLUSIONS

In this chapter a three dimensional (3D) explicit finite element (FE) model of a wheel rolling over a 1:9 crossing rail has been developed. To address the associated FE modelling difficulties, a coupling strategy (called 'eFE-CS') that combines the two dimensional (2D) geometrical contact analyses has been proposed. The necessity of this coupling strategy has been investigated through the comparisons of FE simulated dynamic contact forces with those obtained from the 'conventional' FE model. Also, the accuracy of presented 'eFE-CS' model has been evaluated through effective experimental validations. The FE simulated stress solutions of dynamic impact at S&C have been presented. The further improvements and applications of the developed 'eFE-CS' model have been discussed. Based on the results and discussions, the following conclusions are drawn:

- (1) The detailed working scheme of coupling strategy has been introduced with application to the analysis of wheel-crossing (W/C) dynamic impact. Using this strategy, both the general and specific W/C FE modelling difficulties (e.g. 'gaps and/or penetrations', 'smooth mesh transitions', etc.) have been addressed. The comparative study shows that the calculation efficiency can be significantly improved using the 'eFE-CS' strategy, which can reduce the amount of elements and increase the calculation time step size. In short, the 'eFE-CS' is effective to address the FE modelling problems of W/C dynamic impact and is, thus, recommended to use in the contact/impact systems that having complex local contact geometries.
- (2) The validation of transition region estimated by the 'eFE-CS' model with the field measured one shows a good (about 100%) agreement at the starting point of the

transition process. As for the ending point, the discrepancies between filed measured and FE predicted results are getting much noticeable. The sources of these discrepancies have been explained (e.g. multiple wheel passages, variable local contact geometries, etc.).

- (3) The validation of crossing accelerations is performed from a statistical perspective. The results show that the magnitude of the impact accelerations from the FE model and the field measurements are comparable, while there are discrepancies observed. The sources of these discrepancies have been explained and categorised into different groups (such as, various operational patterns, unknown vehicle/track parameters, etc.). From these aforementioned experimental validations, it is worth noting that although the tolerable discrepancies exist, the FE results agree reasonably (95.5%, the two standard deviation from the measured mean) well with the field measurements.
- (4) The stress results show that the validated 'eFE-CS' model is capable of providing a detailed rolling contact stress solution of dynamic impact at 1:9 crossing rail. At the most impacted moment, surface normal contact pressure can be 4 times higher than the yield limit. From the subsurface stress analysis, it finds that the high stress state is concentrated in a considerably small volume of material. As a result, the risk of surface degradation (i.e. crack initiation, plastic deformation, etc.) is significantly increased.
- (5) As a major advantage of the 'eFE-CS' model, the detailed stress/strain solutions make it attractive to be used in other advanced applications (e.g. profile design and/or optimisation, Wear/RCF prediction, etc.).

## REFERENCES

- [1] S. Alfi and S. Bruni. Mathematical modelling of train–turnout interaction. *Vehicle System Dynamics*, 47(5):551–574, 2009.
- [2] Y. Bezin, I. Grossoni, and S. Neves. Impact of wheel shape on the vertical damage of cast crossing panels in turnouts. In Rosenberger M., editor, *IAVSD2015: 24th international symposium on dynamics of vehicles on roads and tracks, 17 - 21 August*, pages 1–10, Graz, Austria, 2015.
- [3] S. Bruni, A. Collina, G. Diana, and P. Vanolo. Lateral dynamics of a railway vehicle in tangent track and curve: tests and simulation. *Vehicle system dynamics*, 33 (Suppl.):464–477, 2000.
- [4] A. Cornish, E. Kassa, and R. Smith. Field experimentation and analysis at switches and crossings in UK. In *CM 2012: 9th international conference on contact mechanics and wear of rail/wheel systems, 27- 30 August*, pages 649–651, Chengdu, China, 2012.
- [5] European Committee for Standardization (CEN) EN 13715: 2006 + A1. Railway applications – wheelsets and bogies – wheels – tread profile, 2006.
- [6] I. Grossoni, Y. Bezin, and S. Neves. Optimization of support stiffness at a railway crossing panel. In Pombo J., editor, *Proceedings of the 3rd international conference on railway technology: Research, development and maintenance, 5 - 8 April*, pages 1–19, Cagliari, Italy, 2016.
- [7] J. O. Hallquist. ANSYS/LS-DYNA theoretical manual, 2005.
- [8] H. R. Hertz. Über die Berührung fester elastischer Körper und über die Härte. *Journal für die reine und angewandte Mathematik*, 92:156–171, 1882.

- [9] ANSYS Inc. Ansys release 17.1, mechanical applications theory reference, 2016.
- [10] A. Johansson, B. Pålsson, M. Ekh, J. C. O. Nielsen, M. K. A. Ander, J. Brouzoulis, and E. Kassa. Simulation of wheel–rail contact and damage in switches & crossings. *Wear*, 271(1):472–481, 2011.
- [11] K. L. Johnson. *Contact mechanics*. Cambridge university press, 1987.
- [12] J. J. Kalker. *Three-dimensional elastic bodies in rolling contact*, volume 2. Springer Science & Business Media, 1990.
- [13] E. Kassa and G. Johansson. Simulation of train–turnout interaction and plastic deformation of rail profiles. *Vehicle System Dynamics*, 44(sup1):349–359, 2006.
- [14] E. Kassa and J. C. O. Nielsen. Stochastic analysis of dynamic interaction between train and railway turnout. *Vehicle System Dynamics*, 46(5):429–449, 2008.
- [15] E. Kassa and J. C. O. Nielsen. Dynamic interaction between train and railway turnout: full-scale field test and validation of simulation models. *Vehicle System Dynamics*, 46(S1):521–534, 2008.
- [16] X. Liu, V. L. Markine, and I. Shevtsov. Performance study of a double crossover for facing and trailing directions. In *IAVSD 2015: 24th International Symposium on Dynamics of Vehicles on Roads and Tracks*, 17 - 21 August, pages 1–9, Graz, Austria, 2015. CRC Press.
- [17] Y. Ma, V. L. Markine, A. A. Mashal, and M. Ren. Modelling verification and influence of operational patterns on tribological behaviour of wheel-rail interaction. *Tribology International*, 114:264–281, 2017.
- [18] Y. Ma, V. L. Markine, A. A. Mashal, and Ren M. Improving the performance of finite element simulations on the wheel-rail interaction by using a coupling strategy. *Proceedings of the Institution of Mechanical Engineers, Part F: Journal of Rail and Rapid Transit*, 232(6):1741–1757, 2018.
- [19] Y. Ma, V. L. Markine, A. A. Mashal, and Ren M. Effect of wheel-rail interface parameters on contact stability in explicit finite element analysis. *Proceedings of the Institution of Mechanical Engineers, Part F: Journal of Rail and Rapid Transit*, 232(6):1879–1894, 2018.
- [20] Yuewei Ma, Abdul Ahad Mashal, and Valeri L Markine. Modelling and experimental validation of dynamic impact in 1: 9 railway crossing panel. *Tribology International*, 118:208–226, 2018.
- [21] V. L. Markine and I. Y. Shevtsov. Experimental analysis of the dynamic behaviour of railway turnouts. In B.H.V. Topping, editor, *The 11th international conference on computational structures technology, 4 - 7 September*, pages 1–10, Dubrovnik, Croatia, 2012.
- [22] V. L. Markine, M. J. M. M. Steenbergen, and I. Y. Shevtsov. Combatting RCF on switch points by tuning elastic track properties. *Wear*, 271(1):158–167, 2011.
- [23] A. A. Mashal. Analysis & improvement of railway crossing using explicit finite element method. Master of Science Thesis, Delft University of Technology, 2016.
- [24] M. Molodova, Z. Li, A. Núñez, and R. Dollevoet. Validation of a finite element model for axle box acceleration at squats in the high frequency range. *Computers & Structures*, 141:84–93, 2014.
- [25] International Union of Railways (UIC) Code: 515-1 OR. Passenger rolling stock - trailer bogies - running gear - general provisions applicable to the components of trailers bogies. Leaflet, 2003.
- [26] B. A. Pålsson. Design optimisation of switch rails in railway turnouts. *Vehicle System Dynamics*, 51(10):1619–1639, 2013.
- [27] B. A. Pålsson. Optimisation of railway crossing geometry considering a representative set of wheel profiles. *Vehicle system dynamics*, 53(2):274–301, 2015.
- [28] B. A. Pålsson and J. C. O. Nielsen. Wheel–rail interaction and damage in switches and crossings. *Vehicle system dynamics*, 50(1):43–58, 2012.

- [29] M. Pletz, W. Daves, and H. Ossberger. A wheel passing a crossing nose: Dynamic analysis under high axle loads using finite element modelling. *Proceedings of the Institution of Mechanical Engineers, Part F: Journal of rail and rapid transit*, 226(6):603–611, 2012.
- [30] M. Pletz, W. Daves, and H. Ossberger. A wheel set/crossing model regarding impact, sliding and deformation - explicit finite element approach. *Wear*, 294:446–456, 2012.
- [31] O. Polach. Creep forces in simulations of traction vehicles running on adhesion limit. *Wear*, 258(7):992–1000, 2005.
- [32] P. Pütz. User manual ESAH-M v2.2., 2011.
- [33] X. Shu, N. Wilson, C. Sasaoka, and J. Elkins. Development of a real-time wheel/rail contact model in nucars® 1 and application to diamond crossing and turnout design simulations. *Vehicle System Dynamics*, 44(sup1):251–260, 2006.
- [34] J. Tunna, J. Sinclair, and J. Perez. A review of wheel wear and rolling contact fatigue. *Proceedings of the Institution of Mechanical Engineers, Part F: Journal of Rail and Rapid Transit*, 221(2):271–289, 2007.
- [35] E. A. H. Vollebregt. User guide for contact, vollebregt & kalker's rolling and sliding contact model, technical report TR09-03, version, 2013.
- [36] E. A. H. Vollebregt. Numerical modeling of measured railway creep versus creep-force curves with contact. *Wear*, 314(1):87–95, 2014.
- [37] E. A. H. Vollebregt and P. Wilders. Fastsim2: a second-order accurate frictional rolling contact algorithm. *Computational Mechanics*, 47(1):105–116, 2011.
- [38] C. Wan and V. L. Markine. Parametric study of wheel transitions at railway crossings. *Vehicle System Dynamics*, 53(12):1876–1901, 2015.
- [39] C. Wan, V. L. Markine, and I. Y. Shevtsov. Improvement of vehicle–turnout interaction by optimising the shape of crossing nose. *Vehicle System Dynamics*, 52(11):1517–1540, 2014.
- [40] C. Wan, V. L. Markine, and I. Shevtsov. Optimisation of the elastic track properties of turnout crossings. *Proceedings of the Institution of Mechanical Engineers, Part F: Journal of Rail and Rapid Transit*, 230(2):360–373, 2016.
- [41] Z. Wei, C. Shen, Z. Li, and R. P. B. J. Dollevoet. Wheel–rail impact at crossings: Relating dynamic frictional contact to degradation. *Journal of Computational and Nonlinear Dynamics*, 12(4):041016, 2017.
- [42] J. Wiedorn, W. Daves, U. Ossberger, H. Ossberger, and M. Pletz. Simplified explicit finite element model for the impact of a wheel on a crossing—validation and parameter study. *Tribology International*, 111:254–264, 2017.
- [43] M. Wiest, E. Kassa, W. Daves, J. C. O. Nielsen, and H. Ossberger. Assessment of methods for calculating contact pressure in wheel-rail/switch contact. *Wear*, 265(9):1439–1445, 2008.
- [44] P. Wriggers and T. A. Laursen. *Computational contact mechanics*, volume 30167. Springer Science & Business Media, 2006.
- [45] L. Xin, V. L. Markine, and I. Y. Shevtsov. Numerical analysis of the dynamic interaction between wheel set and turnout crossing using the explicit finite element method. *Vehicle System Dynamics*, 54(3):301–327, 2016.
- [46] X. Zhao and Z. Li. The solution of frictional wheel–rail rolling contact with a 3D transient finite element model: Validation and error analysis. *Wear*, 271(1):444–452, 2011.
- [47] Z. H. Zhong and J. Mackerle. Contact-impact problems: A review with bibliography. *Applied Mechanics Reviews*, 47(2):55–76, 1994.





# 6

## CONCLUSIONS AND RECOMMENDATIONS

## 6.1 CONCLUSIONS

A three-dimensional (3D) explicit finite element (FE) model of W/R interaction has been developed in ANSYS LS-DYNA. To improve the performance of this model, a novel modelling strategy, called ‘enhanced explicit FE-based coupling strategy’ (abbreviated as ‘eFE-CS’), has been devised and implemented.

Following that, an in-depth study on the choice of interface parameters (penalty scale factor, mesh density, mesh uniformity, contact damping) on the performance of explicit FE model of W/R interaction has been performed, since the default values of the interface parameters provided in the commercial FE packages are not always suitable for the modelling of W/R rolling contact.

Also, to examine the accuracy of the FE model, a very-detailed verification of the FE model of W/R interaction against CONTACT has been carried out.

Finally, the FE model of W/R interaction has been further extended/upgraded to analyse the dynamic impact behaviour between wheel and crossing rail. The validity of this model has been assessed by comparing the simulated accelerations and transition regions with the filed measured ones.

In this section, the main conclusions of this study, addressing the research questions presented in [Chapter 1](#), are summarised.

**Q1:** *What kind of measures should be taken to guarantee and to improve the accuracy & efficiency of the FE model for the analysis of W/R interaction?*

[Chapter 2](#) aims to address the research question **Q1**. To improve the performance of the developed FE model of W/R interaction, a novel modelling strategy (‘eFE-CS’ modelling strategy) has been developed and presented.

### **Novel modelling strategy**

According to this ‘eFE-CS’ modelling strategy, the 2D geometrical contact method is used for

- Adjusting the W/R contact bodies to the “Just-in-contact” point,
- Predicting the FE mesh refinement in the potential contact areas,
- Determining the amount of traction corresponding to the actual rolling radius of the wheel, to be applied.

### **Accuracy & efficiency**

Using the proposed novel modelling strategy, the calculation accuracy & efficiency of explicit FE model of W/R interaction are assessed.

- The convergence problems of the FE simulations, resulting from the initial “gaps or penetrations”, are addressed.
- The compromise between calculation accuracy and efficiency is achieved, by making the economic mesh refinement (not redundant, insufficient or mismatched) in the potential contact areas.

- Using the adaptive mesh refinement procedure, the mesh patterns of the W/R FE model change depending on the location of the contact area and the local geometry of wheel and rail. Due to the adaptive mesh refinement, the calculation time could be reduced significantly (2~3 times) as compared to the regular mesh is ensured.
- The problems of initial slips, which are caused by the inaccurate estimation of the relationship between the angular and translational velocities exerted on the wheel, can be addressed. Efficient steady-state tangential solutions (within a short traveling distance of 50 mm) by applying the appropriate amount of traction are guaranteed.

**Q2:** *What is the effect of the interface parameters (penalty scale factor, mesh density, mesh uniformity, contact damping) on the performance of explicit FE simulations? How to make the choice of interface parameters, that are suitable for the analysis of W/R interaction?*

Chapter 3 aims to answer the research question **Q2**. A study on the effect of the interface parameters (penalty scale factor, mesh density, mesh uniformity, contact damping) on the accuracy of FE-based contact solutions has been performed.

#### **Phenomenon of “contact instability”**

The simulation results show that, when the interface parameters applied for W/R interaction are improperly selected: such as (1) too small (e.g. 0.1 by default) or too large (e.g. 200) penalty scale factor, (2) mesh size (size of 2.0 mm or even larger), (3) over-critical contact damping (e.g. increased by a factor of 1.8), the phenomenon of “contact instability” is observed.

In this study, the phenomenon of “contact instability” refers to unrealistic contact responses, which include the perturbation of contact force and the under-estimation of contact pressure.

#### **Suggested guidelines & interface parameters**

The guidelines for selecting proper interface parameters are formulated as:

- Increasing the value of penalty scale factor to be as large as possible to minimise the interpenetration during contact/impact, but not so large that the critical contact time step size is smaller than the stable time step size for the explicit time integration algorithm (i.e. central difference method). Here, the contact time step size is determined based on the contact stiffness of the invisible spring-damper contact elements. The stable calculated time step size is determined on the basis of the smallest critical time step value of all the other elements within the FE model.
- Selecting a mesh size, which makes the ratio between the contact area and the number of elements in contact to be around 1.0.

Following these guidelines, an appropriate set of interface parameters is suggested (i.e. penalty scale factor (12.8), damping factor (80), mesh size (dense meshed area: 2.0 mm; solution area: 1.0 mm).

- For the suggested/similar mesh patterns: The interface parameters suggested maintain the contact stability well and further ensure the calculation accuracy. Also, the interface parameters suggested have wide applicability for the cases of different axle loads, train speeds, W/R profiles, etc.
- For different mesh patterns: It means the form (uniformity) and level (density) of mesh discretization changes from the suggested mesh patterns. The interface parameters suggested may not fit. It is recommended to follow the general guidelines to find the suitable interface parameters.

**Q3:** *How to carry out the verification of FE models with realistic W/R profiles?*

Chapter 4 aims to answer the research question **Q3**. A detailed procedure of the explicit FE model verification via comparison of shear stresses, slip-adhesion areas, etc. against the CONTACT model has been devised.

#### **Modelling verification**

The good agreement of FE results with that of CONTACT indicates that the FE-based contact solutions are accurate. Therefore, the model can be used as a basis for further research on the prediction of Wear and RCF fatigue life that the detailed contact solutions are necessary.

#### **Varying operational patterns**

- The simulation results confirm that stress concentrations move towards the W/R surfaces with the increase of friction and/or traction, is helpful for devising proper lubrication strategies so as to mitigate the interface degradation (e.g. wear, rolling contact defects).
- The consideration of plasticity, as one of the most pronounced advantages of the FE method, will reduce the magnitude of the shear stress (55%) and contact pressure (31.8%). Also, the residual stress zone is observed at the distance of 1~2 mm under the surface along wheel travelling path. The lower the material yield strength is, the wider and deeper the residual stress zone will be. This shows the advantage of the FE method (as compared to CONTACT), which accounts for the material plasticity.

**Q4:** *Is it possible to extend/upgrade the FE model of W/R interaction to a new level for analysing the wheel-crossing (W/C) impact behaviour? How to validate this model experimentally?*

Chapter 5 aims to address the research question **Q4**. First, a feasibility study of extending/upgrading the FE model of W/R interaction so as to analyse the W/C impact behaviour has been performed. Based on the results of this study, the following conclusions are drawn.

#### **Modelling of W/C impact**

- The FE model of W/C impact has been developed successfully. The simulation results show the same analysing procedures/techniques applied for the case of W/R interaction, work properly for simulating the dynamic behaviour of W/C impact.

- Also, using the same novel modelling strategy, that is devised for improving the performance of FE simulations of W/R interaction, about 94% calculation time of explicit FE simulations of W/C impact could be saved.
- At the impact moment, the simulation results show that surface normal contact pressure could be 4 times higher than the material yield strength, and the subsurface stress analysis is concentrated in a considerably small volume of material.
- The results of this model give insights of the causes of rapid degradation (i.e. crack initiation/propagation, plastic deformation, etc.) in 1:9 railway crossing rail.

### Experimental validations

To assess the validity of the FE model of W/C impact, two procedures of experimental validation, namely comparing the (1) transition regions and (2) crossing accelerations against the field measured ones, are introduced and used.

- The comparison shows that transition region predicted by the ‘eFE-CS’ model starts at 180 mm from the nose point. This agrees with the field measured one well.
- The validation of crossing accelerations is performed from a statistical perspective. The magnitude of the FE simulated acceleration (38g) exactly falls within the range of the two standard deviation from the measured mean.
- The good agreement of the FE results with field measurements confirms that the FE model enhanced by the proposed modelling strategy can represent the reality well and is an accurate tool to be used for further design improvement or optimisation of railway crossings.

## 6.2 RECOMMENDATIONS

The FE model for attaining the detailed solutions of W/R frictional rolling contact has been developed. Also, the advantages of the novel modelling strategy, which improves the performance of the FE model of W/R interaction, have been demonstrated. Although such a strategy can strongly push the boundaries of what explicit FE models can do, there are still some research gaps to be filled. For instance,

### Further improvements of the FE model

- ◇ To enhance the steering capability: In the present FE model, the steering capability of the wheel is limited, since the yaw motion is not allowed and only roll motion is considered. For the study on the more complex cases of sharp (i.e. curve radius smaller than 500m) curves or the diverging route of turnout, it is necessary to introduce several torsional control units onto the wheel so as to enhance the steering capability.
- ◇ To simulate multiple wheel passages: Since only one wheel passage is considered in the FE model, the influence of the cyclic loading on the contact responses is excluded. For the accurate prediction of the service life of W/R interfaces, it is necessary to take the multiple wheel passages into consideration.

**Future applications of the FE model**

- ◇ To adjust and further extend the present modelling procedure to study the much complicated cases of W/R interaction (e.g. worn wheel and/or rail profiles, impact at insulated joints).
- ◇ To investigate the influence of critical operational conditions, for instance, the degraded adhesion and the presence of contaminants, on the performance of the transient wheel-rolling contact.
- ◇ To model the high frequency impact in the presence of surface defects, such as squats, corrugations and wheel flats by introducing single or multiple artificial semi-spherical/semi-ellipsoidal irregularities on the rail/wheel surfaces.
- ◇ To be used in other advanced applications such as wheel and/or rail profile design & optimisation, Wear/RCF prediction, etc.

# APPENDIX A

## A.1 EXPERIMENTAL METHODS: RECENT ADVANCES

As one of the most straightforward methods for analysing the damage mechanisms, the experimental studies have become increasingly popular.

For instance, the non-destructive testing techniques such as ultrasonic [4, 8], X-ray [18, 20, 24], optical and/or scanning electron microscopy (SEM) [6, 22, 23, 26–28, 33], electron backscatter diffraction (EBSD) [15, 24], etc., have been commonly used to study the formation mechanism of the rolling contact fatigue (RCF) defects. By this means, deep insights into the causes of RCF defects [4, 6, 8, 15, 20, 22, 23, 26–28, 33] can be gained.

The laboratory tests, using the twin-disc or the pin-on-disk test rigs [11], have been performed to analyse the competitive relationship between wear and RCF [5, 7, 29, 34]. Also, the effect of operational/mechanical parameters, such as the angle of attack [32], residual stress [25], traction & friction [3, 14, 21], on the performance of W/R interaction could be assessed. The damage phenomena such as rail corrugation [13], wear [1, 2, 30], etc. could be reproduced. However, given the artificial environment, the laboratory tests may not 100% represent the working condition of W/R interfaces.

On the contrary, field measurement [9, 10, 12, 16, 17, 19] takes place in the real-life settings. Despite the lack of easy accessibility, as compared to the laboratory tests, field measurement has become one of the most important means to assess the real-time structural health conditions of railway components. Both on-board (axle box acceleration (ABA) [12, 19], strain-gauge instrumented wheelset [9, 10]), track-instrumented [16, 17] and track-side measurements [31] have been used for the early detection of RCF defects and/or for the assessment/monitoring of structural health condition.

In this study, a track-instrumented measurement system, called Elektronische System Analyse Herzstijckbereich – Mobil (ESAH-M), is used for the purpose of model validation. More information about the ESAH-M system is given in [Chapter 5](#).

## REFERENCES

- [1] A. Anyakwo, C. Pislaru, A. Ball, and E. Gu. Modelling and simulation of dynamic wheel-rail interaction using a roller rig. In *Journal of Physics: Conference Series*, volume 364, page 012060. IOP Publishing, 2012.
- [2] F. Braghin, R. Lewis, R. S. Dwyer-Joyce, and S. Bruni. A mathematical model to predict railway wheel profile evolution due to wear. *Wear*, 261(11-12):1253–1264, 2006.
- [3] H. Chen and M. Ishida. Influence of rail surface roughness formed by rail grinding on rolling contact fatigue. *Quarterly Report of RTRI*, 47(4):216–221, 2006.
- [4] R. Clark. Rail flaw detection: overview and needs for future developments. *Ndt & E International*, 37(2):111–118, 2004.

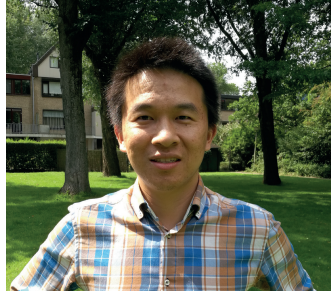


- [5] G. Donzella, A. Mazzù, and C. Petrogalli. Competition between wear and rolling contact fatigue at the wheel—rail interface: some experimental evidence on rail steel. *Proceedings of the Institution of Mechanical Engineers, Part F: Journal of Rail and Rapid Transit*, 223(1):31–44, 2009.
- [6] B. Dylewski, M. Risbet, and S. Bouvier. The tridimensional gradient of microstructure in worn rails—experimental characterization of plastic deformation accumulated by rcf. *Wear*, 392:50–59, 2017.
- [7] D. I. Fletcher and J. H. Beynon. Equilibrium of crack growth and wear rates during unlubricated rolling-sliding contact of pearlitic rail steel. *Proceedings of the Institution of Mechanical Engineers, Part F: Journal of Rail and Rapid Transit*, 214(2):93–105, 2000.
- [8] M. Guagliano and M. Pau. Analysis of internal cracks in railway wheels under experimentally determined pressure distributions. *Tribology International*, 40(7):1147–1160, 2007.
- [9] P. Gullers, P. Dreik, J. C. O. Nielsen, A. Ekberg, and L. Andersson. Track condition analyser: identification of rail rolling surface defects, likely to generate fatigue damage in wheels, using instrumented wheelset measurements. *Proceedings of the Institution of Mechanical Engineers, Part F: Journal of Rail and Rapid Transit*, 225(1):1–13, 2011.
- [10] Y. Ham, D. Lee, S. Kwon, W. You, and T. Oh. Continuous measurement of interaction forces between wheel and rail. *International Journal of Precision Engineering and Manufacturing*, 10(1):35–39, 2009.
- [11] A. Jaschinski, H. Chollet, S. Iwnicki, A. Wickens, and J. Würzen. The application of roller rigs to railway vehicle dynamics. *Vehicle System Dynamics*, 31(5-6):345–392, 1999.
- [12] Z. Li, X. Zhao, C. Esveld, R. Dollevoet, and M. Molodova. An investigation into the causes of squats—correlation analysis and numerical modeling. *Wear*, 265(9-10):1349–1355, 2008.
- [13] Q. Liu, B. Zhang, and Z. Zhou. An experimental study of rail corrugation. *Wear*, 255(7-12): 1121–1126, 2003.
- [14] X. Liu and P. A. Meehan. Investigation of the effect of relative humidity on lateral force in rolling contact and curve squeal. *Wear*, 310(1):12 – 19, 2014. ISSN 0043-1648. doi: <https://doi.org/10.1016/j.wear.2013.11.045>.
- [15] B. Lv, M. Zhang, F. Zhang, C. Zheng, X. Feng, L. Qian, and X. Qin. Micro-mechanism of rolling contact fatigue in hadfield steel crossing. *International Journal of Fatigue*, 44:273–278, 2012.
- [16] V. L. Markine and I. Y. Shevtsov. Experimental analysis of the dynamic behaviour of railway turnouts. In B.H.V. Topping, editor, *The 11th international conference on computational structures technology, September 4 – September 7*, pages 1–10, Dubrovnik, Croatia, 2012. Civil-Comp Press, Stirlingshire, UK.
- [17] V. L. Markine and I. Y. Shevtsov. An experimental study on crossing nose damage of railway turnouts in the netherlands. In B.H.V. Topping and Iványi P., editors, *Proceedings of the fourteenth international conference on civil, structural and environmental engineering computing (CC2013), 3 September – 6 September*, pages 1–11, Cagliari, Sardinia, Italy, 2013. Civil-Comp Press, Stirlingshire, UK.
- [18] M. Matsui and Y. Kamiya. Evaluation of material deterioration of rails subjected to rolling contact fatigue using x-ray diffraction. *Wear*, 304(1-2):29–35, 2013.
- [19] M. Molodova, Z. Li, A. Núñez, and R. Dollevoet. Validation of a finite element model for axle box acceleration at squats in the high frequency range. *Computers & Structures*, 141:84–93, 2014.
- [20] M. Neslušán, J. Čížek, K. Zgútová, P. Kejzlar, J. Šramek, J. Čapek, P. Hruška, and O. Melikhova. Microstructural transformation of a rail surface induced by severe thermoplastic deformation and its non-destructive monitoring via barkhausen noise. *Wear*, 402–403:38 – 48, 2018. ISSN 0043-1648.

- [21] U. Olofsson and K. Sundvall. Influence of leaf, humidity and applied lubrication on friction in the wheel-rail contact: pin-on-disc experiments. *Proceedings of the Institution of Mechanical Engineers, Part F: Journal of Rail and Rapid Transit*, 218(3):235–242, 2004.
- [22] S. Pal, C. Valente, W. Daniel, and M. Farjoo. Metallurgical and physical understanding of rail squat initiation and propagation. *Wear*, 284:30–42, 2012.
- [23] S. Pal, W. J. T. Daniel, and M. Farjoo. Early stages of rail squat formation and the role of a white etching layer. *International Journal of Fatigue*, 52:144–156, 2013.
- [24] Y. Satoh and K. Iwafuchi. Effect of rail grinding on rolling contact fatigue in railway rail used in conventional line in japan. *Wear*, 265(9-10):1342–1348, 2008.
- [25] J. Seo, B. Goo, J. Choi, and Y. Kim. Effects of metal removal and residual stress on the contact fatigue life of railway wheels. *International Journal of Fatigue*, 30(10-11):2021–2029, 2008.
- [26] M. Steenbergen. Squat formation and rolling contact fatigue in curved rail track. *Engineering Fracture Mechanics*, 143:80–96, 2015.
- [27] M. Steenbergen and R. Dollevoet. On the mechanism of squat formation on train rails—part i: Origination. *International Journal of Fatigue*, 47:361–372, 2013.
- [28] M. Steenbergen and R. Dollevoet. On the mechanism of squat formation on train rails—part ii: Growth. *International Journal of Fatigue*, 47:373–381, 2013.
- [29] R. Stock and R. Pippan. Rcf and wear in theory and practice—the influence of rail grade on wear and rcf. *Wear*, 271(1-2):125–133, 2011.
- [30] W. R. Tyfour, J. H. Beynon, and A. Kapoor. The steady state wear behaviour of pearlitic rail steel under dry rolling-sliding contact conditions. *Wear*, 180(1-2):79–89, 1995.
- [31] H. Wang, V. Markine, and X. Liu. Experimental analysis of railway track settlement in transition zones. *Proceedings of the Institution of Mechanical Engineers, Part F: Journal of Rail and Rapid Transit*, 232(6):1774–1789, 2018.
- [32] H. Yokoyama, S. Mitao, S. Yamamoto, and M. Fujikake. Effect of the angle of attack on flaking behavior in pearlitic and bainitic steel rails. *Wear*, 253(1-2):60–66, 2002.
- [33] W. Zhang and Y. Liu. Investigation of incremental fatigue crack growth mechanisms using in situ sem testing. *International Journal of Fatigue*, 42:14–23, 2012.
- [34] W. Zhong, J. Hu, P. Shen, C. Wang, and Q. Lius. Experimental investigation between rolling contact fatigue and wear of high-speed and heavy-haul railway and selection of rail material. *Wear*, 271(9-10):2485–2493, 2011.



# CURRICULUM VITÆ



## Yuewei MA

09-10-1987      Born in Ruzhou, China.

### EDUCATION

2005-2009      Bachelor in Mechanical Engineering  
Henan Institute of Science and Technology  
Xinxiang, China

2009-2012      Master in Engineering Mechanics  
Dalian University of Technology  
Dalian, China

2012-2018      PhD. in Railway/Civil Engineering  
Delft University of Technology  
Delft, The Netherlands

*Dissertation:*      Wheel-Rail Interaction: Enhanced explicit finite element modelling, verification and validation

*Promotor:*          Prof. dr. ir. R.P.B.J. Dollevoet

*Co-promotor:*      Dr. ir. V.L. Markine



# LIST OF PUBLICATIONS

## JOURNAL PAPERS

1. **Yuewei Ma, Valeri Markine, Abdul Ahad Mashal, Mingfa Ren**, *Improving the performance of finite element simulations on the wheel–rail interaction by using a coupling strategy*, Proceedings of the Institution of Mechanical Engineers, Part F: Journal of rail and rapid transit, **232**(6), 1741-1757 (2018).
2. **Yuewei Ma, Valeri Markine, Abdul Ahad Mashal, Mingfa Ren**, *Effect of wheel-rail interface parameters on contact stability in explicit finite element analysis*, Proceedings of the Institution of Mechanical Engineers, Part F: Journal of rail and rapid transit, **232**(6), 1879-1894 (2018).
3. **Yuewei Ma, Valeri Markine, Abdul Ahad Mashal, Mingfa Ren**, *Modelling verification and influence of operational patterns on wheel –rail tribological behaviour*, Tribology International, **114**, 264-281 (2017).
4. **Yuewei Ma, Abdul Ahad Mashal, Valeri Markine**, *Modelling and experimental validation of dynamic impact in 1: 9 crossing panel*, Tribology International, **118**, 208-226 (2018).

## CONFERENCE PAPERS

1. **Yuewei Ma, Valeri Markine**, *Rail surface crack initiation analysis using multi-scale coupling approach*, 24th international symposium on dynamics of vehicles on roads and tracks, Graz, Austria (2015).
2. **Yuewei Ma, Valeri Markine**, *A numerical procedure for analysis of W/R contact Using explicit Finite Element methods*, 10th International Conference on Contact Mechanics, Colorado Springs, USA (2015).
3. **Yuewei Ma, Valeri Markine**, *Numerical Analysis for Fatigue Life Prediction on Railroad RCF Crack Initiation*, 10th International Conference on Contact Mechanics, Colorado Springs, USA (2015).
4. **Yuewei Ma, Valeri Markine, Abdul Ahad Mashal**, *Numerical Analysis of Rail Surface Crack Propagation Under Cyclic Rolling-Sliding Contact Loads*, The Third International Conference on Railway Technology: Research, Development and Maintenance, Cagliari, Sardinia, Italy (2016).
5. **Yuewei Ma, Abdul Ahad Mashal, Valeri Markine**, *Numerical Analysis of Wheel –Crossing Interaction Using a Coupling Strategy*, The Third International Conference on Railway Technology: Research, Development and Maintenance, Cagliari, Sardinia, Italy (2016).



# ACKNOWLEDGEMENTS

Nothing can be accomplished, without the help and support of many dedicated individuals and institutions that I may not include completely.

My sincere gratitude, first and foremost, goes to my co-promotor, Dr. ir. Valeri Markine, for the PhD position that he offered to me, for the support, and for the guidance during the period of my PhD study. His suggestions are always constructive.

I'm indebted to my promotor, Prof. dr. ir. Rolf Dollevoet, who is leading the group of railway engineering towards a better future. The meetings with him are impressive.

Sincere appreciation to Asso. Prof. ir. Lambert Houben for making the invaluable time to read my dissertation and propositions from the perspective of an experienced supervisor, and for providing me numerous helpful comments/suggestions for improvement. Special thanks to the executive secretary, Ir. Sandra Ransdorp, for the great patience, the continuous help and the invaluable encouragement at the last stage of my PhD study. In one word, she is GREAT. Also, many thanks to the very kind help of Ms. Franca Post, Ms. Ilse Oonk and Mr. Jaap Meijer.

I'm grateful to China Scholarship Council for their financial support at the early stage of my PhD research. Moreover, I'm thankful to Prof. dr. Mingfa Ren (Dalian university of technology, China), for introducing me into the field of wheel-rail contact mechanics.

I would like to thank the former and present staff members at railway engineering group, especially to Ms. Jacqueline Barnhoorn. She did help a lot to address various kinds of issues such as hospitality, flight/hotel reservation, car rental, meeting arrangements, etc. Prof. dr. ir. Zili Li, sincere appreciation for taking me from the airport to the hotel during the conference of CM2015(Colorado Springs, USA). Dr. ir. Michaël Steenberg, it is pleasant and rewarding to work with him on the field measurement near Moerdijk bridge, and to exchange the ideas of how to take good care of baby. Dr. ir. Zhiwei Qian, many thanks for inviting me to chair the railway colloquium, and for supporting me to make the event dynamic and interactive. Ir. Evert van Veldhuizen, many thanks for inviting me to experience a real Dutch wedding ceremony, and for translating (together with Ing. Jan Moraal) my PhD summary into Dutch. Moreover, many thanks to the staff members: Dr. Alfredo Nunez Vicencio, Dr. Ling Chang, Ing. Martin Hiensch, Dr. Maha Messaadi, Ir. Jurjen Hendriks, Ing. Ellard Groenewegen, Ir. Behzad Hajizad, Ir. Ivan Ramirez Fonseca, Ir. Joris van Dijk, for the interesting & funny talks in coffee breaks.

I want to thank all the former and present PhD/MSc colleagues and visiting scholars at railway engineering group. To begin with, Abdul Ahad Mashal, a smart and very nice guy, sincere appreciation for the insightful discussions and fruitful collaborations on the MSc topic of wheel-crossing impact. Chang Wan, thanks for introducing me to the railway group and for sharing the valuable experiences of PhD survival. Haoyu Wang, thanks for sharing the (also Xiaoman's) invaluable experiences/techniques of job hunting. The



PhD life full of ups and downs would be the precious possession forever. Xiangyun Deng, Shaoguang Li, Zhen Yang, Zilong Wei, Xiangming Liu, Chen Shen, the parties we had and the happiness we shared, leave me a lot of good memories. Sadeh Akbarnejad, Maider Oregui, Meysam Naeimi, whom I shared office with at the first three years - a pleasant experience with the exchange of many interesting views upon life and research. Omid Hajizad and Ali Jamshidi, thanks for the journey of Beijing Summer school we travelled together. That is indeed joyful. Xiubo Liu, Song Liu, thanks for the coffee breaks and rewarding discussions. Also, many thanks to the colleagues: Nico Burgelman, Anthonie Boogaard, Rong Chen, Pingrui Zhao, Yu Zhou, Hongqin Liang, Xiaoping Wu, Qian Xiao, Xianmai Chen, Hongrui Wang, Pan Zhang, Yunlong Guo, Lei Xu, Li Wang, Wenqiang Liu, Chunyan He, Yang Jin, Siwarak Unsiwilai, Bin Zhu. It is my great fortune & honour to work with these excellent colleagues from day to day.

My deepest gratitude goes to the friends and railway colleagues, whom I met with in the Netherlands. Diederik van Lent, a very nice person, thanks for the wonderful memories of playing table tennis, and for the timely helping hands of double-checking the Dutch summary. Jian Zhang, many thanks for the kind help in all aspects. I'm especially grateful to my friends: Ye Zhang, Yuanhao Guo, Peng Lu, Tao Lv, Xuhong Qiang, Xu Jiang, Zhenshi Li, Junfeng Jiang, Liyuan Fan, Yuan Zhang, Ning Li, Dongya Ren, Meng Wang, Xuan Tao, for the friendship that warms me throughout the journey of my PhD study.

Dr. Ivan Shevtsov, an easy-going railway system specialist, special thanks for initiating the measurement projects, and for preparing the warm/cold drinks and delicious cookies during the hot/cold days/nights of field measurements. Ruud van Bezooijen, many thanks for managing/coordinating those projects, and for organising those impressive meetings at Rail-OK. Greg Lambert, an experienced driver and a knowledgeable welder, it's very kind of him to shuttle the passengers (PhD colleagues including me) safely back and forth from the measurement sites to the campus, and to share the invaluable experience/wisdom about welding and life.

I also need to thank my parents, relatives and friends in China. Without their continuous support & encouragement, it is hardly possible for me to step out of the comfortable zone, and to go the Netherlands to challenge myself.

Finally to my wife, Hongxia Zhou, I'm obliged to express my greatest gratitude to her, for spending so much time to read and correct the drafts of my papers & dissertation, for the enduring patience and understanding, and for bringing our lovely daughter, Lanyi Ma (thanks for joining us), to the world. You are the source of my inspiration.

Yuewei Ma  
November, 2017  
Delft, The Netherlands